INAUGURAL - DISSERTATION

submitted to the
Combined Faculties for the Natural Sciences and for Mathematics
of the Ruperto-Carola University of Heidelberg, Germany
for the degree of
Doctor of Natural Sciences

Put forward by
Dipl.-Phys. Fabian Zimmer
born in Offenburg

Oral examination: July 22, 2014

Development of Arterial Spin Labeling Techniques for Quantitative Perfusion Measurements at 3 Tesla

Referees: Prof. Dr. Lothar Schad
Prof. Dr. Wolfgang Schlegel

to my parents

Development of Arterial Spin Labeling Techniques for Quantitative Perfusion Measurements at 3 Tesla

Microvascular perfusion is an important parameter of high clinical value as it provides important information on tissue viability and function. In contrast to dynamic contrast-enhanced magnetic resonance imaging (DCE-MRI), arterial spin labeling (ASL) is a method to assess quantitative perfusion values non-invasively by MRI. The main goal of this work was the development of a 3D ASL technique that allows the quantitative perfusion measurement within a whole volume. Further, the diagnostic significance of ASL was tested by applying it in dedicated renal disease models. ASL yielded significantly ($P < 0.01$) different values in healthy kidneys ($(500 \pm 91)\,\mathrm{ml/100\,g/min}$) compared to kidneys with acute kidney injury ($(287 \pm 83)\,\mathrm{ml/100\,g/min}$) as well as for acutely rejected transplanted kidneys compared to chronically rejected grafts. A comparison to DCE-MRI showed no significant differences. While literature reports on 3D ASL sequences show a prevalence for spin-echo based data acquisitions, the presented sequence employs a 3D balanced steady-state free precession (bSSFP) readout that has the ability to overcome some of the drawbacks of spin-echo based 3D sequences. The developed 3D ASL technique includes several features, each of which has been optimized separately. Special emphasis was put on design, simulation, and implementation of a slice-selective adiabatic inversion pulse. In an initial measurement, the whole-brain perfusion of a healthy volunteer was assessed with an isotropic resolution of 3 mm. Mean perfusion values were $f_{\mathrm{GM}} = (51 \pm 17)\,\mathrm{ml/100\,g/min}$ and $f_{\mathrm{WM}} = (24 \pm 8)\,\mathrm{ml/100\,g/min}$ for gray and white matter, respectively, which are in very good agreement with findings from the "gold-standard" method of ^{15}O-positron emission tomography. The diagnostic value of ASL in combination with the possibility to assess absolute perfusion values in a whole volume makes it a promising technique for future clinical diagnosis.

Entwicklung von Arterial Spin Labeling-Techniken für die quantitative Perfusionsmessung bei 3 Tesla

Die mikrovaskuläre Perfusion liefert wertvolle Informationen über Gewebefunktion und -vitalität und ist damit ein wichtiger Parameter von hohem klinischen Wert. Im Gegensatz zur dynamischen kontrastmittelunterstützten Magnetresonanztomographie (DCE-MRT), stellt Arterial Spin Labeling (ASL) eine nicht-invasive Methode zur quantitativen Perfusionsmessung mittels MRT dar. Das Hauptziel dieser Arbeit war die Entwicklung einer 3D ASL-Technik, die die quantitative Perfusionsmessung innerhalb eines ganzen Volumens erlaubt. Darüber hinaus sollte die diagnostische Aussagekraft von ASL anhand von Krankheitsmodellen der Niere getestet werden. Die Messungen zeigten signifikant unterschiedliche Werte ($P < 0.01$) in gesunden Nieren ($(500 \pm 91)\,\mathrm{ml/100\,g/min}$) und Nieren mit akutem Nierenversagen ($(287 \pm 83)\,\mathrm{ml/100\,g/min}$), sowie in akut abgestoßenen Transplantatnieren verglichen mit chronisch abgestoßenen Transplantaten. Ein Vergleich zur DCE-MRT zeigte keine signifikanten Unterschiede. Während die Mehrzahl der in der Literatur beschriebenen 3D ASL Sequenzen Spin-Echo basierte Datenaufnahmen verwendet, wird in der vorgestellten Sequenz eine balancierte steady-state free precession (bSSFP) Auslese benutzt, die sich dafür eignet, einige Nachteile von Spin-Echo basierten 3D Sequenzen zu beseitigen. Die entwickelte 3D ASL Methode umfasst mehrere Funktionen, die jede für sich optimiert wurde. Besonders viel Wert wurde auf die Entwicklung, Simulation und Implementation eines schichtselektiven, adiabatischen Inversionspulses gelegt. In einer ersten Messung wurde die Perfusion des kompletten Gehirns eines gesunden Freiwilligen mit einer isotropen Auflösung von 3 mm bestimmt. Es wurde eine mittlere Perfusion von $f_{\mathrm{GM}} = (51 \pm 17)\,\mathrm{ml/100\,g/min}$ und $f_{\mathrm{WM}} = (24 \pm 8)\,\mathrm{ml/100\,g/min}$ in grauer bzw. weißer Materie gemessen. Diese Werte stimmen sehr gut mit denen überein, die mit der "Goldstandardmethode" ^{15}O-Positronen-Emissions-Tomographie gewonnen wurden. Der diagnostische Wert und die Möglichkeit absolute Perfusionswerte in einem kompletten Volumen zu messen, machen ASL zu einer vielversprechenden Technik für den zukünftigen Einsatz in der klinischen Diagnostik.

Contents

1 Introduction

Since its invention in the 1970s, magnetic resonance imaging (MRI) has become one of the most important diagnostic modalities in clinical routine. MRI bases on the intrinsic spin of nuclei and the associated magnetic moment. In a strong external magnetic field, the moments align with the streamlines of the field and produce a macroscopic magnetization which can be excited by radio waves. After excitation, the magnetization realigns with the external field and meanwhile emits a weak radio-frequency signal that can be detected with appropriate coils. Fortunately, the human body mainly consists of water providing a sufficient number of protons to detect a measurable signal. Although MRI involves radiation exposure, the deposited energy is extremely low and nonhazardous compared to the ionizing radiation used in modalities like computer tomography (CT) or positron emission tomography (PET). Furthermore, it is possible to image arbitrarily positioned slices and even whole volumes. Besides the superior soft-tissue contrast and the option to detect other nuclei that have a magnetic moment, one of the biggest assets of MRI is the possibility to examine functional parameters like diffusion, oxygenation and perfusion.

Perfusion describes the delivery of oxygen and nutrients to the tissue capillary bed driven by arterial blood flow. This comprises the transfer of water, hormones, electrolytes and even heat. It is therefore an important parameter for tissue viability and function providing pathophysiological information about the condition of an organ. For instance, its accurate measurement can yield information on cerebral ischemia [Ames 3rd et al., 1968], cardiac infarction [Ito et al., 1992], kidney function [Michaely et al., 2007] and can help targeting tumor areas [Weber et al., 2010]. Moreover, epilepsy, cancer, and neurodegenerative diseases are commonly accompanied by changes in blood flow.

Generally, perfusion is measured by following the path or the amount of a systemic substance, i.e. arterial blood, in the organ of interest. This tracking has to be enabled by using an appropriate tracer. Since the first quantitative measurements of perfusion by Kety and Schmidt [1945] who used nitrous oxide to trace the arterial blood supply in the brain, different measurement methods have been developed to assess per-

fusion in different parts of the body. Single photon emission computerized tomography (SPECT) and PET use photon and positron emitting tracers, respectively. In CT, iodinated contrast agents or stable xenon (Xe-CT) are utilized to track blood delivery to the tissue. However, the named methods either comprise the application of radioactive substances or the usage of X-rays. Thus, the patient is exposed to ionizing radiation which leaves MRI as the only modality that allows the determination of perfusion without this drawback. Furthermore, it offers a superior spatial resolution compared to the nuclear medicine methods SPECT and PET.

Different approaches exist to estimate and quantitate perfusion with MRI. One class of methods involves the injection of a contrast agent, normally a gadolinium chelate, that alters the magnetic properties in its vicinity. The associated signal drop due to magnetic susceptibilities and the signal enhancement due to higher relaxation rates, respectively, can be monitored by repeated imaging of the same field-of-view (FOV). The corresponding methods are named dynamic susceptibility-weighted MRI (DSC-MRI) [Rosen et al., 1990] and dynamic contrast-enhanced MRI (DCE-MRI) [Tofts and Kermode, 1991], respectively. Especially DCE-MRI has the advantage, that it allows the assessment of different functional parameters besides perfusion. For example, the glomerular filtration rate of the kidneys can be measured by applying an appropriate model to the data [Sourbron and Buckley, 2013]. However, in the last years, cases of nephrogenic systemic fibrosis (NSF) associated with gadolinium based contrast agents have been reported [Broome, 2008]. Furthermore, the application of contrast agent may be contraindicated in patients with certain conditions, like renal failure, or in pediatric populations. The second class of MRI-based methods for perfusion measurement does not have this disadvantages as it uses magnetically labeled water protons in arterial blood as an endogenous tracer. It is called arterial spin labeling (ASL) [Detre et al., 1992] and represents a completely non-invasive method, which makes it especially valuable for functional studies [Kim and Tsekos, 1997] or patients who require repetitive follow-up measurements. Further, it is useful for pharmacological studies [Salmeron and Stein, 2001] when physiological changes are monitored over time or possible interactions with contrast agents need to be avoided. To design a perfusion-sensitive experiment, ASL combines one of the three main labeling schemes (pulsed ASL (PASL) [Edelman et al., 1994], continuous ASL (CASL) [Williams et al., 1992], pseudo-continuous ASL (pCASL) [Dai et al., 2008]) with an adequate imaging sequence. A perfusion-weighted image is then created by subtracting a control image from an image of a perfusion-sensitive measurement, which effectively eliminates the signal of static tissue. One of the major drawbacks of ASL is its low signal-to-noise ratio (SNR), which makes the perfusion signal extremely prone to movement, physiological noise and any kind of technical imprecisions. While initial ASL experiments were single-slice brain feasibility measurements, ASL techniques have been steadily improved since its development in 1992. The influence of physiological parameters on absolute perfusion values was reduced [Wong et al., 1998b; Luh et al., 1999], background suppression techniques have been introduced to enhance the perfusion signal [Ye et al., 2000], and new quantitation models have been proposed [Buxton et al., 1998; Parkes, 2005; Petersen et al., 2006b], to name only a few. Furthermore, advances

in imaging sequences made it possible to acquire 3D ASL data sets [Günther et al., 2005; Dai et al., 2008] and to apply ASL in organs outside the brain, e.g. the kidneys [Roberts et al., 1995; Prasad and Priatna, 1999]. Still, even ASL brain perfusion measurements have not yet found their way into clinical routine. First commercial implementations of ASL exist on clinical MR scanners but the variety of labeling schemes, read-out options and quantitation models have restricted its accessibility to experts in this field. Recently published recommendations for its clinical application in the brain [Alsop et al., 2013] are at least a first step to improve this situation. Although the reproducibility of ASL has been tested [Bokkers et al., 2010; Artz et al., 2011a] and it has been compared to techniques that use exogenous tracers [Petersen et al., 2010; Gevers et al., 2011], its clinical acceptance and credibility is still very low. Especially studies that test the diagnostic significance of ASL in organs outside the brain are rare.

Generally, the perfusion signal of an ASL experiment can be recorded with any imaging sequence. However, due to the intrinsically low contrast, sequences with a high sensitivity should be preferred. Much of the published ASL techniques use echo-planar imaging (EPI) [Mansfield, 1977] due to its short acquisition time and high sensitivity. However, if ASL MRI of a whole volume rather than a single slice is desired, either 2D multislice or 3D readouts are necessary. Multi-slice acquisitions have the disadvantage of a slice dependency of the perfusion signal and an intrinsically lower sensitivity due to the smaller number of signals sampled in each voxel. For that reason, the preferred method to extent the imaging region is the employment of 3D sequences. The poor image quality of 3D EPI due to the long echo train in presence of T_2^* relaxation and the associated increase in sensitivity to magnetic field inhomogeneities and susceptibilities, essentially disqualifies EPI for 3D ASL measurements, particularly in the abdomen. First whole-volume acquisitions in combination with ASL, were spin-echo based multishot spiral sequences [Ye et al., 2000; Talagala et al., 2004] that were later replaced by spin-echo based single-shot 3D sequences like GRASE [Günther et al., 2005] or spiral FSE [Duhamel and Alsop, 2004]. While these sequences, both multishot and singleshot, have the disadvantage of signal variations due to inconsistent phase errors, the multishot approach additionally suffers from unequal perfusion weighting due to the multiple excitations. Further, background suppression can only be timed to null the tissue signal at one specific time point which makes it less powerful in combination with multishot sequences. While the 3D-FSE sequence is purely spin-echo based, the 3D-GRASE sequence uses a combination of gradient- and spin-echoes. Both readouts reduce image distortions induced by T_2^* relaxation compared to EPI. However, a trade-off between SNR and blurring due to T_2 relaxation has to be found. In contrast, balanced steady-state free precession (bSSFP) sequences offer a high SNR per unit time while signal losses due to T_2 relaxation are negligible and the advantages of single-shot sequences are conserved. Although the successful application of PASL in combination with 2D bSSFP sequences was shown in the brain [Boss et al., 2007] and in the kidneys [Martirosian et al., 2004], the promising combination of a 3D bSSFP sequence with PASL remains unexplored.

Due to the reasons mentioned above, this work had two objectives:
The major aim of this work was to develop and test a sophisticated 3D ASL sequence for quantitative perfusion measurements that uses an optimized 3D bSSFP readout. Besides the investigation of PASL in combination with a 3D bSSFP, this aim was further motivated by the successful employment of a 2D bSSFP sequence for renal ASL in small animals. As its quality is crucial for PASL experiments [Yongbi et al., 1999], special emphasis was put on the design and simulation of a refined slice-selective adiabatic inversion pulse in the development of the sequence. A further goal was to verify and test the clinical value of quantitative ASL measurements by comparing it to the findings of DCE-MRI, and by applying it in dedicated disease models. Hereby, focus was put on the ability to discriminate between normal and abnormal perfusion caused by pathophysiological changes. Against the background that chronic kidney diseases (CKD) are a global health issue with a predicted increase by more than 17% over the next decades [World Kidney Day, 2014], animal models of acute kidney injury and renal transplantation were chosen. To facilitate the transfer into clinical research or even routine, the aim was to establish the necessary ASL measurement on a clinical whole-body MR scanner.

2 Basics

In this chapter, the necessary basics for this work are outlined. After the explanation of the physical principles of nuclear magnetic resonance (NMR), the fundamentals of magnetic resonance imaging (MRI) are described. Finally, the term perfusion is defined and methods to assess and quantitate this parameter with MRI are presented.

2.1 Nuclear Magnetic Resonance

The origin of nuclear magnetic resonance may be found in the Stern-Gerlach experiment from 1921 [Gerlach and Stern, 1922a,b]. There, the quantization of angular momenta and therefore, intrinsic quantum properties of atoms and electrons, were first observed. Wolfgang Pauli was the first to propose a new quantum number to describe the observed discrepancies between molecular spectra and the upcoming theory of quantum mechanics [Pauli, 1924], the quantum number of the nuclear spin. In 1939, Isidor Isaac Rabi performed a nuclear spin experiment verifying Pauli's theory of the magnetic moment of an atomic nucleus [Rabi et al., 1939]. For his work, Rabi was awarded the Nobel Prize in Physics in 1944. In 1946, Felix Bloch and Edward Mills Purcell, independently of each other, published results of the first successful NMR experiment with protons [Bloch, 1946; Purcell et al., 1946]. In 1952, their work was honored with the Nobel Prize in Physics. This section describes the basic principles of NMR. For a more detailed description the reader is referred to the work of Abragam [1961], Slichter [1990] and Levitt [2008].

2.1.1 Nuclear Spin and Magnetic Moment

Atomic nuclei consist of protons and neutrons. Like all unpaired elementary particles, protons and neutrons possess a quantum property called spin, which is an intrinsic form of angular momentum. For the mentioned particles, the associated quantum number is 1/2. In nuclei with an odd nuclear number the spins of neutrons and protons do not cancel. Hence, these nuclei have a non-zero nuclear spin $\hat{\boldsymbol{I}}$ that is linked to a magnetic moment

$$\hat{\boldsymbol{\mu}} = \gamma \hat{\boldsymbol{I}}, \tag{2.1}$$

where γ is the nucleus-specific gyromagnetic ratio, that can be expressed as:

$$\gamma = \frac{g_I \mu_N}{\hbar}. \tag{2.2}$$

The constants g_I and $\hbar$ represent the particle-specific g-factor and the Planck constant ($\hbar = h/2\pi = 1.0545 \cdot 10^{-34}\,\mathrm{Js}$), respectively. The nuclear magneton μ_N is given by:

$$\mu_\mathrm{N} = \frac{e\hbar}{2m_\mathrm{p}}, \tag{2.3}$$

with the elementary charge e and the mass of the proton m_p. The magnetic moment can be orientated parallel or anti-parallel to the nuclear spin. Like every spin operator, the angular momentum operator $\hat{\boldsymbol{I}}$ obeys the commutation relations:

$$[\hat{I}_i, \hat{I}_j] = \mathrm{i}\hbar\varepsilon_{ijk}\hat{I}_k \qquad , \qquad [\hat{\boldsymbol{I}}^2, \hat{I}_i] = 0. \tag{2.4}$$

By choosing the eigenvectors $|I, m_I\rangle$ of $\hat{\boldsymbol{I}}^2$ and $\hat{I}_z$ as a basis (without loss of generality the quantization axis is parallel to the z-axis), the following eigenvalue equations hold:

$$\begin{aligned} \hat{I}_z|I, m_I\rangle &= m_I\hbar|I, m_I\rangle, \\ \hat{\boldsymbol{I}}^2|I, m_I\rangle &= I(I+1)\hbar^2|I, m_I\rangle, \end{aligned} \tag{2.5}$$

where we used the magnetic quantum number m_I and the spin quantum number I of the nuclear angular momentum. They can attain the following values:

$$\begin{aligned} I &= 0, \frac{1}{2}, 1, \frac{3}{2}, 2, \frac{5}{2}, \dots \\ m_I &= -I, -I+1, \dots, I-1, I. \end{aligned} \tag{2.6}$$

This means that $(2I+1)$ possible states exist for every quantum number I. The next section describes how this degeneracy disappears when an external field is applied.
In this work, NMR experiments have been solely conducted with the nucleus of hydrogen ^{1}H, i.e. the proton. Therefore, the following explanations and considerations will focus on the hydrogen nucleus. The magnetic moment of the proton is $\mu_\mathrm{p} = 2.79\,\mu_\mathrm{N} = 1.41 \cdot 10^{-26}\,\mathrm{J/T}$. Its gyromagnetic ratio is $\gamma_\mathrm{p} = 42.58\,\mathrm{MHz/T}$. Due to this large gyromagnetic ratio compared to other nuclei (cf. Table 2.1), the proton possesses a very good NMR sensitivity compared to other nuclei. This fact together with its high natural abundance, render an ideal candidate for magnetic resonance imaging.

2.1.2 Zeeman-Effect

The Hamiltonian of a particle with mass m and electric charge e in an external electromagnetic field is given by:

$$\hat{\mathcal{H}} = \frac{1}{2m}\left(\frac{\hbar}{\mathrm{i}}\nabla - e\boldsymbol{A}(\hat{\boldsymbol{r}}, t)\right)^2 + \mathrm{e}V(\hat{\boldsymbol{r}}, t), \tag{2.7}$$

Table 2.1: *List of selected nuclei with their corresponding spins, magnetic moments, gyromagnetic ratios and relative abundance in the human body. The negative algebraic sign of oxygen indicates the antiparallel magnetic moment with respect to the nuclear spin. Table adopted from Haacke et al. [1999].*

nucleus	spin	magnetic moment [μ_N]	γ [MHz/T]	abundance
hydrogen ^{1}H	1/2	2.793	42.58	88 M
sodium ^{23}Na	3/2	2.216	11.27	80 mM
phosphorus ^{31}P	1/2	1.131	17.25	75 mM
oxygen ^{17}O	5/2	-1.893	-5.77	16 mM
fluorine ^{19}F	1/2	2.627	40.08	4 µM
chlorine ^{35}Cl	3/2	4.17	0.36	76 mM

where $\boldsymbol{A}$ represents the vector potential and V the scalar potential, defined by the electric field and the magnetic field. With the Coulomb gauge condition $\nabla \boldsymbol{A} = 0$ the Hamiltonian can be rewritten:

$$\hat{\mathcal{H}} = -\frac{\hbar^2}{2m}\Delta + \frac{\mathrm{i}\hbar e}{mc}\boldsymbol{A}\cdot\nabla + \frac{e^2}{2m}\boldsymbol{A}^2 + eV. \tag{2.8}$$

For a constant magnetic field $|\boldsymbol{B}| = B_0$ the vector potential can be written as $\boldsymbol{A} = -1/2(\hat{\boldsymbol{r}} \times \boldsymbol{B})$ and the Hamiltonian simplifies to [Schwabl, 1998]:

$$\hat{\mathcal{H}} = -\frac{\hbar^2}{2m}\Delta - \frac{e}{2m}\hat{\boldsymbol{J}}\boldsymbol{B} + \frac{e^2}{8m}(\hat{\boldsymbol{r}} \times \boldsymbol{B})^2, \tag{2.9}$$

For a particle with no orbital angular momentum, the angular momentum operator $\hat{\boldsymbol{J}}$ can be replaced by the spin operator. The first term in Equation (2.9) is independent of the spin. Further, if $\langle \hat{\boldsymbol{J}} \rangle \neq 0$, the third term can be neglected with regard to the second term. Therefore, the Hamiltonian for a proton in an external magnetic field $\boldsymbol{B} = (0, 0, B_0)^\top$ along the z-axis is then given by:

$$\mathcal{H}_\mathrm{Z} = -g_I \frac{e}{2m}\hat{I}_z B_0 = -\gamma \hat{I}_z B_0, \tag{2.10}$$

where $\hat{I}_z$ is the z-component of the nuclear spin operator. By using the Schrödinger equation and Equation (2.5), the energy eigenvalues E_m of a proton in an external homogeneous magnetic field can be calculated:

$$\mathcal{H}_\mathrm{Z}|I, m_I\rangle = E_m|I, m_I\rangle = -\gamma \hat{I}_z B_0 |I, m_I\rangle = -\omega_0 m_I \hbar |I, m_I\rangle. \tag{2.11}$$

In the last step, the fundamental Larmor relation

$$\omega_0 = \gamma B_0, \tag{2.12}$$

with the Larmor frequency ω_0, was introduced. Equation (2.11) shows that there are $2I + 1$ energy levels with equal energy gaps $\Delta E = \hbar\omega_0$ between adjacent energy levels. The energy difference depends on the gyromagnetic ratio and the strength of the external magnetic field. This splitting of spectral lines is called Zeeman effect, after its discoverer Pieter Zeeman. Transitions between the energy levels can be induced and detected by the transmission and the reception of on-resonant photons. This interaction is called nuclear magnetic resonance. The nuclear spin of hydrogen is $I = 1/2$. In an external magnetic field this results in two states with $m_I = +1/2$ and $m_I = -1/2$. For $B_0 = 3\,\mathrm{T}$ the Larmor frequency amounts to 127.7 MHz. Figure 2.1 illustrates the splitting of the spectral lines for protons.

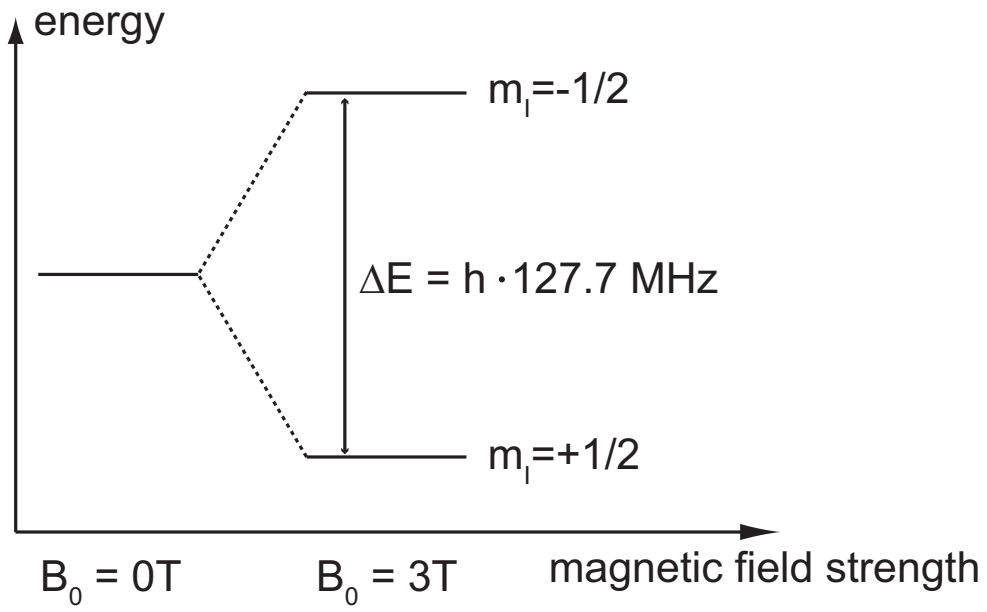

Figure 2.1: *Zeeman energy levels of hydrogen. Without an external magnetic field the energy levels are degenerated. In an external magnetic field, the energy levels split up. At $B_0 = 3\,T$, the energy difference between the two levels is $\Delta E = h \cdot 127.7\,MHz$.*

2.1.3 Macroscopic Magnetization

Magnetic resonance imaging does not deal with single protons but rather with a large number of hydrogen nuclei. A typical volume that is imaged is at least of the order of a few cubic millimeters. Regarding the Avogadro number ($N_\mathrm{A} = 6.022 \cdot 10^{23}\,\mathrm{mol}^{-1}$), the number of protons in such a volume is typically about $\approx 10^{20}$. Therefore, it is valid and convenient to introduce a macroscopic magnetization $\boldsymbol{M}$, that is the sum of the expectation values $\langle\hat{\boldsymbol{\mu}}\rangle$ of the N single magnetic moments in the volume V:

$$\boldsymbol{M} = M_0 = \sum_{i=1}^{N} \frac{\langle\hat{\boldsymbol{\mu}}\rangle}{V} = \sum_{i=1}^{N} \frac{\gamma\langle\hat{I}_z\rangle}{V} = \frac{N}{V} \sum_{m_I=-I}^{+I} p_m \gamma\hbar m_I, \tag{2.13}$$

where p_{m_I} is the probability that the respective energy level is populated and assuming an external magnetic field along the z-axis. From now on, if not otherwise specified, this assumption will be made throughout this chapter. In an external magnetic field, the energy levels split. In thermal equilibrium, the population of the different energy states is described by the Boltzmann statistics:

$$p_{m_I} = \frac{1}{Z} \mathrm{e}^{-E_{m_I}/\mathrm{k_B}T}, \qquad Z = \sum_{m_I=-I}^{+I} \mathrm{e}^{-E_{m_I}/\mathrm{k_B}T}, \tag{2.14}$$

where T is the temperature and $\mathrm{k_B} = 1.38 \cdot 10^{-23}\,\mathrm{J/K}$ the Boltzmann constant. Equation (2.13) can now be rewritten to:

$$M_0 = \frac{N}{V}\gamma\hbar \frac{\sum_{m_I=-I}^{+I} m_I \mathrm{e}^{-m_I\hbar\omega_0/\mathrm{k_B}T}}{\sum_{m_I=-I}^{+I} \mathrm{e}^{-m_I\hbar\omega_0/\mathrm{k_B}T}}. \tag{2.15}$$

The thermal energy at the body temperature ($\mathrm{T} \approx 310\,\mathrm{K}$) is much higher than the energy gap between the Zeemann levels $\hbar\omega_0 \ll \mathrm{k_B}T$. Therefore, the exponential in Equation (2.15) can be expanded in a Taylor series and truncated after the second term, yielding:

$$M_0 \approx \frac{N}{V} \frac{\gamma^2\hbar^2 I(I+1)}{3\mathrm{k_B}T} B_0, \tag{2.16}$$

where the relation $\sum m^2 = 1/3\, I(2I+1)(I+1)$ was used. The last equation shows that the macroscopic magnetization in thermal equilibrium is proportional to the spin density N/V, the square of the gyromagnetic ratio γ^2 and the external magnetic field B_0.

Equation of Motion

The motion of a magnetic moment in an external magnetic field is described by the temporal evolution of its expectation value. Generally, the temporal evolution of an expectation value can be calculated by the Ehrenfest theorem [Ehrenfest, 1927]. For the magnetic moment operator $\hat{\boldsymbol{\mu}}$ it can be expressed as follows:

$$\frac{\mathrm{d}\langle\hat{\boldsymbol{\mu}}\rangle}{\mathrm{d}t} = \langle -\frac{\mathrm{i}}{\hbar}[\hat{\boldsymbol{\mu}}, \mathcal{H}_\mathrm{Z}]\rangle = \gamma\langle\hat{\boldsymbol{\mu}}\rangle \times \boldsymbol{B}. \tag{2.17}$$

By using Equation (2.13) and the commutation relations for angular momentum operators, the above equation can be reformulated for the macroscopic magnetization:

$$\frac{\mathrm{d}}{\mathrm{d}t}\boldsymbol{M} = \gamma \boldsymbol{M} \times \boldsymbol{B}, \tag{2.18}$$

which is equal to a classical torque equation. Solving the equation for $\boldsymbol{B} = (0, 0, B_0)^\top$ shows that the magnetization precesses about the direction of the external field with an angular frequency ω_0.

2.1.4 Excitation

In order to detect the macroscopic magnetization, it needs to be tipped away from its equilibrium orientation to create a non-vanishing component transversal to the external field. Such an excitation can be achieved by inducing transitions between the Zeemann energy levels by means of a time-dependent magnetic field B_1. This can be realized by an electromagnetic wave whose frequency is close or equal to the Larmor frequency. This is why it is also referred to as radiofrequency (RF) excitation. The magnetic component of the RF field needs to be circular polarized and perpendicular to the external magnetic field:

$$\boldsymbol{B}_1(t) = \begin{pmatrix} B_1 \cos(\omega_{\mathrm{RF}} t) \\ B_1 \sin(\omega_{\mathrm{RF}} t) \\ 0 \end{pmatrix}. \tag{2.19}$$

The external field $\boldsymbol{B}_0 = (0, 0, B_0)^\top$ is assumed to point in z-direction. The overall field is then given by $\boldsymbol{B}(t) = \boldsymbol{B}_1(t) + \boldsymbol{B}_0$. By inserting $\boldsymbol{B}(t)$ in Equation (2.18) it states:

$$\frac{\mathrm{d}}{\mathrm{d}t}\boldsymbol{M} = \gamma \boldsymbol{M} \times \begin{pmatrix} B_1 \cos(\omega_{\mathrm{RF}} t) \\ B_1 \sin(\omega_{\mathrm{RF}} t) \\ B_0 \end{pmatrix}. \tag{2.20}$$

To eliminate the precession and the time dependency of the B_1 field, it is convenient to perform a coordinate transformation:

$$\begin{pmatrix} x' \\ y' \\ z' \end{pmatrix} = \begin{pmatrix} x \cos(\omega_{\mathrm{RF}} t) - y \sin(\omega_{\mathrm{RF}} t) \\ x \sin(\omega_{\mathrm{RF}} t) + y \cos(\omega_{\mathrm{RF}} t) \\ z \end{pmatrix}, \tag{2.21}$$

such that the reference frame rotates with the RF frequency ω_{RF} around the z-axis. Without loss of generality, the B_1 field vector is aligned with the y'-axis of the rotating reference frame. In the rotating frame, the equation of motion simplifies to:

$$\frac{\mathrm{d}}{\mathrm{d}t}\boldsymbol{M'} = \gamma \boldsymbol{M'} \times \begin{pmatrix} 0 \\ B_1 \\ B_0 - \frac{\omega_{\mathrm{RF}}}{\gamma} \end{pmatrix} = \gamma \boldsymbol{M'} \times \boldsymbol{B}_{\mathrm{eff}}. \tag{2.22}$$

In the last step the effective magnetic field $\boldsymbol{B}_{\mathrm{eff}}$ was introduced, which has two non-zero components along the y'- and z'-direction. Generally, the equation describes the rotation of the magnetization around the effective field with the frequency $\omega_{\mathrm{eff}} = \gamma \left|\boldsymbol{B}_{\mathrm{eff}}\right|$. In the common case where the RF excitation is on-resonant and $\omega_{\mathrm{RF}} = \omega_0$, the z-component vanishes and the magnetization precesses about the y'-axis. This rotation is illustrated in Figure 2.2, which shows the trajectory of the magnetization during on- and off-resonant excitation in the rotating frame of reference, respectively. There exist special RF pulses for which the above relation does not hold (cf. Section 3.5.1),

however for most RF pulses used in MRI, it is valid. For the derivation of the above results it was assumed that the duration of the RF excitation is short compared to the time scale of relaxation processes, which are described in the next section. Depending on the on the duration T_{pulse} of the RF excitation and the exact shape of the B_1 field, the precession flips the magnetization by an angle α that is given by:

$$\alpha = \gamma \int_0^{T_{\text{pulse}}} B_1(t)\,\mathrm{d}t. \tag{2.23}$$

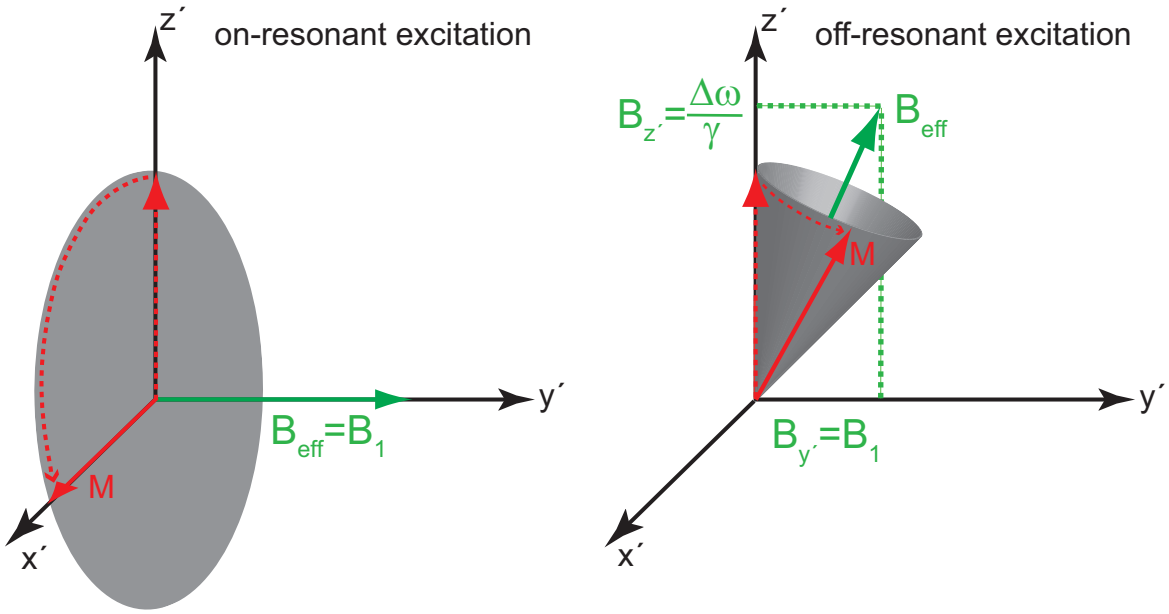

Figure 2.2: *RF excitation in the rotating frame of reference. Without loss of generality, the B_1 field is aligned with the y'-axis. In case the RF pulse is on-resonant ($\omega_0 = \omega_{\text{RF}}$), the magnetization M rotates about the effective field $B_{\text{eff}} = B_1$ and is flipped on the x'-axis. For off-resonant excitation ($\omega_0 \neq \omega_{\text{RF}}$), B_{eff} possesses a component in z'-direction and the magnetization precesses in a tight cone around it.*

2.1.5 Relaxation and Bloch Equations

The equation of motion (Equation (2.18)) and the relations derived from it (cf. Equation (2.22)), are only valid for an ideal ensemble of spins. In such an ensemble the spins are neither interacting amongst themselves nor with their environment. In reality, magnetization that is not in its equilibrium state and aligned with the external magnetic field, e.g. after RF excitation, will return to its thermal equilibrium state. This process is called relaxation. To account for this observation, Felix Bloch added empirical terms to the different components of Equation (2.18) and formulated the

so-called Bloch equations:

$$\begin{aligned}\frac{\mathrm{d}M_x}{\mathrm{d}t} &= \gamma\left(\boldsymbol{M}\times\boldsymbol{B}\right)_x - \frac{M_x}{T_2},\\ \frac{\mathrm{d}M_y}{\mathrm{d}t} &= \gamma\left(\boldsymbol{M}\times\boldsymbol{B}\right)_y - \frac{M_y}{T_2},\\ \frac{\mathrm{d}M_z}{\mathrm{d}t} &= \gamma\left(\boldsymbol{M}\times\boldsymbol{B}\right)_z - \frac{M_0 - M_z}{T_1}.\end{aligned} \tag{2.24}$$

The equations show that two independent relaxation processes are distinguished that occur at different rates. They concern the transversal component M_{xy} and the longitudinal component M_z of the magnetization. The associated relaxation times T_1 and T_2 are referred to as longitudinal and transversal relaxation times, respectively. The inverse of these times are called relaxation rates. In the following, both relaxation processes and their causes and are discussed separately.

Generally, the magnetic moment of the proton in an external field is not only affected by the static field but also by fluctuating local fields. In fluids, these randomly fluctuating fields originate from the thermal movement (translation and rotation) of the surrounding molecules and their interaction, mainly through dipole-dipole interaction. Depending on the properties of the sample, the local field has a typical spectral energy density $J(\omega)$.

Spin-Lattice Relaxation

The excitation of magnetization corresponds to a change of the population numbers of the Zeemann energy levels. In thermal equilibrium, all spins contributing to the macroscopic magnetization are aligned with the external magnetic field, i.e. the energy state with the lower energy. Spins that occupy the higher energy level after excitation tend to realign with the external field. However, the energy that is released during this process, has to be transferred to the surrounding, i.e. the lattice. Given that $J(\omega)$ has frequency components oscillating at the Larmor frequency, this energy transfer is possible and can be understood as a reversed RF excitation. Therefore, mainly the transversal components of the local field contribute to longitudinal relaxation. The relaxation time T_1 is thereby determined by the amplitude of $J(\omega)$ at the Larmor frequency ω_0. Spin-lattice or T_1 relaxation is described by the Bloch equation for the z-component of the magnetization. For an homogeneous external magnetic field the equation reads:

$$\frac{\mathrm{d}M_z}{\mathrm{d}t} = \frac{1}{T_1}(M_0 - M_z), \tag{2.25}$$

which is a first order linear differential equation whose solution is given by:

$$M_z(t) = M_0\left(1 - \mathrm{e}^{-t/T_1}\right) + M_z(0)\mathrm{e}^{(-t/T_1)}. \tag{2.26}$$

$M_z(0)$ denotes the initial longitudinal magnetization, e.g. directly after RF excitation. Typical T_1 relaxation times of tissue can be found in Table 2.2.

Table 2.2: *Tissue relaxation times for* ^{1}H *at 3 T as published in Stanisz et al. [2005] and de Bazelaire et al. [2004]*

tissue	T_1 [ms]	T_2 [ms]
brain		
gray matter	1820	99
white matter	1084	69
kidney		
cortex	1142	76
medulla	1545	81
subcutaneous fat	382	68
blood	1932	275

Spin-Spin Relaxation

Directly after excitation, the transversal components of different magnetization vectors are in phase. The longitudinal components of the local fluctuating fields, which add up to to the static field, result in locally varying Larmor frequencies. Hence, the individual magnetic moments precess at different speeds and the phase coherency is lost over time. Eventually, it results in a vanishing transversal component of the magnetization. This relaxation process is called transversal or spin-spin relaxation. For the high frequency components of $J(\omega)$, the time average is zero. For that reason, spin-spin relaxation is mainly caused by the low frequency components. However, also transversal components of the local fields, that oscillate at ω_0 contribute to the transversal relaxation. This is due to the fact, that they cause rotations about an axis in the transversal plane which not only result in a change of the z-component of the magnetization vector but also in a change of the transversal component. Hence, spin-spin relaxation mainly depends on the amplitude of $J(\omega)$ and $J(0)$. It is convenient to express the transversal component as a complex number:

$$M_{xy} = M_x + \mathrm{i}M_y = |M_{xy}|\,\mathrm{e}^{\mathrm{i}\Phi}. \tag{2.27}$$

By using this expression, the Bloch equations for x- and y-component of the magnetization can be combined. Assuming $\boldsymbol{B} = (0, 0, B_0)^\top$, they can be rewritten to:

$$\frac{\mathrm{d}M_{xy}}{\mathrm{d}t} = -\mathrm{i}\gamma B_0 M_{xy} - \frac{M_{xy}}{T_2}. \tag{2.28}$$

The solution of this differential equation is:

$$M_{xy}(t) = M_{xy}(0)\mathrm{e}^{-\mathrm{i}\gamma B_0 t}\mathrm{e}^{-t/T_2}. \tag{2.29}$$

The equation describes the precession of the transversal magnetization around the z-axis with the Larmor frequency ω_0 and its exponential decay with the time constant T_2. $M_{xy}(0)$ is the initial transversal magnetization.

In reality, transversal relaxation is not only driven by the local fluctuating field but further by static field inhomogeneities. The relaxation time that accounts for both effects is the effective transversal relaxation time T_2^* defined as:

$$\frac{1}{T_2^*} = \frac{1}{T_2} + \frac{1}{T_2'}, \tag{2.30}$$

where $1/T_2'$ is the rate that originates from the static inhomogeneities. Figure 2.3 illustrates the combination of both spin-spin and spin-lattice relaxation in the laboratory frame of reference after excitation with a 90° RF pulse. A theoretical description of all relaxation processes can be found in the so-called Bloembergen-Purcell-Pound (BPP) theory [Bloembergen et al., 1947].

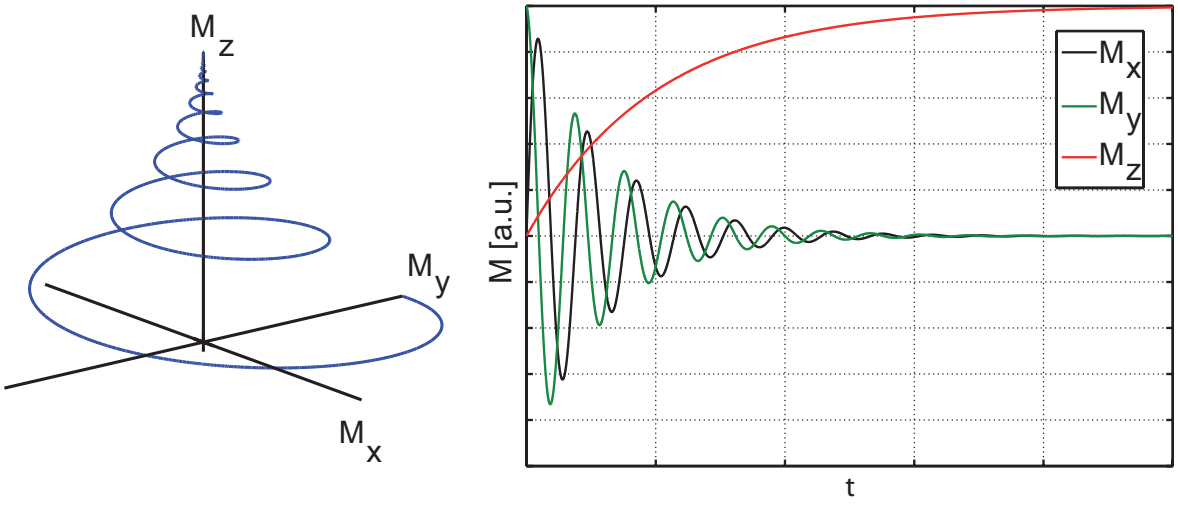

Figure 2.3: *Relaxation after a 90° excitation pulse. The left image depicts the trajectory of the magnetization vector spiraling towards its equilibrium state. On the right-hand side, the corresponding time course of the three magnetization components is shown.*

2.1.6 Signal Detection in NMR

In order to detect an NMR signal, the macroscopic magnetization needs to be excited to create a magnetization component perpendicular to the external field. After excitation, the transversal component M_{xy} precesses around the axis of the external field (cf. Equation (2.29)) and produces a time-dependent magnetic flux $\Phi(t)$. By positioning a receive coil whose normal is perpendicular to the main magnetic field, the changing magnetic flux induces a voltage V_{ind} in the coil, as described by Faradays's law:

$$V_{\text{ind}}(t) = -\frac{\partial \Phi}{\partial t} = -\frac{\partial}{\partial t} \int \boldsymbol{B}\, \mathrm{d}\boldsymbol{S}. \tag{2.31}$$

By using the vector potential $\boldsymbol{A}$, the magnetic field $\boldsymbol{B}$ can be expressed as $(\nabla \times \boldsymbol{A})$. Then, the above equation can be rewritten as a line integral using Stoke's theorem:

$$V_{\text{ind}}(t) = -\frac{\partial}{\partial t} \int (\nabla \times \boldsymbol{A}) \, \mathrm{d}\boldsymbol{S} = -\frac{\partial}{\partial t} \oint \boldsymbol{A} \, \mathrm{d}\boldsymbol{l}. \tag{2.32}$$

To derive a formula that is more useful for NMR, the explicit expression for $\boldsymbol{A}$ and the principle of reciprocity are used. The latter reverses the role of the detection coil and the magnetization source, i.e. the flux through the detection coil induced by the magnetization can be found by calculating the flux that would produce this magnetization. The induced voltage is then given by:

$$V_{\text{ind}}(t) = -\frac{\partial}{\partial t} \int \boldsymbol{B}_1(\boldsymbol{r}) \boldsymbol{M}(\boldsymbol{r}, t) \, \mathrm{d}\boldsymbol{r}, \tag{2.33}$$

where $\boldsymbol{B}_1$ denotes the "receive" field of the coil. Eventually, the signal S that is detected by the coil and the associated electronics, is proportional to V_{ind} yielding:

$$S \propto \omega_0 \int \mathrm{e}^{-t/T_2(\boldsymbol{r})} M_{xy}(\boldsymbol{r}, 0) B_{1,xy}(\boldsymbol{r}) \sin(\omega_0 t + \Phi_B(\boldsymbol{r}) - \phi_M(\boldsymbol{r})) \, \mathrm{d}\boldsymbol{r}, \tag{2.34}$$

where we used Equation (2.29) to express the transversal magnetization and introduced the transversal component $B_{1,xy}$ of the "receive" field with its initial phase angle Φ_B and ϕ_M the initial phase angle of M_{xy}. Further, as the time derivatives of e^{-t/T_1} and e^{-t/T_2} can be neglected compared to the derivative of $\mathrm{e}^{-\mathrm{i}\omega_0 t}$, we assumed the rapid Larmor oscillation of M_{xy} as the only source of signal induction in the receive coil. By demodulating the signal with ω_0, Equation (2.34) states:

$$S \propto \omega_0 \int \mathrm{e}^{-t/T_2(\boldsymbol{r})} M_{xy}(\boldsymbol{r}, 0) B_{1,xy}(\boldsymbol{r}) \mathrm{e}^{\mathrm{i}(\Phi_B(\boldsymbol{r}) - \phi_0(\boldsymbol{r}))} \, \mathrm{d}\boldsymbol{r}. \tag{2.35}$$

A more detailed discussion of the NMR signal and its detection with receive coils can be found in Haacke et al. [1999].

2.2 Magnetic Resonance Imaging

This section describes the methods to generate spatially resolved images of the NMR signal. Magnetic resonance imaging (MRI) was developed in the 1970s. In 1973 Paul Lauterbur had the groundbreaking idea that the spatial position of an NMR signal can be determined by adding gradient fields [Lauterbur et al., 1973]. In 2003, he was awarded the Nobel Prize in Physiology or Medicine together with Sir Peter Mansfield who developed the mathematical methods for a fast conversion of NMR signals to image data. Further, he developed the first imaging technique that allowed an image acquisition below one second. The technique bases on fast field gradients and is known as echo planar imaging (EPI) [Mansfield, 1977]. Besides the description of the basics of MRI, the section covers elemental MR sequences and image contrasts. For further reading, the reader is referred to [Haacke et al., 1999] and [Bernstein et al., 2004].

2.2.1 Spatial Encoding and *k*-Space

By adding additional magnetic gradient fields $\boldsymbol{G}$ parallel to the main magnetic field $\boldsymbol{B} = (0, 0, B_0)^\top$, the Larmor frequency becomes spatially dependent. For a gradient field of the form:

$$\boldsymbol{G}(t) = (G_x(t), G_y(t), G_z(t))^\top = \left(\frac{\partial B_z}{\partial x}, \frac{\partial B_z}{\partial y}, \frac{\partial B_z}{\partial z}\right)^\top, \tag{2.36}$$

the Larmor frequency is determined by the superposition of both magnetic fields and reads:

$$\omega(\boldsymbol{r}, t) = \gamma(B_0 + \boldsymbol{G}(t)\boldsymbol{r}) = \omega_0 + \omega_\mathrm{G}(\boldsymbol{r}, t). \tag{2.37}$$

By applying the additional gradient fields for a time t, the magnetization at the position $\boldsymbol{r}$ acquires an additional phase ϕ that is given by:

$$\phi(\boldsymbol{r}, t) = -\int_0^t \omega_\mathrm{G}(\boldsymbol{r}, t')\,\mathrm{d}t' = -\gamma\boldsymbol{r}\int_0^t \boldsymbol{G}(t')\,\mathrm{d}t' = -\boldsymbol{k}(t)\boldsymbol{r}, \tag{2.38}$$

The wave number vector $\boldsymbol{k}$ represents a point in the so-called k-space as is defined as:

$$\boldsymbol{k}(t) = (k_x(t), k_y(t), k_z(t))^\top = \gamma\int_0^t \boldsymbol{G}(t')\mathrm{d}t'. \tag{2.39}$$

Rewriting Equation (2.35) by accounting for the additional phase acquisition $\phi(\boldsymbol{r}, t)$ yields:

$$S \propto \omega_0 \int \mathrm{e}^{-t/T_2(\boldsymbol{r})} M_{xy}(\boldsymbol{r}, 0) B_{1,xy}(\boldsymbol{r}) \mathrm{e}^{-\mathrm{i}(\boldsymbol{k}(t)\boldsymbol{r} - \Phi_B(\boldsymbol{r}) + \phi_\mathrm{M}(\boldsymbol{r})))}\,\mathrm{d}\boldsymbol{r}. \tag{2.40}$$

This equation can be simplified by neglecting relaxation and assuming a homogeneous "receive" field $B_{1,xy}(\boldsymbol{r}) = \text{const.}$:

$$S(\boldsymbol{k}(t), t) \propto \int M_{xy}(\boldsymbol{r}) \mathrm{e}^{-\mathrm{i}(\boldsymbol{k}(t)\boldsymbol{r})}\,\mathrm{d}\boldsymbol{r}, \tag{2.41}$$

where $M_{xy}(\boldsymbol{r}, t) = M_{xy}(\boldsymbol{r}, 0)\mathrm{e}^{\mathrm{i}\phi_\mathrm{M}(\boldsymbol{r})}$ was used. Equation (2.41) shows that the signal is proportional to the Fourier transform (FT) [Fourier, 1822] of the spatial distribution of the transversal magnetization. This means that the distribution $M_{xy}(\boldsymbol{r})$, i.e. the MR image, can be calculated by an inverse FT:

$$M_{xy}(\boldsymbol{r}) \propto \int S(\boldsymbol{k}(t), t) \mathrm{e}^{2\pi\mathrm{i}\boldsymbol{k}(t)\boldsymbol{r}}\,\mathrm{d}\boldsymbol{k}. \tag{2.42}$$

By altering $\boldsymbol{k}$ with the help of appropriate gradient coils, the signal at any point in k-space can be sampled. Eventually, a spatially resolved image can be reconstructed by using the inverse FT. The low frequencies are found in the center of k-space and contribute the contrast information whereas the information about fine details is provided by the high frequencies in outer k-space (cf. Figure 2.8).

In the following, spatial encoding is explained using the example of an MRI experiment where a 2D slice of an object is imaged. Three encoding techniques known as slice selection, phase encoding and frequency encoding are necessary.

Slice Selection

In order to detect a signal, the magnetization needs to be tipped away from its equilibrium orientation, which is achieved by RF excitation (cf. Section 2.1.4). Without any gradient fields the complete magnetization within the range of the transmitter coil is flipped. For 2D imaging, slice-selective excitation is used that only produces transversal magnetization in the desired slice. This is achieved by applying a magnetic gradient field parallel to the slice normal while transmitting the RF pulse. As a consequence of the so-called slice-selection gradient, the Larmor frequency along its direction is spatially dependent and the resonance condition is only fulfilled at the desired slice position. Given that the RF pulse has a bandwidth of $\Delta\omega$, the thickness Δz of the excited slice is given by:

$$\Delta z = \frac{\Delta\omega}{\gamma G}, \tag{2.43}$$

where G denotes the constant slice-selection gradient amplitude. For small flip angles and constant gradient amplitudes, the excitation profile of the RF pulse is given by the Fourier transform of its B_1 envelope (cf. Section 3.5.3). Figure 2.4 illustrates the influence of $\Delta\omega$ and G on Δz using the example of a *sinc*-shaped excitation pulse. The combination of slice-selection gradient and RF pulse is also used for slice-selective inversion.

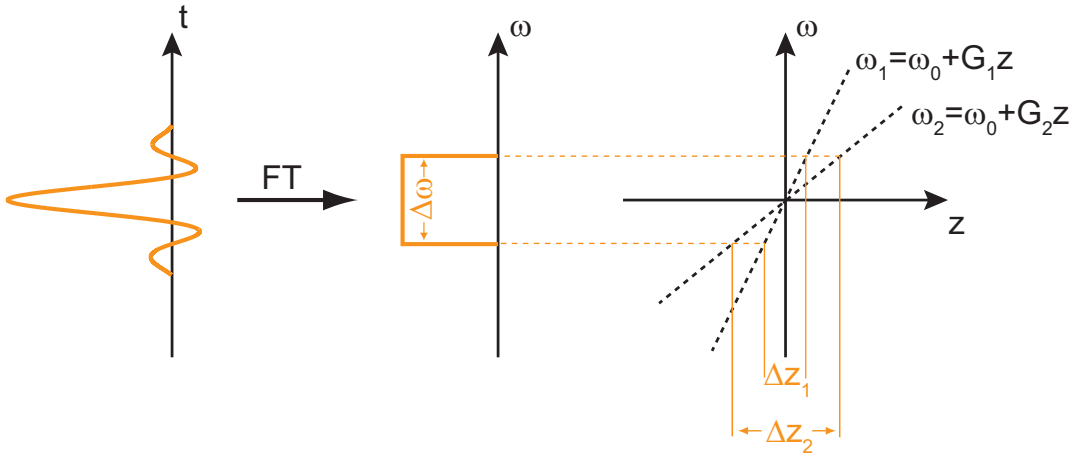

Figure 2.4: *Principle of slice-selective inversion using the example of a sinc-shaped excitation pulse and two different gradient amplitudes. The sinc-shaped B_1 envelope results in the excitation of a rectangular spectrum with bandwidth $\Delta\omega$ in the frequency domain. Depending on the gradient amplitude G, the thickness Δz of the excited slice varies. For a given G, Δz can also be altered by changing $\Delta\omega$.*

Phase Encoding

After the excitation of the desired slice, the two remaining directions need to be encoded (without loss of generality the x- and y-direction). By applying a gradient along the y-axis, the magnetization acquires an additional phase (cf. Equation (2.38)), that depends on the spatial position in y-direction as well as the amplitude and the duration (i.e. the gradient moment) of the so-called phase-encoding gradient. Depending on the spatial resolution and the imaged field-of-view, several phase encoding steps need to be performed, each with different gradient momenta. Figure 2.5 illustrates the principle of phase-encoding.

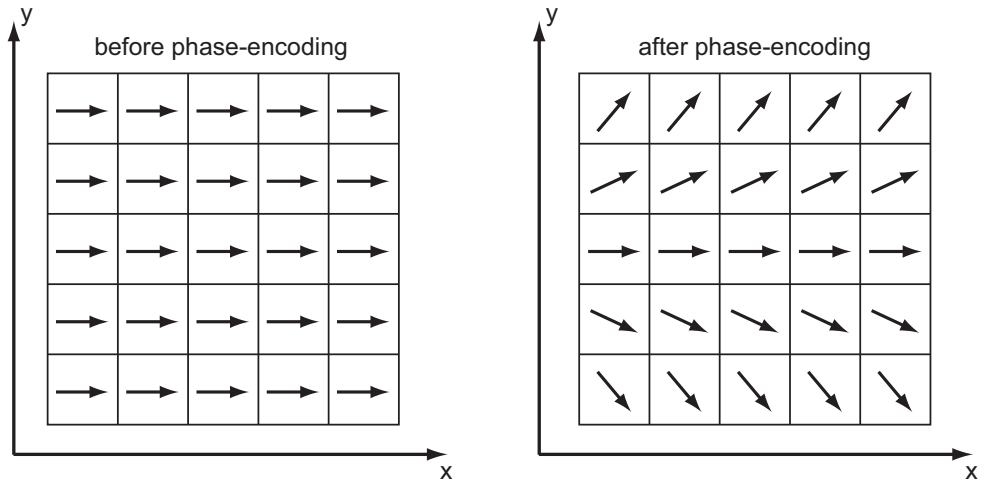

Figure 2.5: *Principle of phase-encoding. After RF excitation the phase of the transversal magnetization is coherent (left panel). After application of a phase-encoding gradient (right panel) in y-direction, the position along the y-axis is encoded in the phase of the magnetization. Adapted from Bernstein et al. [2004].*

Frequency Encoding

As a last step the spatial positions in x-direction need to be encoded. Therefore, a so-called frequency-encoding or readout gradient is applied along the x-axis during data acquisition. As a consequence, each spatial position x can be clearly identified by its unique Larmor frequency (cf. Equation (2.37)). The impact of frequency encoding on the signal and the image is depicted in Figure 2.6. The Figure shows two samples of water placed into a homogeneous external magnetic field B_0. Without the application of an additional gradient field (a), the Larmor frequency is identical in both samples. Accordingly, the the frequency of the signal recorded after excitation (2) equates to the Larmor frequency. A Fourier transformation of the signal yields its spectrum (c) and shows a single peak at the Larmor frequency whose width is defined by T_2^*. With the application of a frequency-encoding gradient (d), the signal is composed of different frequencies (e). Now, the spectrum of the signal (f) reflects the spin-density along the frequency-encoding direction showing the projections of both water samples. In 3D imaging, the slice-selective excitation is replaced by a non-

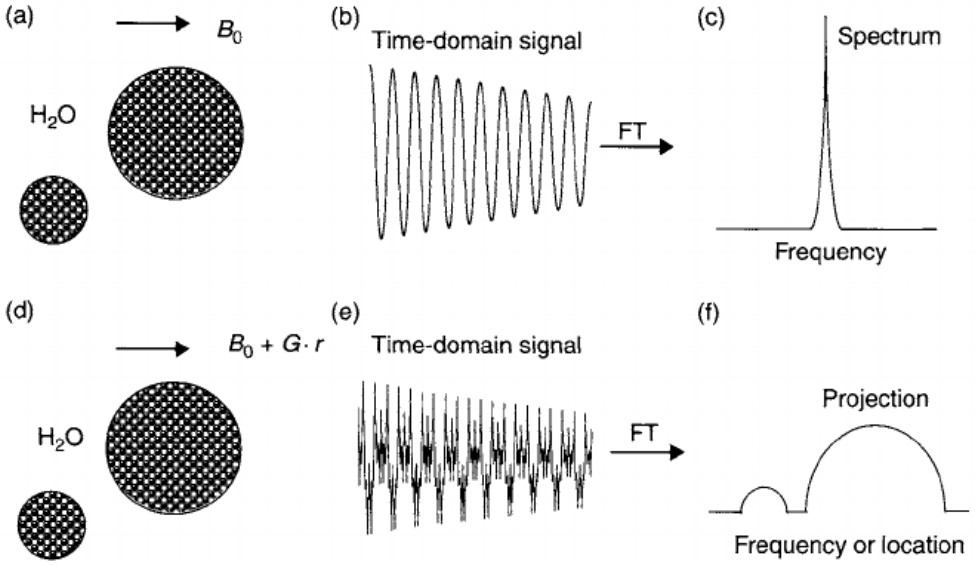

Figure 2.6: *Principle of frequency-encoding and its impact on the NMR signal. Without the application of an additional gradient field (a), the Larmor frequency is identical in both samples. Accordingly, the frequency of the NMR signal (2) equates to the Larmor frequency and a Fourier transformation of the signal yields a single peak (c). With the application of a frequency-encoding gradient (d), the signal is composed of different frequencies (e). Now, the spectrum of the signal (f) reflects the spin-density along the frequency-encoding direction showing the projections of both water samples. From Bernstein et al. [2004]*

selective excitation. Normally, a rectangular shaped RF pulse is used. To encode all three dimensions, phase-encoding is performed in two directions. For the missing third dimension, frequency-encoding is used.

2.2.2 Discrete *k*-Space Sampling and Image Resolution

Due to technical and temporal limitations, k-space cannot be sampled continuously and only to a limited extend. The consequences of discrete and limited k-space sampling are outlined in the following. With out loss of generality, all derivations are performed for the one-dimensional case but can generally be expanded to cover more dimensions. For a constant readout gradient G and a sampling in constant time intervals of Δt, the distance of k-space points where signal is recorded, is given by $\Delta k = \gamma G \Delta t$. The sampled signal $S_{\text{sampled}}(k)$ can be interpreted as a continuous signal multiplied by a sampling function $u(k)$, that is given by a sum of equally spaced Dirac-Delta functions and known as *Dirac comb* or *Shah* function [Bracewell, 1980]. The sampled signal then reads:

$$S_{\text{sampled}}(k) = S(k) \cdot u(k) = S(k) \cdot \Delta k \sum_{n=-\infty}^{\infty} \delta(k - n\Delta k) \cdot r(k), \tag{2.44}$$

where $r(k)$ is a rectangle function accounts for the limited k-space coverage with a maximal extend of $2k_{\max}$:

$$r(k) = \begin{cases} 1 & -k_{\max} \leq k \leq k_{\max} \\ 0 & \text{else.} \end{cases} \tag{2.45}$$

$k_{\max}$ depends on the gradient moment. By using Equation (2.42) and the convolution theorem, the MR image calculated from S_{sampled} is given by:

$$M_{\text{sample}}(r) = \mathcal{F}^{-1}[S_{\text{sampled}}(k)] = M_{xy}(r) \otimes \mathcal{F}^{-1}[u(k)] \otimes \mathcal{F}^{-1}[r(k)], \tag{2.46}$$

where $\otimes$ denotes a convolution. The inverse FT of $u(k)$ and $r(k)$ can expressed analytically:

$$\mathcal{F}^{-1}[u(k)] = \sum_{n=-\infty}^{\infty} \delta\left(r - \frac{n}{\Delta k}\right), \tag{2.47}$$

$$\mathcal{F}^{-1}[r(k)] = 2k_{\max}\,\text{sinc}(2\pi k_{\max} r). \tag{2.48}$$

Equation 2.47 represents a *Shah* function, but with a periodicity of $1/\Delta k$. This leads to periodically repeated and equally spaced copies of the real imaged object in image space. The separation of the copies is $1/\Delta k$. To avoid overlapping and the appearance of another copy of the object within the desired field-of-view (FOV), the so-called Nyquist criterion [Nyquist, 1928] has to be fulfilled:

$$\Delta k \overset{!}{\leq} \frac{1}{\text{FOV}}. \tag{2.49}$$

Image artifacts due to an unfulfilled Nyquist criterion or due to objects outside the FOV are referred to as aliasing artifacts. A violation of the Nyquist criterion is shown in Figure 2.7. The left-hand side shows a completely sampled k-space (1) and the resulting

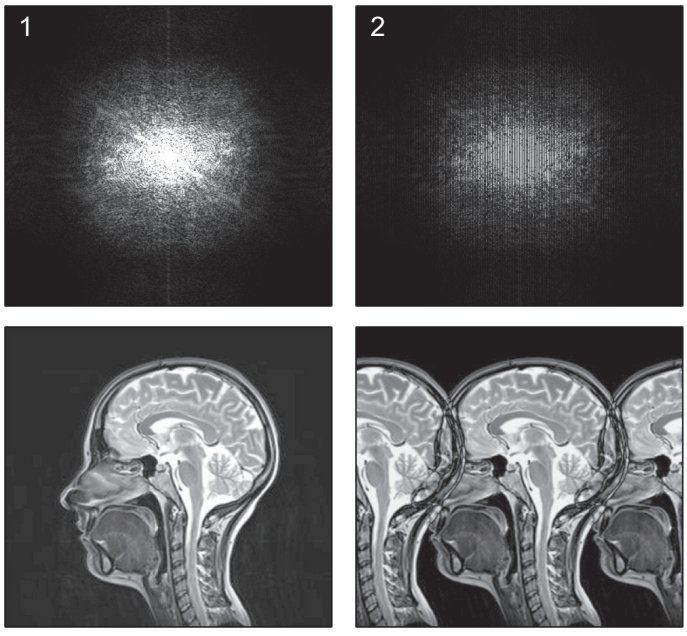

Figure 2.7: *Raw k-space data (upper panels) and the reconstructed MR images (lower panels). The left-hand side shows a completely sampled k-space (1) and the resulting image. On the right, k-space was subsampled by factor of two in one direction (2), which results in aliasing artifacts in the image.*

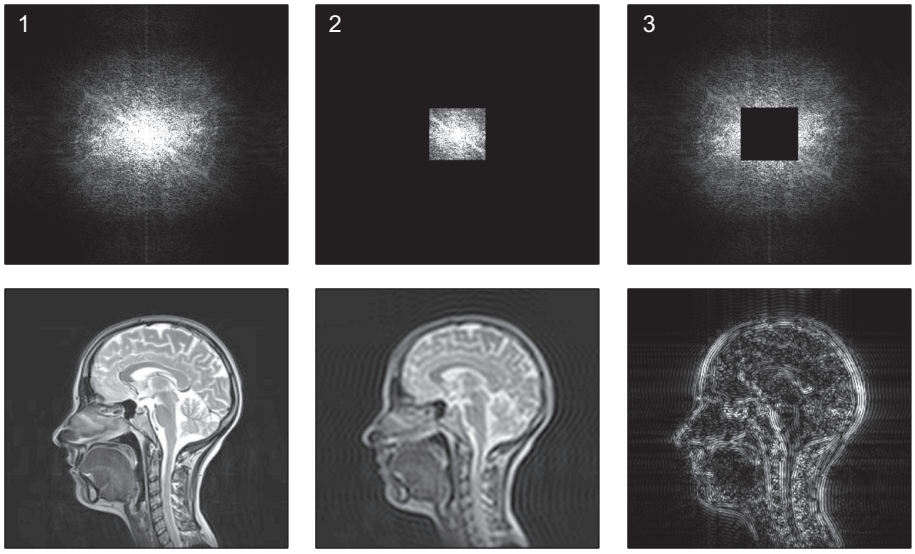

Figure 2.8: *Raw k-space data (upper panels) and the corresponding MR images (lower panels) obtained by Fourier transformation. On the left, the result of a complete k-space sampling (1) is shown. The two central panels (2) illustrate the influence of $k_{\max}$, which was reduced to 20% of the original value resulting in a lower resolution of the MR image. The right-hand side (3) shows the inverse case, which demonstrates that the outer k-space points contribute to the fine structures in the MR image.*

image. On the right, k-space was subsampled by factor of two in one direction (2), which results in aliasing artifacts in the image. The solution of the inverse FT of $r(k)$ yields the relation between the image resolution Δr and $k_{\max}$. Equation (2.48) states that a point-shaped object will be imaged as a sinc function. The resolution is then defined as the full width half maximum (FWHM) of the sinc function:

$$\Delta r = \frac{1}{2k_{\max}} \tag{2.50}$$

A further implication of the sinc function or more precisely its side-lobes, is the occurrence of so-called Gibbs ringing, spurious ring-shaped signals that appear near edges. Figure 2.8 shows raw k-space data (upper panels) and the corresponding MR images (lower panels), obtained by Fourier transformation. On the left, the result of a complete k-space sampling (1) is shown. The two central panels (2) illustrate the influence of $k_{\max}$, which was reduced to 20% of the original value resulting in a lower resolution of the MR image. The right-hand side (3) shows the inverse case, which demonstrates that the outer k-space points contribute the fine structures in the MR image.

2.2.3 Basic MR Imaging Techniques

In order to acquire an MR image, k-space needs to be sampled according to the desired image resolution, FOV and image contrast. Therefore, an appropriate sequential arrangement of RF excitation and magnetic field gradients is required, which is called pulse sequence or simply sequence. The visualization is carried out in so-called se-

quence diagrams. Apart from hardware limitations, the amplitudes and waveforms of gradients and RF pulses are generally arbitrary. In this section, three basic MR sequences are described.

Gradient Echo

In gradient echo (GRE) sequences, the phase acquisition induced by the application of magnetic gradient fields is utilized to create a signal echo. Therefore, the magnetization is first dephased and then realigned by the frequency-encoding gradient with the opposite polarity. Normally, the moment of the dephasing gradient is half as big as the moment of the readout gradient, such that the echo is formed in the middle of data acquisition. Figure 2.9 shows the diagram of a 2D gradient echo sequence (left) and the associated k-space trajectory (right). First the imaging slice is excited using an RF pulse and a slice-selection gradient in z-direction (1). The dephasing caused by the slice-selection gradient is rephased. Simultaneously, a phase-encoding gradient is applied in y-direction and the magnetization is dephased along the x-axis (2). As a result, k-space is traversed from the origin to the beginning of the dedicated k-space line. For spatial encoding in x-direction, a readout gradient is switched on (3). During

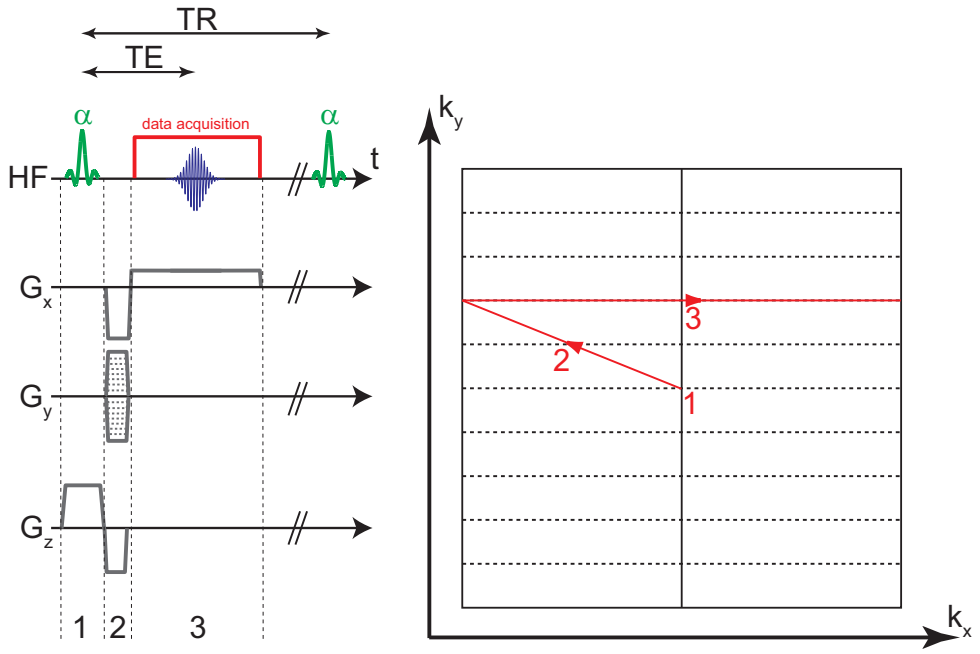

Figure 2.9: *2D gradient echo sequence (left) and the associated k-space trajectory (right). First the imaging slice is excited using an RF pulse and a slice-selection gradient in z-direction (1). The dephasing caused by the slice-selection gradient is rephased. Simultaneously, a phase-encoding gradient is applied in y-direction and the magnetization is dephased along the x-axis (2). As a result, k-space is traversed from the origin to the beginning of the dedicated k-space line. For spatial encoding in x-direction, a readout gradient is switched on (3). During the time in which the frequency-encoding gradient has a constant amplitude, data acquisition takes place and the k-space line is sampled.*

the time in which the frequency-encoding gradient has a constant amplitude, data acquisition takes place and the k-space line is recorded. This scheme is repeated until all lines in k-space are recorded. Therefore, the amplitude of the phase-encoding gradient changes each repetition and also its polarity may vary. The time between consecutive applications of the presented pulse sequence is called repetition time (TR). The time span between the RF excitation and the formation of the echo is referred to as echo time (TE). The GRE cannot compensate for magnetic field inhomogeneities. Hence, the signal underlies transversal relaxation and is T_2^*-weighted during data acquisition. GRE sequences are commonly used for fast imaging (cf. Section 3.2.1). By repeated de- and rephasing of the magnetization, several gradient echoes can be produced after one excitation. An extreme case is EPI [Mansfield, 1977], that covers the complete k-space with one excitation.

Spin Echo

Unlike, the usage of gradients for echo formation as discussed above, the spin echo (SE) sequence employs the combination of a 90° excitation pulse and a 180° refocusing pulse to form an echo. The spin echo was discovered by Hahn [1950], its principle is illustrated in Figure 2.10. By using a 90° RF pulse at the time $t = 0$, the magneti-

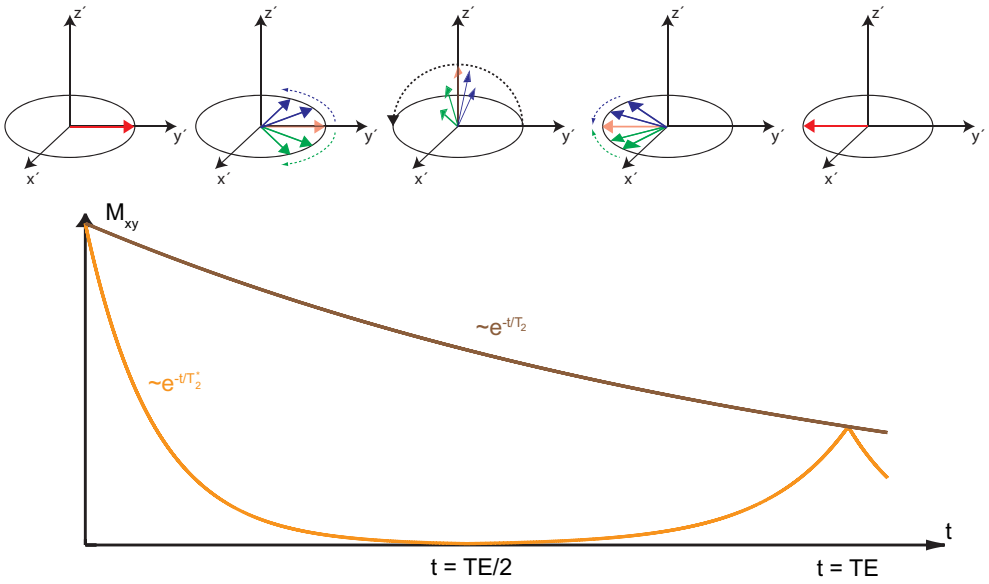

Figure 2.10: *Principle and formation of a spin echo (upper images) and the corresponding time course of the NMR signal (lower plot). At t=0, a 90° RF pulse flips the magnetization to the transversal plane. Without loss of generality, it is then aligned with x'-axis of the rotating reference frame. Right, after excitation the magnetization starts to dephase due to T_2^* relaxation. At the time $t = TE/2$, a 180° pulse is applied which rotates the magnetization around the x'-axis. Now, the same relaxation mechanisms cause a rephasing as the precession direction is inverted. This leads to the formation of an echo at $t = TE$ due to the regained coherence of the magnetization vectors. The effects of temporally varying magnetic fields remain cannot be compensated by the 180° pulse. Therefore, the signal is is T_2-weighted at TE.*

zation is flipped into the transversal plane. Without loss of generality, the rotation is performed around the x'-axis of the rotating frame. Right, after excitation the magnetization starts to dephase due to T_2^* relaxation. At the time $t = TE/2$, a 180° pulse is applied which rotates the magnetization around the x'-axis. Now, the same relaxation mechanisms cause a rephasing as the precession direction is inverted. This leads to the formation of an echo at $t = TE$ due to the regained coherence of the magnetization vectors. The refocusing 180° pulse is able to compensate for relaxation due to static field inhomogeneities and susceptibility. However, the effects of temporally varying magnetic fields remain, which is why the signal is T_2-weighted at the echo time TE. A basic 2D SE sequence diagram and the corresponding k-space trajectory are shown in Figure 2.11. The desired slice is excited by a slice-selective 90° RF pulse (1). It is followed by the simultaneous application of the slice rephasing gradient (z-direction), the phase encoding gradient (y-direction) and the dephasing frequency-encoding gradient (x-direction) (2). Afterwards, the 180° refocusing pulse is applied in combination with the slice-selection gradient to rephase the magnetization in the excited slice (3). In k-space , the refocusing pulse leads to a point reflection with respect to the k-space center. To avoid imaging artifacts, the gradient is surrounded by so-called crusher

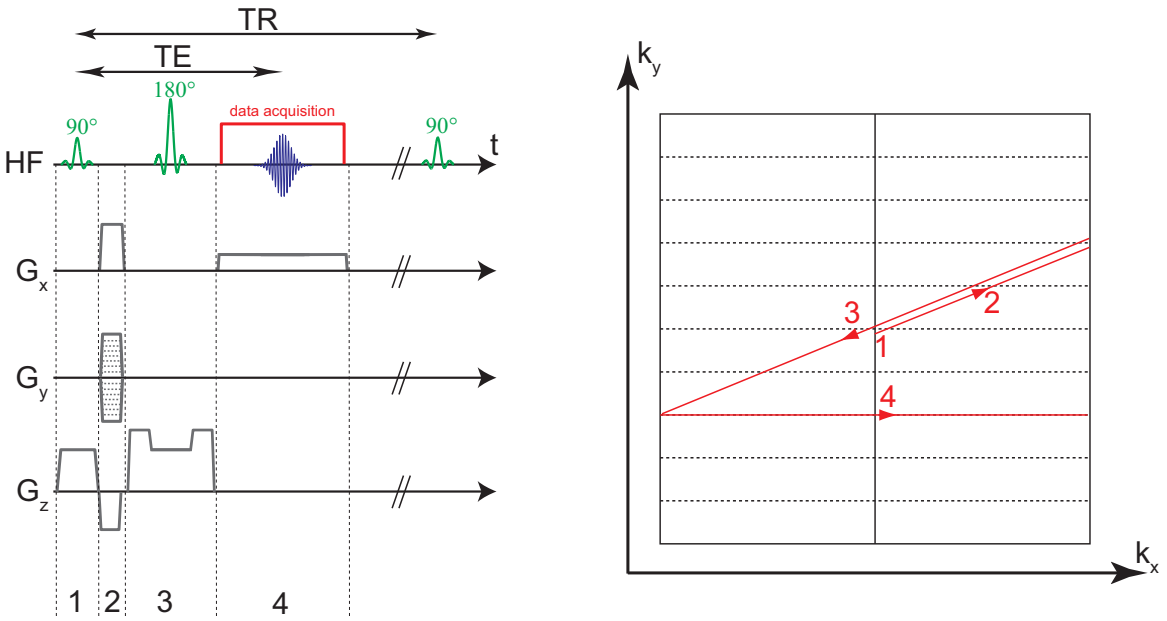

Figure 2.11: *2D gradient echo sequence (left) and the associated k-space trajectory (right). The desired slice is excited by a slice-selective 90° RF pulse (1). It is followed by the simultaneous application of the slice rephasing gradient (z-direction), the phase encoding gradient (y-direction) and the dephasing frequency-encoding gradient (x-direction) (2). Afterwards, the 180° refocusing pulse is applied in combination with the slice-selection gradient to rephase the magnetization in the excited slice (3). In k-space , the refocusing pulse leads to a point reflection with respect to the k-space center. To avoid imaging artifacts, the gradient is surrounded by so-called crusher gradients. Finally, data acquisition takes place during the application of the readout gradient and the k-space line is sampled (4).*

gradients. The right crusher gradient eliminates unwanted signal contributions due to possible imperfections of the 180° pulse. The left crusher gradient is balancing the phase dispersion that is later caused by the right crusher gradient. Finally, data acquisition takes place during the application of the readout gradient and the k-space line is sampled (4). The moment of the readout gradient is normally twice as big as that of the dephasing readout gradient. For a full k-space coverage, the sequence needs to be repeated with different phase encoding gradients. The acquisition time of a spin-echo sequence can be accelerated using several refocusing pulses during one TR, which produces multiple spin echos after one excitation [Hennig et al., 1986].

Inversion Recovery

The preparation of magnetization by an inversion pulse and an adjacent waiting time TI, preceding an imaging sequence, is called inversion recovery. TI is generally referred to as inversion time. The method represents an important tool for the measurement of T_1 relaxation times and the generation of a T_1-weighted image contrast. A 180° RF pulse inverts the magnetization which is then aligned with the (-z)-axis. During TI, the magnetization relaxes according to its T_1 relaxation time, recovering to its equilibrium state. An NMR signal is generated by flipping the available longitudinal magnetization to the transversal plane. Therefore, the signal of the subsequent imaging sequence is heavily dependent on the T_1 relaxation time of the tissue and TI. Figure 2.12 shows the longitudinal magnetization for two different T_1 species dependent on TI. It can be seen that the inversion time can be chosen to null the signal of a certain T_1 species or to maximize the contrast between two types of tissue. To measure T_1, an IR experiment and the subsequent imaging is repeatedly performed with different TI. This way, the recovery process of the longitudinal magnetization is sampled and the signal equation:

$$M_z(TI) = M_0 \left(1 - 2\mathrm{e}^{-TI/T_1}\right), \tag{2.51}$$

can be fitted to the data to estimate T_1. The IR experiment represents the basis for arterial spin labeling (ASL) (cf. Section 2.3.3), where TI will be referred to as inflow time.

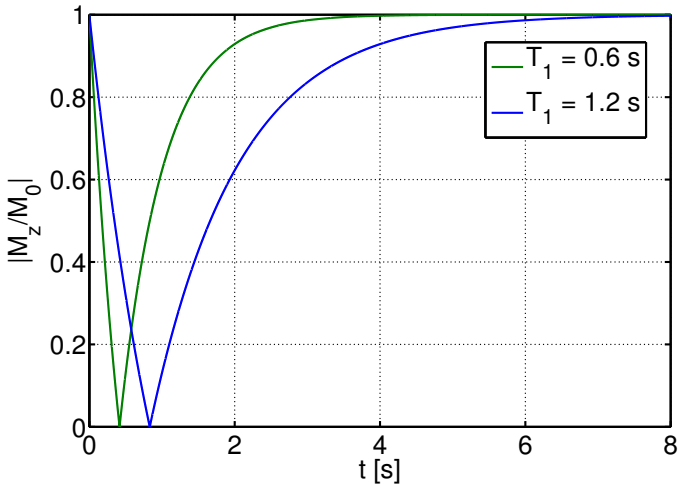

Figure 2.12: *Time course of the absolute longitudinal magnetization during an inversion recovery experiment with two different T_1 species. In case the inversion recovery is followed by an imaging sequence, TI can be chosen to null the signal of one species or to maximize the signal contrast between both.*

2.2.4 Image Contrast

The image contrast in MRI is produced by varying physical properties between different types of tissue. These are mainly the spin density and the relaxation times. Hence, three kinds of weightings are distinguished which can be achieved by choosing TR and TE appropriately:

T_1-weighted images are created by choosing $TR \approx T_1$. Tissue with a short T_1 will regain more of its equilibrium magnetization during one TR than species with a slow relaxation rate. Thus, tissue with a short T_1 will contribute more signal after the next excitation. Further, a short $TE \ll T_2^*$ has to be chosen. This way, T_2^* relaxation will have no influence on the image contrast.

T_2^*-weighting can be achieved by choosing $TE \approx T_2^*$. Tissue whose transversal magnetization decays slower contributes more signal than tissue with a short T_2^*. To suppress the influence of varying T_1 times, a long TR is chosen, enabling the complete relaxation before the next RF excitation. By using a spin echo sequence, transversal relaxation due to static field inhomogeneities are compensated and a T_2-weighting can be accomplished.

By choosing a long $TR \gg T_1$ and a short $TE \ll T_1^*$, neither transversal nor longitudinal relaxation has an impact on the image contrast. The resulting image is called spin-density-weighted as its contrast arises from the spatial distribution and density of the hydrogen nuclei.

Figure 2.13 shows exemplary images of all three weightings.

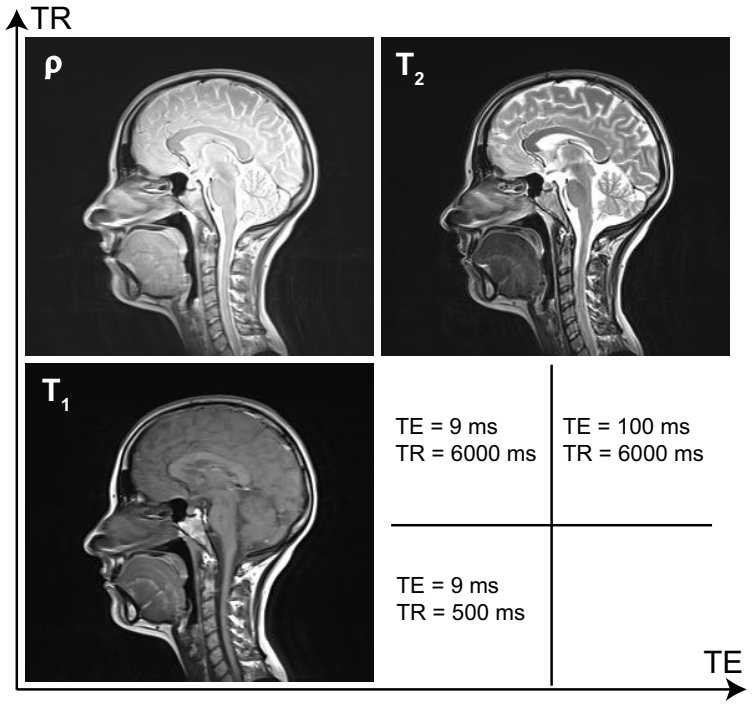

Figure 2.13: *Different image contrasts and their dependency on TR and TE. Images have been acquired using a spin echo sequence. The respective imaging parameters TR and TE are shown in the lower right panel.*

2.3 Perfusion Measurement

This section describes the term perfusion and basics of the MRI perfusion measurement techniques employed in this work. After defining perfusion, a general introduction to tracer kinetics is given. Finally, the concepts of dynamic contrast-enhanced MRI and arterial spin labeling are discussed including quantitation approaches.

2.3.1 Perfusion

The word perfusion describes the process of oxygen and nutrient delivery to the capillary bed of a specific tissue. When talking of perfusion, this process is always driven by arterial blood flow. It further comprises the transfer of water, hormones, electrolytes and even heat from the blood to the cells surrounding the capillaries. Perfusion is quantitated by the blood volume ΔV that is delivered through to a tissue of mass m during the time Δt. Therefore, it is normally expressed as:

$$[\text{perfusion}] = \left[\frac{\Delta V}{m \cdot \Delta t}\right] = \frac{\text{ml}}{100\,\text{g} \cdot \text{min}}. \tag{2.52}$$

Sometimes, perfusion is defined as blood volume per time that is delivered to a unit volume of tissue. It is then a quantity measured in inverse time. As the signal measured in MRI originates from a particular volume rather than from a particular mass, the latter definition might be more convenient. The measurement of perfusion is of high clinical value as its dysfunction is among the leading causes of medical morbidity [Detre et al., 2009]. A reduced or abnormal perfusion can be a direct indicator for an impaired organ function or vascular disorders. For that reason, for example, the measurement of perfusion in the brain under neuroscientifical aspects is a vivid field of research. However, due to their high perfusion and the necessity for an early detection of functional changes, the assessment of renal blood flow is of growing importance. Especially with regard to the avoidance or the maintenance of kidney transplants. Table 2.3 shows some typical perfusion values of different organs. Although, the methods to assess absolute perfusion with MRI are steadily refined and improved, the most widely accepted "gold-standard" for perfusion measurement *in vivo* is PET scanning with ^{15}O-labeled water [Detre et al., 2009].

Table 2.3: *Blood flow in different tissue types. Adapted from Sourbron [2005].*

Organ	Perfusion [ml/100 g/min]
Brain	50
Heart	70
Bronchi	25
Kidneys	360
Liver	95

2.3.2 General Theory of Tracer Kinetics

The challenge of measuring perfusion can be accomplished by following the course of the blood flow through the organ or tissue of interest which is called bolus tracking. As blood by itself and in its natural state is not separately detectable, an indicator or a tracer has to be introduced in the physiological system. Although, a tracer is strictly spoken not an indicator [Sourbron and Buckley, 2013] it has become a convention to speak about tracers in all cases [Lassen and Perl, 1979]. By modeling the kinetics of the tracer as it passes through the tissue of interest, physiological parameters such as perfusion can be derived. A fundamental tracer-kinetic model is given by the "indicator-dilution" theory [Meier and Zierler, 1954; Zierler, 1962]. The basic parameters that are used in the model are:

- $C_{\mathrm{T}}(t)$: the tracer concentration in the tissue of interest defined as the quantity of indicators relative the tissue volume in mol. This quantity is directly measurable.
- λ: the dimensionless volume of distribution, i.e. the fraction of tissue accessible to the tracer. Mostly expressed in ml/100 ml. λ is also referred to as blood-tissue partition coefficient.
- $C_{\mathrm{A}}(t)$: the tracer concentration within its volume of distribution in mol, i.e. the arterial tracer concentration. By definition it is: $C_A(t) = C_T(t)/\lambda$.
- f: the perfusion or clearance in 1/min.

There exist two kinds of tracers, freely-diffusible and intravascular tracers. While freely-diffusible tracers can be distributed throughout the entire tissue volume, intravascular tracers are restricted to remain in the vasculature which only represents a fraction of the full tissue volume. Of course the volume of distribution λ heavily depends on the tracer type. Given that the distribution has come into equilibrium, we find $\lambda \approx 1$ for freely-diffusible tracer and for intravascular tracer λ approximately reflects the blood volume. Due to the fact that the tracer is neither destroyed nor created within the physiological system, the mass of the tracer is conserved. The rate of change of the tissue concentration $C_T(t)$ of a tissue with i inlets and o outlets is then given by the difference between total influx and outflux:

$$\frac{\mathrm{d}C_{\mathrm{T}}(t)}{\mathrm{d}t} = \sum_i f_i C_{\mathrm{A},i}(t) - \sum_o f_o C_{\mathrm{A},o}(t). \tag{2.53}$$

The link between inlet and outlet flux is given by the time that elapses during the tracer's passage through the tissue voxel. As there are several individual paths, the passage is characterized by a probability distribution function h of transit times whose shape depends on the flow and the structure of the tissue. For example, the expectation value for the mean transit time of tracer particle taking path i is:

$$\overline{T}_i = \int_0^\infty h_i(t)\, t \,\mathrm{d}t. \tag{2.54}$$

In case the transport function h does neither depend on the time when the tracer is injected nor on the tracer concentration $C_A(t)$, the tissue is called stationary and linear,

respectively. In the following, this shall be assumed. The function $h_i(t)$ is the fraction of the tracer that flew into the tissue through inlet i at $t = 0$ and already left it at the time t. Inversely, the residue function $r_i(t)$ describes the fraction of the same tracer that is still present in the tissue at the time t:

$$r_i(t) = 1 - \int_0^t h_i(t')\,\mathrm{d}t'. \tag{2.55}$$

The fact that $h_i(t)$ is a non-negative function with unit area, implies that $r_i(t)$ is a positive and monotonically decreasing function. Its value is unity for $t = 0$ and it converges to zero for $t \to \infty$. Equation (2.55) can be reformulated to:

$$h_i(t) = -\frac{\mathrm{d}r_i(t)}{\mathrm{d}t}. \tag{2.56}$$

The relation between $h(t)$ and $r(t)$ for an arbitrarily chosen transport function is shown in Figure 2.14. The function $h(t)$ can further be used to rewrite the total outflux in terms of a convolution [Lassen and Perl, 1979]:

$$\sum_o f_o C_{\mathrm{A},o}(t) = \sum_i h_i(t) \otimes f_i C_{\mathrm{A},i}(t), \tag{2.57}$$

where $\otimes$ denotes the convolution. Integrating Equation (2.53) using of the last equation and Equation (2.55) yields:

$$C_T(t) = \sum_i r_i(t) \otimes f_i C_{\mathrm{A},i}(t), \tag{2.58}$$

which gives a direct relation between the tracer concentration in the tissue and at the inlets. The "tracer-dilution" theory forms the basis for all tracer-kinetic models as well as the model-free deconvolution analysis. In particular, all quantitation approaches used for MRI perfusion data can be derived from it.

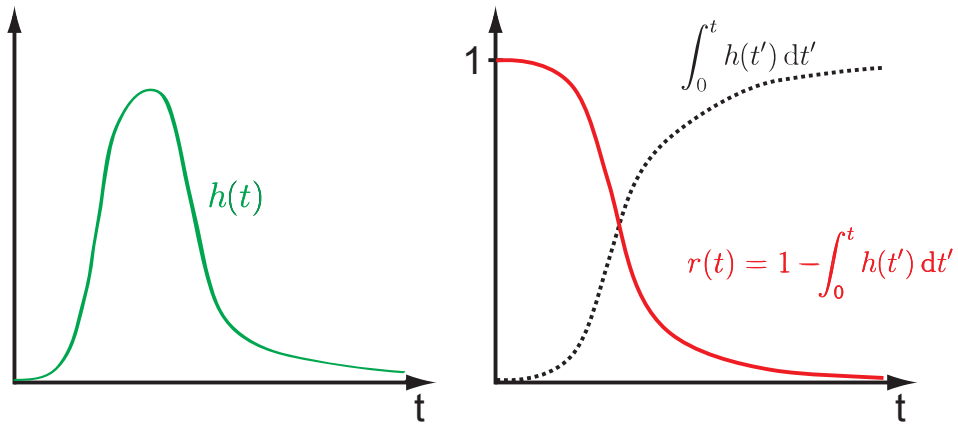

Figure 2.14: *Simplified depiction of the relation between the transport function h(t) (left) and the residual function r(t) (right). Adapted from Ahlgren [2011].*

2.3.3 Arterial Spin Labeling

Arterial spin labeling (ASL) is a non-invasive technique to measure perfusion with MRI. It was first proposed in 1992 by John Detre, Donald Williams, John Leigh and Alan Koretsky [Detre et al., 1992; Williams et al., 1992] who described how arterial blood water itself can be employed as an endogeneous, freely-diffusible tracer by manipulating (labeling) its longitudinal magnetization. In an independent work published in the same year, Kwong et al. [1992] used the same principle to visualize brain activity, however, did not calculate absolute perfusion values. A good review of ASL is given by Petersen et al. [2006a] part of which is outlined in the following.

Principle

To use arterial blood as a tracer, it has to be labeled in order to differentiate the tracer signal from "normal" blood water signal. Labeling is usually performed by inverting (sometimes saturating) the magnetization of water protons in blood. In a simple ASL experiment the blood water is labeled in a region proximal to the imaging volume which contains the organ or tissue of interest. To allow the labeled blood to flow into the tissue of interest, the labeling region should contain vessels that feed this tissue. During a sufficiently long temporal delay between labeling and imaging, called inflow time (TI), the labeled blood then reaches the imaging volume and the tissues capillary bed where it exchanges with tissue water. Finally, the volume is imaged with a dedicated imaging sequence to detect signal change due to the delivered magnetization, i.e. the labeled arterial blood water. To detect the signal change due to the delivered, labeled magnetization, which is typically about 0.5 % - 1.5 % of the total signal, every ASL experiment involves the measurement of a "control" and a "tag" image. In case of the "control" image the volume of interest is imaged without prior labeling, while the "tag" image is the "flow-sensitized" measurement that includes labeling of inflowing blood water. Ideally, the signal of static tissue is identical in both images such that the signal in the difference image ΔM of "tag" and "control" image only contains the signal of blood water that flowed into the tissue during TI. Figure 2.15 depicts the basic concept of ASL using the example of a brain perfusion measurement. It shows the longitudinal magnetization (arrows) for the tag and control image at two points in time. In case of the tag image, at $t = 0$ the arterial blood is labeled by a selective (green box) inversion proximal to the imaging region. After the inflow time TI the tagged blood arrived in the imaging region (red). In this simple example, the magnetization is unprepared for the control image. The signal in the difference image ΔM of tag and control image, both acquired at $t = TI$, solely originates from the magnetization that flowed into the imaging region during TI. The illustration neglects relaxation and MT effects. Eventually, ΔM is a perfusion-weighted image that directly reflects local perfusion. However, the perfusion signal does not only depend on vascular flow but rather on several physiological and physical parameters like the longitudinal relaxation times of blood and tissue, proton density, the transit time from labeling to imaging region or the inflow time TI, to only name a few. These dependencies have to be taken into account when deriving absolute perfusion values from the perfusion-weighted image ΔM. Due to the low signal-to-noise ratio in the ΔM images, multiple "tag-control" pairs are normally averaged.

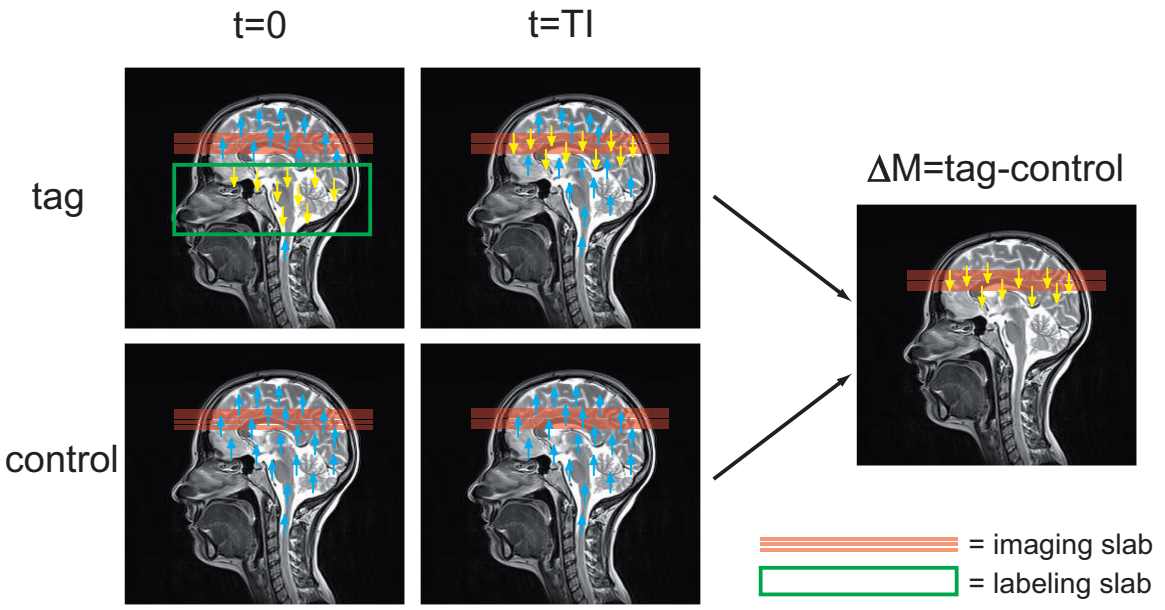

Figure 2.15: *The basic concept of ASL using the example of a brain perfusion experiment. The figure depicts the longitudinal magnetization (arrows) for tag and control image at two points in time. In case of the tag image, at $t = 0$ the arterial blood is labeled by a selective (green box) inversion proximal to the imaging region. After the inflow time TI the tagged blood (yellow) arrived in the imaging region (red). In this simple example, the magnetization is unprepared for the control image. The signal in the difference image ΔM of tag and control image, both acquired at $t = TI$, solely originates from the magnetization that flowed into the imaging region during TI. The illustration neglects relaxation and MT effects. Figure adapted from Petersen et al. [2006a].*

Magnetization Transfer

Magnetization transfer (MT) is an effect that can lead to an erroneous ASL signal. It was discovered by Forsén and Hoffman [1963] in MR-spectroscopy. Later, the effect was also observed for MRI [Wolff and Balaban, 1989]. It describes the exchange of magnetization between free water protons and those bound to macromolecules. Free water protons have a long transversal relaxation time T_2 that leads to a sharp peak in the absorption spectrum. In contrast, water bound to macromolecules has a broad absorption line due to its short T_2 relaxation time. Figure 2.16 shows the frequency spectrum of free water protons (free pool) and bound protons (bound pool). Through dipolar coupling and chemical exchange [Henkelman et al., 2001], magnetization can be transferred from one pool to the other. In MRI, the MT effect is used to enhance the contrast between different tissue structures or to acquire specific tissue parameters by quantitating exchange rates and pool sizes. In case of an off-resonant RF pulse, the bound pool is saturated. Eventually, the MT effect leads to a saturation of the magnetization in the bound pool. This is an important detail that needs to be considered for ASL.

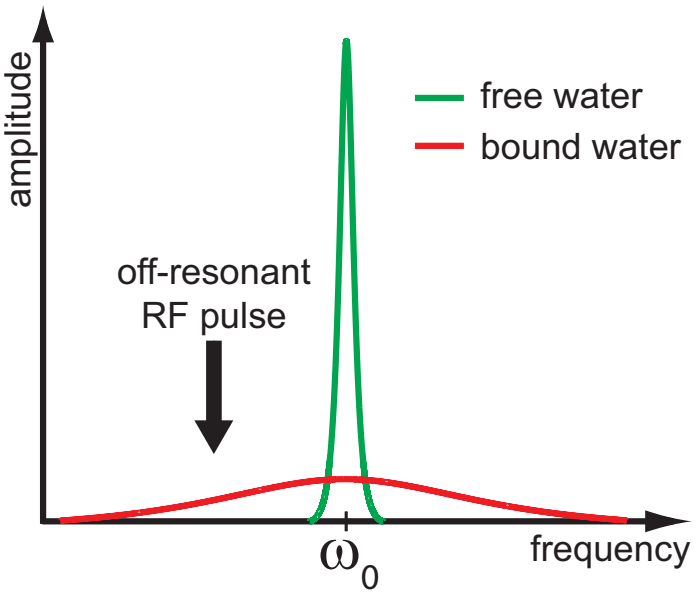

Figure 2.16: *Simplified depiction of the absorption lines of free (green) and bound (red) water protons . An RF pulse that is off-resonant with respect to the Larmor frequency ω_0 can saturate the bound pool. Eventually, the MT effect causes the saturation of the free pool which decreases the MR signal.*

ASL techniques can be divided into two major groups which differ in the way in which the labeling is performed. Below, each group will be discussed. Following the historic development, continuous arterial spin labeling is treated first.

Continuous Arterial Spin Labeling

Continuous ASL (CASL) is the technique used by the ASL pioneers [Detre et al., 1992; Williams et al., 1992]. Labeling is performed by a continuous inversion pulse in a slice proximal to the imaging region. The typical pulse duration is 2-4 s. By applying a field gradient in flow direction during the RF pulse, the blood water experiences a slow variation of the resonance frequency as it flows through the labeling region. This results in the inversion of arterial magnetization (cf. Section 3.5.1) and is therefore called flow-driven adiabatic inversion. A technique previously employed in angiography by Dixon et al. [1986]. Typical inversion efficiencies lie in the range of 80% to 95% [Petersen et al., 2006a]. An important issue of CASL is the magnetization transfer (MT) effect. Due to the long RF pulse, that is off-resonant with respect to the imaging region, it will saturate the macromolecular pool. Magnetization transfer will then saturate the free water pool in the imaging region and decreases the signal [Henkelman et al., 1993]. In case the MT effect is only present in the tag image, this results in a overestimated perfusion signal, as static tissue does not fully cancel when subtracting control from tag image. Early implementations of CASL compensated the MT effect by applying a distal inversion pulse before taking the control image. However, this is only applicable for single imaging slices or thin imaging slabs, respectively. A method that allows to acquire a larger imaging volume was proposed by Alsop and Detre [1998] who made use of two closely-spaced inversion pulses to produce a "tag-identical" MT effect. Another technique to compensate the MT effect in CASL experiments are separate labeling and imaging coils [Silva et al., 1995; Zhang et al., 1995; Mildner et al., 2003]. Figure 2.17 illustrates the principle design of a CASL experiment.

Pulsed Arterial Spin Labeling

In contrast to continuous ASL, the technique of pulsed ASL (PASL) uses relatively short RF pulses (10 ms to 20 ms) to label the arterial blood. Again, a volume proximal to the imaging region is labeled, however the labeling pulses used for PASL normally cover a larger region than the CASL labeling. Due to the much shorter labeling pulse duration, the MT effect is not as prominent as in CASL. However, it is not negligible and needs to be compensated when the control image is acquired. Figure 2.17 shows the principle design of a CASL and a PASL experiment. The first pulsed ASL scheme was proposed by Edelman et al. [1994]. Their method, named EPISTAR (EchoPlanar Imaging and Signal Targeting with Alternating Radiofrequency), employs a labeling slice proximal to the imaging region. For the control image the labeling pulse is applied in a distal slice. Both pulses are symmetrical with respect to the imaging region, such that for a single imaging slice, the MT effect is compensated. The STAR labeling scheme by Edelman et al. [1994] provided the basis for other PASL schemes which all employ proximal labeling pulses, however differ in the way the MT effect is balanced in tag and control image. For example, the PICORE (Proximal Inversion with a Control for Off-Resonance Effects) scheme proposed by Wong et al. [1997] uses an inversion pulse at the same off-resonant frequency relative to the imaging slab but without the application of a slice-selection gradient. However, so far, the STAR-based techniques did not allow an artifact-free multislice or 3D imaging as the spatial domain where the MT effect is compensated, is very thin. The TILT scheme proposed by Golay et al. [1999] uses two successive, proximal 90° pulses in the tagging and the control preparation. For the control image the second RF pulse is applied with a phase difference of 180°. The net MT effect is then identical for both cases and the scheme allows to image a larger volume. In a similar concept, called PULSAR (PULsed Star Labeling of Arterial

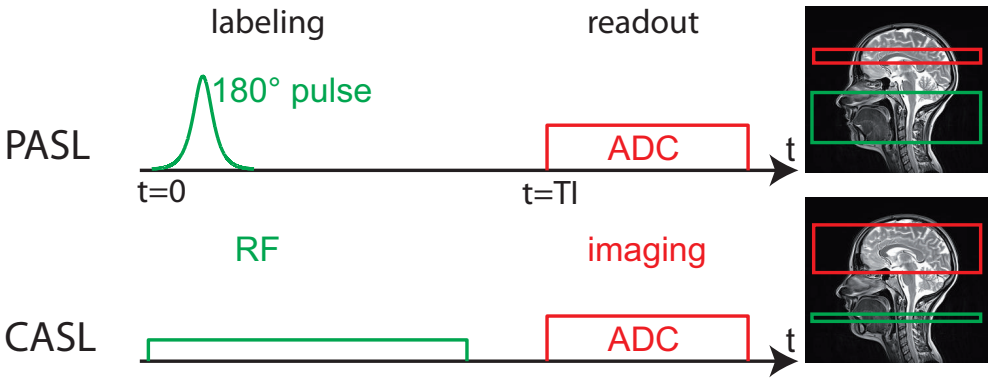

Figure 2.17: *Illustration of the two basic ASL techniques: pulsed and continuous arterial spin labeling. While for pulsed ASL the labeling is performed with a short inversion pulse, CASL employs a continuous RF application with a low amplitude. Usually, the labeling region of CASL is smaller compared to the inversion slab of PASL. Both methods comprise an imaging module that starts at a time $t = TI$ after the labeling has started. Independent of the method, this can be a 2D, 3D or a multislice readout. The sketch does not show the control phase of the ASL experiments. Figure adapted from Gregori [2009].*

Regions), Golay et al. [2005] use one proximal inversion pulse for the tag preparation and two 180° pulses for the control image. For the latter, the RF power is decreased to one half of the tagging pulse' power. Eventually, not only the net flip angle is zero, but the same amount of energy is deposited in the macromolecular pool and the MT effect compensates. A different approach to deal with the MT effect in PASL was independently proposed by Kwong et al. [1995] and by Kim [1995] who named it FAIR (Flow Alternating Inversion Recovery). In comparison to a proximal, asymmetric labeling, the FAIR scheme uses a non-selective inversion pulse for the tag image and a selective inversion pulse for the control image. Due to the fact that the slice-selective 180° pulse inverts the magnetization in the imaging slab, the MT effect is automatically compensated. The labeling efficiency of PASL is improved compared to CASL, however the T_1 relaxation of the label occurs during the inflow time. Theoretically, this reduces the perfusion signal. Due to imperfect slice profiles of the selective inversion, the time it takes for the labeled blood to arrive in the tissue (transit delay), is increased. This can result in a further reduction of the perfusion signal. Nevertheless, PASL is a popular choice as it is easy to implement and faces less practical problems than CASL. A promising method that combines both ASL techniques was proposed by Wu et al. [2007] and Dai et al. [2008]. The technique uses flow-driven adiabatic inversion, however instead of one continuous pulse, a train of short (∼1 ms) slice-selective pulses is used for labeling. This combines the high tagging efficiency of PASL with the higher perfusion signal of CASL. Due to its hybrid nature it is called pseudocontinuous ASL (pCASL).

Quantitation of ASL Data

The first scientist who described a method to accurately measure quantitated perfusion were Kety and Schmidt [1945] who used the inhalation of nitrous oxide (N_2O), a gas and freely-diffusible tracer, to estimate a global value of cerebral perfusion. They measured rate of gas inhalation as well as the arterial and venous tracer concentration until equilibrium was reached. By adopting Fick's principle they calculate the cerebral perfusion (CBF):

$$\frac{\mathrm{d}C_\mathrm{T}(t)}{\mathrm{d}t} = CBF \cdot (C_\mathrm{A}(t) - C_\mathrm{V}(t)), \tag{2.59}$$

where the known quantities were used and C_V is the venous tracer concentration. The equation is equal to the mass conservation formula of the tracer-dilution theory (cf. Equation (2.53)) if only one inlet and one outlet is considered. In case of a rapid tracer exchange between blood and tissue, the model describes a single well-mixed compartment. Its solution is then given by Equation (2.58) with $r(t) = \mathrm{e}^{-ft/\lambda}$ [Buxton, 2009].

Bloch Equation Approach To derive absolute perfusion values from ASL experiments, Detre et al. [1992] and Williams et al. [1992] adapted the model of Kety and Schmidt [1945] and modified the Bloch equations accordingly:

$$\frac{\mathrm{d}M_\mathrm{T}(t)}{\mathrm{d}t} = \frac{M_{0,\mathrm{T}} - M_\mathrm{T}(t)}{T_{1,\mathrm{T}}} + f\left(M_\mathrm{A}(t) - M_\mathrm{V}(t)\right). \tag{2.60}$$

The equation describes the change of the tissue magnetization M_{T} depending on the perfusion f, the equilibrium magnetization of the tissue $M_{0,\mathrm{T}}$, the longitudinal relaxation times of tissue $T_{1,\mathrm{T}}$ and the magnetization of arterial and venous blood M_{A} and M_{V}, respectively. To actually solve Equation (2.60), several simplifications were made that include the assumption of a single well-mixed compartment, the conservation of the label until the arterial blood exchanges with tissue water and the similar relaxation times of blood and tissue. Nevertheless, the modified Bloch equation of Detre, Williams and co-workers laid the basis for most of the early quantitative ASL analyses, e.g Kwong et al. [1992, 1995] or Calamante et al. [1996].

The General Kinetic Model A more general model to describe the kinetics of arterial blood water as a tracer was proposed by Buxton et al. [1998]. The "general kinetic model" can reproduce the models based on the Bloch equation approach but furthermore allows a more detailed description and includes some of the effects that were simplified or neglected in the early models. It is the application of the general tracer kinetics model derived above (cf. Equation (2.58)) to ASL and treats the magnetization difference ΔM between tag and control image, i.e. the signal difference, as the tracer concentration. Then, ΔM depends on the arterial flow, the venous clearance and the longitudinal relaxation time of the tissue and the labeled blood. The model is described by three functions [Buxton et al., 1998]:

- $c(t)$: the delivery function represents the normalized arterial concentration of magnetization arriving in the imaged voxel at the time t,
- $r(t, t')$: the residue function is the amount of tagged water that entered the voxel at time t' and still remains at time t,
- $m(t, t')$: the magnetization relaxation function gives the fraction of the original longitudinal magnetization of tagged blood carried by the water molecules that arrived at time t' that remains at t'.

Right after the inversion pulse, the magnetization difference ΔM is $2\,M_{0,\mathrm{A}}$, where $M_{0,\mathrm{A}}$ is the equilibrium magnetization of arterial blood. In reference to Section 2.3.2, the tracer concentration $C_{\mathrm{A}}(t)$ is then given by $2\,M_{0,\mathrm{A}}\,m(t)c(t)$ and Equation (2.58) can be rewritten:

$$\Delta M(t) = 2\,M_{0,\mathrm{A}}\,f \int_0^t c(t')\,r(t-t')\,m(t-t')\mathrm{d}t'. \tag{2.61}$$

By modeling the dynamic functions and applying certain exchange mechanisms (compartment models), this model is generally applicable to any ASL experiment.

To gain an analytical solution Buxton et al. [1998] proposed the model of a single well-mixed compartment known as the "Standard Kinetic Model". It includes the assumption of so-called uniform plug flow and the complete and instantaneous extraction of labeled water after its arrival in the tissue. This means that no labeled blood arrives in the tissue before a transit delay Δt and that the label initially decays with the longitudinal relaxation time $T_{1,\mathrm{A}}$ of arterial blood but after arrival in the tissue decays

with $T_{1,\mathrm{T}}$, the longitudinal relaxation rate of the tissue. The functions read:

$$\begin{aligned} c(t) &= \begin{cases} 0 & 0 < t < \Delta t, \\ \alpha\, \mathrm{e}^{-t/T_{1,\mathrm{b}}}\ (\mathrm{PASL}) & \Delta t < t < \Delta t + T, \\ \alpha\, \mathrm{e}^{-\Delta t/T_{1,\mathrm{A}}}\ (\mathrm{CASL}) & \Delta t < t < \Delta t + T, \\ 0 & \Delta t + T < t, \end{cases} \\ r(t) &= \mathrm{e}^{-ft/\lambda}, \\ m(t) &= \mathrm{e}^{-t/T_{1,\mathrm{T}}}. \end{aligned} \tag{2.62}$$

The factor α describes the inversion efficiency in terms of the fraction of the maximum available change of the longitudinal magnetization. T denotes the total bolus duration. Solving Equation (2.61) for PASL yields:

$$\Delta M = \begin{cases} 0 & 0 < t < \Delta t, \\ -2\,\alpha\, M_{0,A}\, f\, (t - \Delta t)\, \mathrm{e}^{-t/T_{1,\mathrm{A}}}\, q(t) & \Delta t < t < \Delta t + T, \\ -2\,\alpha\, M_{0,A}\, f\, T\, \mathrm{e}^{-t/T_{1,\mathrm{A}}}\, q(t) & \Delta t + T < t, \end{cases}$$

with

$$q(t) = \begin{cases} \frac{\mathrm{e}^{k(t-\Delta t)}-1}{k\,(t-\Delta t)} & \Delta t < t < \Delta t + T, \\ \\ \frac{\mathrm{e}^{k(t-\Delta t)}-\mathrm{e}^{k(t-(T+\Delta t))}}{k\,T} & \Delta t + T < t, \end{cases} \tag{2.63}$$

and

$$k = \frac{1}{T_{1,\mathrm{A}}} - \frac{1}{T_{1,T}} - \frac{f}{\lambda}.$$

Figure 2.18 shows the ASL signal of a PASL experiment in terms of ΔM as calculated with the "Standard Kinetic Model". The chosen values $T_{1,\mathrm{b}} = 1.5\,s$, $T_{1,\mathrm{t}} = 1.4\,s$, $\lambda = 0.9$ and f are typical values for a brain perfusion experiment. The value of $M_{0,\mathrm{b}}$ has been set to 100. The curves reveal two critical issues of ASL: the low perfusion signal, and the underestimation of perfusion due to transit delays. The quantitation models based on the ansatz of Buxton et al. [1998] (cf. Equation (2.61)), which comprises the Bloch equation approach of Detre et al. [1992] (cf. Equation (2.60)), serve as the basis for nearly all quantitative evaluations of ASL data. An exception is the model-free approach proposed by Petersen et al. [2006b]. The method comprises the acquisition of ASL data at multiple inflow times. This way, an arterial input function as well as an effective residue function can be sampled which allows to calculate the blood flow by means of deconvolution (cf. Equation (2.58) and (2.61)).

2.3.4 Dynamic Contrast-Enhanced MRI

The measurement of tissue perfusion by means of signal changes after the injection of an endogenous tracer was first proposed in the mid 1980s [Runge et al., 1984; Pettigrew et al., 1986]. The contrast agent (cf. Section 3.4.1), a gadolinium compound, decreases the relaxation times of its vicinity which leads to a different contrast behavior. By

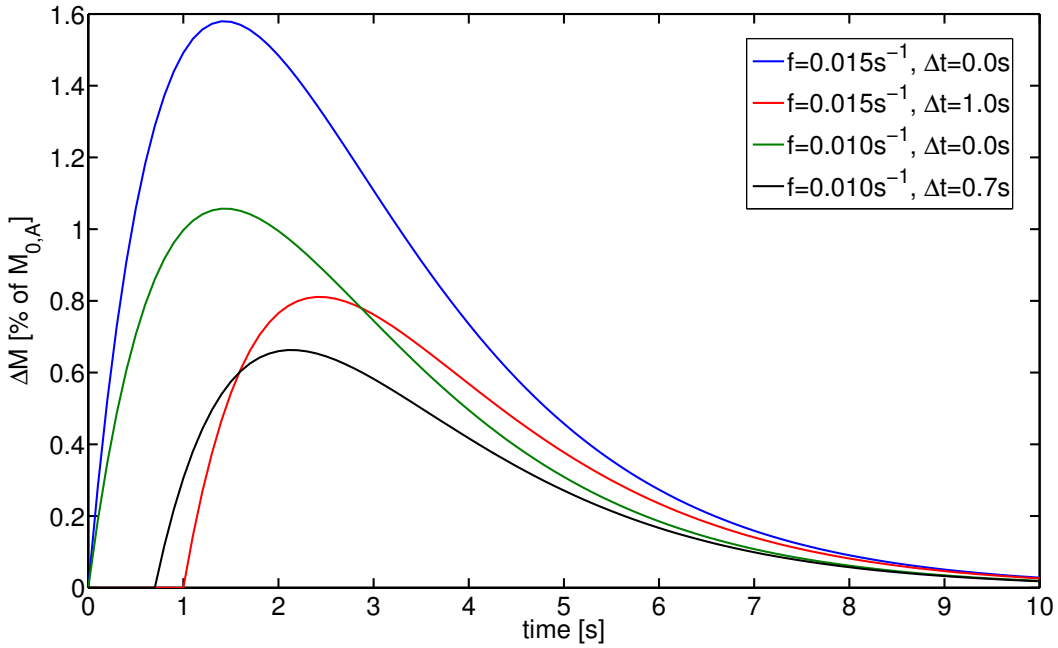

Figure 2.18: *Calculated perfusion signal time courses of a pulsed ASL experiment for different perfusion values f and transit delays Δt, based on the Standard Kinetic Model of Buxton et al. [1998]. The chosen values $T_{1,A}$=1.5 s, $T_{1,T}$=1.4 s, λ=0.9 and f are typical for a brain perfusion experiment. $M_{0,A}$ has been set to 100. Curves for two different perfusion values, each with two different transit delays are plotted. The calculations assume an ideal inversion and an infinitely long bolus. The plot reveals two critical issues of ASL: the low signal and the underestimation of perfusion due to the delayed arrival of the bolus.*

repeated imaging with a high temporal resolution, the dynamics of the contrast agent can be monitored in the imaged region. The concept of dynamic contrast-enhanced MRI (DCE-MRI) uses T_1-weighted images to track the bolus concentration. As regions with a higher concentration of contrast agent yield a higher signal in the T_1 -weighted images, the bolus of contrast agent can be tracked by means of changes in the MR signal. Figure 2.19 illustrates the dynamic series of T_1-weighted images after the injection of contrast agent. The data allows a voxel-wise extraction of signal curves, that show the concentration of the tracer over time. By deriving signal time curves in the tissue of interest and applying the principles of tracer kinetics and tracer kinetic models [Sourbron and Buckley, 2013], several physiological parameters including perfusion, can be assessed [Brix et al., 1991]. DCE-MRI is the standard method for perfusion imaging in organs other than the brain [Jerosch-Herold et al., 2004; Brix et al., 2004; Dujardin et al., 2005]. Due to the variety of functional parameters that can be estimated [Sourbron et al., 2008], it is especially valuable in the kidneys.

Quantitation of DCE-MRI Data

Like for ASL, all approaches to assess quantitative perfusion values from DCE-MRI data, base on the "tracer-dilution" theory described in a previous section. Generally,

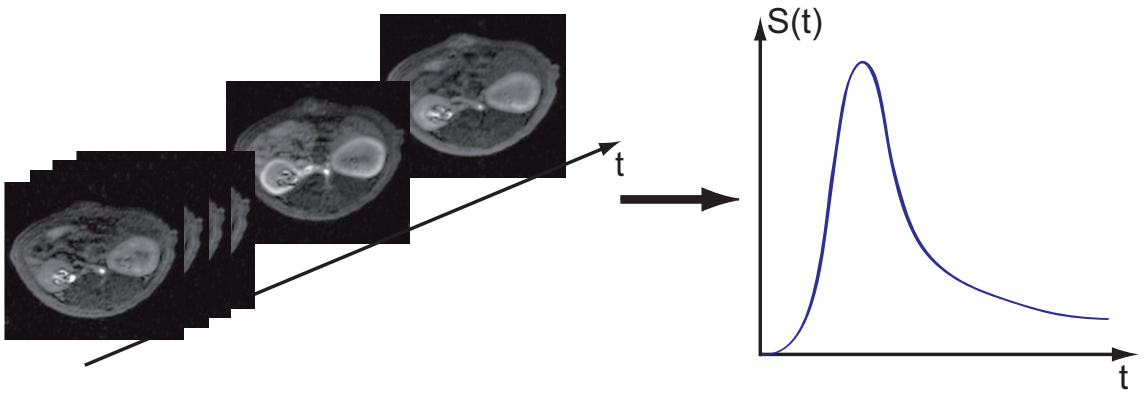

Figure 2.19: *Illustration of a DCE-MRI signal time course. After administration of the contrast agent a series of T_1-weighted images is acquired with high temporal resolution. A signal time curve that shows the passage of the agent in the tissue of interest can be derived for every voxel.*

two types of approaches can be distinguished: the model-free approach and the approaches that model the physiology of the underlying tissue, e.g. multi-compartment models.

Model-Free Analysis For a model-free analysis no assumptions on the interior structure of the underlying tissue are made and the tissue sample is assumed to have a single inlet through which arterial blood is delivered. In this case, Equation (2.58) reads:

$$C_T(t) = C_A(t) \otimes I(t) = f \int_0^t C_\mathrm{A}(t')r(t-t')\mathrm{d}t', \tag{2.64}$$

where we introduced the tissue-characteristic impulse response function $I(t) = f \cdot r(t)$. Equation (2.64) includes two functions that are directly accessible via DCE-MRI: the time course of the tissue tracer concentration $C_T(t)$ and that in an artery feeding the tissue sample $C_A(t)$. The latter is referred to as arterial input function (AIF). To access the impulse response function $I(t)$, $C_T(t)$ is numerically deconvolved with the AIF [Østergaard et al., 1996b]. After $I(t)$ is calculated, the perfusion f is directly accessible and given by:

$$f = I(0) = \max(I), \tag{2.65}$$

since $r(0) = 1$. In practice, it is preferred to use the maximal value of the response function, as the initial value $I(0)$ is prone to numerical errors [Sourbron et al., 2004] and dispersion of the contrast bolus.

Compartment Models Information and knowledge about structure, physiology, and processes in the underlying tissue can be used to model the tracer kinetics. Compared to the model-independent deconvolution, one can gain additional functional parameters, such as exchange or filtration rates. Compartment models describes the tissue with a single or multiple compartments by assuming a specific analytical expression for $r(t)$. In the latter case, the compartments are connected and interacting,

such that the outlet of one compartment is the inlet of another. A compartment is thereby considered to be a volume where the diffusion of the tracer and its exchange rate with potential sub-compartments is very high. This way, it represents a region with a homogeneous tracer distribution, even if the concentration of the tracer is a function of time. A variety of different compartment models exist which again can be adapted to various constraints and assumptions. A detailed discussion of the models is given in Sourbron and Buckley [2013].

3 Materials & Methods

This chapter describes the hardware used in this work. Further, a detailed explanation of imaging sequences, perfusion measurement methods and special RF pulses are given. In addition, the employed animal models are described.

3.1 MR Hardware

The magnetic resonance tomographs used for this work, as well as the used receive coils are described.

MR Scanner

All measurements presented in this work were performed on 3 T whole-body MR scanners. Two different tomographs were used, both manufactured by Siemens (Siemens Healthcare, Erlangen, Germany). They are shown in Figure 3.1.

Magnetom Trio All animal studies were conducted on a Magnetom Trio. The magnetic field is generated by superconducting coils that are kept at 4.3 K by the usage of liquid helium. The magnet has a length of 198 cm and a bore size of 60 cm. The main magnetic field has a homogeneity of typically 0.1 ppm in a 50 cm diameter spherical volume around the isocenter. Inhomogeneities induced by objects in the scanner, can be compensated with integrated shim coils. To reduce the scatter field of the main magnet an active shielding is used. The installed gradient system allows field gradients up to 40 mT/m in x- and y-direction and 45 mT/m along the direction of the main magnetic field (z-direction). The maximum allowed gradient slew rates are 180 T/m/s and 220 T/m/s, respectively. A field-of-view (FOV) of up to 50 cm can be imaged.

Magnetom Skyra The 3D ASL as well as the inversion profile measurements were performed on a Magnetom Skyra. The main magnetic field is also actively shielded and generated by superconducting coils that are cooled with liquid helium. The magnet length of the Skyra system is 163 cm, the bore diameter is 70 cm. The homogeneity of

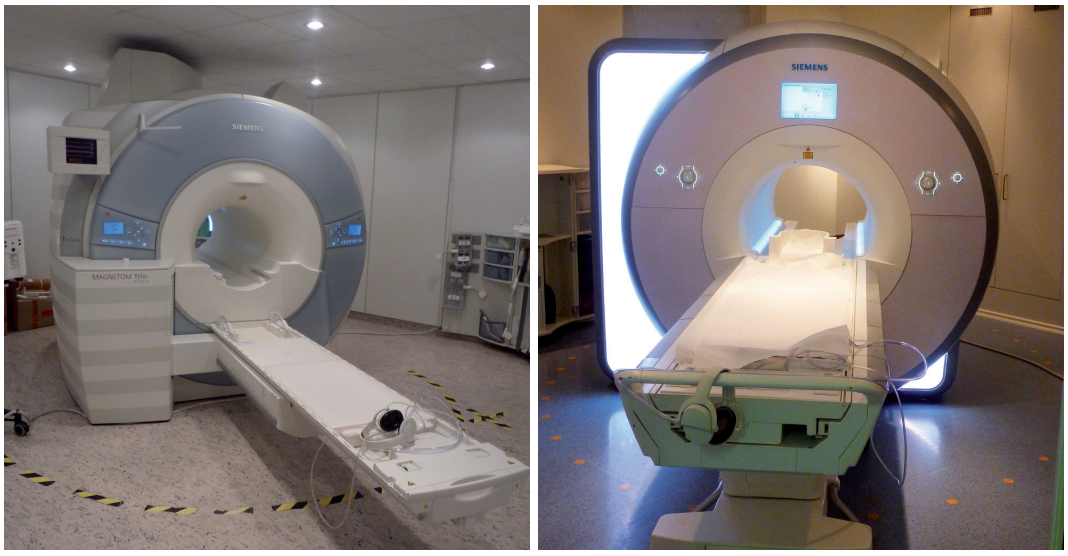

Figure 3.1: *The MR tomographs Magnetom Trio (left) and Skyra (right) used for all MRI experiments in this work.*

the main magnetic field is below 1.4 ppm in a 40 cm diameter spherical volume and can be readjusted by shim coils, if necessary. Despite the compact design the system allows to image a FoV of up to 50 cm×50 cm×45 cm. The gradient system offers a maximum gradient amplitude of 45 mT/m on all axes with a maximal slew rate of 200 T/m/s.

Coils

Besides the standard 20 channel head/neck coil and the integrated body coil delivered with the MR scanner, a dedicated coil for small animal imaging has been used.

Eight Channel Rat Array Imaging small animals on a whole-body scanner requires dedicated receive coils to achieve a sufficient signal-to-noise ratio and a high enough resolution. For that reason, an eight channel receive-only volumetric rat array shown in Figure 3.2 was used for all animal experiments. The coil was manufactured by Rapid (Rapid Biomedical GmbH, Rimpar, Germany). It has an inner diameter of 72 mm and a length of 210 mm allowing a FoV of 18 cm. The 2×4 coil elements are actively decoupled and allow to employ parallel imaging methods. Preamplifiers are integrated in the coil.

3.2 Imaging Sequences

This section describes the imaging sequences that were used in this work. Besides the sequences used for data and image acquisition in ASL and DCE-MRI experiments, the sequence used to measure the profiles of slice-selective inversion pulses is described. The 3D ASL sequence and the inversion profile measurement were programmed or adapted in the Siemens development environment IDEA (Integrated Developement Environment for Applications) using the computer language C++.

Figure 3.2: *Eight channel receive-only volumetric rat array manufactured by Rapid (Rapid Biomedical GmbH, Rimpar, Germany). The coil allows to image small animals on a whole-body scanner.*

3.2.1 Steady-State Free Precession

In this work, all imaging sequences used for perfusion measurements belong to the class of steady-state free precession (SSFP) sequences. SSFP sequences are gradient-echo sequences, which are all based upon the periodic application of RF pulses that are separated by a constant time interval *TR*. During *TR* the echo is generated and spatial encoding and signal acquisition are performed.

Evolution of Magnetization

The influence of periodic RF excitation and gradients on the magnetization can be expressed recursively [Hargreaves et al., 2001]:

$$\boldsymbol{M}_{k+1} = \boldsymbol{\mathcal{A}}\boldsymbol{M}_k + \boldsymbol{B}, \tag{3.1}$$

where $\boldsymbol{M}_k$ represents the magnetization vector at the *k-th* period. The 3×3 matrix $\boldsymbol{\mathcal{A}}$ and the vector $\boldsymbol{B}$ describe the magnetization change due to excitation, relaxation and precession of the magnetization. The magnetization is in a so-called steady state, when the following relation holds:

$$\boldsymbol{M}_{k+1} = \boldsymbol{M}_k = \boldsymbol{M}_{\mathrm{ss}}. \tag{3.2}$$

The steady-state magnetization is then given by:

$$\boldsymbol{M}_{\mathrm{ss}} = \left(\boldsymbol{\mathcal{I}} - \boldsymbol{\mathcal{A}}\right)^{-1} \boldsymbol{B}, \tag{3.3}$$

with $\boldsymbol{\mathcal{I}}$ being the 3×3 identity matrix. To estimate $\boldsymbol{\mathcal{A}}$ and $\boldsymbol{B}$, in order to calculate the steady-state signal, the evolution of the magnetization within one *TR* needs to be analyzed: The effect of an RF pulse with flip angle α on the magnetization can be

described by a rotation matrix $\boldsymbol{\mathcal{R}}(\alpha)$ which is given by:

$$\boldsymbol{\mathcal{R}}(\alpha) = \begin{pmatrix} 1 & 0 & 0 \\ 0 & \cos(\alpha) & \sin(\alpha) \\ 0 & -\sin(\alpha) & \cos(\alpha) \end{pmatrix}, \tag{3.4}$$

in case the rotation is performed around the x'-axis. Free precession is induced by the applied gradients and by off-resonances $\Delta\omega$ relative to the Lamor frequency. It is described by:

$$\boldsymbol{\mathcal{P}}(\Phi) = \begin{pmatrix} \cos(\Phi) & \sin(\Phi) & 0 \\ -\sin(\Phi) & \cos(\Phi) & 0 \\ 0 & 0 & 1 \end{pmatrix}, \tag{3.5}$$

representing a rotation about the z-axis by the angle Φ. Finally, relaxation effects are described by the multiplying the magnetization vector with a matrix $\boldsymbol{\mathcal{C}}$:

$$\boldsymbol{\mathcal{C}}(TR, T_1, T_2) = \begin{pmatrix} \mathrm{e}^{-\frac{TR}{T_2}} & 0 & 0 \\ 0 & \mathrm{e}^{-\frac{TR}{T_2}} & 0 \\ 0 & 0 & \mathrm{e}^{-\frac{TR}{T_1}} \end{pmatrix}, \tag{3.6}$$

and adding a vector $\boldsymbol{D}$:

$$\boldsymbol{D}(TR, T_1) = \begin{pmatrix} 0 \\ 0 \\ 1 - \mathrm{e}^{-\frac{TR}{T_1}} \end{pmatrix}. \tag{3.7}$$

The magnetization after the *k-th TR* period is then given by:

$$\boldsymbol{M}_k = \underbrace{\boldsymbol{\mathcal{R}} \cdot \boldsymbol{\mathcal{C}} \cdot \boldsymbol{\mathcal{P}}}_{\boldsymbol{\mathcal{A}}} \cdot \boldsymbol{M}_{k-1} + \underbrace{\boldsymbol{\mathcal{R}} \cdot \boldsymbol{D}}_{\boldsymbol{B}}, \tag{3.8}$$

which allows the direct identification of $\boldsymbol{\mathcal{A}}$ and $\boldsymbol{B}$ by comparing the equation with Equation (3.1).

3.2.2 FLASH

The data and image acquisition of the DCE-MRI experiments presented in this work, were conducted with a FLASH (Fast Low Angle Shot) sequence that was first proposed by [Haase et al., 1986]. FLASH belongs to the class of spoiled SSFP sequences. This means that the transversal magnetization is destroyed at the end of each *TR*-interval. This is accomplished by the application of strong gradients that lead to a strong phase dispersion of the magnetization. Additionally, the phase of the RF pulse is incremented each *TR*-interval [Zur et al., 1991] to avoid phase coherent transversal magnetization that forms over several *TR*-cycles. The two techniques are referred to as gradient and HF spoiling, respectively. Figure 3.3 shows the diagram of a FLASH sequence.

FLASH Steady-State Signal

Ideally, the transversal magnetization is completely destroyed at the end of each *TR*-interval, which is equal to the assumption of a vanishing transversal relaxation rate $T_2 = 0\,s$ [Ganter, 2006]. Thereby, the matrix $\boldsymbol{\mathcal{C}}$ simplifies and by using the Equations (3.3) and (3.8) the steady-state magnetization can be calculated:

$$\boldsymbol{M}_{\mathrm{ss}}^{\mathrm{FLASH}} = \begin{pmatrix} 0 \\ M_0 \frac{(1-E_1)\sin(\alpha)}{1-\cos(\alpha)E_1} \\ M_0 \frac{(1-E_1)\cos(\alpha)}{1-\cos(\alpha)E_1} \end{pmatrix}, \tag{3.9}$$

with $E_1 = \mathrm{e}^{-TR/T_1}$ and the scaling factor M_0. This yields the steady-state signal of a FLASH sequence:

$$\begin{aligned} S_{\mathrm{ss}}^{\mathrm{FLASH}} &= \sqrt{M_{\mathrm{ss},x}^2 + M_{\mathrm{ss},y}^2} \\ &= M_0 \frac{1-E_1}{1-\cos(\alpha)E_1} \sin(\alpha). \end{aligned} \tag{3.10}$$

The equations show that a FLASH sequence produces T_1-weighted images.

3.2.3 TrueFISP

For all ASL measurements a balanced SSFP (bSSFP) sequence called TrueFISP (True Fast Imaging with Steady-State Precession) was used. It was first proposed by Oppelt et al. [1986]. In a balanced SSFP sequence, all gradient moments are nulled at the end of each *TR*-interval and the transversal magnetization is refocused. Further, the phase of the RF pulses is incremented by 180° each *TR*-period, leading to an alternation between 0° and 180°. The sequence schema of a TrueFISP sequence is illustrated in Figure 3.3.

TrueFISP Steady-State Signal

With the Equations (3.3) and (3.8) the steady-state magnetization and signal of the TrueFISP sequence can be calculated. Ideally, the off-resonance $\Delta\omega$ is zero. Further, all gradients are balanced, so that $\Phi = 0$. However, when calculating $\boldsymbol{\mathcal{P}}$, the alternating phase of the RF pulses can be accounted for by assuming a phase acquisition of 180° during each *TR*-period [Hinshaw, 1976]. The steady-state magnetization of the TrueFISP sequence is then given by:

$$\boldsymbol{M}_{\mathrm{ss}}^{\mathrm{TrueFISP}} = \begin{pmatrix} 0 \\ M_0 \frac{(1-E_1)\sin(\alpha)}{1-E_1E_2-(E_1-E_2)\cos(\alpha)} \\ M_0 \frac{(1-E_1)(E_2+\cos(\alpha))}{1-E_1E_2+(E_1-E_2)\cos(\alpha)} \end{pmatrix}, \tag{3.11}$$

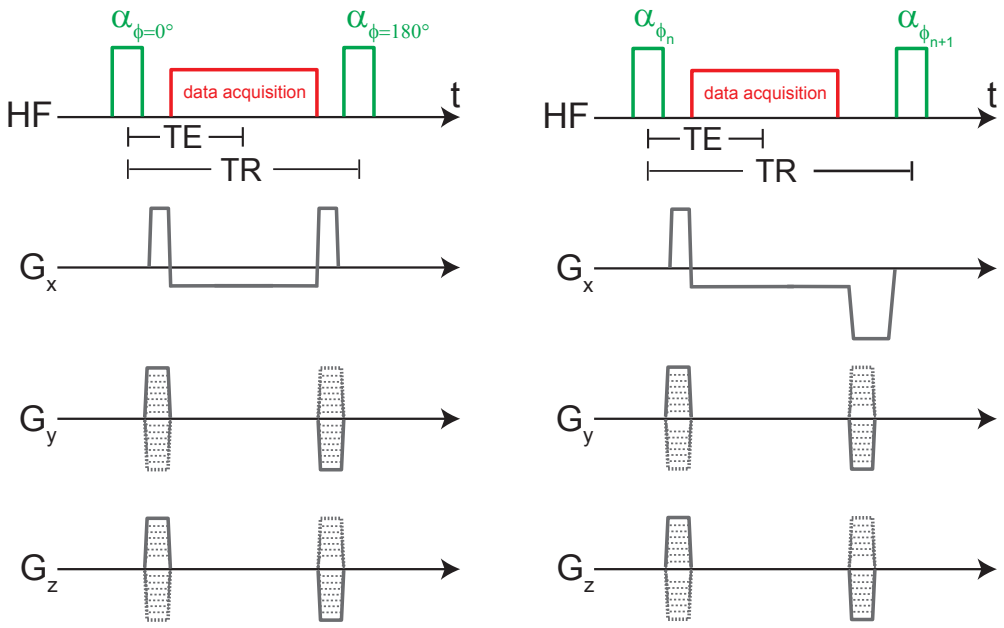

Figure 3.3: *Sequence scheme of a balanced (left, TrueFISP) and a spoiled (right, FLASH) 3D SSFP sequence. RF excitation is carried out globally. Without loss of generality, the direction of the readout gradient has been chosen to be in x-direction. Accordingly, the phase encoding occurs in y- and in z-direction. The gradients of the TrueFISP sequence are completely balanced over one TR-interval. For FLASH, only the phase encoding gradients are balanced while the readout gradient is followed by a spoiler gradient. Instead of an alternating phase between 0° and 180°, which is used for TrueFISP, the phase of the FLASH RF pulses is quadratically incremented by $\Phi_{spoil} \leq 50°$ each TR-cycle.*

with $E_2 = \mathrm{e}^{-TR/T_2}$ and M_0 and E_1 as defined above. The steady-state signal can now be calculated as:

$$\begin{aligned} S_{\mathrm{ss}}^{\mathrm{TrueFISP}} &= \sqrt{M_{\mathrm{ss},x}^2 + M_{\mathrm{ss},y}^2} \\ &= M_0 \frac{1 - E_1}{1 - E_1 E_2 - (E_1 - E_2)\cos(\alpha)} \sin(\alpha). \end{aligned} \tag{3.12}$$

For most applications of the TrueFISP sequence the relation $TR \ll T_{1,2}$ holds and allows the approximation $E_{1,2} = \mathrm{e}^{-TR/T_{1,2}} \approx 1 - TR/T_{1,2}$. Equation (3.12) then simplifies to:

$$S_{\mathrm{ss}}^{\mathrm{TrueFISP}} = M_0 \frac{\sin(\alpha)}{1 + \cos(\alpha) + (1 - \cos(\alpha))\frac{T_1}{T_2}}, \tag{3.13}$$

which shows that the steady-state signal for $TR \ll T_{1,2}$ is independent of TR and only depends on the flip angle α and the ratio T_1/T_2. While the composite contrast of T_1 and T_2 is often undesired in clinical routine, the TrueFISP sequence has the advantage of delivering the highest SNR per time of all steady-state sequences. For $T_1 = T_2$ and α=90° the steady-state signal equals half of the equilibrium magnetization.

Transient-State and Off-Resonance

The period during which the magnetization has not yet reached the steady-state, is called transient phase. This period is characterized by strong oscillations in longitudinal and transversal magnetization. Figure 3.4a shows the time course of signal and magnetization over several TR intervals. The oscillation can be reduced by preparing the magnetization. In the simplest case, an RF pulse with half of the flip angle ($\alpha/2$) is applied a time $TR/2$ before the first excitation pulse [Deimling and Heid, 1994]. The evolution of signal and magnetization with a preceding $\alpha/2$ pulse is shown in Figure 3.4b. Another approach is to use preparation pulses whose flip angles follow a Kaiser-Bessel function [Le Roux, 2003] (Kaiser-Bessel ramp). Independent of the preparation, the steady-state is normally reached after $\sim 5\,T_1/\,TR$ excitation cycles. Another drawback of bSSFP sequences is their sensitivity to off-resonances. Deviations from the Larmor frequency can cause so-called banding artifacts [Zur et al., 1988]. At the location of the banding artifacts the signal is approximately zero. The corresponding off-resonance frequency ω_{band} is given by odd integer multiples of the inverse of twice the time interval TR:

$$\omega_{\text{band}} = \frac{1}{2\,TR}. \tag{3.14}$$

As a consequence, TR should be kept as small as possible. Prior to the measurement, macroscopic inhomogeneities of the magnetic field should be compensated with the appropriate adjustment of the shim coils. The signal dependency on the resonance frequency and the number of TR cycles is plotted in Figure 3.5.

3.2.4 *k*-Space Sampling Strategies

Conventional sequences employ a Cartesian sampling of k-space. Starting with $-k_{\text{max}}$, k-space is normally traversed in a linear fashion until k_{max} is reached. For a bSSFP sequence, this means that the central k-space lines are first acquired after approximately half of the TR-intervals. As the k-space center carries the contrast information of an image, such a linear sampling can be inappropriate in case the relevant information is gained from the image contrast. Especially in cases where the contrast has a high temporal dynamic or when magnetization preparation schemes are used, alternative sampling strategies have to be considered.

Centric and Spiral Reordering

The steady-state signal of a bSSFP sequence is independent of the initial magnetization. Therefore, the impact of different initial conditions on the signal is only visible during the transient phase. Arterial spin labeling is a subtraction technique that relies on small contrast differences due to different initial longitudinal magnetizations. These differences are reduced with each TR cycle until they finally vanish when the steady-state is reached. Therefore, contrast relevant data has to be acquired first to gain a maximum contrast difference. This is achieved by sampling the central k-space region directly after the magnetic preparation. For a 2D data acquisition with one phase encoding direction the employed technique is called “centric reordering”. During the first TR interval after preparation, the central k-space line is sampled, followed

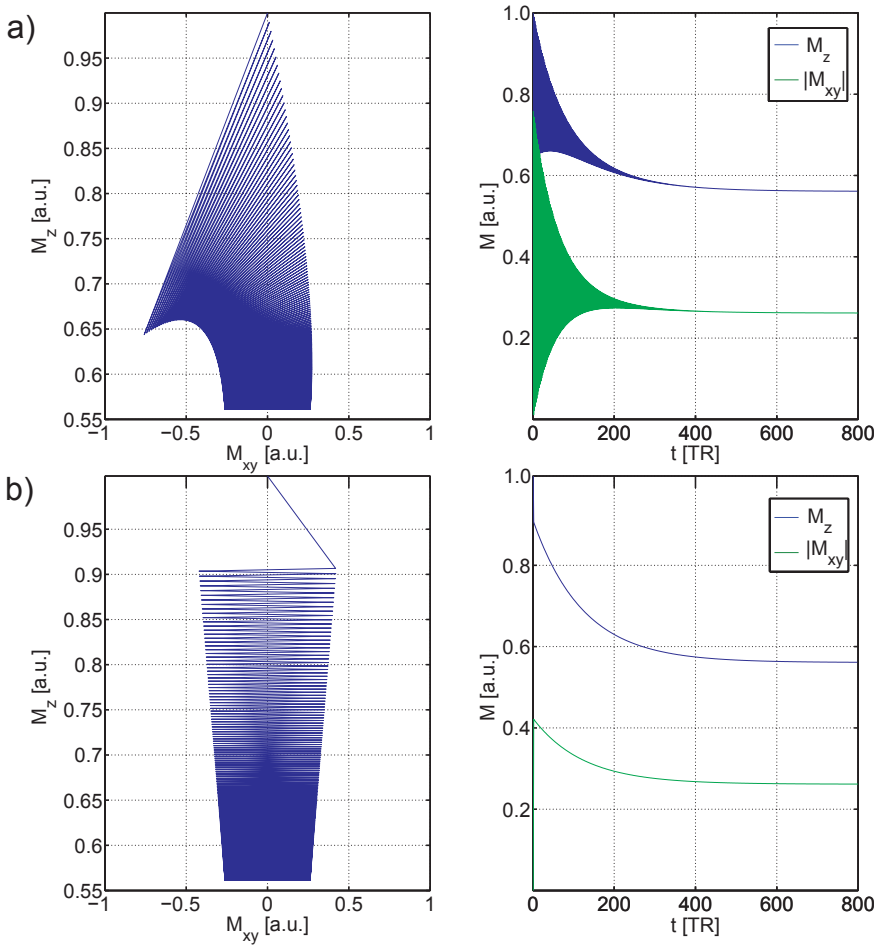

Figure 3.4: *Evolution of the magnetization of a balanced steady-state free precession sequence. The upper row (a) shows the temporal development with no magnetic preparation, the lower row (b) with an $\alpha/2$ pulse applied $TR/2$ before the first excitation pulse. The left panels display the trajectory of the tip of an on-resonant magnetization vector. The right panels depict the according evolution of the longitudinal magnetization and the signal. Overall, the first 800 TR-intervals are shown. In case no magnetic preparation is used, strong oscillations of magnetization and signal can be observed during the transient phase. In contrast, the usage of an $\alpha/2$ pulse leads to a smooth trend towards the steady-state magnetization.*

by the two lines directly below and above, respectively, and so on until k-space is completely sampled. The principle of centric reordering is shown in Figure 3.6a. In case of 3D imaging and two phase encoding directions, a similar technique called "spiral reordering" is used. Again, the central k-space line is recorded first. The progression outwards to higher k-values is now a two-dimensional problem that offers different pathways. Given that the readout direction is along the x-axis, phase encoding is defined in the k_y-k_z plane. With spiral reordering, one starts the center of the k_y-k_z plane and spirals out in a square manner [Wilman and Riederer, 1996]. Figure 3.6b illustrates spiral reordering. The respective reordering techniques have been used for all ASL measurements in this work.

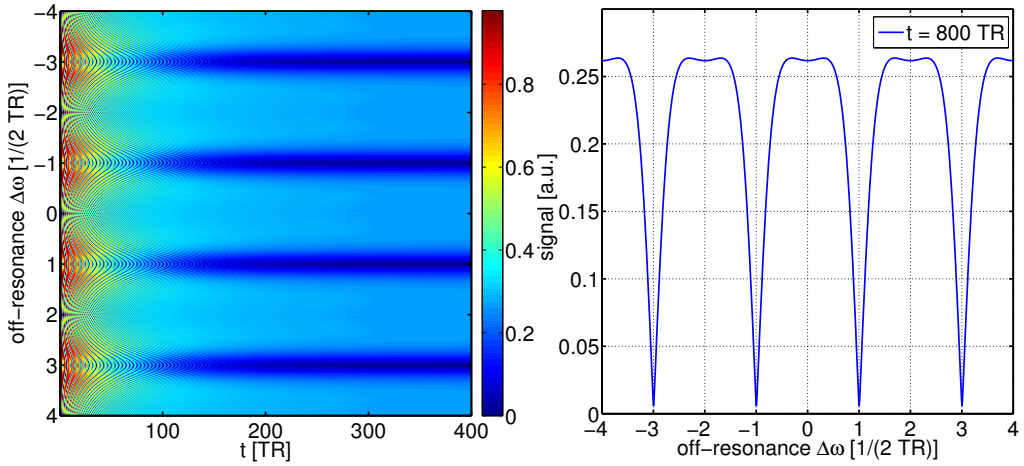

Figure 3.5: *Signal of a bSSFP sequence as a function of the off-resonance frequency $\Delta\omega$. The left plot displays the signal dependency on off-resonance and number of TR-cycles without prior magnetic preparation. The right panel shows the steady-state signal plotted against the off-resonance frequency. Both images show the banding artifacts, i.e. signal drops at frequencies that are odd integer multiples of 1/(2 TR).*

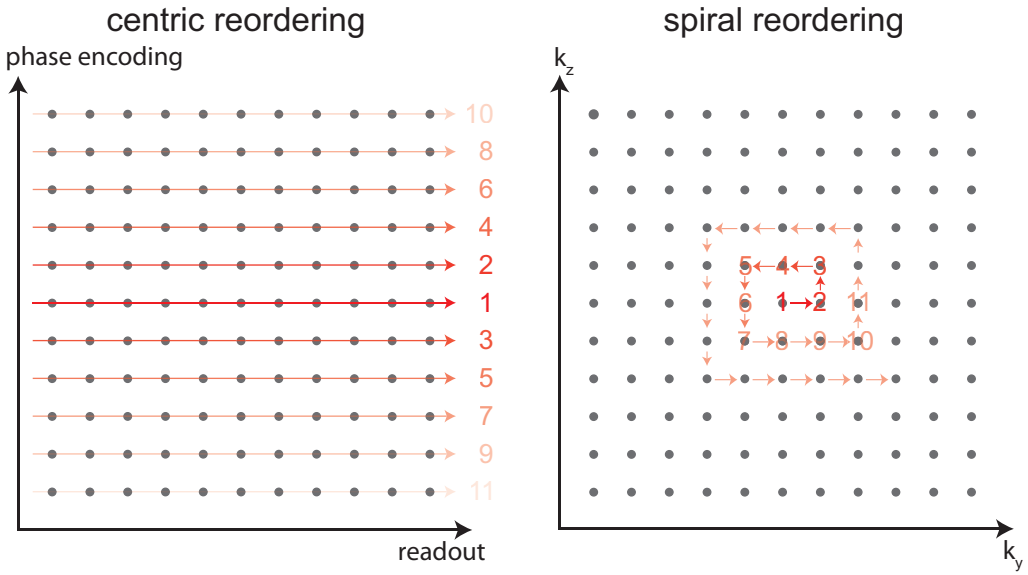

Figure 3.6: *Centric (left panel) and spiral (right panel) reordering of Cartesian k-space acquisition. Centric reordering is used for 2D imaging. In contrast to a conventional sampling, the central k-space line is recorded first. The remaining k-space lines are sorted after their distance to the central line and are sampled in this order. Spiral reordering is used for 3D imaging. The illustration shows the plane spanned by the two phase encoding directions k_y and k_z. The readout directions points into and out of the drawing plane, respectively. Starting with the central line, the phase encoding trajectory follows a spiral pattern until the complete k-space is recorded. In both images, numbers indicate the order of data recording.*

TWIST

Besides a high spatial resolution, DCE-MRI requires a high temporal resolution, to guarantee a sufficiently high tracking rate of the contrast bolus. When imaging a whole volume with conventional k-space sampling strategies, the required temporal resolution can only be achieved with heavy losses in spatial resolution. By using a sampling strategy called TWIST (time-resolved imaging with stochastic trajectories) [Vogt et al., 2007], a satisfying balance between spatial and temporal resolution can be found, even for three-dimensional imaging. A detailed explanation of TWIST is found in Song et al. [2009]. The TWIST scheme is depicted in Figure 3.7. Assuming phase encoding in the directions k_y and k_z, all points (each corresponding to one readout line) in the phase encoding plane k_y-k_z are first sorted by increasing radial distance d_r from the k-space center and then by their azimuthal angle Ψ. Then, k-space is divided in two regions: region A covers the central points with radial distance smaller than a critical value d_c. This region contains the contrast information. Region B covers the remaining k-space containing the high-frequency information. Finally, region B is divided in N disjoint and non-overlapping subsets of points. When acquiring the dynamic 3D image series, k-space is only covered fully for the first and the last image. For all other images, only the data in region A is completely recorded. Sampling starts at $d_r \approx d_c$, proceeds towards the origin and then back outwards to the edge of region A. During the inward

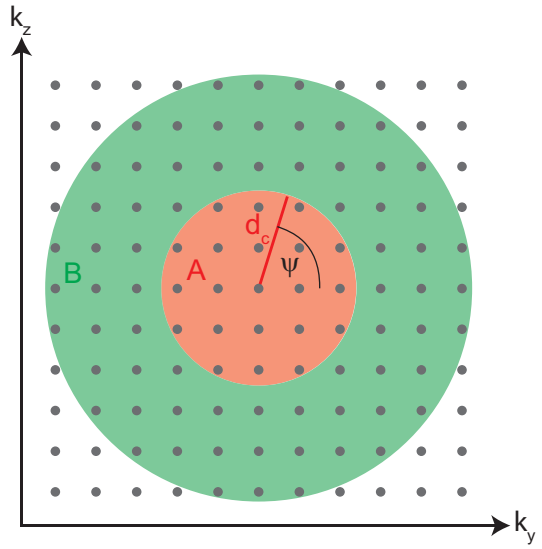

Figure 3.7: *Illustration of the TWIST k-space sampling strategy for 3D imaging with high temporal and spatial resolution. The illustration shows the plane spanned by the two phase encoding directions k_y and k_z. The readout directions points into and out of the drawing plane, respectively. All points (actually readout lines) in the phase encoding plane are first sorted after their distance to the central point and then after their azimuthal angle ψ. By defining a critical radial distance d_c, k-space is divided in two regions. Each data acquisition, region A is sampled completely while only 1/N-th of region B is recorded. To reconstruct an image, the missing data in region B is copied from previous or subsequent recordings.*

movement all odd points of the sorted list are sampled, even points are recorded on the way out. In contrast, only $1/N$-*th* of region B is recorded. Starting at the border of region A and B, odd points are sampled when proceeding towards larger d_r and even points are sampled on the way back to d_c. Effectively, the k-space trajectory within region B follows a spiral patterns. The sampled subset of points in region B is different for each image such that all its points are recorded after N acquisitions. The missing data in a single image is copied from previous (forward-data sharing) or subsequent (backward-sharing) images, i.e. different sampling trajectories of region B are twisted into each other. The nominal acquisition time of one TWIST image is given by:

$$TA_{\mathrm{TWIST}} = TA_{\mathrm{full}} \left(\frac{S_{\mathrm{A}}}{S_{\mathrm{PE}}} + \left(1 - \frac{S_{\mathrm{A}}}{S_{\mathrm{PE}}} \right) \rho_{\mathrm{B}} \right), \tag{3.15}$$

where S_{A} and S_{PE} denote the area of region A and the total phase encoding area, respectively. $\rho_B = 1/N$ is the sampling density of region B and TA_{full} the full k-space acquisition time. Hence, the temporal resolution can be improved decreasing S_{A} or by increasing N. The latter will decrease the fidelity of fine image structures, while the former will sacrifice contrast information.

Parallel Imaging

A further method to accelerate imaging speed and k-space sampling, is parallel imaging. The method makes use of multichannel or phased array receive coils. Such coils do not only allow an increased SNR [Roemer et al., 1990] but also offer the probability of utilizing the differing sensitivities of the single receive coils to reconstruct a subsampled k-space. For a Cartesian acquisition scan time is linearly proportional to the number of phase-encoding steps. In parallel imaging only every R-*th* k-space line is sampled, however the extend of k-space (the resolution) is conserved. R is referred to as acceleration factor. As a consequence of the increased Δk the FoV is reduced. Depending on the size of the imaged object, this leads to aliasing or wrap-around artifacts. Parallel imaging conserves the FoV and prevents these artifacts by using the information of the single receive coils in the phased array. Basically, two parallel imaging techniques exist: k-space methods that reconstruct the missing data in k-space [Sodickson and Manning, 1997] and image space methods that remove aliasing after the Fourier transform [Pruessmann et al., 1999].

For this work the parallel imaging method GRAPPA (general autocalibrating partially parallel acquisition) proposed by Griswold et al. [2002], was used. GRAPPA is an improved method of AUTO-SMASH [Jakob et al., 1998] and belongs to the class of k-space methods. The complex exponential functions corresponding to the missing phase-encoding lines are approximated by linear combinations of the coil sensitivities. GRAPPA uses an indirect sensitivity measurement where so-called autocalibration signal (ACS) lines are acquired to determine the weighting factors of each coil. These lines are additional, Nyquist-sampled lines near the center of k-space. Besides the extra ACS lines, not only a single line but a group of nearby measured lines is used to synthesize an omitted k-space line. Due to the sub-sampled k-space, imaging speed is increased

at the expense of image quality (SNR $\propto 1/\sqrt{R}$). GRAPPA can be employed for 2D and 3D imaging, omitting lines in one and two phase-encoding directions, respectively.

3.2.5 Inversion Profile Measurement

To measure the profile of the slice-selective inversion pulses a modified gradient echo sequence was used. The sequence used to measure the inversion profiles is shown in Figure 3.8. First the dedicated inversion pulse is transmitted while applying the slice selection gradient. Then, the remaining transversal magnetization is spoiled by applying gradient fields on all three axes. The length of these gradients was set to 3 ms, the amplitude was 22 $\frac{\text{mT}}{\text{m}}$. Directly after the spoiler gradients, a 90° excitation pulse is transmitted which flips the magnetization into the transversal plane. For this purpose a non-selective, rectangular pulse was used acting on the complete magnetization within the range of the transmitter coil. The excitation pulse is followed by a readout gradient in slice-selection direction. No phase-encoding was used.

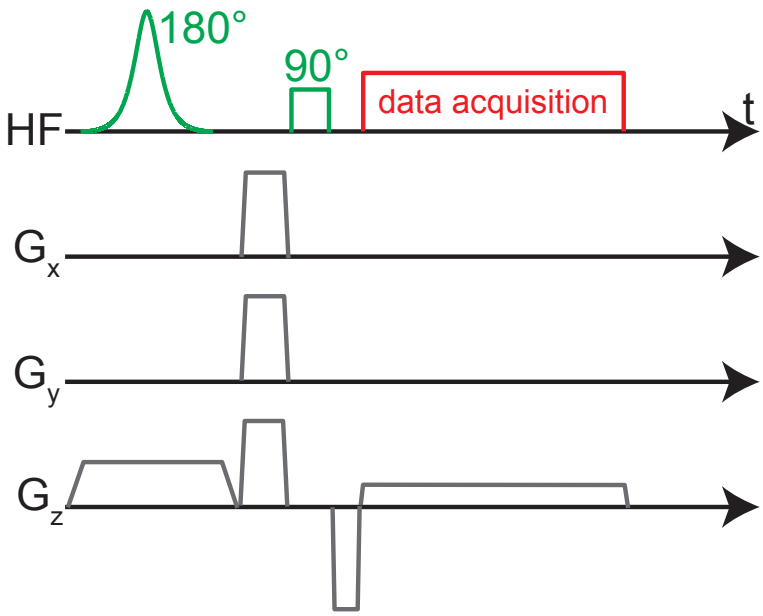

Figure 3.8: *Schematic representation of the sequence used to measure the inversion profiles. After the slice-selective inversion pulse the remaining transversal magnetization is destroyed by spoiler gradients. Then a globally acting 90° excitation pulse is flipping the longitudinal magnetization into the transversal plane. By applying a readout gradient in slice-selection direction, the profile of the inversion is detected.*

3.3 Perfusion Measurement with Arterial Spin Labeling

In this section the employed methods to measure perfusion with ASL are described. At first, the applied labeling scheme is presented. Afterwards, the 2D ASL sequence utilized in the animal study and the developed 3D ASL sequence are discussed. For each sequence, the respective quantitation approach is outlined. All non-invasive perfusion measurements in this work were performed with pulsed ASL sequences using adiabatic inversion pulses. This type of inversion pulses have been studied intensively for this work. Hence, a detailed discussion is given in Section 3.5.1.

3.3.1 FAIR Labeling Scheme

Both ASL sequences used in this work employ the flow-sensitive alternating inversion recovery (FAIR) scheme that was briefly introduced in Section 2.3.3. FAIR labeling belongs to the class of pulsed ASL sequences and was proposed by Kim [1995]; Kwong et al. [1995]. In contrast to other labeling schemes, the preparation of the tag image is accomplished by the slice-selective inversion of the imaging region itself. For the control image, a global inversion is used which means that the complete magnetization within the range of the transmitter coil is inverted. Therefore, the acquisition of tag and control image can be considered as two separate inversion recovery experiments. In case of the slice-selective inversion the recovery of longitudinal magnetization in the imaging region is sensitive to inflowing blood water, while it remains undisturbed for the control case. Compared to ASL sequences with a labeling proximal to the imaging region, FAIR has the advantage that signal loss due to T_1-relaxation of tagged blood water on its way into the imaging region is minimized. Further, due to its symmetric nature erroneous perfusion signals due to MT effects are inherently compensated. For the tag image, at $t = 0$ the magnetization in the imaging region is inverted. After the inflow time, uninverted magnetization has entered the imaging region, effectively increasing the longitudinal relaxation time in the tissue of interest. For the control image, a global inversion is performed at $t = 0$ and no effect other than the undisturbed T_1 relaxation occurs during TI. In both cases, the region of interest is imaged after the inflow time. Due to its intrinsic compensation of the MT effect, FAIR allows larger imaging volumes such that besides the two dimensional imaging of a single slice also multi-slice and 3D imaging are possible. Ideally the signal of static tissue is identical for both preparations. The difference image ΔM of tag and control image is then completely perfusion-weighted, as the signal depends on the magnetization that flowed into the imaging region during TI. ΔM is often referred to as perfusion-weighted image, while tag and control are known as slice-selective and non-selective inversion. Figure 3.9 illustrates the FAIR scheme using the example of a brain perfusion measurement right before imaging, i.e. after the inflow time TI.

3.3.2 FAIR Perfusion Quantitation

The model used to derive absolute perfusion values from a FAIR ASL experiment was proposed by Kim [1995]. The model bases on the modified Bloch equation [Detre et al., 1992] for the longitudinal magnetization that includes additional terms for arterial and venous flow. The equation was introduced in Section 2.3.3. Assuming a well-mixed compartment the magnetization of the venous outflow is equal to that in the tissue water [Williams et al., 1992] such that $M_{\mathrm{V}}(t) = M_{\mathrm{T}}(t)/\lambda$ (this is equivalent to the assumption of a residual function of the form $r(t) = \mathrm{e}^{-\mathrm{ft}/\lambda}$ for the "general kinetic model" [Parkes, 2005]). Using this relation, Equation (2.60) for the rate of change of the longitudinal tissue magnetization, reads:

$$\frac{\mathrm{d}M_{\mathrm{T}}(t)}{\mathrm{d}t} = \frac{M_{\mathrm{T},0} - M_{\mathrm{T}}(t)}{T_{1,\mathrm{T}}} + f\left(M_{\mathrm{A}}(t) - \frac{M_{\mathrm{T}}(t)}{\lambda}\right). \tag{3.16}$$

For the slice-selective (ss) inversion in a FAIR experiment, the magnetization of in-

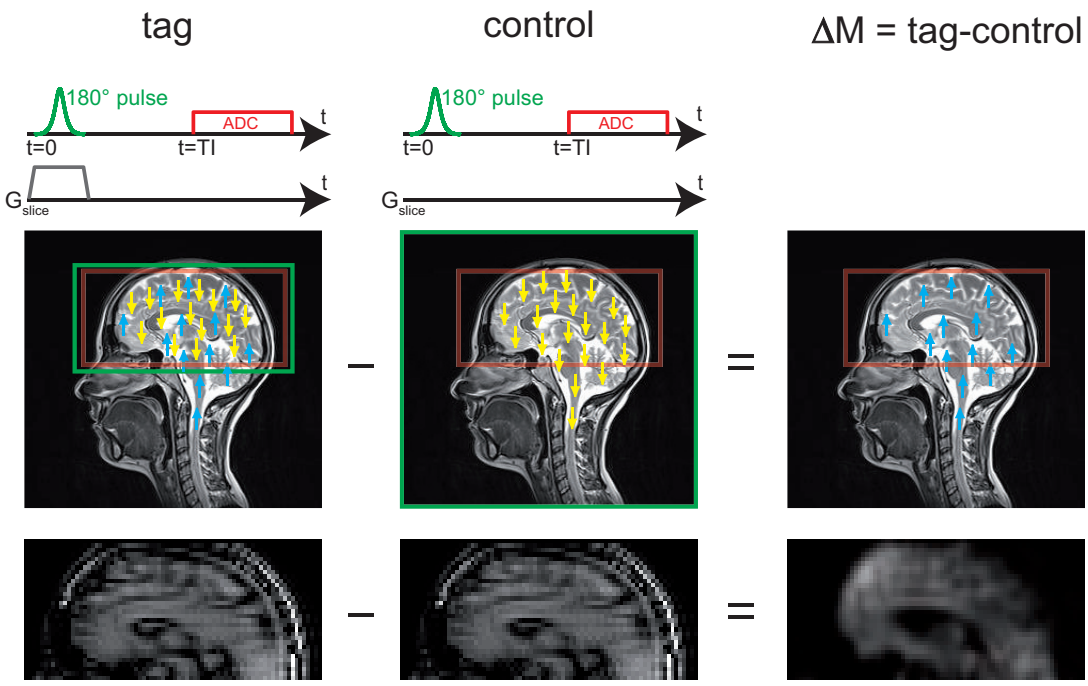

Figure 3.9: *Design of a FAIR ASL experiment for brain perfusion measurement. The images show the situation at $t = TI$, i.e. at the beginning of the imaging module. Both preparations involve an inversion pulse. For the tag image, the inversion pulse (green) applied at $t = 0$ is slice-selective and solely inverts the magnetization in the imaging region (red). Due to uninverted spins that flow into the brain during TI, the T_1-relaxivity is effectively accelerated and can be described by an apparent longitudinal relaxation time $T_{1,app} < T_{1,T}$. The generation of the control image requires a global inversion of magnetization (green box). Hence, the longitudinal magnetization of blood water inside and outside the imaging region is identical such that the relaxation is not influenced by inflowing spins. At $t = TI$ the brain is imaged through the readout module of the ASL sequence. Ideally, the signal of static tissue is identical in tag and control image. Then, the signal in the difference image ΔM of tag and control image depends on the amount of magnetization delivered into the brain tissue during TI, a quantity directly related to the perfusion f.*

flowing arterial water $M_{\mathrm{A}}(t)$ is fully relaxed and therefore time-independent:

$$M_{\mathrm{A}}(t) = M_{0,\mathrm{A}} = \frac{M_{0,\mathrm{T}}}{\lambda}. \tag{3.17}$$

Equation (3.16) can then be solved and yields the time-dependent longitudinal magnetization of the tissue:

$$M_{\mathrm{T,ss}}(t) = M_{0,\mathrm{T}} \left(1 - 2\,\alpha\,\mathrm{e}^{-t/T_{1,\mathrm{app}}}\right), \tag{3.18}$$

with the apparent longitudinal relaxation of the tissue:

$$\frac{1}{T_{1,\mathrm{app}}} = \frac{1}{T_{1,\mathrm{T}}} + \frac{f}{\lambda}. \tag{3.19}$$

As in case of the "general kinetic model", the factor α describes the inversion efficiency in terms of the fraction of the maximum available change of the longitudinal magnetization. In case of the non-selective (ns) inversion in a FAIR experiment, the longitudinal magnetization of inflowing arterial blood is initially inverted and relaxes during the inflow time. On its way to the capillaries, the relaxation is described by the longitudinal relaxation time $T_{\mathrm{A},1}$ of arterial blood. After entering the tissue, this value changes to the longitudinal relaxation rate $T_{1,\mathrm{T}}$ of tissue. The model of Kim [1995] simplifies this process by assuming an identical relaxation time T_1 of arterial blood and tissue water. Then, $M_{\mathrm{A}}(t) = M_{\mathrm{T}}(t)/\lambda$ and the solution to Equation (3.16) is given by an inversion recovery:

$$M_{\mathrm{T,ns}}(t) = M_{0,\mathrm{T}} \left(1 - 2\,\alpha\,\mathrm{e}^{-t/T_1}\right). \tag{3.20}$$

The magnetization in the difference image is then given by:

$$\begin{aligned} \Delta M(t) = M_{\mathrm{T,ss}}(t) - M_{\mathrm{T,ns}}(t) &= -2\,\alpha\,M_{0,\mathrm{T}}\,\mathrm{e}^{-t/T_1}\left(\mathrm{e}^{-ft/\lambda} - 1\right) \\ &\approx 2\,\alpha\,M_{0,\mathrm{T}}\,\frac{ft}{\lambda}\,\mathrm{e}^{-t/T_1}, \end{aligned} \tag{3.21}$$

where the exponential term was expanded in a Taylor series and truncated after the second term, yielding $\mathrm{e}^{-ft/\lambda} \approx 1 - ft/\lambda$. The approximation is valid as normally $f \ll \lambda$. According to Equation 3.21, the maximal signal difference is expected for $t = T_1$. Finally, the perfusion f for a FAIR experiment with inflow time TI can be calculated:

$$f(TI) = \frac{\lambda}{2\,TI\,\alpha}\,\frac{\Delta M(TI)}{M_{0,\mathrm{T}}}\,\mathrm{e}^{TI/T_1}. \tag{3.22}$$

The value for the equilibrium magnetization of the tissue $M_{0,\mathrm{T}}$ can either be accessed by choosing an inflow time $TI \gg T_1$ or by imaging without prior inversion. α has to be estimated experimentally, while values for T_1 and λ can be found in the literature.

3.3.3 Q2TIPS

The quantitation of perfusion based on ASL data acquired at exactly one TI can lead to erroneous absolute perfusion values as the signal in the perfusion-weighted image is not only depending on the inflow time but, amongst others, primarily on the transit delay Δt. In the brain, the time it takes for the labeled blood to arrive in the voxel of interest, i.e. the transit delay, can be of the order of one second. Further, it changes between different regions. In areas with a large transit delay, this leads to an underestimation of perfusion (cf. Figure 2.18). In a simple PASL experiment, the temporal length of the labeled blood bolus T is limited by the inversion slice profile and the coil geometry and is an unknown quantity. Even if it was known, waiting until all voxels are filled is not an option, as the signal decay would lead to an even smaller perfusion signal. To avoid quantitation errors due to varying transit delays, Wong et al. [1998a] proposed QUIPSS (quantititative imaging of perfusion using a single subtraction) and QUIPSS II for pulsed ASL. The method was later refined by Luh et al. [1999] who named it Q2TIPS (QUIPSS II with thin-slice TI_1 periodic saturation). The idea is to use additional saturation pulses to define the temporal length T of the labeled blood bolus. The saturation pulses are applied such that no new labeled blood enters the imaging

region after a time $t > T$. If TI and T are chosen such that $T + \Delta t < TI$, the perfusion signal differences due to varying transit delays cancel out. Figure 3.10 illustrates the time course of the perfusion signal with and without Q2TIPS saturation pulses for two voxels with equal blood flow but different transit times. Similar to Equation (3.22), the absolute perfusion f from an ASL experiment that uses Q2TIPS is calculated as:

$$f(TI) = \frac{\lambda}{2\,T\,\alpha}\,\frac{\Delta M(TI)}{M_{0,\mathrm{T}}}\,\mathrm{e}^{TI/T_1}. \tag{3.23}$$

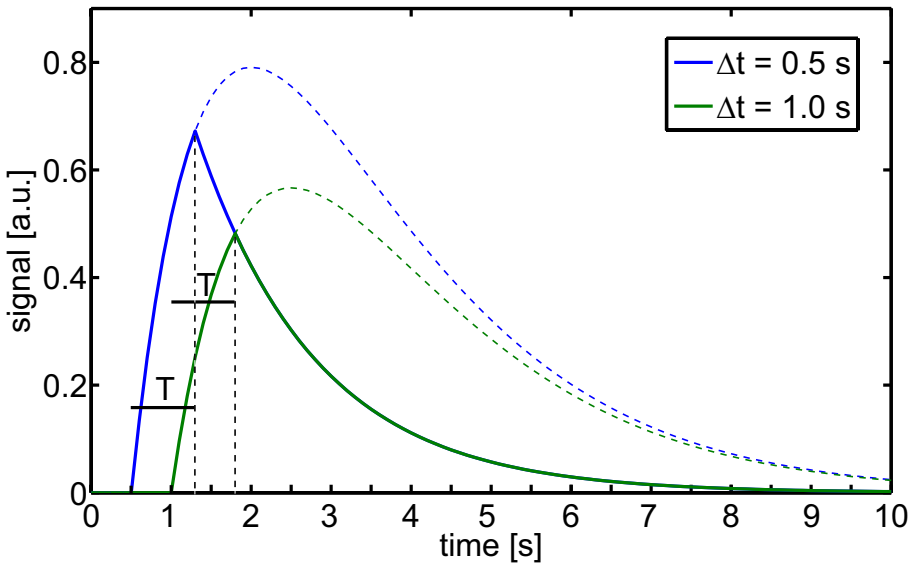

Figure 3.10: *Time course of the perfusion signal in two voxels with equal perfusion but different transit delays. The solid lines show the evolution of the signal using Q2TIPS and a bolus length of T, the dotted lines represent the signal without the additional saturation and an infinitely long bolus. It can be seen that the Q2TIPS signal of both voxels is identical for $t > T + \Delta t$.*

3.3.4 WET Saturation

Water suppression enhanced through T_1 effects (WET) is a saturation method to minimize water signal. For ASL measurements, it can be used to saturate the imaging region prior to labeling. This way the initial conditions for all experiments are identical and the signal of static tissue is reduced. The advantage of WET is the effective saturation over a broad range of T_1 and B_1 values, allowing the saturation of different tissue species even with deviating flip angles. The WET scheme was originally proposed for spectroscopy by Ogg et al. [1994] and was first applied for ASL by Golay et al. [2005]. The scheme uses the combination of single water suppression modules each consisting of an RF pulse with flip angle θ_i followed by dephasing gradients that eliminate the transversal magnetization. At a fixed time τ after the beginning of one module, the next one starts. By neglecting the finite width of the RF pulses, the

longitudinal magnetization after the *i-th* module is given by:

$$M_{z,i} = M_{z,i-1}\, e^{-\tau/T_1} \cos(\theta_i) + M_0(1 - e^{-\tau/T_1}), \tag{3.24}$$

with the longitudinal relaxation time T_1 of the specific species and its equilibrium magnetization M_0. In case the initial longitudinal magnetization is M_I the equation reads:

$$\begin{aligned} M_{z,i} = {} & M_I\, e^{-i\tau/T_1} \cos(\theta_1)\cos(\theta_2)\ldots\cos(\theta_i) \\ & + M_0(1 - e^{-\tau/T_1})[1 + e^{-(i-1)\tau/T_1}\cos(\theta_2) \\ & \ldots\cos(\theta_i) + \cdots + e^{-\tau/T_1}\cos(\theta_i) + 1]. \end{aligned} \tag{3.25}$$

Both equations assume the complete dephasing of transversal magnetization in between RF pulses. Given a number of pulses i and a delay time τ, Equation (3.25) allows to find a set of flip angles $[\theta_1, \ldots, \theta_i]$ that minimizes the residual magnetization $M_{z,i}$ for a broad range of T_1 values. This can be achieved by means of numerical optimization. Typically, four RF pulses are used for WET. Figure 3.11 shows a typical four-pulse WET scheme with an inter-pulse duration τ. Each selective RF pulse with flip angles θ is followed by spoiler gradients to eliminate transversal magnetization. For ASL, the enhanced water suppression of WET can be used to pre-saturate the imaging region prior to the inversion pulse of tag and control image. This allows a homogeneous preparation and a reduced influence of longitudinal magnetization in the readout. For some labeling schemes, like STAR, it also allows a drastic reduction of the time between subsequent images. Further, when applying WET right after the inversion pulse, this post-saturation enables a defined start time of the bolus and may represent the saturation required for background suppression discussed in the next section. Depending on the labeling scheme, post-saturation can also compensate for MT effects. WET can further be used to achieve a well-defined length of the bolus, e.g. for Q2TIPS [Luh et al., 1999].

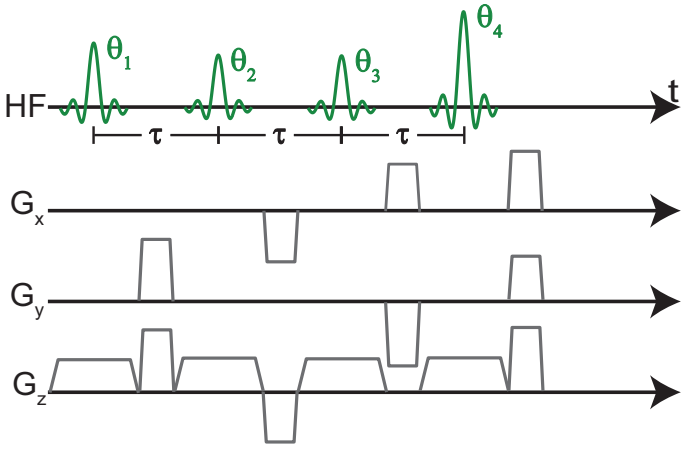

Figure 3.11: *Scheme of a four-pulse signal suppression with WET. The selective RF pulses are followed by spoiler gradients that eliminate the transversal magnetization. The time lag of two subsequent RF pulses is τ. The flip angles θ_i are optimized in order to minimize the residual longitudinal magnetization after the last spoiler gradients.*

3.3.5 Background Suppression

When calculating the perfusion-weighted image by subtracting control from tag image, the signal of static tissue is to be eliminated. However, due to the low signal-to-

noise ratio (SNR) of the perfusion signal of only a few percent compared to the tissue signal, even small fluctuations in the tissue signal can corrupt the ASL signal. The idea of background suppression is to strongly reduce the signal of static tissue at the time of the signal acquisition by means of a preceding saturation recovery and the application of non-selective inversion pulses. The technique was originally suggested for angiography [Dixon et al., 1991; Mani et al., 1997] and has later been adapted for ASL measurements [Ye et al., 2000]. It is similar to the WET scheme described above. However, instead of finding the optimal suppression for a complete range of T_1 times, background suppression uses inversion pulses to explicitly eliminate the signal of tissue associated with certain relaxation rates. After the initial saturation of longitudinal magnetization, non-selective inversion pulses are applied at specific points in time. The timing is calculated such that the magnetization is re-nulled a predetermined time after saturation. In order to null the signal of n tissue species, each with its specific longitudinal relaxation rate, n global inversion pulses are needed. At a time TI after saturation, the normalized longitudinal magnetization M_z of a tissue component with the longitudinal relaxation rate T_1 is given by:

$$M_z(T_1) = 1 + (-1)^{n+1} e^{TI/T_1} + 2 \sum_{i=1}^{n} (-1)^i e^{-\tau_i/T_1}. \tag{3.26}$$

Here, n is the number of inversion pulses and τ_i is the time from the i-th inversion to when M_z is measured. Generally, there is no analytical solution for an arbitrary set of n different T_1 that are to be nulled at TI and the resulting system of n equations has to be solved numerically.

The implementation of background suppression in an ASL experiment requires that the final signal difference ΔM is not altered. By solely saturating the imaging region at the beginning of the background suppression, this can be achieved. For n ideal inversion pulses, the final signal difference is then given by [Ye et al., 2000]:

$$\Delta M^* = (-1)^n \Delta M, \tag{3.27}$$

where ΔM denotes the signal in the perfusion-weighted image in case no background suppression is applied. Figure 3.12 shows time course of longitudinal magnetization in an ASL experiment with and without the application of background suppression, respectively. For each case, the magnetization of two tissue species and of inflowing blood, both for tag and control image, is shown. In contrast to the full signal contribution of tissue in case of no background suppression, the signal of both tissue species is nulled at the time of the readout when background suppression is used. The signal difference ΔM, however, is identical in both cases.

3.4 Perfusion Measurement with Dynamic Contrast-Enhanced MRI

This section describes the contrast agent and the quantitation model used for the DCE-MRI experiments. The basics of DCE-MRI are explained in Section 2.3.4.

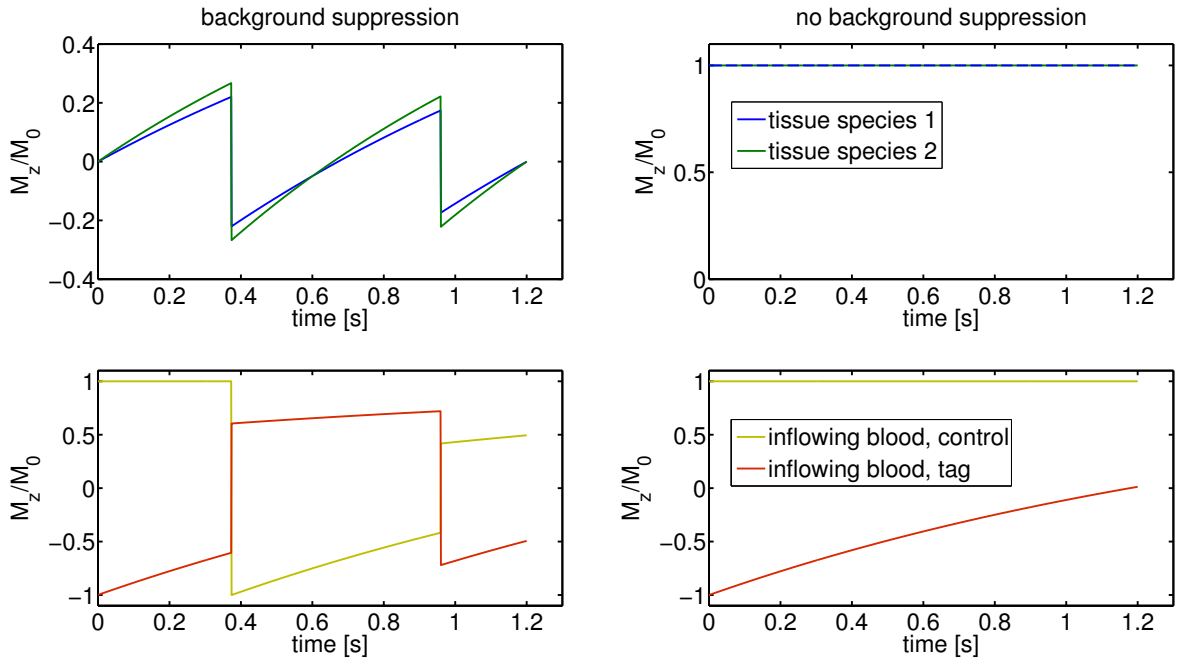

Figure 3.12: *Time course of normalized longitudinal magnetization in an ASL experiment with (left panels) and without (right panels) background suppression. The upper panels show the development of the magnetization of two tissue species with a T_1 of 1.5 s (blue) and 1.2 s (green), respectively. The lower row shows the magnetization of inflowing blood for tag (red) and control (yellow) over time. The inflow time of the experiment is 1.2 s and the inversion pulses were calculated to be applied 0.37 s and 0.96 s after saturation. In contrast to the full signal contribution of tissue in case of no background suppression, the signal of both tissue species is nulled at the time of the readout when background suppression is used. The signal difference ΔM is identical in both cases.*

3.4.1 Contrast Agent

The contrast agent used to conduct the DCE-MRI experiments was Dotrarem® (Guerbet, Roissy CdG Cedex, France). One milliliter aqueous solution contains 279.32 mg Gadoteric acid (Gd-DOTA), which is a macrocycle-structured gadolinium-based molecule. The molecule is a complex of a gadolinium ion (Gd^{3+}) and the chelating agent 1,4,7,10-tetraazacyclododecane-1,4,7,10-tetraacetic acid (DOTA). In the contrast agent Gadoteric acid is used in form of the meglumine salt. Figure 3.13 shows the chemical structure of Gadoteric acid. The central gadolinium atom determines the physical properties of the contrast agent. Due to its electron configuration ($[Xe]\,4f^7\,5d^1\,6s^2$) it has seven unpaired electrons in the f shell. Therefore, above its Curie temperature of 292.5 K, it has strong paramagnetic properties. As a consequence, the relaxation rates of protons in the direct surrounding of Gadoteric acid are increased. Particularly, the longitudinal relaxation time T_1 is shortened. After intravenous injection, the molecule is distributed in vasculature and interstitium where it leads to an increased contrast compared to surrounding tissues. Especially in a T_1-weighted image, regions with a

higher contrast agent concentration will appear brighter. An effect that is amongst others utilized for angiography, perfusion MRI or tumor detection. Gadoteric acid is rapidly excreted by the kidneys and leaves the body unchanged.

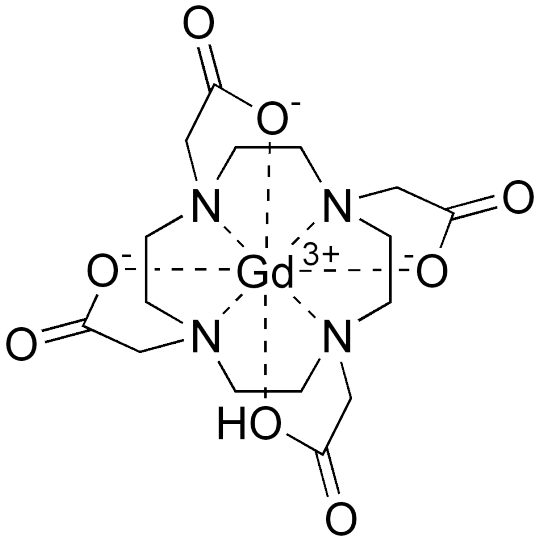

Figure 3.13: *Molecular structure of Gadoteric acid with its central gadolinium ion. Due to the high toxicity of free gadolinium ions for humans, it is embedded in the chelating agent DOTA.*

3.4.2 Perfusion Quantitation via Deconvolution

To obtain absolute perfusion values from the DCE-MRI data sets, the model-independent approach introduced in Section 2.3.4 was followed. The tissue response function is thereby computed by means of numerical deconvolution. This is an ill-posed problem and requires regularization methods to derive physically reasonable values. Here, the truncated singular value decomposition (TSVD) method proposed by Østergaard et al. [1996b,a] is used. It is outlined in the following and was later refined by Sourbron et al. [2007a]. Assuming a uniform sampling with time steps Δt of both the AIF $C_{\mathrm{A}}(t)$ and tissue concentration function $C_{\mathrm{T}}(t)$, Equation (2.64):

$$C_{\mathrm{T}}(t) = C_A(t) \otimes I(t) = \int_0^t C_{\mathrm{A}}(t')I(t-t')\mathrm{d}t', \tag{3.28}$$

can be reformulated in a matrix equation. Starting at $t = 0$ when the bolus arrives, the tissue tracer concentration for the j-th time step is:

$$C_{\mathrm{T}}(t_j) = C_T(j\Delta t) \approx \Delta t \sum_{i=0}^{j} C_A(t_i)I(t_j - t_i), \tag{3.29}$$

which yields the matrix equation:

$$\boldsymbol{C} = \boldsymbol{\mathcal{A}}\boldsymbol{I}. \tag{3.30}$$

In case of n time steps, $\boldsymbol{C}$ represents an n-element vector and $\boldsymbol{\mathcal{A}}$ an $n \times n$ matrix. The relation between AIF, tissue concentration function and impulse response function is depicted in Figure 3.14. Depending on the discretization method, the exact form of the matrix $\boldsymbol{\mathcal{A}}$ differs. For this work, the volterra convolution in Equation (2.64) was discretized with the approach proposed by Sourbron et al. [2003] that is described in Sourbron et al. [2007b]. The algebraic solution of Equation (3.30) is very sensitive to noise in the data. Therefore, the general approach is to solve the least-squares problem:

$$\min_{\boldsymbol{I}} \|\boldsymbol{C} - \boldsymbol{\mathcal{A}}\boldsymbol{I}\|_2. \tag{3.31}$$

To calculate a solution for $\boldsymbol{I}$, the matrix $\boldsymbol{\mathcal{A}}$ is rewritten using a singular value decomposition (SVD):

$$\boldsymbol{\mathcal{A}} = \boldsymbol{\mathcal{U}}\boldsymbol{\mathcal{S}}\boldsymbol{\mathcal{V}}^{\top}, \tag{3.32}$$

where $\boldsymbol{\mathcal{U}}$ and $\boldsymbol{\mathcal{V}}$ are orthogonal matrices. $\boldsymbol{\mathcal{S}}$ is a diagonal matrix that holds the singular values σ_i of $\boldsymbol{\mathcal{A}}$. After truncating $\boldsymbol{\mathcal{S}}$, i.e. setting all singular values below a certain threshold κ to zero, $\boldsymbol{I}$ and therefore $I(t)$ is found as:

$$\boldsymbol{I} = \boldsymbol{\mathcal{A}}^{-1}\boldsymbol{C}, \tag{3.33}$$

with the pseudo-inverse:

$$\boldsymbol{\mathcal{A}}^{-1} = \boldsymbol{\mathcal{V}}\boldsymbol{\mathcal{S}}^{-1}\boldsymbol{\mathcal{U}}^{\top}. \tag{3.34}$$

Given that after the singular value truncation, $\mathrm{rank}(\boldsymbol{\mathcal{S}}) = r$ it is:

$$\boldsymbol{\mathcal{S}}^{-1} = \mathrm{Diag}(1/\sigma_1, \ldots, 1/\sigma_r, 0, \ldots, 0). \tag{3.35}$$

After the calculation of $I(t)$, the perfusion f can be readily accessed as it is the maximum of the response function (cf. Section (2.3.4)). Zöllner et al. [2013] implemented the described deconvolution method in an open source software tool called *UMMPerfusion*. All evaluations of DCE-MRI data in this work were carried out with this software using the TSVD to derive absolute perfusion values.

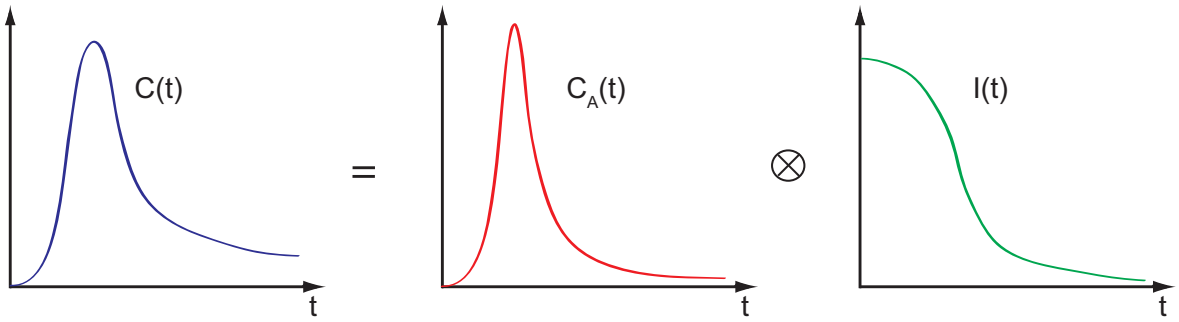

Figure 3.14: *Depiction of the relation between tissue tracer concentration C_T, arterial tracer concentration $C_A(t)$, i.e. the AIF and tissue response function $I(t)$. The measurable functions $C_\mathrm{T}(t)$ and $C_\mathrm{A}(t)$ are used to calculate the tissue response function by means of a deconvolution. The perfusion f is then given by the maximal value of $I(t)$.*

3.5 RF Pulses

The manipulation of magnetization by means of RF excitation and inversion plays an important role in this work. This section describes the design and implementation of sophisticated slice-selective inversion pulses as well as methods to reduce the B_1 amplitude of RF pulses. Further, dual-band excitation is outlined by means of a k-space formalism for small flip angles and then transferred to inversion pulses. Finally, the simulation of RF pulses with respect to inversion and excitation profiles is explained.

3.5.1 Adiabatic Inversion Pulses

In general, adiabatic pulses represent a special class of RF pulses [Tannús et al., 1997]. While most of the RF pulses used in pulsed NMR experiments have a constant carrier frequency, adiabatic pulses make use of a carrier frequency that changes with time. This so-called "frequency-sweep" is just the opposite of the continuous wave (CW) approach of the first NMR experiments [Purcell et al., 1946; Bloch, 1946], where the amplitude of the B_0-field was varied in the presence of a static B_1-field to achieve resonance. Adiabatic pulses have the advantage that they are insensitive to variations of the B_1-field. They flip the magnetization uniformly even if the B_1-field is inhomogeneous, e.g. due to the properties of the imaging object or the usage of a surface coil. This property of adiabatic pulses implies that the conventional relation between flip angle θ and B_1-field amplitude (cf. Equation 2.23) of an RF pulse of length. T_{pulse} is not obeyed:

$$\theta \neq \gamma \int_0^{T_{\text{pulse}}} B_1(t)\,\mathrm{d}t. \tag{3.36}$$

Hence, spatially or temporally varying B_1-fields do not necessarily result in different flip angles. In fact, the flip angle of an adiabatic pulse depends on the way in which the B_1-field amplitude $A(t)$ and the frequency $\omega_{\text{rf}}(t)$ or the phase, are modulated during the pulse.

Adiabatic Passage Principle The concept of the effective field $\boldsymbol{B}_{\text{eff}}$ introduced in chapter 2.1.4 is essential to understand how adiabatic pulses work. In a reference frame rotating with the time-dependent frequency $\omega_{\text{rf}}(t)$, the effective field $\boldsymbol{B}_{\text{eff}}(t)$ can be split up in two orthogonal components $\boldsymbol{B}_{\text{eff},\perp}(t)$ and $\boldsymbol{B}_{\text{eff},\parallel}(t)$:

$$\boldsymbol{B}_{\text{eff}}(t) = \boldsymbol{B}_{\text{eff},\perp}(t) + \boldsymbol{B}_{\text{eff},\parallel}(t) \tag{3.37}$$

one in the transversal xy-plane and one parallel to $\boldsymbol{B}_0$, respectively. Without loss of generality, we assume that the transversal component $\boldsymbol{B}_{\text{eff},\perp}(t)$ is aligned with the y'-axis of the rotating frame such that:

$$\boldsymbol{B}_{\text{eff}}(t) = B_y(t)\hat{\boldsymbol{y}} + B_z(t)\hat{\boldsymbol{z}}, \tag{3.38}$$

where $\hat{\boldsymbol{y}}$ and $\hat{\boldsymbol{z}}$ represent the unit vectors of the rotating frame in y'- and z'-direction, respectively. For an adiabatic pulse, the two components result in:

$$B_y(t) = A(t) \tag{3.39}$$

and

$$B_z(t) = B_0 - \frac{\omega_{\mathrm{rf}}(t)}{\gamma} = \frac{1}{\gamma}(\omega_0 - \omega_{\mathrm{rf}}) = \frac{\Delta\omega(t)}{\gamma}. \tag{3.40}$$

The polar angle Ψ and the amplitude of the effective field are given by:

$$\Psi(t) = \arctan\left(\frac{B_y(t)}{B_z(t)}\right) \tag{3.41}$$

and

$$|\boldsymbol{B}_{\mathrm{eff}}(t)| = \sqrt{B_y(t)^2 + B_z(t)^2}, \tag{3.42}$$

respectively.
The adiabatic principle states that when the change of the direction of the effective field is small during one precession period of the magnetization of a spin system, the magnetization will follow the effective field and precess around it. This is also known as the adiabatic condition and can be expressed as:

$$\left|\frac{\mathrm{d}\Psi}{\mathrm{d}t}\right| \ll \gamma\,|B_{\mathrm{eff}}(t)|\,. \tag{3.43}$$

Generally, adiabatic pulses can be used to excite, refocus and invert magnetization. However, these types of adiabatic pulses all differ from one another regarding the modulation of the B_1-field amplitude and the waveform of the frequency sweep. In this work, only adiabatic inversion pulses are used which is why in the following only this specific type will be discussed.

Hyperbolic Secant Pulses

The inversion pulses used in this work base on the Silver-Joseph-Hoult or hyperbolic secant (HS) pulse, proposed by Silver et al. [1984]. By transforming the rotating-frame Bloch equations (neglecting relaxation) into a Ricatti differential equation, it was shown [Silver et al., 1985] that the hyperbolic secant pulse represents a special case for which an analytical solution can be found. Especially for a spatially selective inversion, it is one of the most prominent and prevalent choices in MR. The functions used for the amplitude modulation $A(t)$ and the phase modulation $\phi(t)$ are:

$$A(t) = A_{\max}\,\mathrm{sech}(\beta t), \tag{3.44}$$

and

$$\phi(t) = -\mu\, ln(\mathrm{sech}(\beta t)) + \mu\, ln(A_{\max}). \tag{3.45}$$

A_{max} represents the maximum of the B_1-field amplitude, β is a pulse parameter having the unit of an angular frequency and μ is a dimensionless parameter. The frequency modulation function defining the "frequency-sweep" is calculated by taking the time derivative of $\phi(t)$. The off-resonance $\Delta\omega$ relative to the Larmor frequency ω_0 is therefore given by:

$$\Delta\omega(t) = \omega_0 - \omega_{\mathrm{rf}}(t) = \frac{\mathrm{d}\phi}{\mathrm{d}t} = -\mu\beta\tanh(\beta t) \tag{3.46}$$

Combining Equations (3.44) and (3.45) a general hyperbolic secant pulse $B_1(t)$ is given by:

$$B_1(t) = A(t)e^{i\phi(t)} = [A_{\max}\,\mathrm{sech}(\beta t)]^{1+i\mu}. \tag{3.47}$$

Equations 3.44 and 3.46 state that while the time runs from $-\infty$ to $+\infty$ the frequency sweeps from $-\mu\beta$ to $+\mu\beta$ and the pulse amplitude $A(t)$ starts and ends with zero and reaches its peak value $A_{\max}$ at the time $t = 0$. Exemplary modulation functions $A(t)$ and $\Delta\omega(t)$ for $T_{\text{pulse}} = 10.24\,\text{ms}$, $\beta = 1171\,\frac{\text{rad}}{\text{s}}$, $\mu = 2.68$ and $A_{\max} = 15\,\mu\text{T}$ are plotted in Figure 3.15.

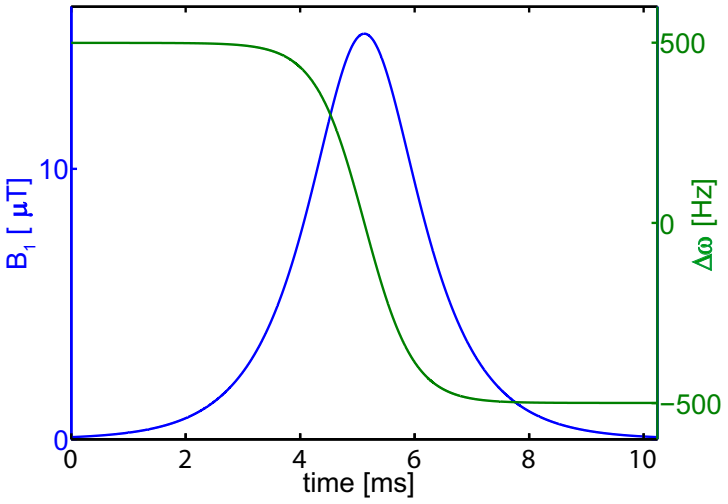

Figure 3.15: *Amplitude (blue) and frequency modulation function (green) of a hyperbolic secant pulse with a duration of 10.24 ms and a maximum amplitude of 15 µT. The other pulse parameters were $\beta = 1171$ rad/s and $\mu = 2.68$ leading to a frequency sweep from 500 Hz to -500 Hz.*

Inversion Mechanism In case of the Silver-Hoult pulse by using Equations (3.44) and (3.46), equations (3.41) and (3.42) can be rewritten as:

$$\Psi = \arctan\left(-\frac{\gamma A_{\max}\mathrm{sech}(\beta t)}{\mu\beta\tanh(\beta t)}\right) = \arctan\left(-\frac{\gamma A_{\max}}{\mu\beta\sinh(\beta t)}\right) \tag{3.48}$$

and

$$|\boldsymbol{B}_{\text{eff}}(t)| = \sqrt{A_{\max}^2\,\mathrm{sech}^2(\beta t) + \frac{\mu^2\beta^2}{\gamma^2}\tanh^2(\beta t)}, \tag{3.49}$$

respectively. It can then be shown [Bernstein et al., 2004] that the adiabatic condition given in Equation (3.43) yields:

$$A_{\max} \gg \frac{\sqrt{\mu}\beta}{\gamma}. \tag{3.50}$$

Given that Equation (3.43) holds, the mechanism behind the adiabatic inversion can now be easily understood and is illustrated in Figure 3.16:

- At the time $t = 0$ the polar angle Ψ equals zero. This means that the effective field is aligned with the equilibrium magnetization.

- With decreasing off-resonance $\Delta\omega(t)$, the effective field tilts towards the transversal plane while the magnetization is precessing around it in a tight cone.
- At $t = T_{\text{pulse}}/2$ the off-resonance equals zero and the effective field lies within the transversal plane. The cone of the precessing magnetization is still centered around the effective field.
- The off-resonance starts increasing again, however changed its sign compared to the first half of the pulse. The effective field and the magnetization move towards the negative z-axis.
- At the end of the pulse, the effective field is aligned with the negative z-axis. The magnetization is inverted.

All adiabatic inversion pulses work this way. Therefore, to design an adiabatic inversion pulse, generally any frequency- and amplitude modulation function can be used as long as the appropriate trajectory (described above) of the effective field is given and the adiabatic condition holds.

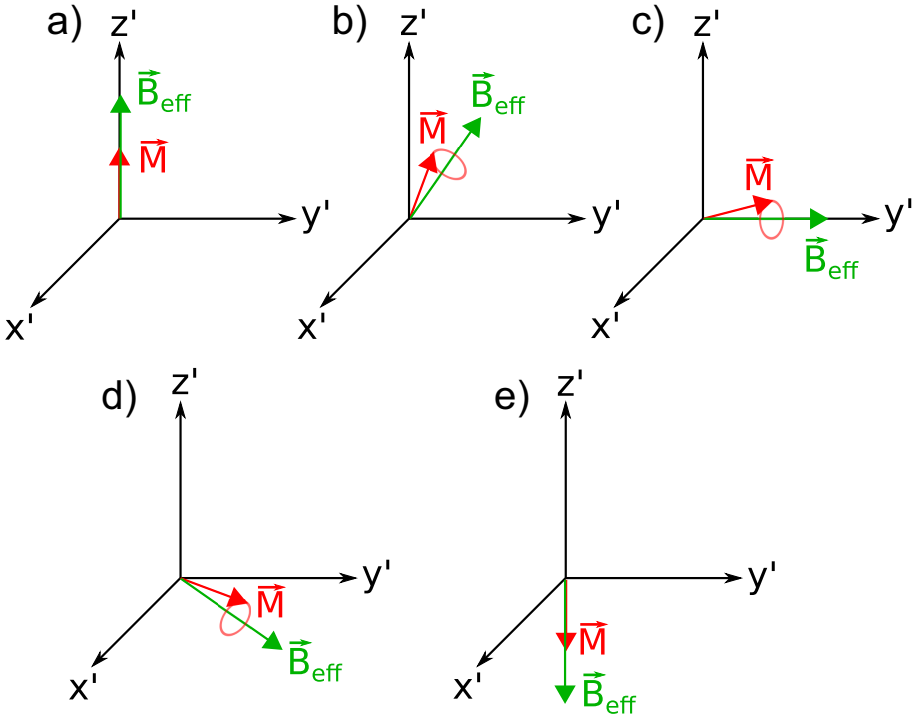

Figure 3.16: *Illustration of the inversion process of an adiabatic inversion pulse: (a) The effective field is aligned with the equilibrium magnetization. (b) With decreasing off-resonance the effective field moves towards the transversal plane. (c) At $t = T_{pulse}/2$ the effective field is aligned with the y'-axis. $A(t)$ reaches its maximum value. (d) With increasing off-resonance, but negative $\Delta\omega(t)$, the effective field moves towards the negative z'-axis. (e) At the end of the pulse the effective field is aligned with the negative z'-axis. Given that the adiabatic condition is met, the magnetization precesses around the effective field on a tight cone during the complete pulse. Thus, the magnetization is inverted.*

Practical Considerations and Parameter Estimation Generally, there are four open parameters for a hyperbolic secant pulse: the duration T_{pulse}, the two parameters μ and β and the maximum amplitude A_{max}. It is known that the latter has to be chosen according to Equation (3.43) and depends on μ and β. However, these two parameters are somewhat unintuitive. It is therefore useful to calculate them based on more handy parameters:

- bandwidth BW, and
- percentage of the maximum amplitude $B_{1\text{trunc}}$,

at which the pulse is truncated.

Like for non-adiabatic pulses, the bandwidth (in combination with the gradient) determines the thickness and the profile of the inverted slice. It can be shown that for a Silver-Hoult pulse the bandwidth in Hertz is given by:

$$BW = \frac{\mu\beta}{\pi}, \tag{3.51}$$

while the truncation percentage is:

$$B_{1\text{trunc}} = \operatorname{sech}\left(\beta\frac{T_{\text{pulse}}}{2}\right). \tag{3.52}$$

It is now known that higher values of the parameter μ yield squarer inversion profiles [Silver et al., 1984]. For a certain bandwidth this means that β should be decreased as far as possible. However, it should be considered that reducing β increases the width of the pulse and therefore, given a certain pulse length, increases $B_{1\text{trunc}}$.

Frequency Offset Corrected Inversion Pulses

As stated above, the profile of the inversion is improved by choosing higher values of μ yielding sharper and steeper transition zones between uninverted and fully inverted magnetization. This is a well-known behavior, as a higher value for μ corresponds to a higher bandwidth. This, in turn, means higher gradient strengths for the same slice thickness, which leads to an improved separation of different frequencies and therefore to sharper profiles and less displacement by chemically shifted species. For slice-selective pulses it is therefore generally beneficial to increase the bandwidth as far as possible. Thereby, the limiting factors are the specific absorption rate and the maximum available gradient strength. However, for adiabatic pulses the bandwidth is foremost limited by the maximal available coil voltage of the transmitter coil as the adiabatic condition has to be met (cf. Equation (3.50)). To achieve the properties of a pulse played out in combination with a high gradient amplitude while still obeying the adiabatic condition, Ordidge et al. [1996] proposed a new adiabatic inversion pulse, the frequency offset corrected inversion (FOCI) pulse. This class of pulse is based on the hyperbolic secant pulse and uses a modulation function $C(t)$ by which the pulse is multiplied.

Modulation Function To improve the inversion profile, i.e. the transition zones of the inversion, it is primarily necessary to increase the gradient at the beginning and the end of the pulse. There, the edges of the inversion profile are defined. It is not necessary to increase the gradient at the central part of the hyperbolic secant where the magnetization in the middle of the selected slice is inverted. To maintain the adiabatic pulse when modulating the gradient strength during the pulse, it is only necessary to preserve the direction of the effective field at every moment in time compared to the original and unmodulated pulse. Given that the gradient $G_{\mathrm{HS}}(t)$ of the HS pulse is multiplied by the modulation function $C(t)$, this means that the RF amplitude $A_{\mathrm{HS}}(t)$ and the frequency offset $\Delta\omega_{\mathrm{HS}}(t)$ of the hyperbolic secant should also be multiplied by $C(t)$ such that:

$$G_{\mathrm{FOCI}}(t) = C(t) \cdot G_{\mathrm{HS}}(t) \tag{3.53}$$

$$A_{\mathrm{FOCI}}(t) = C(t) \cdot A_{\mathrm{HS}}(t) \tag{3.54}$$

$$\Delta\omega_{\mathrm{FOCI}}(t) = C(t) \cdot \Delta\omega_{\mathrm{HS}}(t) \tag{3.55}$$

This way, especially the polar angle Ψ and its time derivative are left unchanged (cf. equation (3.43)). Figure 3.17 illustrates the effective field of a hyperbolic secant pulse and the according FOCI pulse at the same moment in time in the rotating reference frame. It can be seen that the direction of the effective field of the FOCI pulse is preserved compared to In case the HS pulse, that is modulated, is just meeting the adiabatic condition by using the maximal available coil voltage, the only constraint to the modulation function $C(t)$ is that the central part of the amplitude function $A(t)$ should not be further increased and kept at A_{max}. Ordidge et al. [1996] proposed three different modulation functions adequate to cope with this prerequisite. In this work, solely the so called "C-shaped" modulation function has been used. This function is

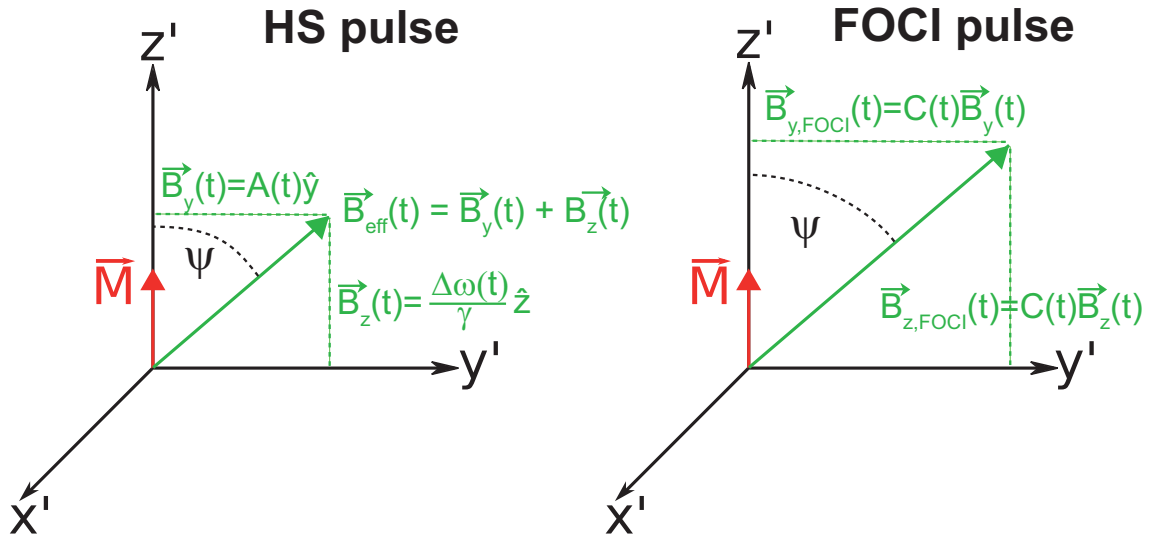

Figure 3.17: *Effective field of a hyperbolic secant and a FOCI pulse at the same moment in time. In reference to Equation* (3.40) *and* (3.39) *the two components B_y and B_z of the effective field are shown. It can be seen that the absolute value of B_{eff} is increased for the FOCI pulse. However, the angle ψ is conserved.*

designed such that the gradient $G_{\mathrm{HS}}(t)$ is increased by a certain factor F (FOCI factor) at the beginning and end of the pulse, and in the central part shaped such that the amplitude is kept at the constant value A_{max}. Figure 3.18 is depicting amplitude, off-resonance and gradient for a HS pulse and its FOCI pulse pendant for $F = 5$. Besides a scaling factor, i.e. $G(t)$, the modulation function $C(t)$ is reflected by $G_{\mathrm{FOCI}}(t)$. It can be seen that the maximum values of gradient and off-resonance frequency of the FOCI pulse are increased compared to the HS pulse, the maximum B_1 amplitude however is equal.

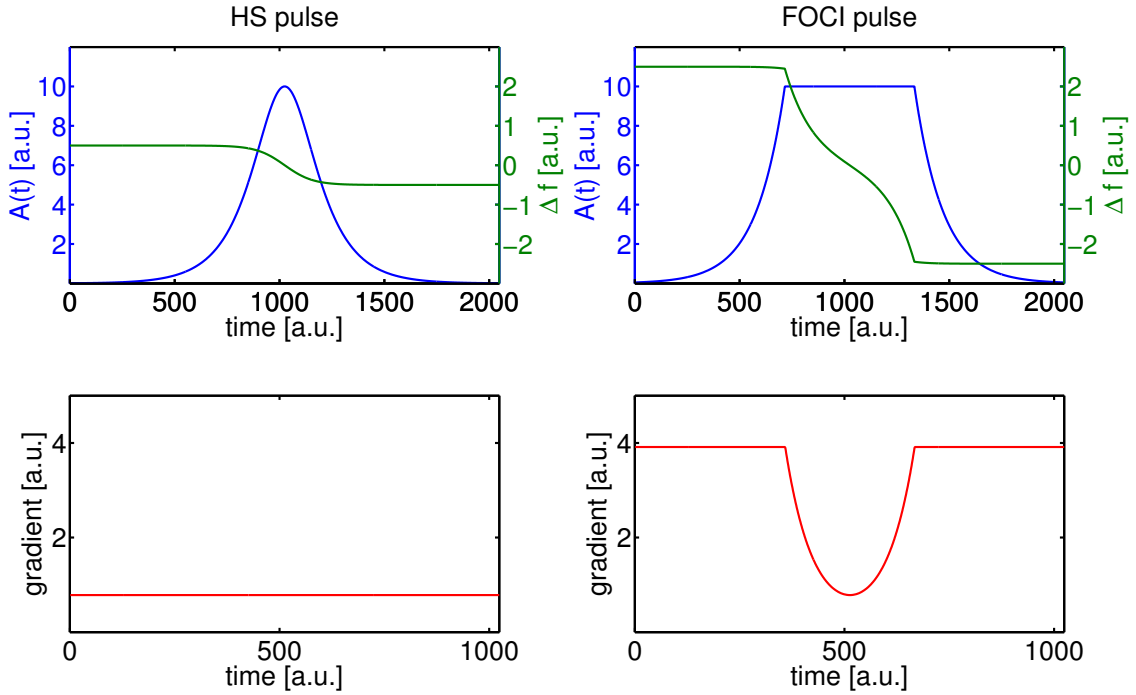

Figure 3.18: *Amplitude (blue), off-resonance frequency (green) and gradient waveform (red) of a HS pulse (left panels) and its FOCI transformed pendant (right panels). A FOCI factor of five was chosen. For a better comparison the axes of corresponding waveforms are scaled equally. While the maximum values of gradient and off-resonance frequency of the FOCI pulse are increased compared to the HS pulse, the maximum B_1 amplitude however is equal.*

Implementation

Given a certain bandwidth, pulse duration and B_1-truncation, all inversion pulses used in this work, both HS and FOCI, have been designed and implemented as proposed by Payne and Leach [1997].

HS pulses The value of μ was maximized such that the resulting β in combination with T_{pulse} was barely consistent with the value chosen for $B_{1\mathrm{trunc}}$.

FOCI pulses Based on a HS pulse with an optimized β the modulation function was calculated the following way:

$$C(t) = \begin{cases} \frac{1}{\operatorname{sech}(\beta t)} & \operatorname{sech}(\beta t) < \frac{1}{F} \\ F & \text{otherwise} \end{cases} \tag{3.56}$$

Gradient, amplitude and frequency offset were then calculated according to equations (3.53)-(3.55). The factor F was chosen such that the maximal value of $G_{\mathrm{FOCI}}(t)$ was less than or equal to the maximal available gradient strength. The amplitude values were calculated in time steps of $5\,\mu s$, the gradient strength in time steps of $10\,\mu s$. For the implementation it was necessary to convert the frequency offset in phase values. This was done by numerically integrating equation (3.46) using time steps of 5 µs. To fulfill equation (3.50) all pulses were transmitted using the highest voltage available for the specific coil.

3.5.2 Variable-Rate Selective Excitation

The "refabrication" of RF pulses in order to reduce the specific absorption rate (SAR) of a given RF pulse was first introduced by Conolly et al. [1988]. Based on a previously designed pulse the proposed algorithm computes both, a new amplitude waveform and a new waveform of the slice selection gradient. The "refabricated" pulse has a significantly lower peak amplitude but produces the exact same excitation as the original pulse. Compared to "normal" RF pulses with a constant gradient, the used method bases on a time-varying amplitude of the slice selection gradient. The method is therefore called variable-rate selective excitation (VERSE).

VERSE Principle The general VERSE approach is based on the fundamental relation between the Larmor frequency and the magnetic field strength, which is given in Equation 2.12. During an RF pulse the rotation angle ϕ of the magnetization and the rotation axis depends on the effective field $\boldsymbol{B}_{\mathrm{eff}}$ (cf. Section 3.5.4) and therefore on the local gradient $G(t)$ and the RF field $B_1(t)$. During a infinitesimal small time interval $\mathrm{d}t$, the effective field is constant. This leads to a rotation with the angle $\Delta\phi = \gamma\,|\boldsymbol{B}_{\mathrm{eff}}| \cdot \mathrm{d}t$ about the effective field. A selective excitation is the product of succeeding rotations of the magnetization vectors (cf. Chapter 3.5.4) at their dedicated positions. If each of the individual, temporally constant rotations are unchanged the product remains unchanged and the profile of the selective excitation will be preserved. As the single rotations are independent, this implies that they can be arbitrarily varied as long as the net rotation stays the same. The explanation above can be mathematically described [Conolly et al., 1991] by the Bloch equation which in the rotating reference frame states:

$$\dot{\boldsymbol{M}}(t,z) = \boldsymbol{M}(t,z) \times \gamma \boldsymbol{B}_{\mathrm{eff}}(t,z). \tag{3.57}$$

$\boldsymbol{M}(t,z)$ is the magnetization vector and $\boldsymbol{B}_{\mathrm{eff}}(t,z) = (B_x(t),\, B_y(t),\, G\cdot z)$ is the effective field given by the excitation B field and the slice selection gradient G. The dot denotes the time derivative and without loss of generality the direction of the slice selection gradient has been chosen to be in z-direction.

We now define a time-dilation waveform $\tau(t)$ with $\dot{\tau}(t) > 0$ and a "dilated" magnetization vector $\boldsymbol{m}(t,z) = \boldsymbol{M}(\tau(t),z)$. The Bloch equation for $\boldsymbol{m}(t,z)$ then states:

$$\begin{aligned}\dot{\boldsymbol{m}}(t,z) &= \dot{\tau}(t)\,\dot{\boldsymbol{M}}(\tau,z) \\ &= \dot{\boldsymbol{M}}(\tau,z) \times \gamma\,\dot{\tau}\,\boldsymbol{B}_{\text{eff}}(\tau,z) \\ &= \boldsymbol{m}(t,z) \times \gamma\,\dot{\tau}(t)\,\boldsymbol{B}_{\text{eff}}(\tau(t),z).\end{aligned} \tag{3.58}$$

By comparing Equation (3.57) and Equation (3.58) we find that if:

$$\dot{\tau}(t)\,\boldsymbol{B}_{\text{eff}}(\tau(t),z) = \boldsymbol{B}_{\text{eff}}(t,z), \tag{3.59}$$

then $\boldsymbol{B}_{\text{eff}}(t,z)$ and $\boldsymbol{M}(t,z)$ are excited in the same way which leads to identical excitation profiles. Equation (3.59) is known as the continuous-time variable rate theorem. When interpreting $\dot{\tau}(t)$ as a scaling function $s(t)$, a VERSE-transformed RF pulse B_{VERSE} and the according gradient G_{VERSE} can be calculated in the following manner:

$$\begin{aligned}B_{\text{VERSE}}(t) &= s(t)\,B(\tau(t)) \\ G_{\text{VERSE}}(t) &= s(t)\,G(\tau(t)),\end{aligned} \tag{3.60}$$

with

$$\tau(t) = \int_0^t s(t')\mathrm{d}t'. \tag{3.61}$$

Here, B represents the original RF pulse and G the according original slice selection gradient. In general, B can be complex, like in the case of the hyperbolic secant pulse. If the length of the original pulse T_{pulse} is to be conserved the relation:

$$\tau(T_{\text{pulse}}) = T_{\text{pulse}} \tag{3.62}$$

should hold. In this work, all VERSE-transformed pulses have been designed to keep the original length.

Two-Speed VERSE

Most RF pulses reach their peak B_1 amplitude in the middle of the pulse. To reduce the SAR, it is therefore practical to redistribute the power deposition such that the B_1 amplitude of the outer lobes of the pulse are increased and the central amplitude is decreased. This can be easily achieved by traveling through the excitation k-space at two different speeds: at higher velocity in the outer parts and at a lower speed during the central part of the pulse. To implement this so-called two-speed VERSE, $s(t)$ has to be chosen such that the outer parts of the original gradient are increased and the central part is decreased. Figure 3.19 shows such a VERSE-transformed RF pulse and its gradient. Additionally, the original pulse and the corresponding gradient is shown. In practice, the maximum available gradient slew rate $\rho_{\max}$ and the maximal available gradient strength $G_{\max}$ of an MR scanner are limited. Hence, a gradient waveform as shown in Figure 3.19 cannot be implemented. For a correct application, one has to account for these limitations. Under the condition that the original pulse length T_{pulse} is conserved and the original gradient G is constant, $s(t)$ can be calculated. s_{fast} is the

factor by which the outer parts of the gradient are increased, t_{slow} as the fraction of the total pulse length during which the gradient is reduced and ρ as the slew rate. The factor s_{slow} by which the central part of the gradient has to be decreased in order to keep the original pulse duration is then given by:

$$s_{\text{slow}} = \frac{\frac{p}{2} + \sqrt{((\frac{p}{2})^2 - q)} + G}{G} \tag{3.63}$$

with

$$p = t_{\text{slow}} \cdot \rho + 2 \cdot G \cdot (s_{\text{fast}} - 1) \tag{3.64}$$

and

$$q = \rho \cdot G \cdot (s_{\text{fast}} - 1)(2 \cdot T_{\text{pulse}} - t_{\text{slow}}) - (G \cdot (s_{\text{fast}} - 1))^2 \tag{3.65}$$

The total duration of the outer parts t_{fast} as a fraction of the total pulse length then is:

$$t_{\text{fast}} = T_{\text{pulse}} - t_{\text{slow}} - 2 \cdot \frac{(s_{\text{fast}} - s_{\text{slow}}) \cdot G}{\rho} \tag{3.66}$$

Now the complete scaling function $s(t)$ can be constructed by applying linear interpolation between s_{fast} and s_{slow}. Care has to be taken that the used parameters ρ and $G \cdot s_{\text{fast}}$ are in agreement with $\rho_{\max}$ and $G_{\max}$.

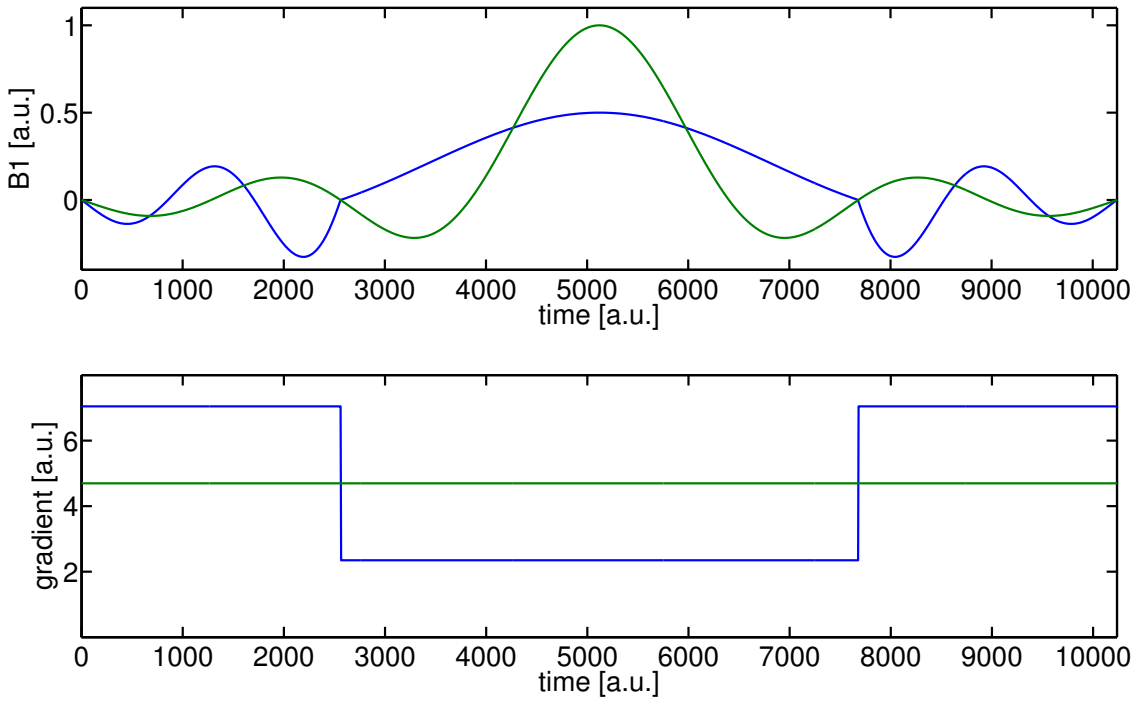

Figure 3.19: *Amplitude (upper panel) and gradient waveform (lower panel) of a sinc-shaped RF pulse (green) and the VERSE-transformed pendant (blue). The parameters s_{fast} and t_{slow} for the VERSE transformation were 1.5 and 0.5, respectively. No limitations were assumed for the gradient slew rate.*

Analytical Scaling Function

Scaling functions for VERSE transformations can also be analytical functions. They have the advantage that they are not composite functions and a closed expression for the complete function exists. An analytic scaling function that has similar properties as the two-speed scaling function described above, was proposed by Gai and Zur [2007]. The function bases on the Fermi function and is also designed such that the central part of the pulse is stretched and the outer parts are compressed. The scaling function depends on three parameters and is given by:

$$s(x) = (A - B)\, F_n(x) + B, \qquad \text{with } x \in [-1; 1]. \tag{3.67}$$

The function $F_n(x)$ is supposed to be zero for $x = 1$ and $x = -1$ and should yield unity for $x = 0$. $s(x)$ then yields a maximum value of $B \geq 1$ at the beginning and end of the pulse and the minimum value of $A \leq 1$ at the center. These requirements are fulfilled if we define:

$$F_n(x) = \frac{F_i(x) - 0.5}{F_i(0) - 0.5}, \tag{3.68}$$

which uses the Fermi function

$$F_i(x) = \frac{1}{1 + \mathrm{e}^{(|x|-1)/t}}. \tag{3.69}$$

For $x \in [-1; 1]$, the Fermi function F_i varies from 0.5 for $|x| = 1$ to its maximum value $F_i(0)$. Through the definition of $F_n(x)$, the Fermi function is stretched to the range $[0; 1]$. When implementing $s(x)$, the values for A and t were fixed and B was numerically estimated such that the original pulse length was kept. The total pulse duration was mapped to the interval $[-1, 1]$. A and t where chosen such that the VERSE-transformed gradient did neither violate the maximum slew rate nor the maximum gradient strength available on the MR scanner. Figure 3.20 shows four exemplary scaling functions $s(x)$ for A $= 0.6$, $t = 0.07$, $t = 0.1$, $t = 0.25$ and $t = 0.5$. With the prerequisite that the pulse duration is conserved, the respective values for B were 4.69, 3.47, 1.88 and 1.53.

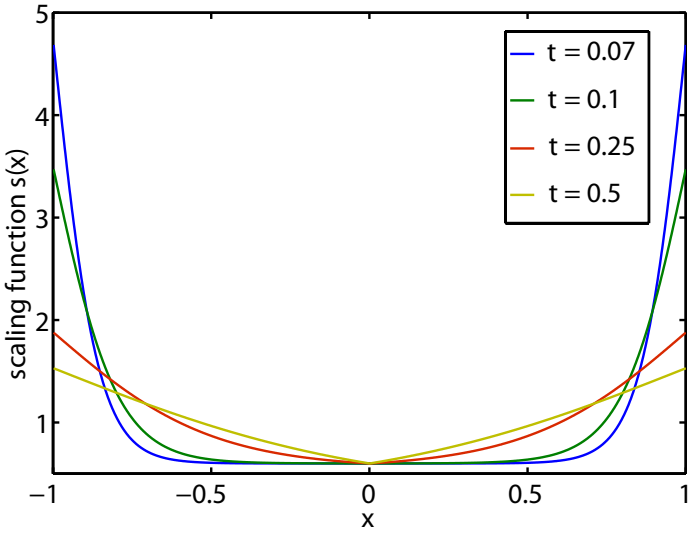

Figure 3.20: *Fermi scaling functions s(x) for A = 0.6, t = 0.07, t = 0.1, t = 0.25 and t = 0.5. With the prerequisite that the pulse duration is conserved, the respective values for B were 4.69, 3.47, 1.88 and 1.53.*

3.5.3 Dual-Band RF Pulses

For certain applications it can be desirable to excite two spatially separated slices at the same time. Possible scenarios are the saturation of magnetization at both sides of an imaging volume, for example to suppress the signal of inflowing magnetization. If the thickness of the two separated slices is identical, such an excitation can be realized with a single RF pulse.

Excitation *k*-Space

By assuming $M_z \approx M_0 = \text{const.}$ which is valid in the small tip angle regime, the transversal components in the Bloch equation for RF excitation (cf. Equation (3.82)) can be decoupled from the longitudinal. The transversal magnetization $M_{xy} = M_x + \mathrm{i}M_y$ after an RF excitation of length T_{pulse} is then given by:

$$M_{xy}(\boldsymbol{r}) = \mathrm{i}\gamma M_0 \int_0^{T_{\text{pulse}}} B_1(t)\mathrm{e}^{\mathrm{i}\boldsymbol{r}\boldsymbol{k}(t)}\mathrm{d}t, \tag{3.70}$$

where $B_1(t) = B_{1,x} + \mathrm{i}B_{1,y}$ and

$$\boldsymbol{k}(t) = -\gamma \int_t^{T_{\text{pulse}}} \boldsymbol{G}(t')\mathrm{d}t'. \tag{3.71}$$

Other than for data acquisition, $\boldsymbol{k}(t)$ here is defined by the remaining gradient $\boldsymbol{G}(t)$. By using the three-dimensional delta function ${}^3\delta(\boldsymbol{k})$ we can avoid the time dependency of the exponential. The reformulated equation then reads:

$$M_{xy}(\boldsymbol{r}) = \mathrm{i}\gamma M_0 \int_K \int_0^{T_{\text{pulse}}} B_1(t)\,{}^3\delta(\boldsymbol{k}(t) - \boldsymbol{k})\mathrm{d}t\,\mathrm{e}^{\mathrm{i}\boldsymbol{k}\boldsymbol{r}}, \mathrm{d}\boldsymbol{k} \tag{3.72}$$

which in case that the k-space trajectory does not cross itself, can be expressed as:

$$M_{xy}(\boldsymbol{r}) = \mathrm{i}\gamma M_0 \int_K W(\boldsymbol{k})S(\boldsymbol{k})\mathrm{e}^{\mathrm{i}\boldsymbol{k}\boldsymbol{r}}\mathrm{d}\boldsymbol{k}. \tag{3.73}$$

In the last step we introduced the spatial weighting function $W(\boldsymbol{k})$ and the sampling function $S(\boldsymbol{k})$:

$$W(\boldsymbol{k}(t)) = \frac{B_1(t)}{\gamma\,|\boldsymbol{G}(t)|}, \tag{3.74}$$

$$S(\boldsymbol{k}) = \int_0^{T_{\text{pulse}}} {}^3\delta(\boldsymbol{k}(t) - \boldsymbol{k}) \left|\dot{\boldsymbol{k}}(t)\right| \mathrm{d}t. \tag{3.75}$$

This means that the transversal magnetization is the Fourier transform of the k-space trajectory weighted by the RF waveform which itself is inversely weighted by the velocity excitation k-space is passed through. This solution holds very well even if excitation profiles for flip angles up to 70° are calculated.

Dual-Band Property Mathematically the dual-band property of a slice-selective RF pulse can be achieved by a convolution of $M_{xy}(\boldsymbol{r})$ with two delta functions. For a

symmetrical separation $|\boldsymbol{r} - \boldsymbol{r}_0|$ of the excitation profiles with respect to the original position $\boldsymbol{r}$, a function that fulfills the requirements is:

$$d(\boldsymbol{r}, \boldsymbol{r}_0) = \frac{\delta(\boldsymbol{r} - \boldsymbol{r_0}) + \delta(\boldsymbol{r} + \boldsymbol{r_0})}{2}. \tag{3.76}$$

The convolution can be calculated by multiplying the Fourier transforms $\mathfrak{F}$ of $d(\boldsymbol{r}, \boldsymbol{r_0})$ and $M_{xy}(\boldsymbol{r})$ which are given by:

$$\mathfrak{F}[d(\boldsymbol{r}, \boldsymbol{r}_0)] = \cos(2\pi f_0 t) = \cos(2\pi \boldsymbol{k}(t)\boldsymbol{r}_0) \tag{3.77}$$

and

$$\mathfrak{F}[M_{xy}(\boldsymbol{r})] \sim W(\boldsymbol{k}(t))S(\boldsymbol{k}). \tag{3.78}$$

This result implies that in order to excite two slices with a single RF pulse, excitation k-space has to be weighted with a cosine by modulating the B_1-field of the RF pulse. For a constant slice selection gradient $\boldsymbol{G}$, the modulation frequency is $f_0 = \gamma \boldsymbol{G}\boldsymbol{r}_0$. For a time-varying gradient, one has to account for the velocity k-space is traversed with. A disadvantage of dual-band pulses is the fact that due to the denominator in Equation (3.76) the peak RF power needs to be doubled in order to conserve the original flip angle.

Dual-Band Adiabatic Inversion

Besides a dual-band excitation, it is also possible to simultaneous invert two equally thick slices with a single adiabatic inversion pulse. Although not in the small flip-angle regime, measurements and numerical simulations show that a dual-band inversion can be achieved by following the approach described above. Hence, the original amplitude function $A(t)$ of the adiabatic inversion pulse has to be modulated with a cosine function. Given that d is the distance between the centers of the slices, the modulated amplitude function $A'(t)$ reads:

$$A'(t) = \cos\left(2\,\pi\,\frac{d}{2}\left(-\frac{k_{\max}}{2} + k(t)\right)\right) \cdot A(t), \tag{3.79}$$

where

$$k(t) = \int_0^t G(t')\mathrm{d}t' \tag{3.80}$$

and

$$k_{\max} = \int_0^{T_{\text{pulse}}} G(t')\mathrm{d}t', \tag{3.81}$$

to gain a symmetric weighting of the k-space trajectory. $G(t)$ represents the slice selection gradient and T_{pulse} the total pulse duration. Due to the denominator in Equation (3.76), the adiabatic threshold for dual-band inversion pulses is twice as high. If the maximum coil voltage is not sufficient, this requires special measures, for example VERSE transformation.

3.5.4 RF Pulse Simulation and Calculation

The effect of a time varying RF field $\boldsymbol{B}_1(t) = (B_{1,x}(t), B_{1,y}(t), 0)^\top$ on a magnetization vector $\boldsymbol{M} = (M_x, M_y, M_z)^\top$ at spatial location $\boldsymbol{r}$ can be described by the Bloch equations. In the reference frame rotating with the RF carrier frequency $\omega_{\mathrm{rf}}(t)$ they read:

$$\dot{\boldsymbol{M}}(\boldsymbol{r}, t) = \gamma \begin{pmatrix} 0 & \boldsymbol{G}(t)\boldsymbol{r} + \frac{\Delta\omega(t)}{\gamma} & -B_{1,y}(t) \\ -\boldsymbol{G}(t)\boldsymbol{r} - \frac{\Delta\omega(t)}{\gamma} & 0 & B_{1,x} \\ B_{1,y} & -B_{1,x} & 0 \end{pmatrix} \boldsymbol{M}(\boldsymbol{r}, t). \tag{3.82}$$

$\boldsymbol{G}(t)$ represents the slice selection gradient and relaxation effects are neglected. $\Delta\omega(t)/\gamma = B_0 - \omega_{\mathrm{rf}}(t)/\gamma$ represents the additional magnetic field in z-direction in case the RF carrier frequency does not match the Larmor frequency. Jaynes [1955] showed that this equation can be solved by using a 3×3 rotation matrix $\boldsymbol{\mathcal{R}}$. The final magnetization after the RF pulse with duration T_{pulse} then reads:

$$\boldsymbol{M}(T_{\mathrm{pulse}}) = \boldsymbol{\mathcal{R}}\boldsymbol{M}(0), \tag{3.83}$$

where $\boldsymbol{M}(0)$ represents the initial magnetization. In general, $\boldsymbol{\mathcal{R}}$ itself cannot be calculated directly, but is the product of an infinite number of infinitesimal rotations:

$$\boldsymbol{\mathcal{R}} = \lim_{n\to\infty} \boldsymbol{\mathcal{R}}_n. \tag{3.84}$$

In the special case that the applied RF field and the slice selection gradient are constant and have the duration Δt, the rotation of the magnetization can be expressed in terms of the Cayley-Klein parameters [Jaynes, 1955; Pauly et al., 1991]:

$$\begin{pmatrix} M_{xy}^+ \\ M_{xy}^{+*} \\ M_z^+ \end{pmatrix} = \begin{pmatrix} (\alpha^*)^2 & -\beta^2 & 2\alpha^*\beta \\ -(\beta^*)^2 & \alpha^2 & 2\alpha\beta^* \\ -\alpha^*\beta^* & -\alpha\beta & \alpha\alpha^* - \beta\beta^* \end{pmatrix} \begin{pmatrix} M_{xy}^- \\ M_{xy}^{-*} \\ M_z^- \end{pmatrix}, \tag{3.85}$$

with $M_{xy} = M_x + iM_y$. Here, * denotes the complex conjugate and the superscripts $-$ and $+$ indicate the magnetization directly before and after the application of the RF pulse, respectively. The Cayley-Klein parameters are given by:

$$\alpha = \cos\left(\frac{\phi}{2}\right) - in_z \sin\left(\frac{\phi}{2}\right) \tag{3.86}$$

and

$$\beta = -i(n_x + in_y)\sin\left(\frac{\phi}{2}\right). \tag{3.87}$$

The parameters necessary to calculate α and β are the rotation angle ϕ and the axis $\boldsymbol{n} = (n_x, n_y, n_z)^\top$ about which the rotation is performed. They are calculated as

follows:

$$\phi = -\gamma \Delta t \sqrt{|\boldsymbol{B}_1|^2 + \left(\boldsymbol{G}\boldsymbol{r} + \frac{\Delta\omega(t)}{\gamma}\right)^2} \tag{3.88}$$

and

$$\boldsymbol{n} = -\frac{\gamma \Delta t}{|\phi|} \begin{pmatrix} B_{1,x} \\ B_{1,y} \\ \boldsymbol{G}\boldsymbol{r} + \frac{\Delta\omega}{\gamma} \end{pmatrix}. \tag{3.89}$$

Hard-Pulse Approximation The hard-pulse approximation assumes that $\boldsymbol{B}_1(t)$, $\boldsymbol{G}(t)$ and if so the off-resonance $\Delta\omega$ of a slice-selective RF pulse are piecewise constant. As shown above, the rotation matrix for each of these steps can be calculated. Assuming that the complete pulse can be decomposed in j pieces of constant gradient and amplitude, the complete RF pulse is represented by one rotation matrix that is the product of the j individual rotation matrices. The final matrix is then given by:

$$\boldsymbol{\mathcal{R}} = \boldsymbol{\mathcal{R}}_j \boldsymbol{\mathcal{R}}_{i-1} \cdots \boldsymbol{\mathcal{R}}_1 = \prod_{i=1}^{j} \boldsymbol{\mathcal{R}}_i, \tag{3.90}$$

where $\boldsymbol{\mathcal{R}}_i$ represents the i-th rotation matrix. By transforming any RF pulse into a piecewise constant pulse and by using Equation (3.85), the final magnetization can be calculated for any initial magnetization. Furthermore, it is possible to calculate the magnetization for any point in time during the RF pulse. The hard pulse approximation is anyway a valid approximation as the implementation of RF pulses and gradients on commercial imaging systems requires the discretization of the respective waveforms.

Relaxation and Off-Resonance When using Equations (3.83) and (3.90) to simulate RF pulses, it is convenient to include the effects of relaxation and off-resonance which are described by the Bloch equations. After a time interval of length Δt the affected magnetization is given by:

$$\boldsymbol{M}^+ = \boldsymbol{\mathcal{A}}\boldsymbol{M}^- + \boldsymbol{b}, \tag{3.91}$$

with the initial magnetization $\boldsymbol{M}^-$,

$$\boldsymbol{\mathcal{A}} = \begin{pmatrix} \mathrm{e}^{\frac{-\Delta t}{T_2}} & 0 & 0 \\ 0 & \mathrm{e}^{\frac{-\Delta t}{T_2}} & 0 \\ 0 & 0 & \mathrm{e}^{\frac{-\Delta t}{T_1}} \end{pmatrix} \begin{pmatrix} \cos(\phi) & -\sin(\phi) & 0 \\ \sin(\phi) & \cos(\phi) & 0 \\ 0 & 0 & 1 \end{pmatrix} \tag{3.92}$$

and

$$\boldsymbol{b} = \begin{pmatrix} 0 \\ 0 \\ 1 - \mathrm{e}^{\frac{-\Delta t}{T_1}} \end{pmatrix}. \tag{3.93}$$

The angle $\phi = 2\pi\Delta f\Delta t$ describes the rotation about the z-axis driven by the off-resonance frequency Δf. T_1 and T_2 denote the longitudinal and the transversal relaxation times, respectively. When including relaxation and off-resonance in the pulse simulation of a time step Δt, Equation (3.91) was applied for $\Delta t/2$, right before and after the rotation given in Equation (3.85).

Shinnar-Le Roux Pulses

As described abve, for a given slice-selective RF pulse, the excitation profile can be calculated by solving the Bloch equations numerically. For small flip angles, even the Fourier transformation is possible. The Shinnar-Le Roux (SLR) algorithm [Le Roux, 1988; Shinnar et al., 1989a,b; Shinnar and Leigh, 1989; Pauly et al., 1991] allows a direct and efficient solution of the forward problem and the inverse problem, i.e. the slice profile is given and the associated RF pulse shape needs to be calculated. The algorithm is not limited to small flip angles. The SLR algorithm uses the hard-pulse approximation described above and the two-dimensional mathematical representation of rotations, the special unitary group SU(2) (cf. [Jaynes, 1955]). With these two key concepts the rotations caused by the B_1-field of the pulse can be described by two polynomials $\alpha_N(z)$ and $\beta_N(z)$ with complex coefficients. The polynomials are known as filters from digital signal processing which shifts the RF pulse problem to a well-known filter design problem. The inverse SLR algorithm translates these polynomials back to j-th component of the RF pulse:

$$(\alpha_N(z), \beta_N(z)) \Longrightarrow B_1(t).$$

This way, by choosing the pair of polynomials $\alpha_N(z)$ and $\beta_N(z)$ that corresponds to the desired excitation profile, the associated RF envelope can be calculated recursively [Bernstein et al., 2004]. In this work, an implementation of the inverse SLR algorithm in *MatLab*, written by Amir Schricker (*http://amirschricker.org/jhuprojects*), was used.

3.6 Animal Models

To acquire and test perfusion measurements in common kidney diseases, animal models have been used. The preparations of an acute kidney injury (AKI) model as well as a renal transplantation model in rats are briefly described. Further, their presumed impact on renal perfusion is explained. A detailed explanation of the animal models, their preparation and the physiological background can be found in Klotz [2013]. All procedures were performed according to the "Guide of Care and Use of Laboratory Animals" published by the National Academy of Sciences and were approved by the local authorities (Regierungspräsidium Karlsruhe) under the reference number AZ-9185.81/G-19/12.

3.6.1 Animals

All animals were obtained from Charles River (Sulzfeld, Germany). Male Lewis rats (LEW/Crl) were used as organ recipients in the transplantation model as well as for

the AKI model. Male Fisher rats (F334/DuCrl) served as organ donors. Animals were kept under standard conditions (temperature: 23° C; humidity 60%; day/night cycle: 12 hours). They were fed with standard rodent chow (Sniff, Soest, Germany) and water ad libitum. At the beginning of the experiments the rats were weighing 250 g to 300 g.

3.6.2 Acute Kidney Injury Model

In the following, the induction of AKI and its impact on renal perfusion are outlined.

Warm Ischemia Model

Ischemia-reperfusion injury (IRI) is a major cause for acute kidney injury [Kinsey et al., 2008; Bonventre and Yang, 2011]. In an experimental setting, acute kidney injury can be induced by the well-standardized warm ischemia model where the renal veins and arteries are clamped for 45 minutes with atraumatic clamps. As described in Zimmer et al. [2013], hypoxia caused by ischemia leads to endothelial lesion (i.e. lesion of cells that line the interior surface of blood and lymphatic vessels [Dorland, 2011]) and damage of the barrier function of the vessels in the kidney. This, in turn, results in interstitial edema [Bonventre and Yang, 2011]. Due to clamping the renal artery, the oxygen delivery is interrupted and renal structures with a high demand of oxygen are strongly impaired. These are foremost the tubular epithelial cells that afterwards show tubulus dilatation and necrosis [Kinsey and Okusa, 2011]. The functional deterioration of the kidney, as a consequence of the microvascular damage and the interstitial edema, can decrease renal perfusion up to 50% [Sutton et al., 2002].

Animal Preparation

For the studies presented in this work, AKI was induced in overall 23 animals. After laparotomy (i.e. opening the abdominal cavity), warm ischemia was induced in the left kidney by following the procedure described above [Klotz, 2013]. The right kidney served as a native control. Figure 3.21 shows both rat kidneys during ischemia. The vessel clamps as well as the ischemic and native kidney are visible. Prior to the procedure, animals were anesthetized with an intraperitoneal injection of a mixture (1 ml/kg body weight) of ketamine (Ketamin 10%®, Intervet GmbH, Unterschleißheim, Germany)) and xylazine (Rompun 2%®, Bayer Vital GmbH, Leverkusen Germany). Heparin (100 I.U. per animal; Heparin-Natrium-25000-ratiopharm®, ratiopharm GmbH, Ulm, Germany) was injected into a tail vein. To maintain anesthesia, isoflurane (3%, Forene®, Abbott GmbH & Co. KG, Wiesbaden, Germany) was used for inhalation. After opening the clamps, reperfusion was evaluated macroscopically. The animals had an analgesic treatment with bupreonorphinhydrochlorid (0.05 mg/kg body weight; Temgesic®, Reckitt Benckiser Healthcare Ltd., Berkshire, United Kingdom). Finally, the MRI perfusion measurements were conducted five days after surgery.

3.6.3 Renal Transplantation Model

Besides the AKI model, an animal model of renal transplantation was used. Perfusion was measured in the recipients either seven days or six month after surgery correspond-

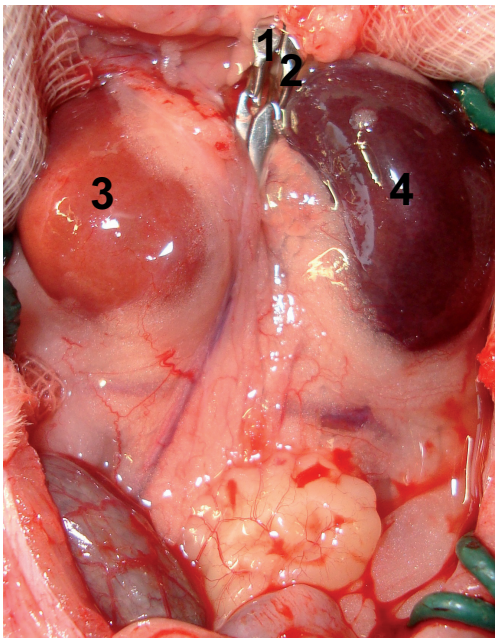

Figure 3.21: *Overview of the rat abdomen during warm ischemia. Both, the arterial (1) and the venous (2) clamp are visible. Due to the venous occlusion, the ischemic left kidney (4) changed its color to dark red and blue compared to the native right kidney (3).*

ing to an acute and chronic rejection, respectively. Despite an improved management of immunosuppressive therapy in the last years, the occurence of an acute or chronic rejection as an immune response against donor alloantigens is a major obstacle [Nankivell and Alexander, 2010]. Depending on their histological appearance and the time of occurrence after transplantation, different types of rejection are distinguished.
After a short description of the renal transplantation model, acute and chronic rejections which are employed in this work, are briefly described. Both types of rejection deteriorate graft function [Nankivell and Alexander, 2010; Amann et al., 2011] and hence have an impact on renal perfusion.

Kidney Transplantation

Renal graft was explanted from male Fisher rats that were anesthetized with an intraperitoneal dose of thiobutabarbital sodium (1 ml per kg body weight; Inactin®, SIGMA-Aldrich Co., Steinheim, Germany). Before explantation, the left kidney was perfused with 1 ml UW-solution (University-of-Wisconsin-solution, ViaSpan®, Bristol-Myers Squibb GmbH & Co. KG, Munich, Germany) and was afterwards stored in UW-solution at 4 °C for 20 hours. Male Lewis rats served as organ recipients. Before implanting the renal graft, the animals were initially anesthetized as described for the warm ischemia model. Isoflurane inhalation was used to maintain anesthesia during surgery. After cold preservation, the renal graft was implanted into the bilateral nephrectomized recipient. To evaluate early and late graft function as well as renal perfusion, the recipients were observed seven days and six months, respectively. Figure 3.22 shows the recipient after nephrectomy and after implantation of the renal graft. For analgesic treatment during all surgeries, buprenorphinhydrochloride (0.05 mg per kg body weight; Temgesic®, Reckitt Benckiser Healthcare Ltd., Berkshire, United Kingdom) was injected subcutaneously.

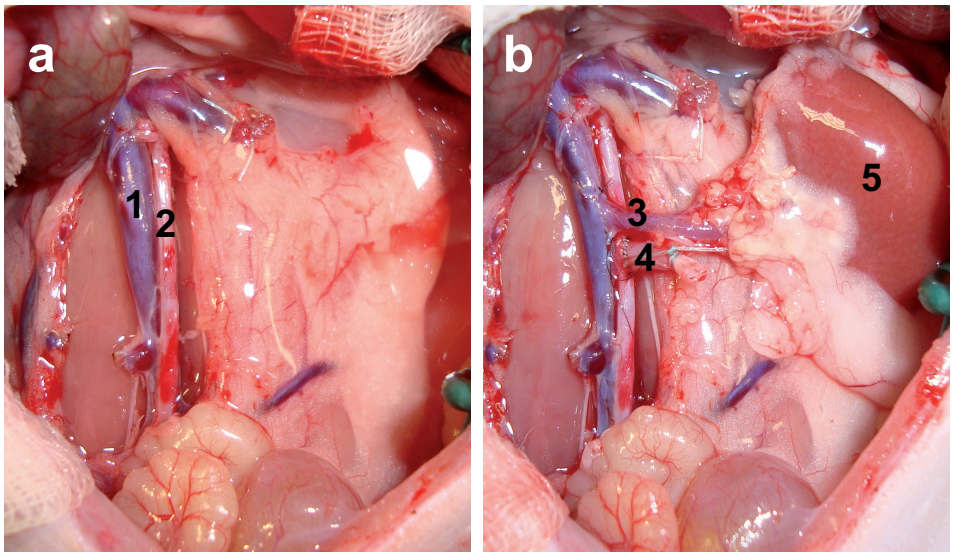

Figure 3.22: *Abdomen of the recipient rat after nephrectomy (a) and after implantation of the renal graft (b). The prepared vena cava caudalis (1) and the aorta (2) can be seen in the left image. The right image shows the adapted venous (3) and arterial (4) part of the perfused renal graft (5).*

Acute and Chronic Rejection

Acute and chronic graft rejection differ with respect to their histological appearance and the time of occurrence after transplantation. While an acute rejection occurs within the first days and weeks after surgery [Colvin and Smith, 2005], chronic rejections appear after several months or years [Waaga et al., 2000]. The acute rejection is mainly characterized by an infiltration of inflammatory cells like macrophages, monocytes and lymphocytes in the interstitium as a first reaction of the recipients immune system [Cornell et al., 2008]. Further, an inflammation of the tubuli (tubulitis) and the vascular system (vasculitis) are histologically evident [Terasaki and Cai, 2005; Nankivell and Alexander, 2010]. Chronic graft rejection, in contrast, is characterized by its progressive etiopathology. It is hallmarked by the atrophy of tubuli and interstitial fibrosis, i.e. the occurrence of fibrin that supplants renal tissue [Nankivell and Alexander, 2010; Nankivell and Kuypers, 2011] and therefore has an essential impact on the long-term graft survival. Both rejection reactions result in an impaired organ function that is reflected by a decreased renal perfusion.

3.7 Software and Evaluation Tools

In this section, algorithms and evaluation tools used for data processing and visualization, are described. If not specified otherwise, data processing and evaluation has been performed with the commercial software Matlab (The MathWorks Inc., Natick, MA, USA). This includes image processing, non-linear optimizations and statistical tests. Further, all RF pulse simulations were conducted with Matlab.

Levenberg-Marquardt Algorithm

For the purpose of data fitting and non-linear optimizations an implementation of the Levenberg-Marquardt algorithm [Levenberg, 1944; Marquardt, 1963] was used.The algorithm provides a numerical solution to the problem of minimizing a function over a set of nonlinear parameters of the function. Levenberg-Marquardt is a downhill gradient/parabolic expansion (gradient-expansion) algorithm that combines the best features of two methods. One is the linearization of the function $f(x, a_1, .., a_M)$ in the parameters $a_1, .., a_M$ and the usage of linear least-squares to determine the optimum value for the parameter increments δa_i. This linearization is equal to a parabolic expansion of the underlying hypersurface. The second method is the gradient-search method that calculates the vector that points to the most rapid decrease of the hypersurface associated with the function. The gradient-expansion algorithm operates between the extremes of the two methods: As the linearization of the fitting function leads to M linear equations in the parameter increments δa_i, these M functions can be treated as one matrix equation. By increasing the diagonal terms of the occurring matrix by a variable factor, the gradient-expansion algorithm interpolates between the two methods mentioned above. For very small increments the algorithm is similar to the linearization of the fitting function, while for large increments it behaves like a gradient-search method. This way, the Levenberg-Marquardt combines the advantages of both methods. On the one hand, due to its gradient-search characteristics, it is able to approach the minimum even from a point far away. On the other hand, it still converges rapidly around the minimum as a consequence of its linearization feature [Bevington and Robinson, 1969].

t-Test

Student's t-test [Student, 1908] is statistical method to test whether two sets of data are significantly different from each other. The test assumes the data to be normal distributed. In case the null hypothesis is supported, e.g. the mean values of the two populations are equal, the test statistic follows a Student's t-distribution. By means of a critical t-value t_c which is defined by the value for which the t-distribution for the corresponding degrees of freedom is smaller than a predetermined significance level α, the test decides whether the null hypothesis is rejected or not. Different types of t-tests exist. In this work, two versions of the two-sample t-test were used.

Unpaired *t*-test For independent samples of two different distributions, the unpaired or two-sample t-test was used. The test does not require equal sample sizes. Depending on the variances of the two samples, two versions are discriminated. Commonly, it is assumed that the distributions of the two samples have a statistically equal variance. Then, in the general case of unequal sample sizes N_1 and N_2, the t-value is given by:

$$t = \frac{\bar{x}_1 - \bar{x}_2}{s_p \sqrt{\frac{1}{N_1} + \frac{1}{N_2}}}, \tag{3.94}$$

with $\bar{x}_1$ and $\bar{x}_2$ being the mean values of the respective samples and s_p denoting the pooled standard deviation defined as:

$$s_p = \sqrt{\frac{(N_1 - 1)s_1^2 + (N_2 - 1)s_2^2}{N_1 + N_2 - 2}}. \tag{3.95}$$

s_1^2 and s_2^2 are the variances of the respective samples:

$$s_{1,2}^2 = \frac{1}{N_{1,2} - 1} \sum_{j=1}^{N_{1,2}} (x_j - \bar{x}_{1,2}). \tag{3.96}$$

The degrees of freedom N_{dof} of the t-distribution are $N_1 + N_2 - 2$.
In case the two sample variances are unequal, the test is referred to as Welch's t-test. The t-value is then calculated as follows:

$$t = \frac{\bar{x}_1 - \bar{x}_2}{\sqrt{\frac{s_1^2}{N_1} + \frac{s_2^2}{N_2}}}, \tag{3.97}$$

with s_1^2 and s_2^2 being the variances of the respective samples. This test statistic does no longer follow a t-distribution. Therefore, a t-distribution is approximated by modifying the degrees of freedom:

$$N_{\text{dof}} = \frac{\left(\frac{s_1^2}{N_1} + \frac{s_2^2}{N_2}\right)^2}{\frac{\left(\frac{s_1^2}{N_1}\right)^2}{N_1 - 1} + \frac{\left(\frac{s_2^2}{N_2}\right)^2}{N_2 - 1}}. \tag{3.98}$$

Paired-Sample *t*-Test For paired samples, i.e. two equally sized samples that are pair-wise dependent, the paired-sample t-test was used. In case the null hypothesis states that the mean of both samples $x_1, x_2, \ldots, x_N$ and $y_1, y_2, \ldots, y_N$ is equal, this test simplifies to a one-sample t-test that tests whether the mean of the distribution of differences $d_i = x_i - y_i$ is zero. The t-value for a paired-sample t-test is:

$$t = \frac{\bar{d}}{s/\sqrt{N}}, \tag{3.99}$$

with

$$\bar{d} = \frac{1}{N} \sum_{i=1}^{N} (x_i - y_i), \tag{3.100}$$

being the mean difference and s denoting the standard deviation of the sample. The degrees of freedom of the paired-sample test $2N - 2$.

Bland-Altman Plots

When measuring the same parameter with two different methods S_1 and S_2, a Bland-Altman plot [Bland and Altman, 1986] can be employed to visualize possible differences between the two methods. By plotting the differences $S_1 - S_2$ over the averages $(S_1 +$

$S_2)/2$, the fluctuation range and offsets can be rated optically. Besides the points with the Cartesian coordinates:

$$S(x, y) = \left(\frac{S_1 + S_2}{2}, S_1 - S_2 \right), \tag{3.101}$$

three more lines are plotted. One line indicating the mean difference and two lines indicating ± 1.96 standard deviations.

4 Results

In this chapter, the results of this work are presented. A 2D ASL technique for quantitative renal perfusion measurement in rats was established on a clinical whole-body scanner. In an initial study, ASL results were compared to absolute perfusion values derived from DCE-MRI. Its clinical value was tested by employing an animal model of acute kidney injury. In two continuitive studies, renal ASL measurements were carried out in further animal models of acute kidney injury as well as in models of renal transplantation. Further, a 3D FAIR ASL sequence for quantitative perfusion measurements was developed. Different features of the sequence are presented with a special emphasis on design, simulation and measurement of adiabatic inversion pulses. Finally, quantitative 3D ASL perfusion data are presented.

4.1 Renal Perfusion MRI in Animal Models

In this section, preliminary measurements, experimental procedures, evaluation and results of the measurement of renal perfusion in rats are outlined. After the presentation of two preparative measurements, the initial study in a model of acute kidney injury is shown. The study involves ASL and DCE-MRI for perfusion estimation. Eventually, the results of ASL measurements in models of acute kidney injury and renal transplantation are presented. All animal model MR scans were operated at the 3 T whole-body MR scanner Magnetom Tim Trio. The dedicated eight channel, receive-only, volumetric rat array described in Section 3.1 was used for signal detection. All rats were placed supine and head first inside the array such that the kidneys were in the RF center. The body coil was used for homogeneous RF transmission.

4.1.1 Preliminary Measurements

All non-invasive perfusion measurements in animals were accomplished by using a WIP (work in progress) 2D FAIR ASL sequence provided by Siemens (WIP 557). Its source code was not available and the adjustment of sequence parameters and limits was restricted to the ones accessible through the user interface. Therefore, two preparative

experiments concerning the quality of the slice-selective inversion and the ratio of imaging slice thickness to inversion slice thickness have been conducted.

Inversion Profile and Efficiency

Profile and efficiency of the slice-selective inversion pulse implemented in the 2D FAIR ASL sequence were verified in an inversion recovery experiment. Therefore, a uniform cylindrical water phantom, whose longitudinal relaxation time was previously determined to $T_1 = 2823 \pm 26\,\text{ms}$ [Schewzow, 2010], was used. First the implemented inversion pulse was applied to invert a central slice with a thickness of 8 mm. After an inversion time of $TI = 66\,\text{ms}$, a 4 mm slice perpendicular to the inversion slice was imaged with the TrueFISP readout. A second image without prior inversion was recorded for normalization. The imaging parameters were $TE/TR/FA = 2\,\text{ms}/4\,\text{ms}/70°$ using a matrix size of 256×256 and a FOV of $144 \times 144\,\text{mm}^2$. The inversion pulse had a fixed length of 15 ms. The pulse was VERSE-transformed (cf. Section 3.5.2). The degree of the transformation was accessible through a parameter called gradient scale. Further, the nominal flip angle was adjustable. A rectangular ROI was drawn in the inverted region to estimate the inversion efficiency . Mean value and standard deviation were read out and corrected for T_1 relaxation during the inversion time. The quality of the slice profile was assessed by a central cut through the normalized image. The inversion profile is shown in Figure 4.1 and shows a sharp transition between inverted and uninverted magnetization and a homogeneous inversion as expected from the small standard deviation of the inversion efficiency. The ideal flip angle was found to be 320° together with a gradient scale of 0.55. With these parameters, the measured inversion efficiency was 0.99 ± 0.03.

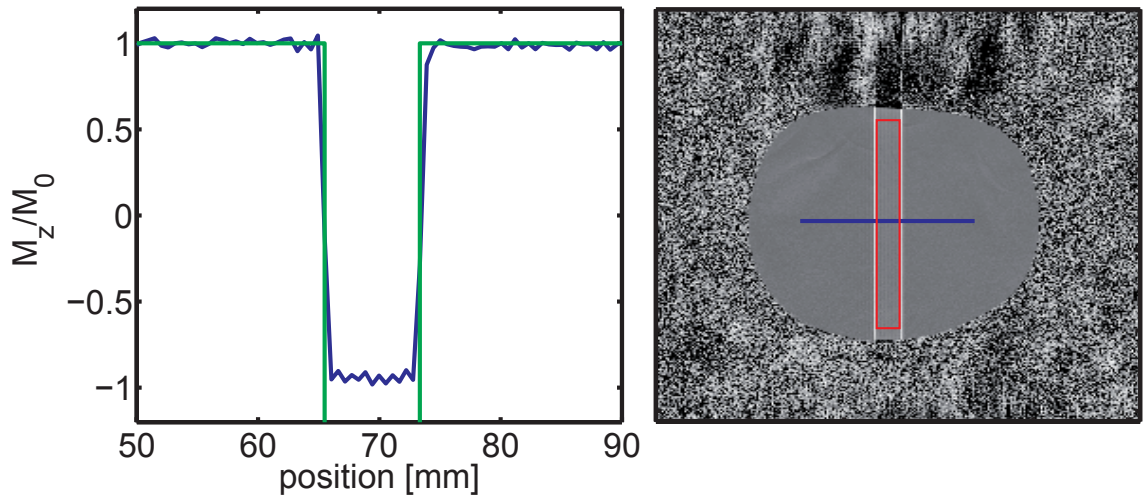

Figure 4.1: *Assessment of inversion profile and efficiency. The left panel shows the inversion profile as extracted (indicated by the blue line) from the normalized axial slice of the cylindrical water phantom shown in the right panel. The green lines indicate an ideal rectangular profile. A rectangular ROI (red) was placed in the inverted region to derive the inversion efficiency . Mean value and standard deviation were read out and corrected for relaxation during the inversion time.*

Minimal Thickness of Slice-Selective Inversion

Although the inversion profile can be measured directly, its impact on the choice of imaging and inversion slice thickness in a FAIR ASL experiment has to be determined separately. For an ideal rectangular inversion profile the imaging slab can be exactly as thick as the inversion slab. Then, in the perfusion-free case, the signal in the ASL difference image ΔM shall be zero. In practice, the inversion profile deviates from an ideal rectangle and the slice thickness of the inversion has to be larger than the imaging slice thickness. Otherwise, ΔM does not vanish in the case of no perfusion, which leads to erroneous perfusion values. The ideal ratio between inversion and imaging slice thickness was estimated in a uniform cylindrical water phantom by conducting a FAIR ASL experiment using the same imaging parameters as for the previous experiment. An axial slice of the phantom was imaged. Overall, 13 FAIR ASL experiments were conducted, each with a different inversion slice thickness. Starting with 8 mm, its thickness was incremented by 1 mm after the acquisition of each tag-control pair. The inversion pulse was the same as used above. Finally, mean value and standard deviation of the signal in each ΔM image was read out at the position of the phantom. The signal intensities in dependency on the thickness of the slice-selective inversion are plotted in Figure 4.2. The experiments suggests that the thickness of the slice-selective inversion should be at least 150 % percent of the imaging slice thickness.

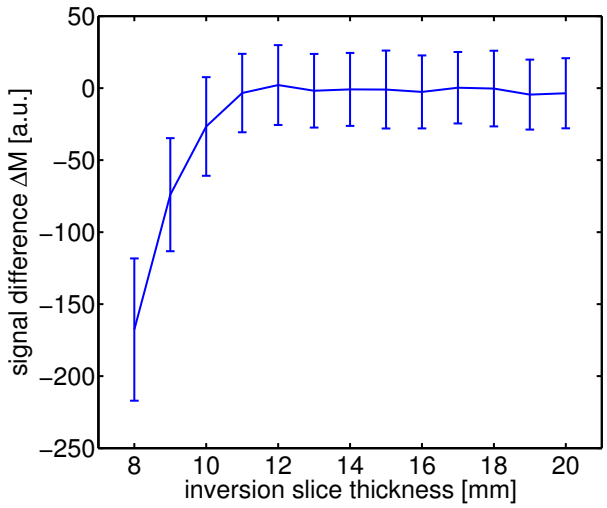

Figure 4.2: *Results of the experiment to estimate the ideal ratio between inversion and imaging slice thickness. In the perfusion-free case the signal difference ΔM should be zero. The plot shows that the inversion slab has to be chosen thicker than the imaging slice. The experiment was conducted with an imaging slice thickness of 8 mm.*

4.1.2 Initial Study

The goal of this initial study was to establish renal ASL perfusion MRI of small animals on a clinical whole-body scanner and to investigate and compare its significance against that of DCE-MRI. Thereby, an animal model of acute kidney injury was employed. The results of the initial study that investigates perfusion estimates of ASL and DCE-MRI in a rat model of acute kidney injury have been published in Zimmer et al. [2013].

Animal Preparation

Six male Lewis rats with a weight of 260 g to 290 g were used for this study. Five animals were subjected to AKI as described in Section 3.6.2, one native rat served as control. MRI was conducted five days after the induction of AKI to ensure sufficient damage. It was histologically confirmed by spot checks. Representative histological slices are shown in Figure 4.3. Ten minutes prior to the MRI measurements, rats were anesthetized with thiobutabarbital sodium. A catheter was inserted in the right vena femoralis prior to the measurement. During DCE-MRI, the catheter was used for the application of contrast agent (Dotarem®, Guerbet, Roissy CdG Cedex, France).

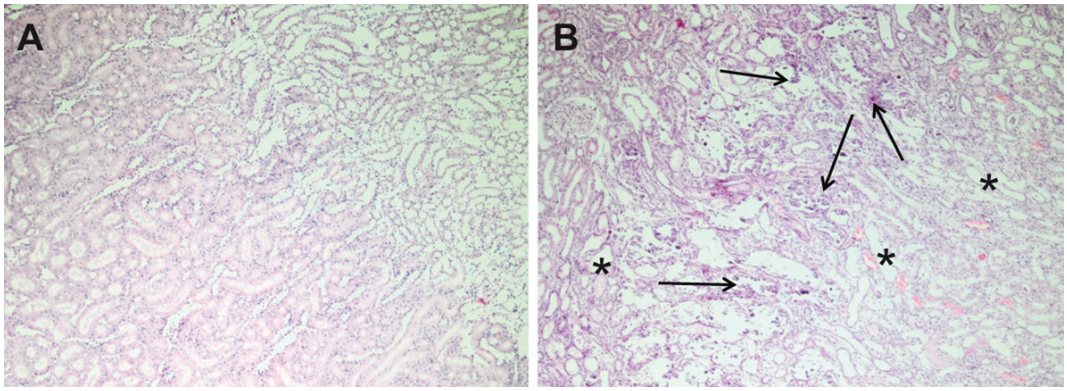

Figure 4.3: *Histological slides (H&E, 40×) of a native kidney (A) and a kidney five days after acute injury (B). Compared to the native kidney the diseased kidney shows main hallmarks of acute renal injury like cellular swelling, necrosis and tubular dilatation. Examples for necrosis and tubular dilatation are marked with arrows and stars, respectively. From Zimmer et al. [2013].*

ASL

The employed ASL sequence uses the combination of a FAIR labeling scheme (cf. Section 3.3.1) and a 2D TrueFISP. A single axial slice with a thickness of 4 mm was imaged. The slice was positioned in a way such that both left and right kidney were imaged at the same time. Images without magnetic preparation (M_0), with global inversion (control) and with slice-selective inversion (tag) were recorded in an interleaved manner. Overall, 90 images were acquired resulting in 30 tag-control pairs and 30 M_0 images. The overall measurement time was 9 min. For both global and slice-selective inversion, a hyperbolic secant pulse was used. The main pulse parameters were fixed and not accessible, however its quality was verified (see section above). The inflow time TI was set to 1.2 s. As a consequence of the preliminary measurement, the slice thickness of the selective inversion was set to 8 mm. Its slab was orientated and located so that it covered the imaging volume completely and symmetrically. The TrueFISP imaging parameters were: TR/TE = 5.44 ms/2.72 ms, flip angle = 70 degree, FOV = 140 ×140 mm^2, matrix = 256×256, bandwidth = 651 Hz/px and GRAPPA factor = 3. Figure 4.4 depicts the positioning of imaging and inversion volume and shows exemplary images of tag, control and M_0 images.

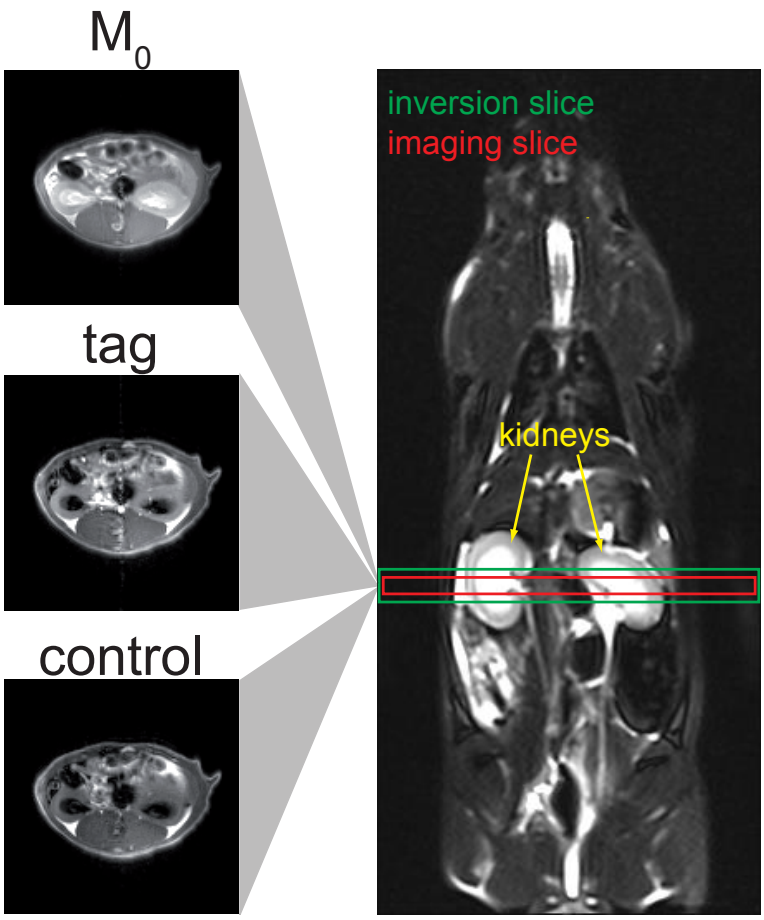

Figure 4.4: *On the left-hand side, exemplary tag, control and M_0 images as recorded during the 2D ASL measurements of renal perfusion in rats are shown. Tag and control image are scaled identically. On the right, the positioning of imaging (red) and inversion slice (green) is illustrated. The underlying image depicts a T_2-weighted coronal slice through the rat abdomen that allows a good identification of the kidneys. The image shows the rat with two healthy kidneys.*

To minimize signal oscillations in the transient phase, an $\alpha/2$ pulse plus ten additional *TR*-intervals without data recording were used before the acquisition. Centric reordering of phase-encoding was used to maximize perfusion contrast. A single image, excluding the inversion time, was recorded in 0.6 s. The inter image time was set to 4.8 s to ensure full longitudinal relaxation and equal initial condition for each labeling mode. All six animals were subjected to an ASL perfusion measurement. To test the within subject variability, four consecutive measurements were performed on two rats. After averaging the recorded data according to its magnetic preparation, perfusion maps were calculated by a pixel-wise application of Equation (3.22) using $\alpha = 1$, $T_{1,\mathrm{T}} = 1.14\,\mathrm{s}$ [de Bazelaire et al., 2004] and $\lambda = 0.8$ [Karger et al., 2000].

DCE-MRI

DCE perfusion imaging was performed immediately after the ASL measurement. For this purpose, a time-resolved angiography with stochastic trajectories (TWIST) 3D FLASH sequence was used. The imaging parameters were: TR/TE = 3.4 ms/1.4 ms, flip angle = 20°, FOV = $114 \times 50 \times 34\,\mathrm{mm}^3$, matrix = $192 \times 84 \times 28$ and GRAPPA factor = 2. TWIST *k*-space acquisition was set to fully cover the central 15% of *k*-space and to sub-sample the outer regions by a factor of 5. This led to a nominal temporal resolution of 0.9 s per volume. Images were continuously acquired for 6 minutes. According to a normal clinical dose and the manufacturer's instruction, about 0.05 ml

of contrast agent (Dotarem®, Guerbet, Roissy CdG Cedex, France) was administered manually after the 15th volume was acquired. The injection was directly followed by a saline flush of 1 ml. All six animals underwent DCE-MRI. Figure 4.5 shows three points in time during an exemplary DCE-MRI measurement showing take-up and filtration of the contrast agent. Absolute perfusion values were calculated with a pixel-by-pixel TSVD deconvolution described in Section 3.4.2 using the software tool *UMMPerfusion*. The software calculates maps of RBF. Each arterial input function was determined by a carefully placed ROI in the abdominal aorta at a point cranial to the branch of the renal arteries. The tissue response function was assessed for every pixel. All data were normalized by subtracting the mean intensity of 15 baseline volumes. Further, a linear relationship of contrast agent concentration to measured signal intensities was assumed. To exclude errors caused by the clearance of contrast agent through the medullary pyramids, only the volumes capturing solely the first pass were used for calculating the perfusion parameters. This amounted to 60 volumes for animal three and 50 volumes for all other animals. Figure 4.6 shows arterial input function and tissue response function for the healthy and the diseased kidney of one rat, respectively.

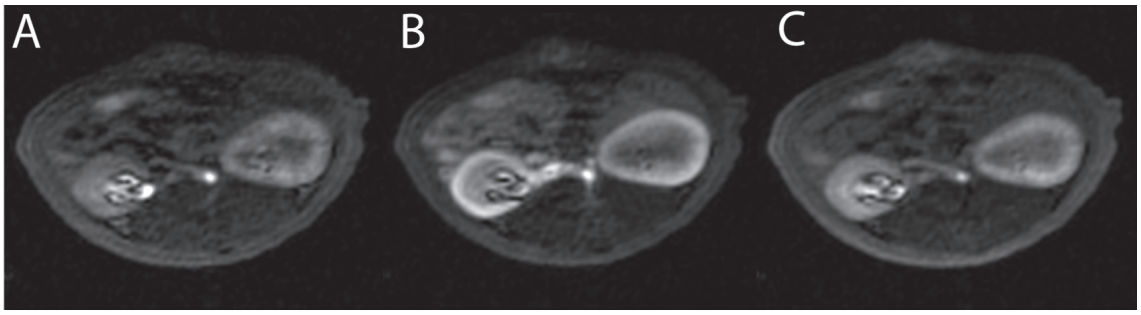

Figure 4.5: *Representative DCE-MRI images at different time points. (A) Baseline image before contrast agent injection. (B) Cortical peak contrast image approximately 40 s after bolus injection and an image (C) taken approximately 4 min later showing increased medullar contrast. Regarding the contrast uptake and its distribution, the AKI kidney (right kidney in the image) can clearly be distinguished from the healthy kidney. Image taken from Zimmer et al. [2013].*

Perfusion Analysis

To extract the mean RBF and standard deviation, regions of interest delineating the renal cortex were drawn into the respective perfusion maps. DCE-MRI regions were drawn in consensus with the regions used for the ASL perfusion maps. Due to the differing slice thickness, the mean value of the three DCE-MRI slices corresponding to the ASL slice, was taken. Figure 4.7 illustrates ASL and DCE perfusion MRI, by showing exemplary images and the according perfusion maps of the respective methods in a rat with AKI. Mean cortical perfusion as estimated with ASL and DCE-MRI are summarized in Table 4.1. For each animal and method, the values for the healthy and the diseased kidney are shown. In the diseased kidney the mean cortical perfusion was found to be $(316 \pm 102)\,\mathrm{ml/100\,g/min}$ for ASL and $(407 \pm 119)\,\mathrm{ml/100\,g/min}$ for DCE-MRI. For the healthy kidneys the respective values are $(416 \pm 124)\,\mathrm{ml/100\,g/min}$ and

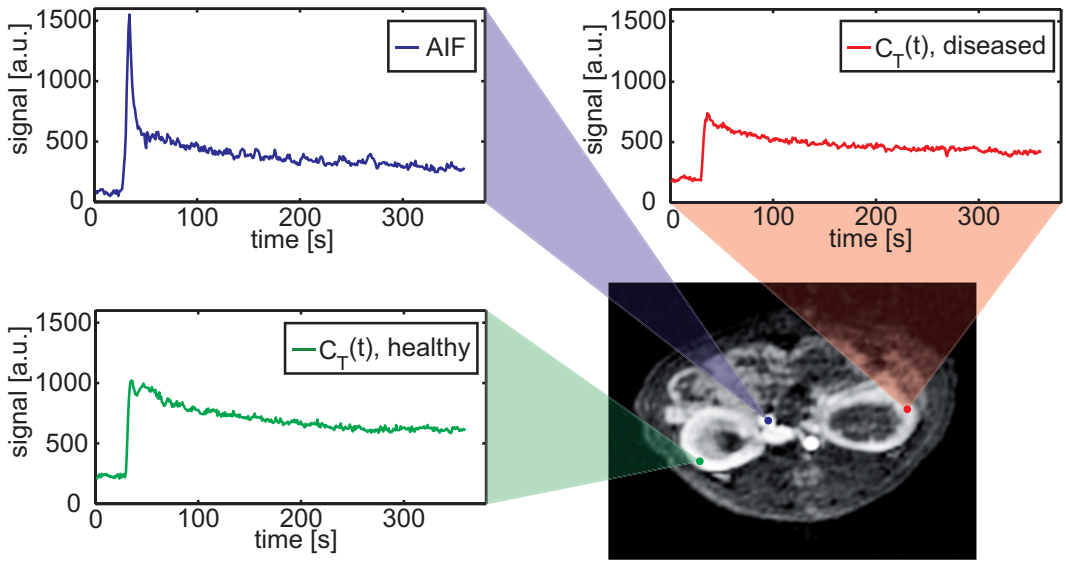

Figure 4.6: *Arterial input function (blue) and tissue response functions of healthy (green) and diseased (red) kidneys, respectively. The functions are extracted from the DCE-MRI time series of the region marked with the corresponding color. The underlying image is an axial slice of the recorded volume that corresponds to the slice imaged for the ASL measurement.*

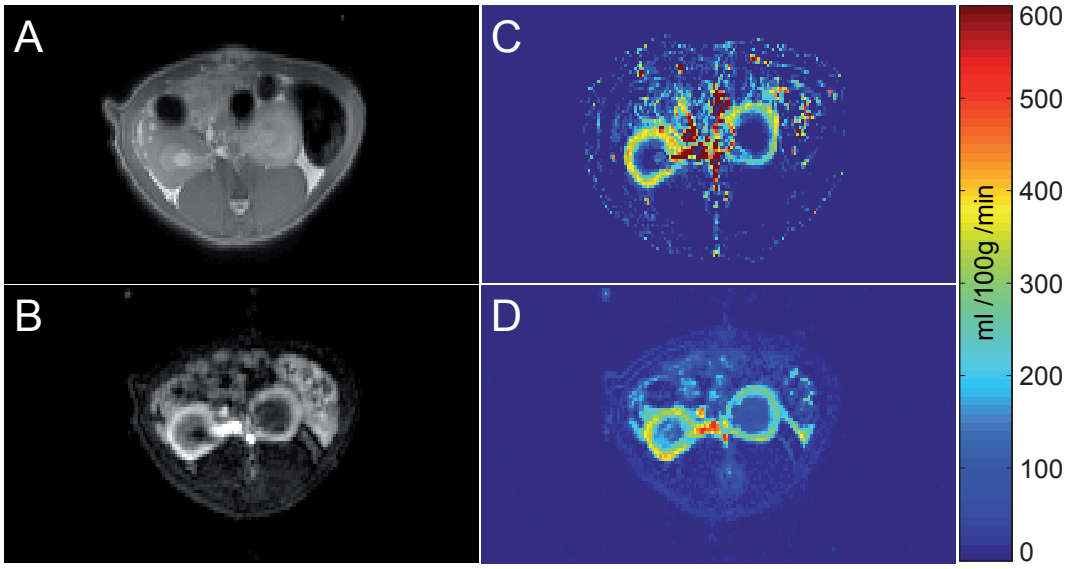

Figure 4.7: *Exemplary images recorded during (A) ASL and (B) DCE-MRI perfusion measurement of a rat with acute kidney injury. The corresponding perfusion maps (C and D) are shown on the right-hand side. All drawings show the same rat and the same axial slice. Differences between the kidney with AKI and the contralateral kidney are clearly visible in the MRI images as well as on the perfusion maps. From [Zimmer et al., 2013].*

Table 4.1: *Cortical perfusion in ml/100 g/min as estimated from ASL and DCE-MRI measurements.*

rat	ASL		DCE-MRI	
	left(AKI)	right(healthy)	left(AKI)	right(healthy)
1*	295 ± 60[1]	304 ± 53	535 ± 154[1]	519 ± 146
2	456 ± 71	634 ± 94	321 ± 125	433 ± 136
3	191 ± 64	344 ± 66	313 ± 93	481 ± 137
4	289 ± 63	504 ± 69	566 ± 182	631 ± 222
5	374 ± 72	462 ± 65	504 ± 135	679 ± 198
6	269 ± 45	371 ± 49	330 ± 104	517 ± 153
mean	316 ± 102	416 ± 124	407 ± 119	542 ± 85

*Animal with two healthy kidneys

[1]Value excluded when calculating the mean perfusion of AKI kidneys, however included in the average RBF of healthy kidneys.

(542 ± 85) ml/100 g/min. Due to the high inter-object variation, the mean value is given with the sample standard deviation. The results of the consecutive ASL measurements in rats number 2 and 4 (cf. Table A.2) show that the variation of the estimates is very small for each kidney and animal. This provides evidence that the measurements are robust and have a low variability within one subject. A paired-sample t-test was applied to test whether the pairwise differences of healthy and diseased kidneys are significantly different from zero. The test was applied to both ASL and DCE-MRI estimates. The test calculated the probability that the differences are random samples of a normal distribution with mean zero, to 0.34% and 0.36% for ASL and DCE-MRI, respectively. This significant difference is also reflected in the Bland-Altman plots in Figure 4.8. Mean differences between healthy and diseased kidneys are (147 ± 47) ml/100 g/min for ASL and (141 ± 46)ml/100 g/min for DCE-MRI. They are in very good agreement. The direct comparison of ASL and DCE-MRI estimates of all kidneys shows systematically higher values for DCE-MRI, however a t-test showed that the estimates are not significantly different. To analyze the data regardless of absolute perfusion values, RBF ratios between left and right kidneys for each animal and method were calculated (cf. Table A.1). They are displayed in Figure 4.9. The mean ratio of rats with unilateral AKI was 0.68 ± 0.11 and 0.73 ± 0.10 for ASL and DCE-MRI, respectively.

4.1.3 Animal Model of Acute Kidney Injury

A second study on rats with AKI and an increased number of animals was conducted to confirm the findings of the initial study and to increase the statistical power. Based on the results of the initial study, ASL was considered to be sufficient to assess pathological changes in renal function.

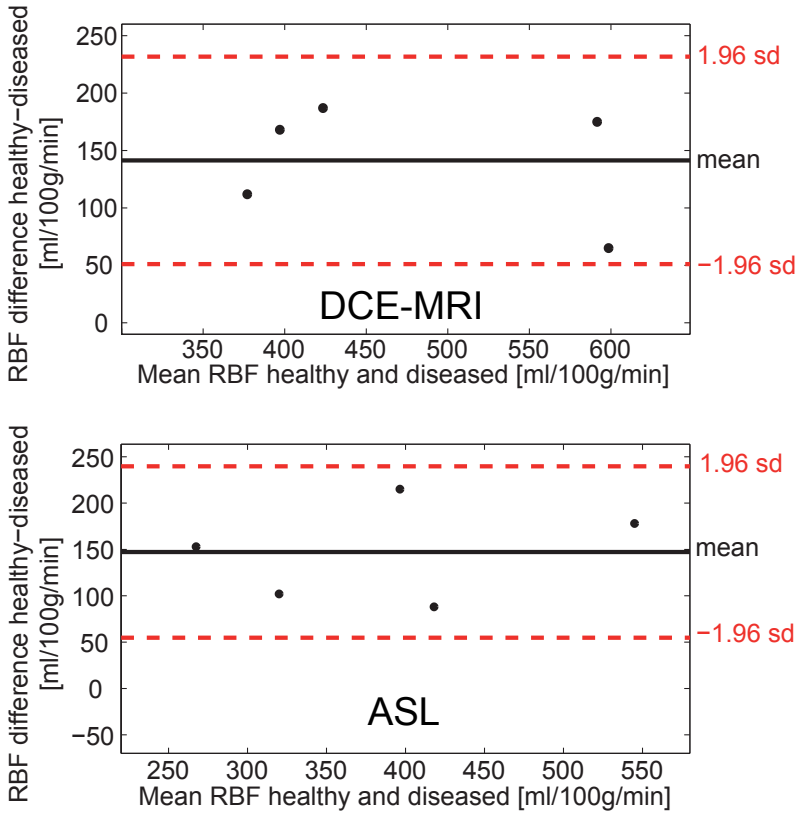

Figure 4.8: *Visualization of differences between healthy and AKI kidneys in renal cortical perfusion. For each method a Bland-Altman plot is shown. The upper plot shows the differences as assessed with DCE-MRI, the lower plot the ASL results. Both mean differences are significantly different from zero, confirming the results of the t-test. Plot as published in [Zimmer et al., 2013].*

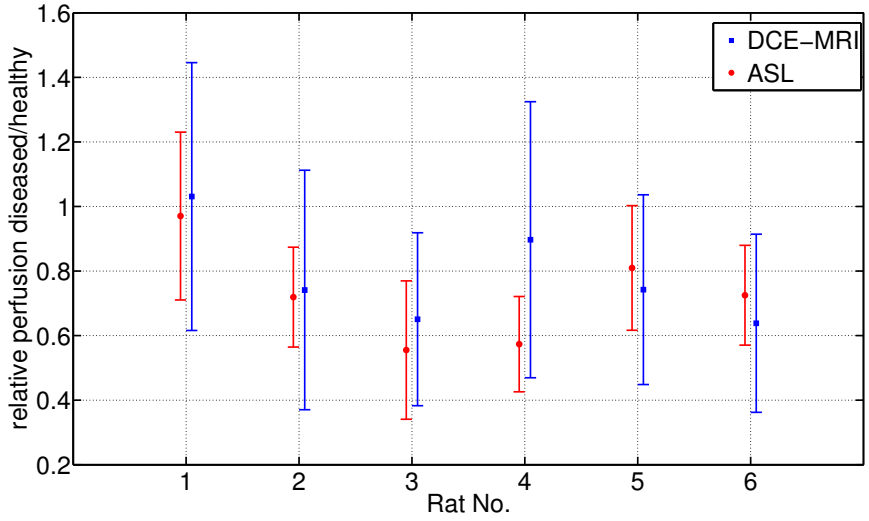

Figure 4.9: *Ratios of renal perfusion between left (diseased) and right (healthy) kidneys. Ratios were calculated from the values given in Table 4.1. The ratios are listed in Table A.1 in the appendix. Estimates from ASL (red) and DCE-MRI (blue) are shown.*

Animals

Fourteen male Lewis rats with a weight of 250 g-300 g were employed for this study. The left kidney of all animals was used to induce an AKI as described in Section 3.6.2. Despite the insertion of a catheter, all animal preparation prior to MRI was conducted as described for the initial study and animals were imaged five days after AKI induction.

ASL Perfusion MRI

Measurement and assessment of renal cortical perfusion was performed as described in Section 4.1.2. All imaging and evaluation parameters were identical. The detailed results are listed in Table A.3 in the appendix. The mean cortical blood flow was $(287 \pm 83)\,\mathrm{ml/100\,g/min}$ for the AKI kidneys and $(500 \pm 91)\,\mathrm{ml/100\,g/min}$ for the healthy kidneys. The error represents the sample standard deviation. The application of a paired sample t-test rejects the null hypothesis that the pairwise differences are samples of a normal distribution with mean zero. The probability was calculated to be smaller than 0.01. The mean perfusion difference between healthy and diseased kidneys is $(213 \pm 80)\,\mathrm{ml/100\,g/min}$. The Bland-Altman plot in Figure 4.10 confirms these results and shows that no systematic errors are present. Figure 4.11 shows a T_2-weighted spin-echo image with a resolution of $0.14 \times 0.14\,\mathrm{mm}^2$. On the right, the perfusion map calculated from the ASL data of the same animal is displayed. The impaired left kidney can be well identified by its pathological appearance and its decreased renal perfusion compared to the healthy kidney. RBF ratios between left and right kidneys for each animal were calculated (cf. Table A.4). They are displayed in Figure 4.12. The mean ratio between diseased and healthy kidney was 0.58 ± 0.15.

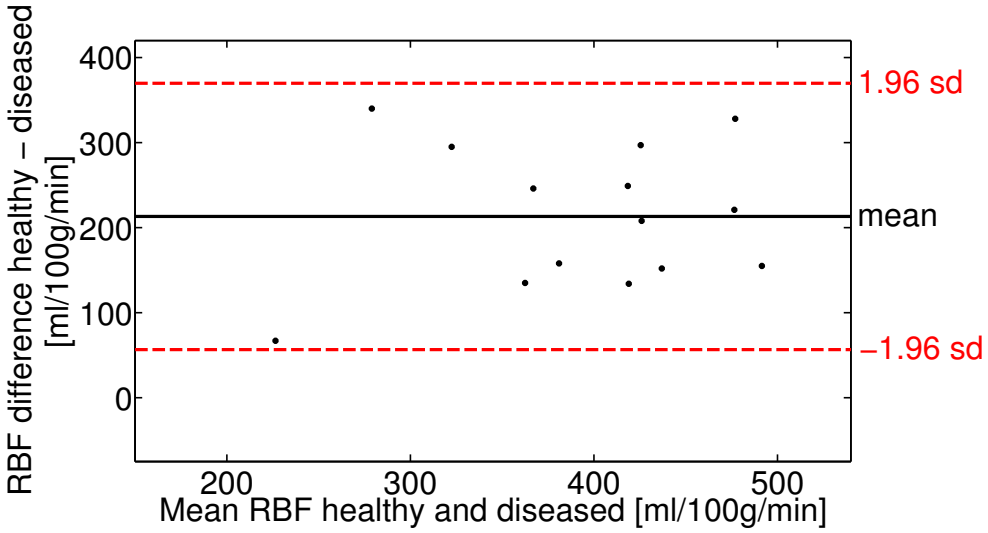

Figure 4.10: *Bland-Altman plot to visualize differences of renal cortical perfusion between healthy and diseased kidneys. The corresponding values are listed in Table A.3. The mean difference is significantly different from zero.*

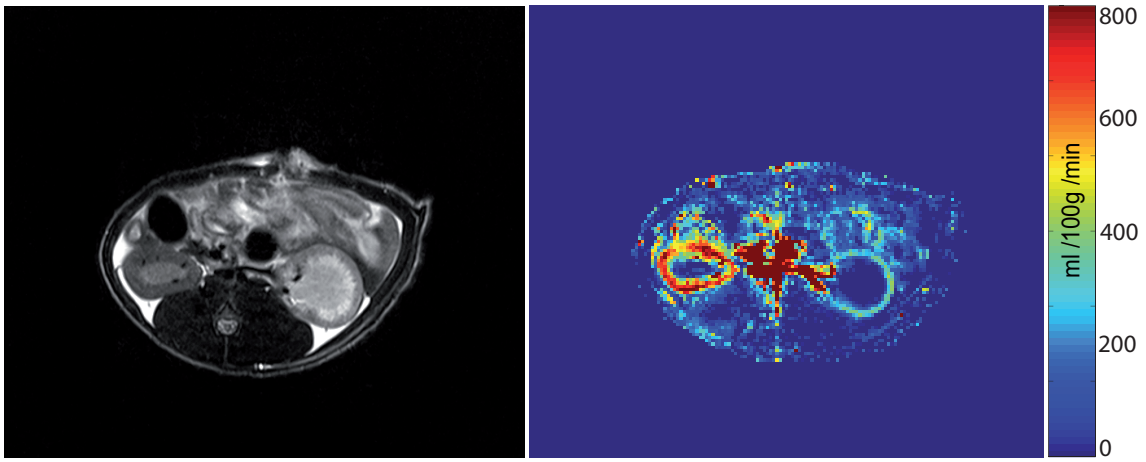

Figure 4.11: *Axial slices of a rat with unilateral acute kidney injury. The left hand side shows a T_2-weighted spin-echo image with an in-plane resolution of $0.14 \times 0.14\,\mathrm{mm}^2$. The perfusion map calculated from the ASL data is shown on the right. The impaired left kidney can be well identified in the morphological image as well as in the perfusion map.*

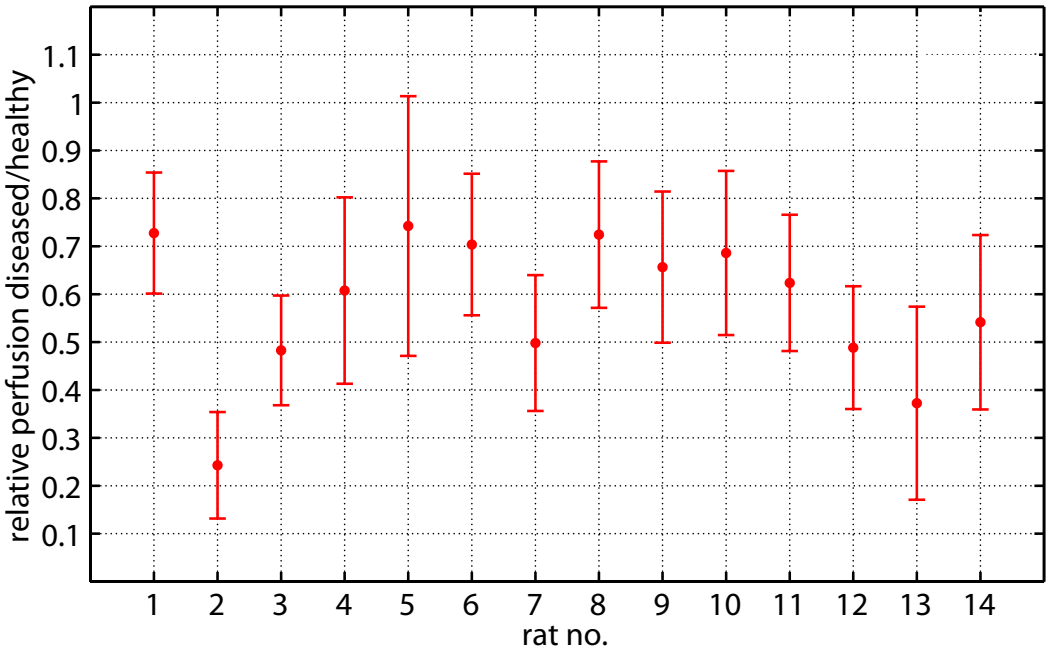

Figure 4.12: *Ratios of renal perfusion between left (diseased) and right (healthy) kidneys assessed with ASL. Values were calculated based on the results given in Table A.3 and are listed in Table A.4.*

4.1.4 Animal Model of Renal Transplantation

In a third study, perfusion was measured in a renal transplantation model. Two different types were employed, either to evaluate acute rejection or to evaluate chronic rejection. Renal perfusion was assessed with ASL.

Animals

Overall, 43 rats were imaged in this study. Male Fisher rats served as organ donors, male Lewis rats as organ recipients. The initial weight of the animals was 250 g-300 g. 23 rats underwent MRI seven days after surgery (acute rejection), 20 animals were imaged six months after surgery (chronic rejection). The preparation of the animals prior to MRI was identical to the AKI study.

ASL Perfusion MRI

The measurement and the assessment of renal cortical perfusion was performed as described for the initial study in Section 4.1.2. Exemplary images and perfusion maps are shown in Figure 4.13. The image shows T_2-weighted spin-echo images on the left-hand side and the perfusion maps as calculated from the ASL data. Images and maps of animals with acute (upper row) and chronic (lower row) transplant rejection are displayed. The mean cortical perfusion was found to be (240 ± 67) ml/100 g/min and (346 ± 112) ml/100 g/min for the model of acute and chronic rejection, respectively. The results for both transplantation models and each animal are listed in Table A.5 in the appendix. Again, due to the high inter-animal variation, the sample standard deviation is given. A two-sample t-test was applied to test whether the two (chronic and acute) samples are from a distribution with equal mean. Due to the differing standard deviations of the samples, unequal variances were assumed. The test rejected the

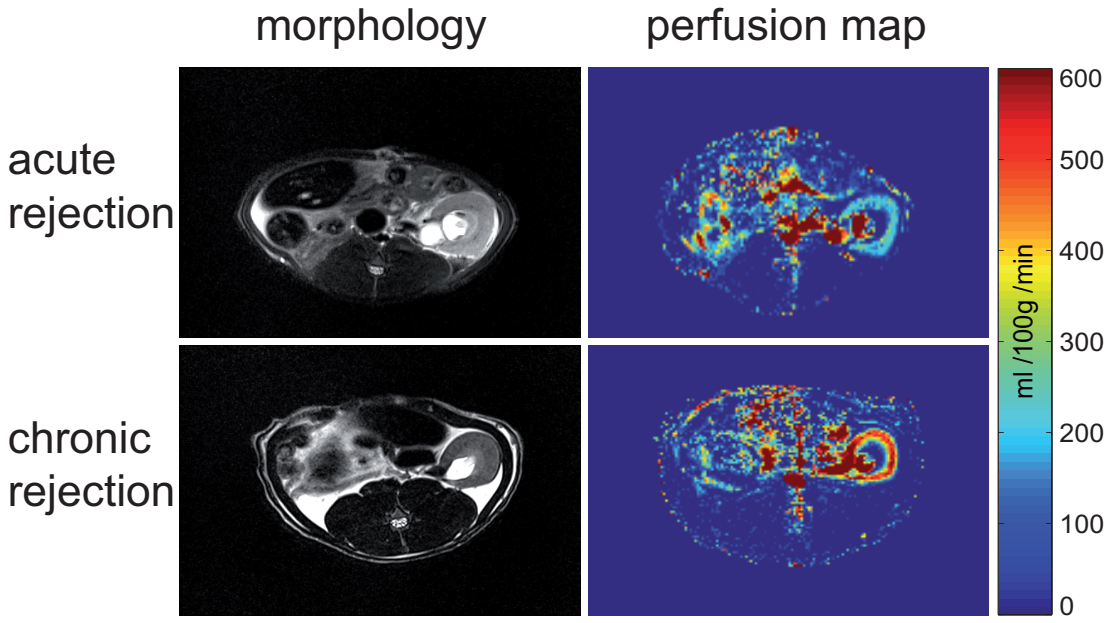

Figure 4.13: *Morphology (left) and perfusion maps (right) of rats with acute (upper row) and chronic (lower row) transplant rejection. The morphological images are T_2-weighted spin-echo images with an in-plane resolution of $0.25 \times 0.25\,\mathrm{mm}^2$ (upper image) and $0.14 \times 0.14\mathrm{mm}^2$ (lower image). The images show the graft as the only kidney of the animals. The perfusion maps shows a higher cortical perfusion for the organ with chronic rejection.*

null hypothesis and calculated the probability of equal means to 0.1 %. To visualize the data Figure 4.14 shows boxplots for both transplantation models. The medians are 236 ml/100 g/min and 365 ml/100 g/min for the acute and the chronic model, respectively. A comparison to the perfusion values found in the healthy kidneys of the AKI animals in the two previous studies suggests that RBF in renal grafts is generally decreased compared to healthy kidneys.

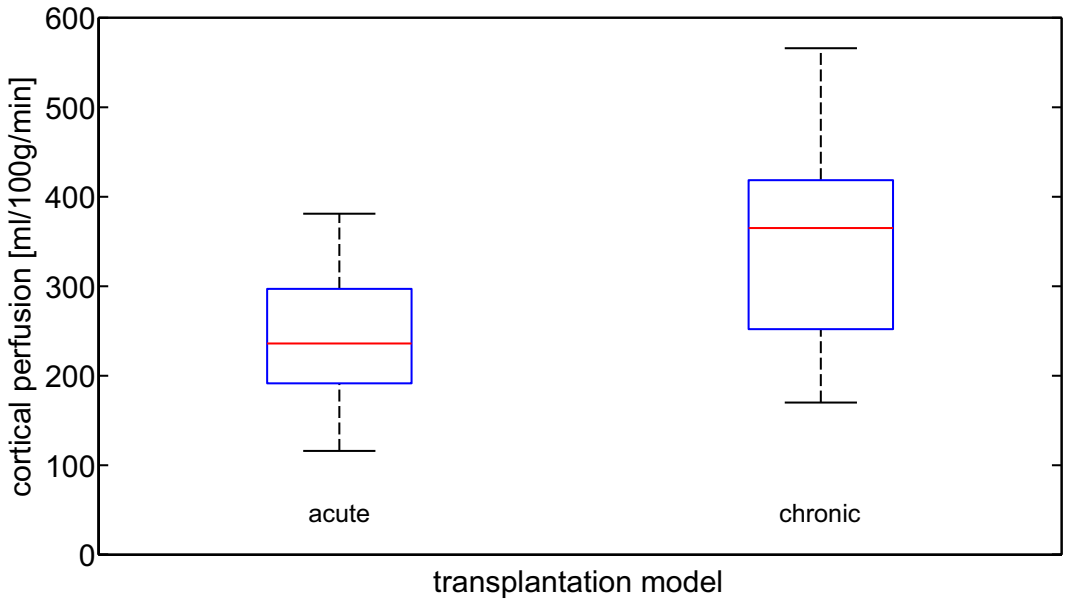

Figure 4.14: *Boxplots of the perfusion data measured in rat models of acute and chronic transplant rejection. The red lines indicate the median, the box delineates the first and third quartiles of the data. The whiskers represent the minimum and maximum of the data.*

4.2 Adiabatic Inversion Pulses

Pulsed ASL sequences demand sophisticated slice-selective inversion pulses. The two major requirements are a complete and homogeneous inversion as well as sharp transition zones between inverted and uninverted magnetization. Further, robustness against frequency offsets and B_1-field variations are required. Therefore, adiabatic inversion pulses were designed which were later implemented in the 3D ASL sequence. In the following, the results of slice profile measurements and simulations of different pulses are presented.

4.2.1 Hyperbolic Secant vs. FOCI Pulse

In this section, the results of measurements and simulations of HS and FOCI pulses are shown and compared. The quality of the inversion profiles and the robustness of both types of adiabatic pulses against typical disturbing factors are presented.

Slice Profile Differences

To verify and analyze the differences between a HS pulse and its FOCI counterpart, the slice profiles of both pulses were assessed experimentally and numerically. Numerical simulations were performed as described in Section 3.5.4. For the measurements, both inversion pulses were implemented in the dedicated sequence (cf. Section 3.2.5) as described in Section 3.5.1. The sequence was alternately used with (ssIR) and without (noIR) the inversion pulse. A bottle of distilled water served as a phantom. In readout direction, a 20 cm field of view and an imaging matrix dimension of 2016 was used. This led to a resolution of 0.10 mm per pixel. TE was 11 ms, TR was set to 18 s to guarantee a complete recovery of the longitudinal magnetization between adjacent measurements. Overall 20 measurements were performed, ten for each magnetic preparation. The parameters of the used HS pulse were: $T_{\text{pulse}} = 10.24\,\text{ms}$, BW $= 1000\,\text{Hz}$, $B_{1,\text{trunc}} = 0.5\,\%$. Accordingly, μ and β were 2.68 and 1171 Hz, respectively. The data were averaged according to their magnetic preparation (ssIR or noIR). Then, one magnitude and one phase image was reconstructed for each preparation. To distinguish magnetization that has the same absolute value but an opposite sign, the phase information is needed in addition to the magnitude image. Due to the spoiled transversal magnetization, a phase jump of π occurs at the positions were the longitudinal magnetization changes its sign. As the phase of the 90° excitation pulse is known, the ssIR phase image allows the determination of the correct sign of the magnetization. The final inversion profile was then reconstructed by normalizing the ssIR magnitude image with the noIR magnitude image and by correcting the sign according to the information gained from the ssIR phase image. The results of the measurement are shown in Figure 4.15 where magnitude and phase of the ssIR data and the signal with corrected algebraic sign, i.e. the slice profile, are displayed. Figure 4.16 shows the comparison of this pulse against its FOCI equivalent with $F = 10$. The slice thickness was set to 50 mm resulting in constant gradient amplitude of 0.47 mT/m for the HS pulse and a maximal amplitude of 4.7 mT/m for the FOCI pulse. In a region with 80 %

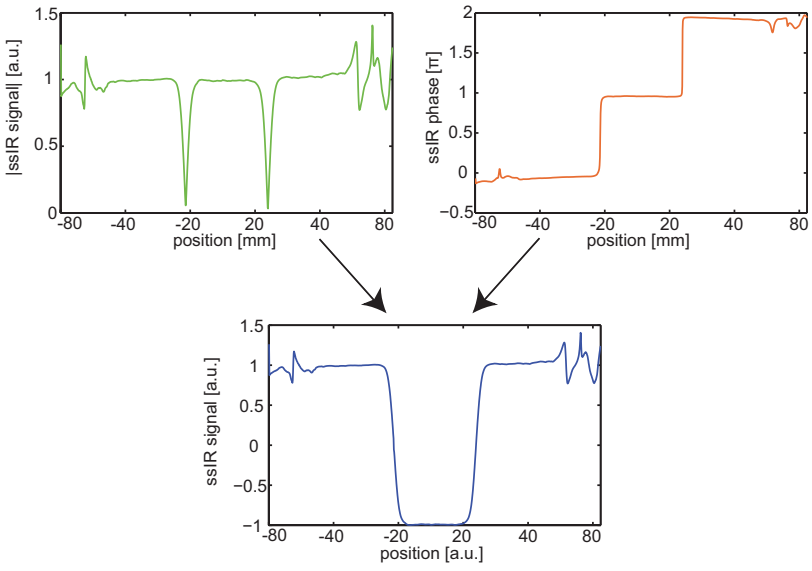

Figure 4.15: *Data of the assessment of an inversion profile. The upper images show magnitude and phase of ssIR data. The information of the phase data is used to determine the position of zero-crossing of the magnetization allowing the reconstruction of the signal with the correct algebraic sign (lower image).*

of the nominal slice thickness, centered around the isocenter, the mean longitudinal magnetization is -0.937 ± 0.104 and -1.000 ± 0.002 for the simulations of HS and FOCI pulse, respectively. For the measured profiles of HS and FOCI pulse, the values are -0.960 ± 0.074 and -0.998 ± 0.004, respectively. For a better understanding of the evolution of the slice profile during the transmission of the RF pulse, the profile of a FOCI pulse was numerically calculated and experimentally assessed for fractions of 20 % to 100 % of the total pulse duration T_{pulse}. The pulse parameters were the

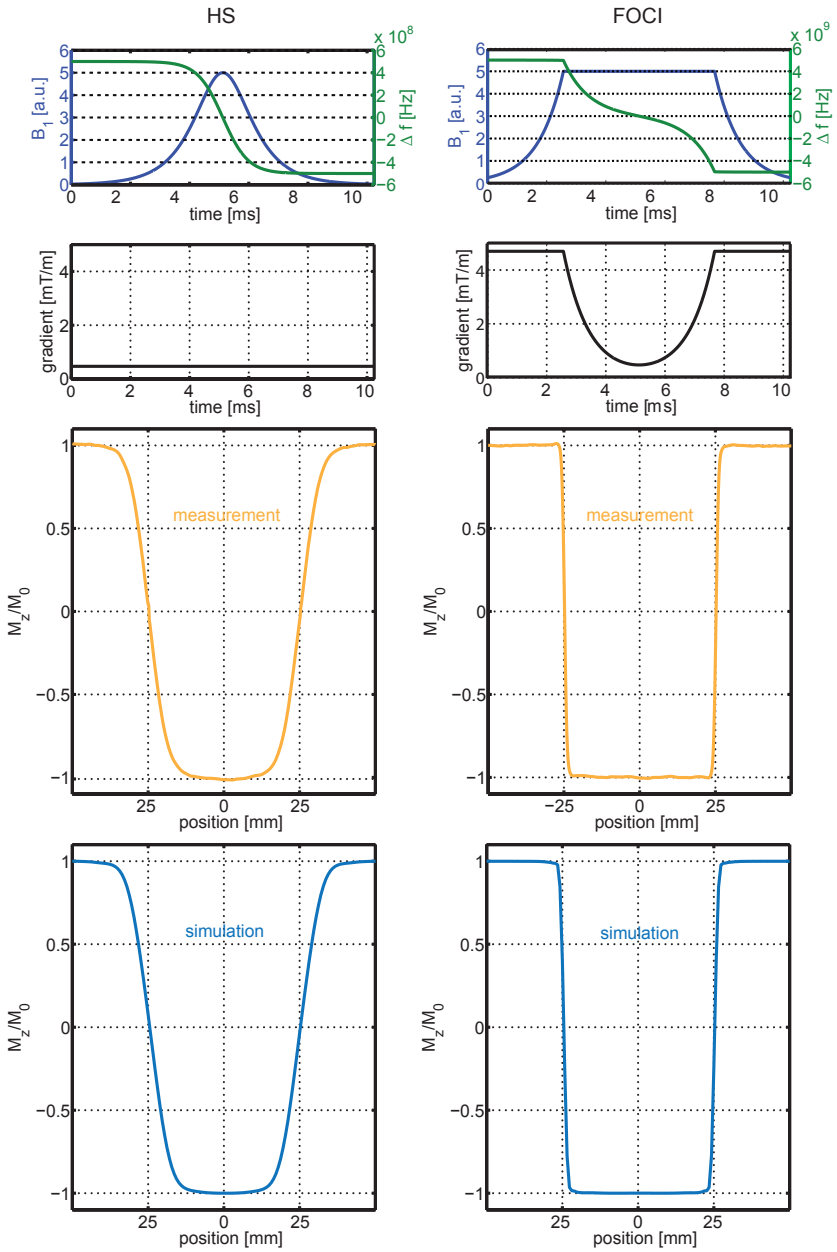

Figure 4.16: *Comparison of a HS pulse and its FOCI equivalent with the respective slice profiles from measurements and simulations. Shown are from top to bottom: B_1-amplitude (blue) and off-resonance (green), gradient, experimental slice profile and simulated slice profile.*

identical to the ones used above, however this time the FOCI pulse with $F = 3$ was used. The pulse was set to invert a 50 mm slice. For the given bandwidth and FOCI factor, this amounts to a maximum slice-selection gradient amplitude of 1.4 mT/m. The results of simulation and measurement are displayed in Figure 4.17. FOCI pulses have the disadvantage that the required maximal gradient amplitude is increased by the factor F, compared to its HS equivalent. Like for non-adiabatic RF pulses, the profile quality might also be improved by increasing the bandwidth. However, while the bandwidth of an RF pulse is normally limited by the SAR, it is confined by the adiabatic condition for adiabatic pulses. Figure 4.18 demonstrates the possible effect of an increased bandwidth on the slice profile when using adiabatic inversion pulses. The RF pulse parameters were $T_{\text{pulse}} = 10.24$ ms, BW = 3000 Hz, $B_{1,\text{trunc}} = 0.5\,\%$ resulting in $\mu = 8.05$ and $\beta = 1171$. For the FOCI pulse $F = 5$ was used. The maximum gradient amplitude was 1.4 mT/m and 7.0 mT/m for HS and FOCI pulse, respectively, such that the inversion slice thickness was 50 mm. The mean longitudinal magnetization in a region with 80 % of the nominal slice thickness was found to be -0.750 ± 0.002 and -0.802 ± 0.059 for the simulations of HS and FOCI pulse, respectively. The experimentally assessed values are -0.758 ± 0.005 and -0.685 ± 0.038 for HS and FOCI pulse, respectively.

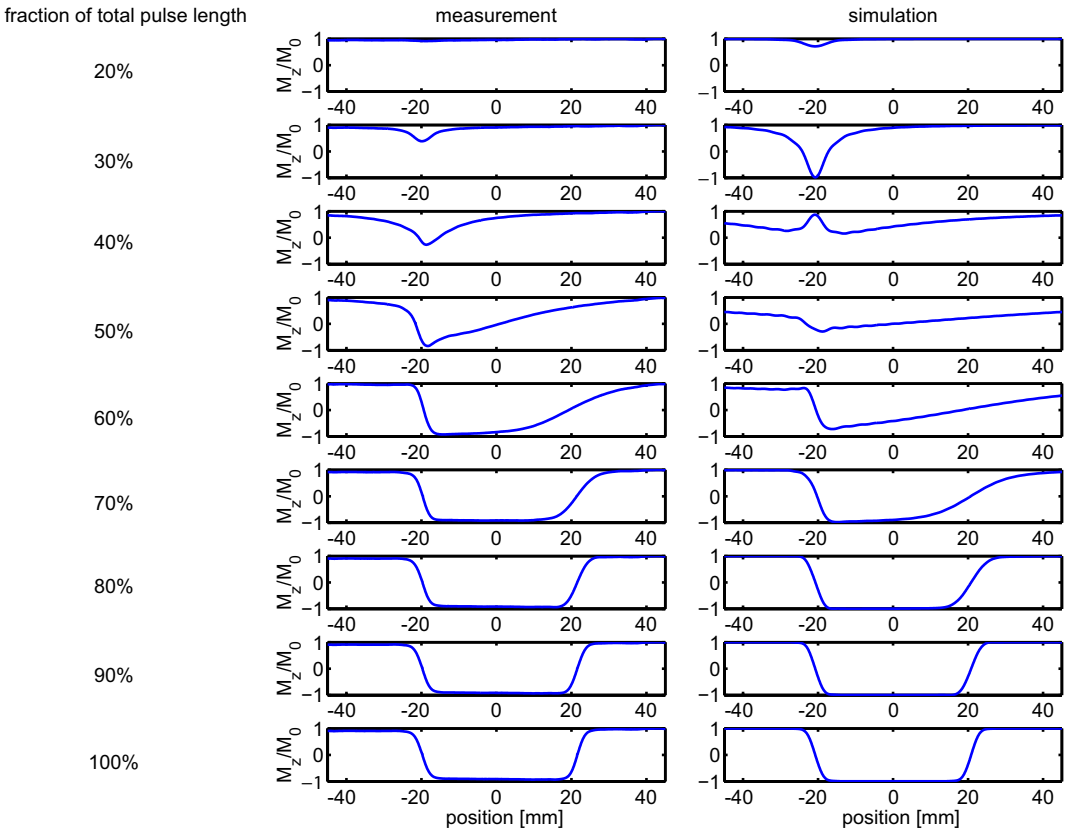

Figure 4.17: *Temporal evolution of the slice profile of a FOCI pulse. The results of measurements (left) and simulations (right) are presented. The fraction of the total pulse length that amounts to the respective profile is indicated on the left next to the profiles.*

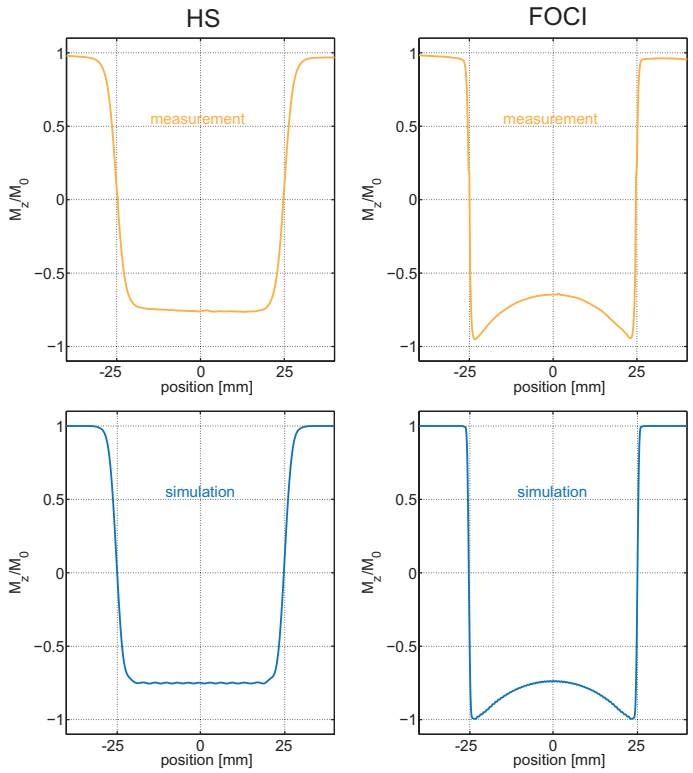

Figure 4.18: *Slice profiles of HS and FOCI pulses with a bandwidth of 3000 Hz. The increased bandwidth leads to a higher adiabatic threshold that can no longer be met by the maximal available coil voltage. This results in an incomplete inversion and inhomogeneous slice profile. Shown are the results of measurements and simulations.*

Off-Resonance Effects

The impact of off-resonance on the slice profiles of adiabatic pulses was evaluated experimentally and numerically (cf. Section 3.5.4). For the measurement, the resonance frequency of the MR scanner was manually shifted. Slice profiles were assessed for a HS pulse and its FOCI counterpart with $F = 10$ at an off-resonance frequency of 400 Hz. For a better comparison, the same pulse as for the initial comparison of HS and FOCI was used (cf. Figure 4.16). The slice profiles are displayed in Figure 4.19. The longitudinal magnetization within the central 80 % of the profile was evaluated. For the simulations the values are -0.936 ± 0.108 and -0.998 ± 0.003, the measurement yielded values of -0.980 ± 0.021 and -0.940 ± 0.010 for HS and FOCI pulse, respectively.

Relaxation Effects

Typically, adiabatic inversion pulses are longer than conventional RF pulses which makes them more prone to relaxation during RF transmission. Therefore, the effects of longitudinal and transversal relaxation on the inversion profiles were investigated using numerical simulations. The effects of T_1 and T_2 relaxation were first assessed separately for a HS pulse and its FOCI equivalent, later the combination of both effects was studied. Figure 4.20 shows the resulting inversion profiles for $T_1 = 10$ ms, $T_2 = 20\,s$ (upper row), $T_1 = 20$ s, $T_2 = 10$ ms (second row), $T_1 = 10$ ms, $T_2 = 10$ ms (third row) and $T_1 = 1$ s, $T_2 = 100$ ms (lower row). The relaxation times of the upper three rows have solely been chosen for the purpose of demonstration and are unlikely to occur in practice. The lower row, however, reflects realistic conditions.

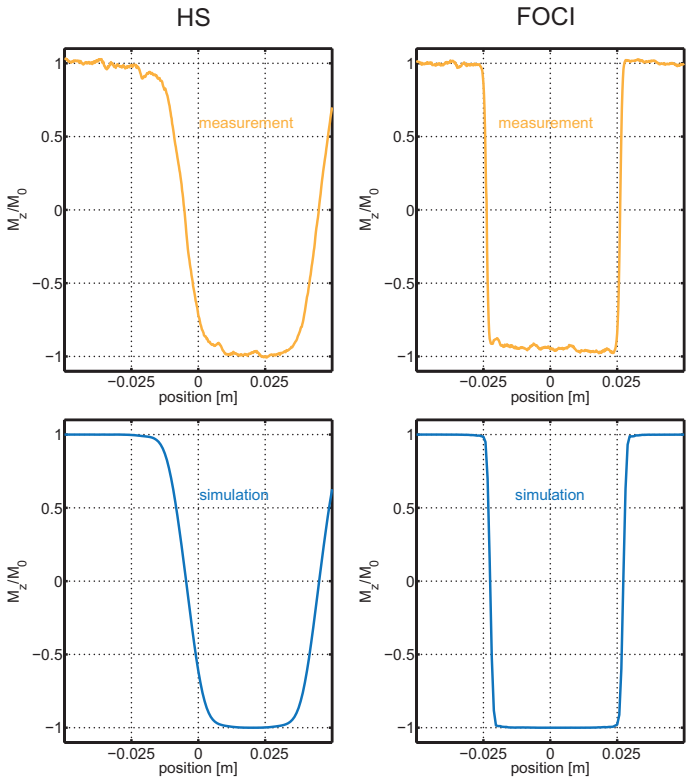

Figure 4.19: *Off-resonance effects on the slice profiles of HS and FOCI pulses. For measurements (upper row) and simulations (lower row) an off-resonance frequency of 400 Hz was used. Compared to the on-resonant slice profiles for the same pulse parameters (cf. Figure 4.16) the profiles are shifted. The shift is much larger for the HS pulse.*

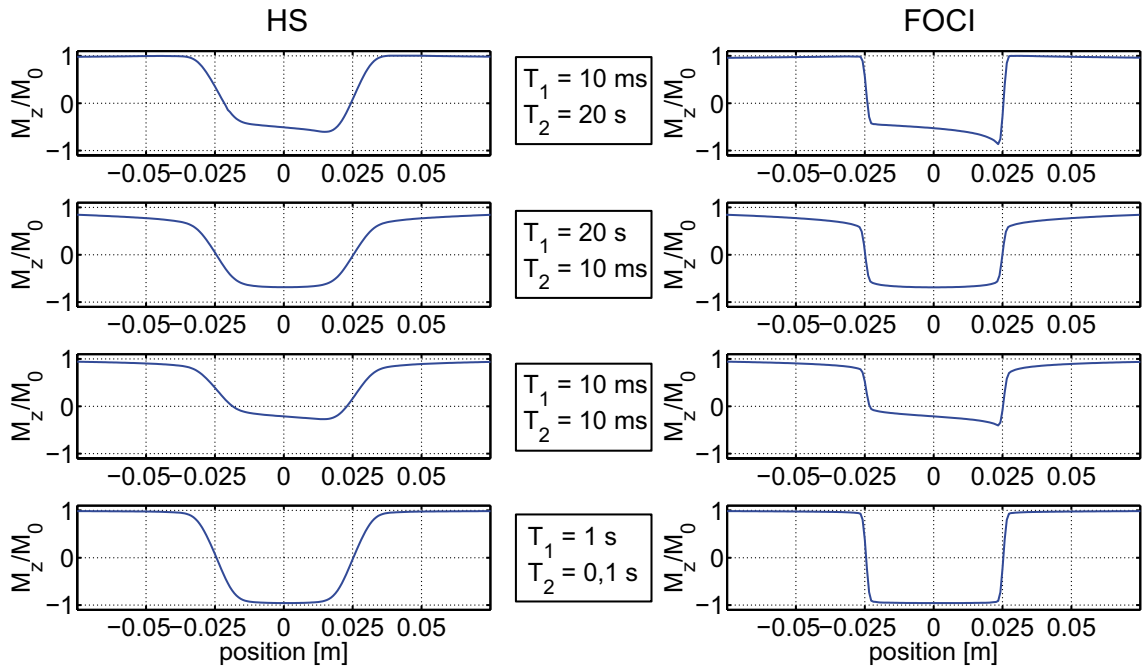

Figure 4.20: *Effects of longitudinal and transversal relaxation on simulated slice profiles of HS and FOCI pulses. The two upper rows demonstrate the impact of longitudinal relaxation (first row) and transversal magnetization (second row), respectively. The third row shows a combination of both. The lower row shows profiles for realistic relaxation times. HS and FOCI pulse parameters are the same as in Figure 4.16.*

4.2.2 Dual-Band Adiabatic Inversion

For certain applications, it might be useful to simultaneously invert two parallel slices. In small flip angle regime, the excitation of two slices with one RF pulse can be achieved by modulating the B_1-amplitude with a cosine (cf. Section 3.5.3). In this section results are presented, which show that the same approach can be used to achieve a dual-band adiabatic inversion.

Modulation

A FOCI pulse with $T_{\text{pulse}} = 10.24\,\text{ms}$, BW $= 1000\,\text{Hz}$ and $B_{1,\text{trunc}} = 0.5\,\%$ was calculated with $F = 5$. The slice thickness was set to 30 mm leading to a maximum gradient amplitude of 3.9 mT/m. The B_1 envelope was modulated according to Equation (3.5.3) to invert two slices whose centers are separated by 50 mm. The B_1 amplitudes of unmodulated and modulated pulse are displayed in Figure 4.21.

VERSE-Transformation

Dual-band pulses require twice the B_1 amplitude of single-band pulses (cf. Equation (3.76)) to achieve the same flip angle. For adiabatic pulses this means that the adiabatic threshold is twice as high and the maximal B_1 should be increased. In case, the maximal coil voltage was VERSE-transformed using an analytical scaling function (cf. Section 3.5.2) with $A = 0.6$ and $t = 0.069$. On the condition that the pulse duration was conserved this resulted in $B = 4.73$. Figure 4.22 depicts the scaling function as well as B_1 amplitude, off-resonance and gradient of the transformed pulse. For a better comparison the scaling of the B_1 amplitude in Figure 4.21 and Figure 4.22 is identical. Both the original and the VERSE-transformed dual-band pulse were implemented in the slice profile sequence and the simulation. The resulting slice profiles are shown in

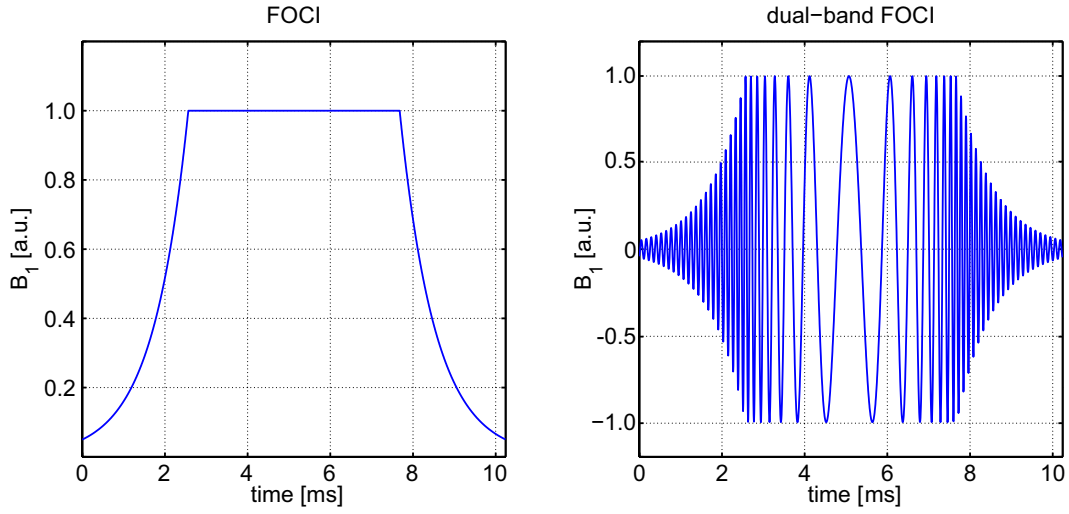

Figure 4.21: *B_1 envelope of the FOCI pulse (left) and the according dual-band pulse (right) used to invert two parallel slices. In practice, negative B_1 values are realized by a phase shift of π and the usage of absolute values.*

Figure 4.23. In the central 80% of the slice profiles the mean longitudinal magnetization of both slices was -0.987 ± 0.010 and -0.984 ± 0.010 for the measurement and the simulation of the VERSE-transformed pulse. The same values for the non-transformed pulse were -0.752 ± 0.103 and -0.753 ± 0.103 for measurement and simulation.

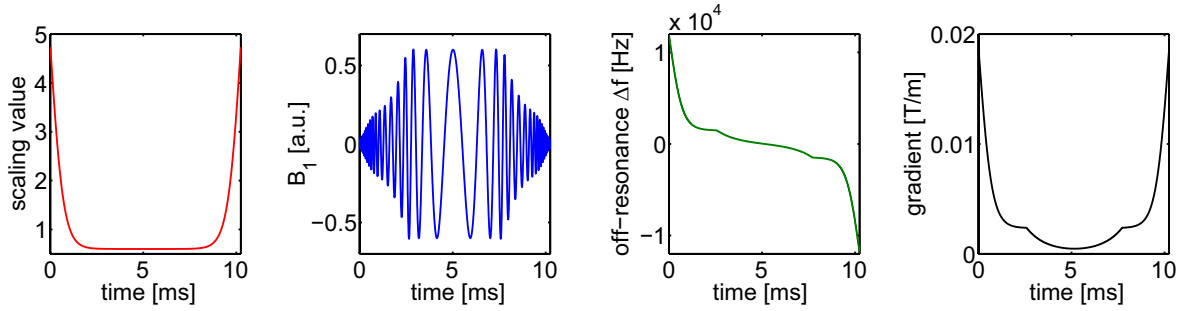

Figure 4.22: *Analytical scaling function (red) used for VERSE transformation of a dual-band FOCI pulse. B_1 amplitude (blue), off-resonance (green) and gradient (black) of the transformed pulse are shown. The scaling of the B_1 amplitude is identical to Figure 4.21 and shows the reduction of the maximal amplitude to 60 % of the original value.*

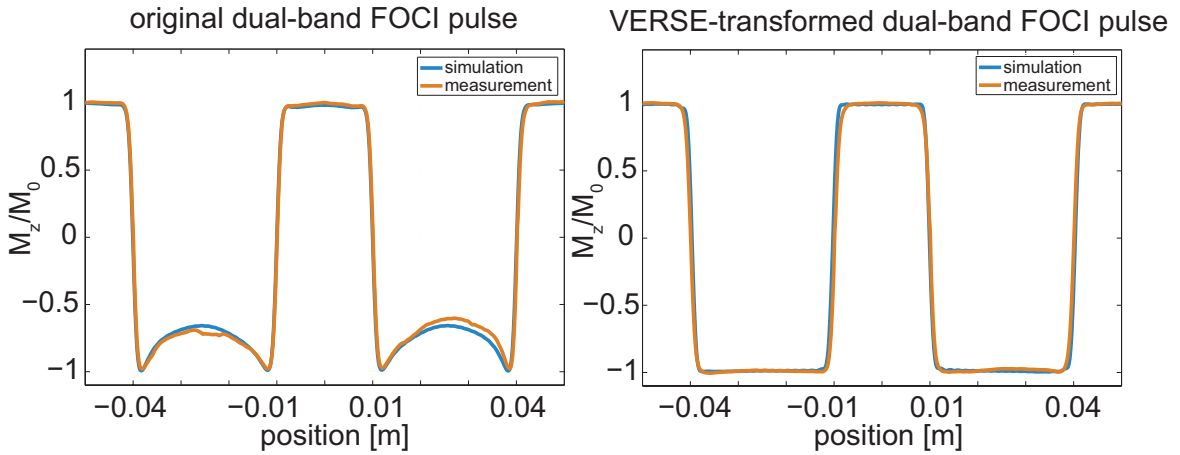

Figure 4.23: *Slice profiles of measurement and simulation of a non-transformed (left panel) and a VERSE-transformed (right panel) dual-band FOCI pulse. The profiles of the original pulse indicate that the adiabatic condition was not met.*

4.3 3D ASL Measurement

An optimized 3D FAIR ASL sequence was developed and used for perfusion measurements in the brain. Optimized parameters of the individual features are presented. Finally, the results of whole-brain quantitative perfusion measurements are shown.

4.3.1 Development of an Optimized 3D FAIR ASL Sequence

The optimized 3D FAIR ASL sequence includes several features. Pre- and post-labeling saturation was implemented, as well as a background suppression and Q2TIPS saturation pulses to define the length of the blood bolus. For data acquisition a 3D TrueFISP sequence was used. The results of the optimization of each feature is presented in the following. Figure 4.24 shows the scheme of the sequence.

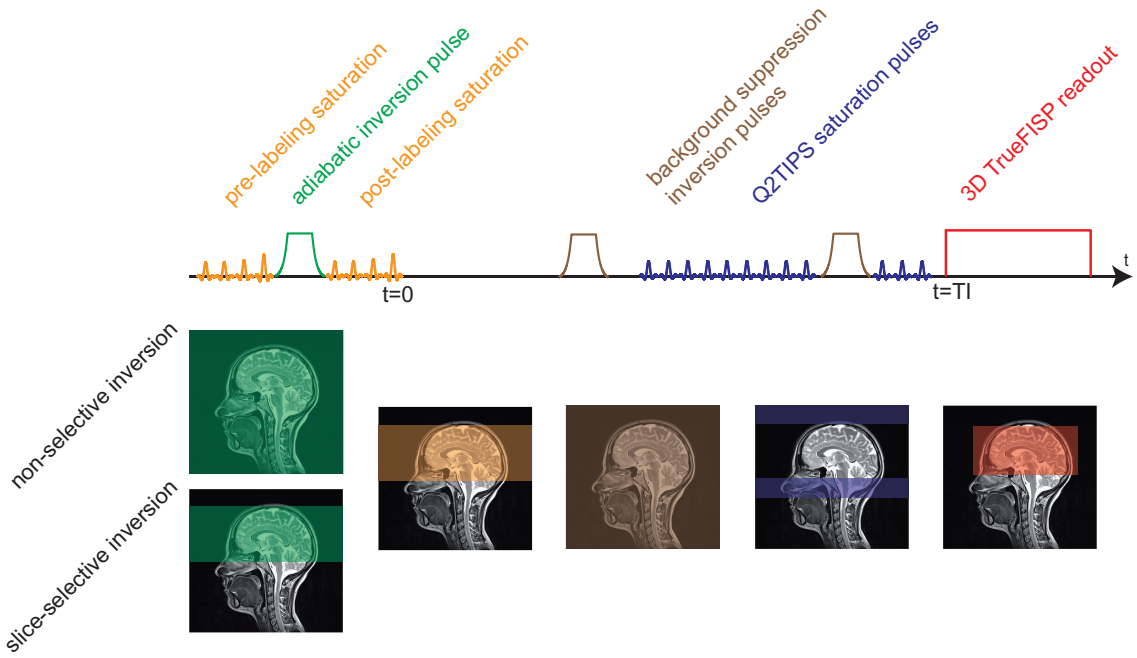

Figure 4.24: *Scheme of the optimized 3D FAIR ASL sequence including pre- and post-labeling saturation, background suppression, Q2TIPS saturation and the 3D TrueFISP readout module. Figure adapted from Gregori [2009].*

Pre-Saturation

The pre-saturation of the imaging volume was accomplished by using the WET saturation scheme. Each pulse had a length of 5.12 ms followed by spoiler gradients with durations of 7 ms. In order to avoid coherences, gradient cycling was used, i.e. polarization, gradient amplitudes and gradient axes where different for each pulse. Gradient amplitudes of 12 mT/m, 18 mT/m and 24 mT/m were used. An optimized set of flip angles was calculated to [68.2°; 72.2°; 77.1°; 117.3°]. Figure 4.25 shows the calculated residual magnetization after WET saturation for a range of T_1 values and deviations from the nominal flip angles. By using SLR pulses, the excitation profiles of the single pulses could be improved compared to the performance of conventional *sinc*-shaped pulses. The SLR pulse generated for the 117° pulse of the WET scheme is shown in Figure 4.26, which additionally shows the simulation of its excitation profile. All pulses had a bandwidth of 3000 Hz. To reduce the SAR, all pulses were VERSE-transformed using a two-speed VERSE approach with $s_{\text{slow}} = 0.35$ and $t_{\text{slow}} = 0.8$. Further, the risk of an insufficient maximal coil voltage and the resulting flip angle deviation, i.e. RF clipping, was avoided.

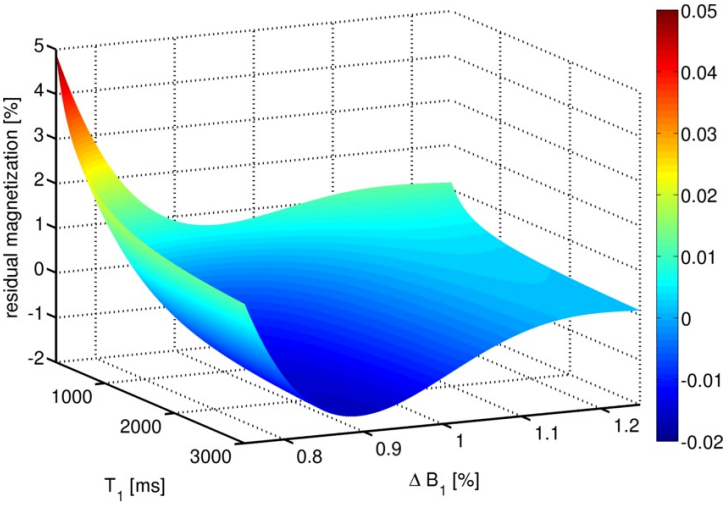

Figure 4.25: *Residual magnetization after WET saturation for different longitudinal magnetizations and varying B_1 fields. The deviation from the nominal B_1, i.e. flip angles, was assumed to be identical for all four pulses. The image shows that WET saturation can achieve a very good signal suppression over a broad range of T_1 and B_1 values.*

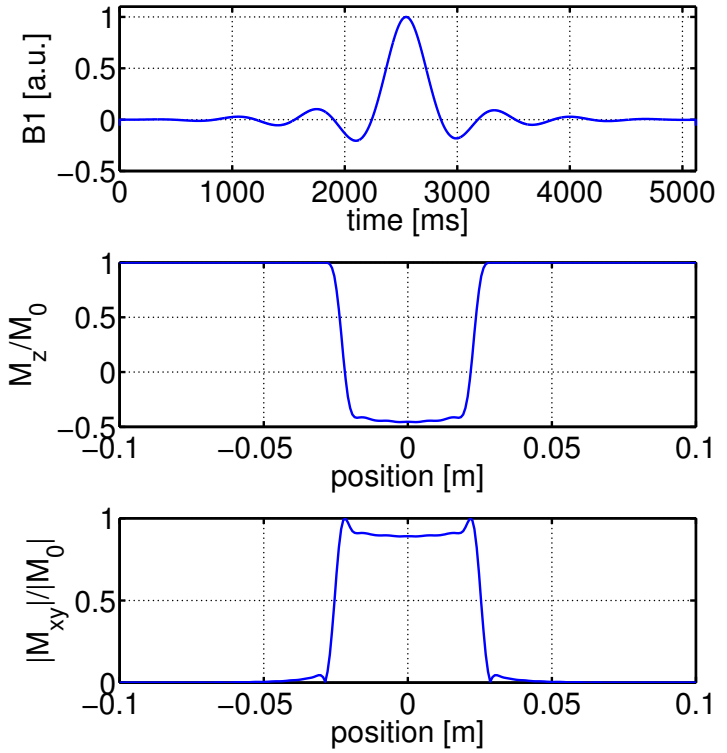

Figure 4.26: *SLR pulse generated for the WET saturation scheme. The pulse was optimized for a flip angle of 117°. The B_1-field (upper row) and simulations of the longitudinal magnetization (middle row), and the signal (lower row) are displayed.*

Adiabatic Inversion

Based on the results of measurements and simulations shown in the previous section, a FOCI pulse was employed for global (control) and slice-selective (tag) inversion. The pulse parameters were $T_{\text{pulse}} = 10.24\,\text{ms}$, $\text{BW} = 1000\,\text{Hz}$, $B_{1,\text{trunc}} = 0.5\,\%$ resulting in the HS parameters $\mu = 2.68$ and $\beta = 1171$. A FOCI factor of $F = 10$ was used. The thickness of the slice-selective inversion has to be chosen larger than the imaging volume to account for an imperfect slice profile. To estimate the minimal inversion slice thickness for the used inversion pulse, a cylindrical water phantom was imaged with a 3D TrueFISP after slice-selective (ssIR) and non-selective inversion (nsIR), respectively.

The imaging volume had a thickness of 130 mm, the slice-selective inversion pulse inverted a central slab of 50 mm. Overall, 52 slices, orientated parallel to the inversion slab were imaged. The slice thickness was 2.5 mm. The nsIR image of each slice was subtracted from the corresponding ssIR image. Mean values and standard deviations of the difference images were extracted. To show the advantage of the FOCI pulse over its HS equivalent with respect to ASL, the experiment was repeated with its HS counterpart. The results are displayed in Figure 4.27. The regions with signal differences smaller than 0.01 had a thickness of 40 mm and 22.5 mm for FOCI and HS pulse, respectively. Compared to the nominal slice thickness of 50 mm, this indicates that the FOCI inversion slice should be at least be chosen 10 mm thicker than the imaging volume. For the HS pulse, the nominal thickness should be increased by 27.5 mm.

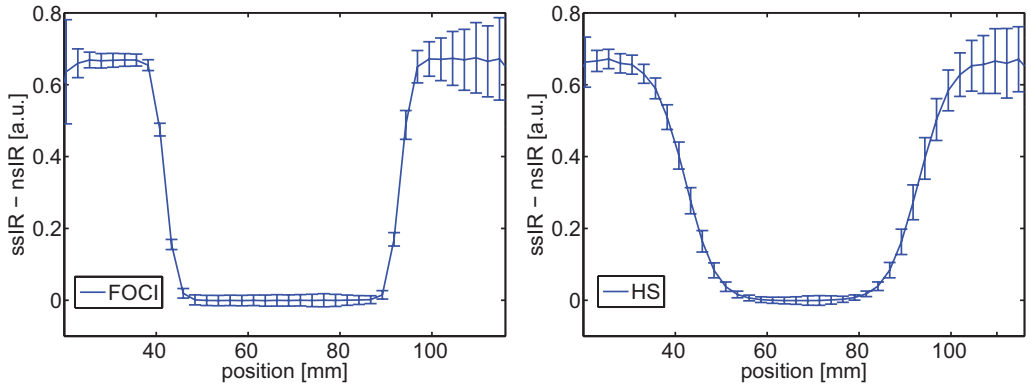

Figure 4.27: *Determination of the minimal inversion slice thickness for 3D FAIR ASL. 52 slices à 2.5 mm were imaged after a slice-selective inversion (ssIR) of 50 mm and after global inversion (nsIR), respectively. Mean and standard deviation of the signal differences between ssIR and nsIR are plotted over the position of the slice. On the left-hand side, the results for the FOCI pulse are shown, the right-hand side displays the results for the HS equivalent.*

Background Suppression

Background suppression (BS) to null the signal of gray and white matter at the beginning of data acquisition was implemented. The necessary saturation was achieved by the application of a WET saturation scheme right after the labeling pulse. The scheme was identical to that used for pre-saturation. Depending on TI, the timing of the inversion pulses was calculated numerically. The longitudinal relaxation times used were $T_{1,\mathrm{GM}} = 1640\,\mathrm{ms}$ and $T_{1,\mathrm{WM}} = 920\,\mathrm{ms}$ [Krämer, 2014] for gray and white matter, respectively. For an inflow time of $\mathrm{TI} = 1800\,\mathrm{ms}$, the inversion times of the pulses were calculated to 1151 ms and 308 ms. In the actual ASL measurement, the zero-crossing was calculated to occur 100 ms prior to the readout leading to inversion pulses applied 1094 ms and 295 ms before data acquisition. This way, errors in the ΔM image due to different algebraic signs (indistinguishable in the magnitude images) of the magnetization in tag and control image, were avoided. Figure 4.28 shows tag,

control, and the resulting ΔM image of the same ASL experiment, once with the usage of BS and once without. Due to the high tissue signal relative to the perfusion signal, the ΔM image without BS is very noisy and shows an erroneous perfusion signal.

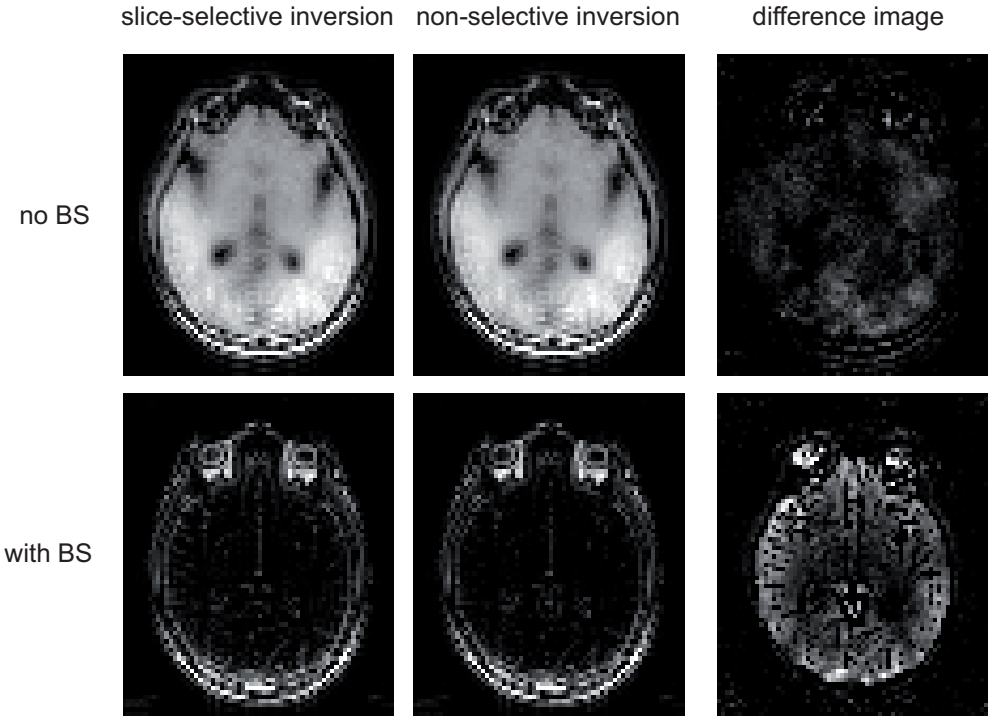

Figure 4.28: *Reduction of gray and white matter signal by using background suppression. Exemplary images of a transversal slice of a 3D ASL data set of the brain after slice-selective (left) and non-selective inversion (middle). The corresponding perfusion-weighted images are displayed on the right side. The upper row shows the data acquired without, the lower row the data acquired with background suppression. For a fair comparison, the colorscale of tag and control images and difference images is identical, respectively. Due to the high tissue signal relative to the perfusion signal, the ΔM image without BS is very noisy and shows an erroneous perfusion signal.*

Q2TIPS

To avoid quantitation errors due to different delay times, the length of the blood bolus was defined by using Q2TIPS. To achieve a bolus of length T, saturation pulses were applied outside the imaging volume at a time T after the post-labeling saturation. The saturation pulses were periodically applied until the beginning of the data acquisition, i.e. $t = \mathrm{TI}$. If necessary, they were interrupted for the global inversion pulses of the background suppression. All saturation pulses had a length of 5.12 ms and were followed by spoiler gradients with durations of 7 ms. Like for the WET saturation scheme, gradient cycling was used to avoid coherences by rephasing the magnetization. The flip angle of all saturation pulses was set to 90°, their bandwidth was 2000 Hz. To allow for a positioning close to the imaging volume, the slice profile of the RF pulses was optimized using SLR pulses. In addition, the RF envelope of the pulses

was modulated to allow for a dual-band saturation of both the distal and the proximal side of the imaging volume. The dual-band approach has the advantage that both the labeled blood bolus is truncated and signal contributions from inflowing venous blood are reduced. Further, any signal from outside the imaging volume is saturated when the readout module starts. This way infolding artifacts are avoided. The peak amplitude of the B_1-field of the dual-band pulses has to be twice as high as for the single-band pulses to conserve the nominal flip angle. Therefore, all pulses were VERSE-transformed using the two-speed approach with $s_{\text{slow}} = 0.35$ and $t_{\text{slow}} = 0.7$. Figure 4.29 shows the RF envelope and the excitation profile of the dual-band VERSE-transformed RF pulse used for Q2TIPS saturation.

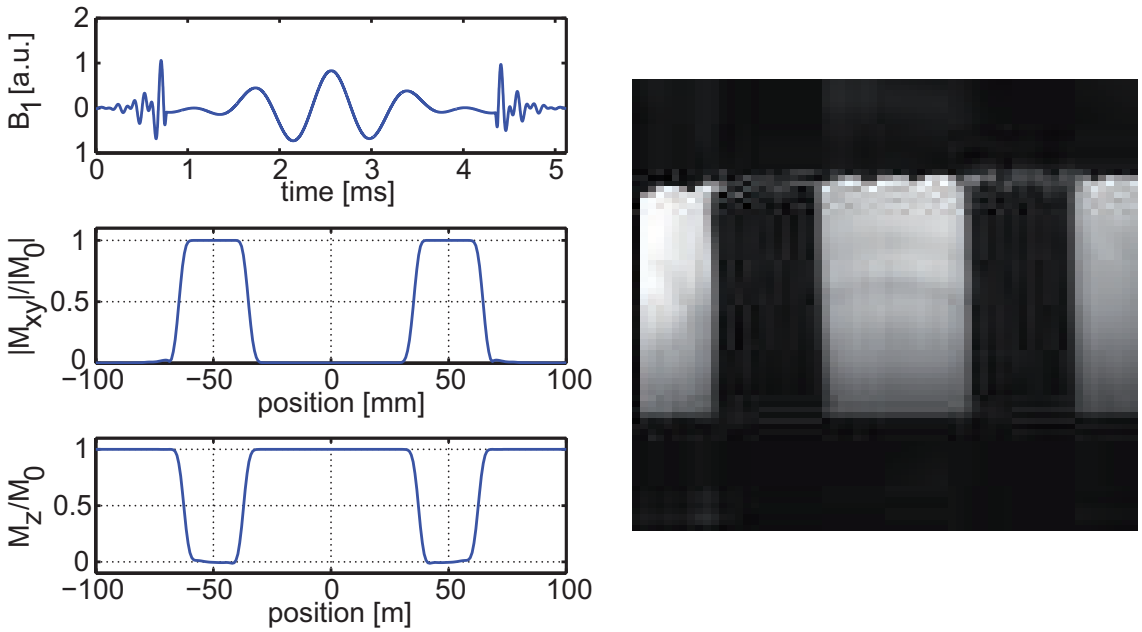

Figure 4.29: *RF envelope, excitation profile and application of the dual-band VERSE-transformed SLR pulse as used for bolus truncation with Q2TIPS. The B_1-field (upper row), as well the longitudinal magnetization (middle row) and the signal (lower row) are displayed. The pulse excites to 30 mm slices whose centers are separated by 100 mm. The image of the right-hand side shows the successful application in a water phantom.*

Read-Out Module

All data were acquired using a 3D TrueFISP readout. To reduce signal oscillations during the transient state, the flip angles of the first ten excitation pulses followed a Kaiser-Bessel function. The results of the simulation of the signal evolution using the Kaiser-Bessel ramp is shown in Figure 4.30. A spiral-reordering scheme was used to record the contrast information in k-space center first. To accelerate the image acquisition GRAPPA was used in one phase-encoding directions. A further reduction of the readout time was possible by using partial fourier (PF), i.e. recording only a certain fraction of k-space and utilizing its symmetry.

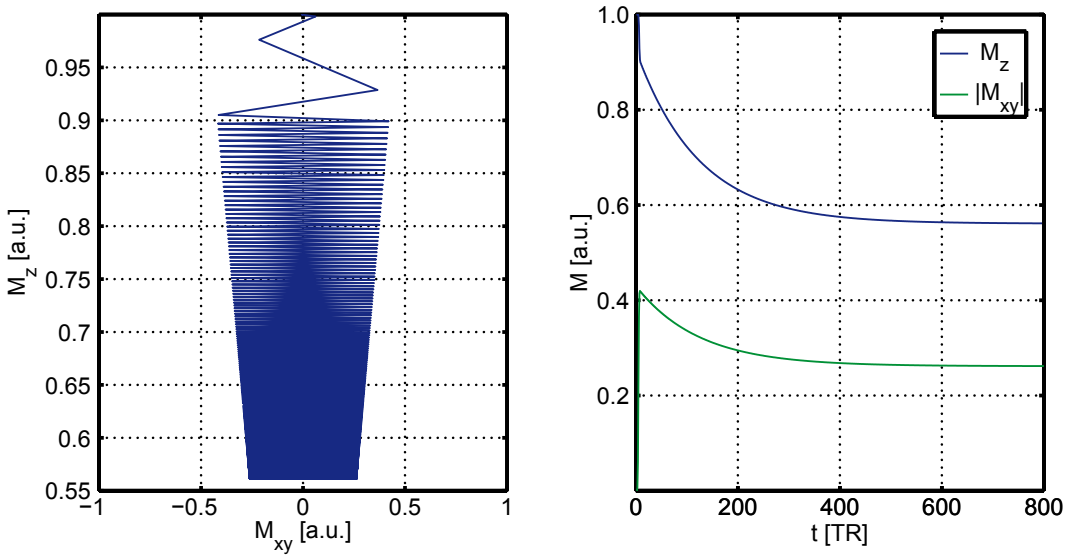

Figure 4.30: *Evolution of magnetization during the TrueFISP sequence when using a Kaiser-Bessel ramp for magnetic preparation. The left panel shows the simulation of the longitudinal magnetization plotted against the transversal magnetization. The increasing flip angel during the first ten excitations can clearly be seen. The simulation of the temporal development of z-magnetization and signal are plotted in the right panel. Both show the first 800 TR-intervals. Due to the Kaiser-Bessel ramp no signal oscillations are present and the signal follows a smooth trend towards its steady-state value.*

4.3.2 3D Brain Perfusion Measurement

The 3D FAIR ASL sequence described above was used to measure brain perfusion on a voxel-wise basis. The imaging volume had a size of $100 \times 237 \times 200\,\text{mm}^3$ (head-feet, anterior-posterior, left-right). By using an imaging matrix of $32 \times 76 \times 64$ an isotropic resolution of 3.1 mm was achieved. The slice-selective inversion pulse had a width of 120 mm and was centered around the imaging volume. The identical slice was used for pre- and post-labeling saturation. The Q2TIPS saturation bands had a thickness of 30 mm, with their centers separated by 160 mm. They were positioned symmetrically around the imaging volume. The imaging parameters of the TrueFISP sequence were: TE/TR = 1.5 ms/3 ms, bandwidth = 801 Hz/px, flip angle = 45°, GRAPPA factor = 2 and PF = 6/8, which lead to a readout time of 8 s. A healthy volunteer was placed head-first supine into the scanner. Prior to the ASL measurement, an M_0 volume was recorded by using the identical 3D TrueFISP readout as for the ASL measurement. No magnetic preparation was used, however, 5000 *TR* intervals were preceding the beginning of k-space sampling. This ensured the steady-state of the magnetization during data recording. During the ASL measurement, 30 tag-control pairs were acquired. A *TI* of 1800 ms was chosen. The timing of the Q2TIPS saturation was such that the labeled bolus had a length of 800 ms. The time between adjacent measurements was set to 8 s to ensure a complete relaxation of blood and tissue magnetization. The overall acquisition time was about 18 min including the M_0 measurement. Data were averaged

according to their magnetic preparation. Afterwards, the perfusion-weighted data ΔM was calculated by subtracting control from control from tag volume. Transversal slices were reconstructed from ΔM and are displayed in Figure 4.31. To calculate absolute perfusion values, Equation (3.23) was applied on a voxel-wise basis using the following values: $\lambda = 0.9\,\mathrm{g/ml}$ [Herscovitch and Raichle, 1985], T_1=1.5 s [Lu et al., 2004] and $\alpha = 1$. $M_{0,\mathrm{T}}$ was calculated from the M_0 volume by using Equation (3.13). For gray matter $T_{1,\mathrm{GM}} = 1640\,\mathrm{ms}$, $T_{2,\mathrm{GM}} = 61\,\mathrm{ms}$ and for white matter $T_{1,\mathrm{WM}} = 920\,\mathrm{ms}$, $T_{2,\mathrm{WM}} = 42\,\mathrm{ms}$ [Krämer, 2014] were used. Figure 4.32 shows a coronal, sagittal and transversal slice through the 3D perfusion map. Additionally, the corresponding slices of the 3D M_0 volume are shown. To asses the absolute perfusion values of gray and white matter, two ROIs were put in the transversal slice shown in Figure 4.32. The mean value and the standard deviation are $f_{\mathrm{GM}} = (51 \pm 17)\,\mathrm{ml/100\,g/min}$ and $f_{\mathrm{WM}} = (24 \pm 8)\,\mathrm{ml/100\,g/min}$ for gray and white matter, respectively.

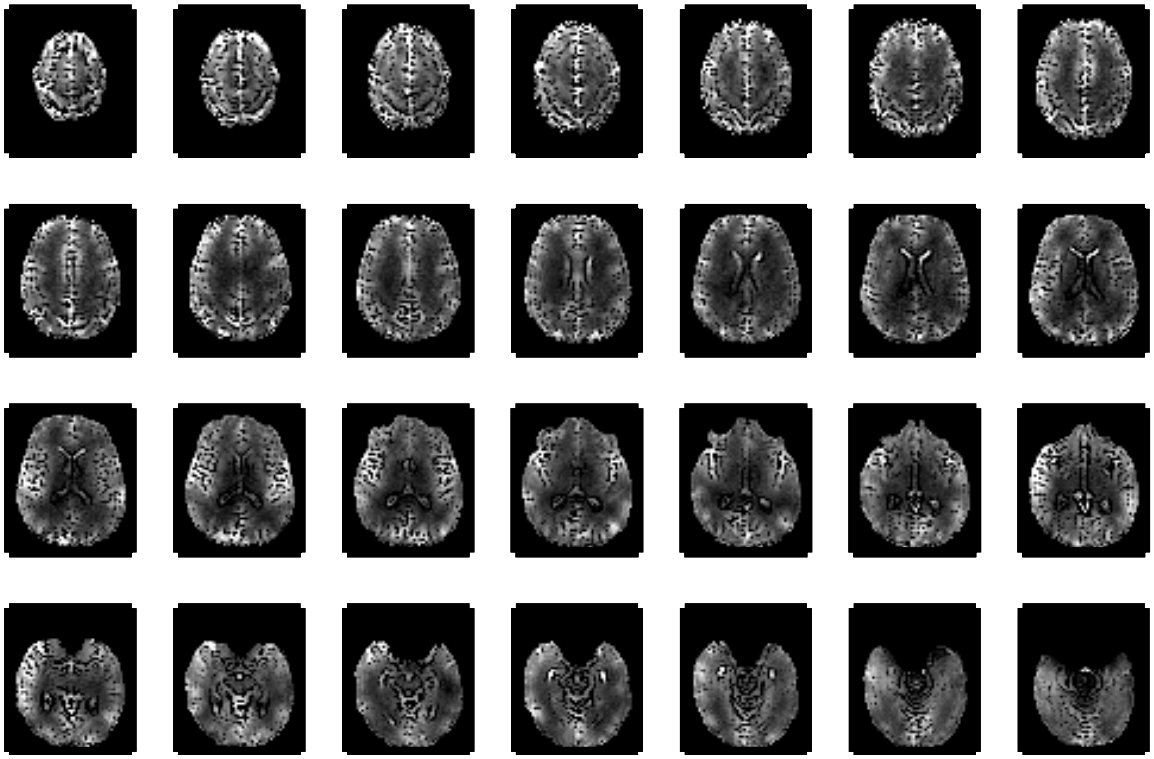

Figure 4.31: *Perfusion-weighted images of 28 transversal slices reconstructed from the 3D ASL data set of the brain.*

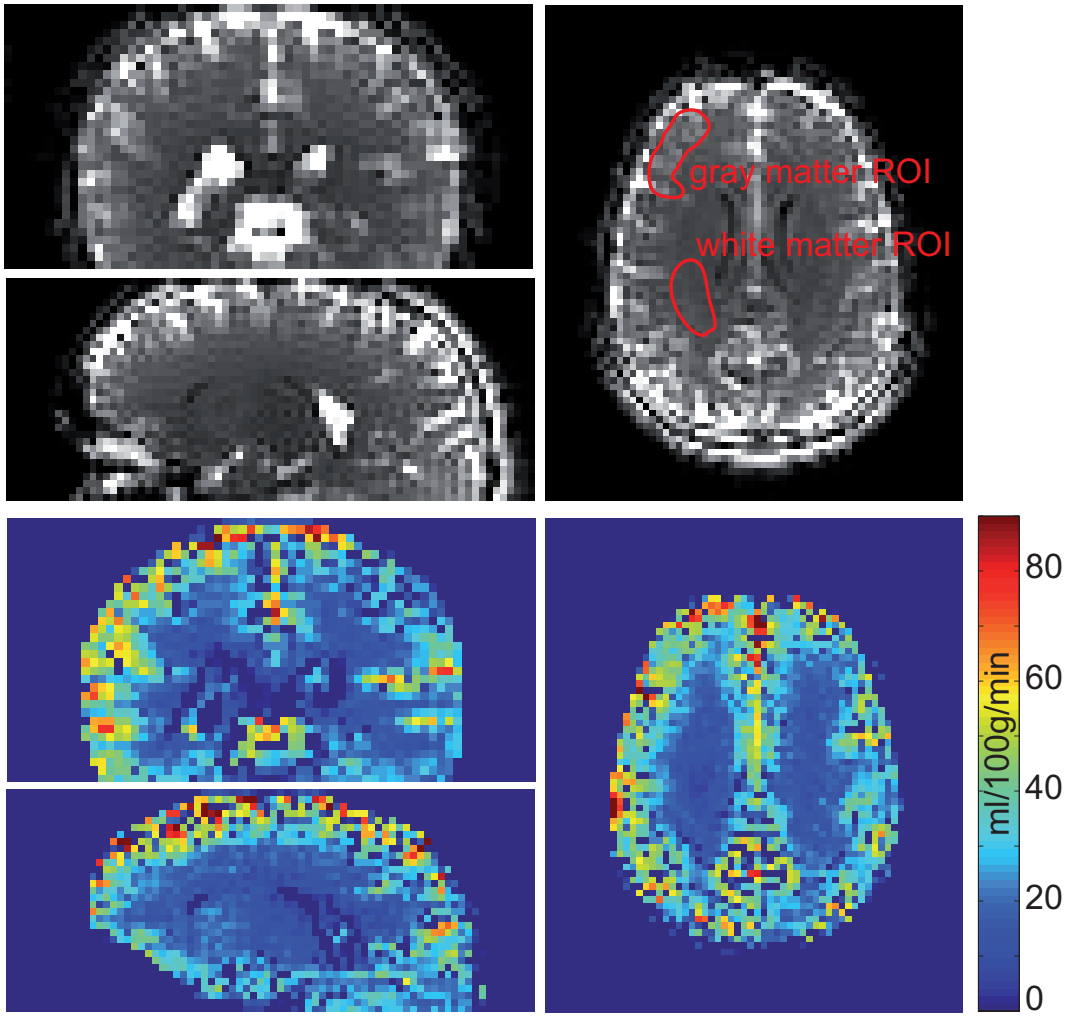

Figure 4.32: *Coronal, sagittal and transversal slice through the M_0 volume (upper images) and the corresponding 3D perfusion maps (lower images). To assess absolute perfusion, ROIs have been drawn in the transversal slice of the M_0 data, depicting grey and white matter,respectively. The obtained mean perfusion values and standard deviations are $f_{\mathrm{GM}} = (51 \pm 17)\, ml/100\, g/min$ and $f_{\mathrm{WM}} = (24 \pm 8)\, ml/100\, g/min$ for gray and white matter, respectively.*

5 Discussion

In this chapter, the results presented in Chapter 4 are discussed. First, the establishment of the 2D ASL technique for renal perfusion measurements in small animals on a whole-body MR tomograph, then the three studies measuring renal blood flow in rats are reviewed. The initial study with the comparison to DCE-MRI as well as the investigation of renal blood flow in acute kidney injury and two different models of graft rejection are covered. Subsequent, the design, simulation and experimental evaluation of sophisticated adiabatic inversion pulses for pulsed ASL are discussed. Finally, the results of the 3D ASL sequence are argued. This last part includes the discussion of results concerning the implemented features, as well as the results of quantitative perfusion measurements.

Renal Perfusion MRI in Animal Models

For all ASL measurements of renal perfusion in small animals, a work-in-progress (WIP) sequence provided by Siemens was used. The sequence was originally designed for the perfusion measurement in human kidneys. A great disadvantage of the sequence was the unavailability of its source code. Thereby, the access to parameters and sequence limits was restricted to those accessible through the sequence card. Unfortunately, this excluded pulse parameters like bandwidth and duration or sequence limits like the minimal slice thickness of imaging or inversion slice. Anyway, to adapt the sequence to measure renal perfusion in rats, the accessible parameters needed to be optimized. In preliminary measurements, two properties of the sequence that are essential for reliable quantitative and qualitative perfusion measurements were verified and estimated.

The inversion efficiency could be estimated to 0.99 ± 0.03 and proofed the good performance of the RF pulse. The standard deviation of this value is mainly related to noise which could not be decreased due to inaccessible sequence parameters. Further, by choosing a large region of interest when estimating the efficiency, also its homogeneity was tested. Regarding the small standard deviation, the inversion can be considered homogeneous. The knowledge of the inversion efficiency and homogeneity is crucial for the quantitation as the absolute perfusion is inversely proportional to it. Furthermore, the perfusion signal of ASL depends on T_1-relaxation. Therefore, the signal loss, dur-

ing the time it takes for the labeled blood to reach the capillary bed of the tissue of interest, has to be minimized. Hence, as the T_1-relaxation of blood is not reducible, the labeling of the arterial blood should be as good as possible to prevent further losses of the small perfusion signal. Besides, the completeness and the homogeneity of the inversion, the transition zones between uninverted and fully inverted magnetization are important and should be as narrow and steep as possible. For example, in a FAIR ASL experiment, broad transition regions of the slice-selective inversion lead to signal loss or erroneous perfusion estimates. The reason therefore is that this shortcoming has to be compensated by choosing the inversion slice thickness significantly larger than the imaging slice which increases the bolus arrival time. In case, this deficiency of the slice-selective inversion pulse is not accounted for, perfusion will be overestimated as the signal in the difference image ΔM will not null, even in the perfusion-free case. In practice, no selective inversion pulse will produce an ideal rectangular profile. This implies that for the FAIR labeling scheme the slice thickness of the inversion always has to be chosen larger than the imaging slice. As previously discussed, the ratio between inversion and imaging slice thickness should be chosen as small as possible to decrease the bolus arrival time, however as large as necessary to guarantee a complete inversion of the imaging region. This ratio cannot be estimated from the inversion profile but has to be measured separately. In the preliminary experiment, tag-control pairs for 13 different ratios were recorded. To guarantee an identical initial situation with the magnetization in thermal equilibrium, an inter-image time of 18 s was chosen in accordance with the T_1 relaxation time of the phantom. The result of the measurement suggests to use a ratio of 1.5. However, one has to consider that this value was gained from a measurement under ideal conditions. In practice, the ratio might be chosen larger to compensate motion-induced displacements.

In the initial study, ASL was successfully established to measure and quantitate renal perfusion in small animals on a whole-body scanner. To compare the results to a different MRI method, absolute values of renal perfusion were additionally estimated with DCE-MRI. Further, an animal model of acute kidney injury, known to decrease renal function was used to test the diagnostic significance of both methods. Part of this discussion can also be found in Zimmer et al. [2013]. The adjustable inversion pulse parameters of the ASL sequence were set to the values estimated in the preparative measurements. In accordance with the preliminary measurement a thickness ratio of inversion to imaging slice of 2 was used. This ensured a complete inversion of the imaging slab and reduced the risk of a displacement of the imaging slab relative to the inversion volume during the respiratory cycle of the rat. The quality of both ASL and DCE-MRI data sets was found to be very good and allowed a pixel-wise estimation of absolute renal perfusion values. Histological slides evaluated after the experiment showed pathological findings that confirmed the impaired function of the AKI kidneys. Compared to the native kidney the diseased kidneys showed main hallmarks of AKI like cellular swelling, necrosis and tubular dilatation. The result showed that both methods of perfusion measurement provide significantly different results when comparing the perfusion of healthy kidneys and kidneys with ischemic AKI. This proofs that ASL and DCE-MRI can detect the decreased perfusion of a kidney with AKI compared to a healthy kidney. The findings of the t-test are confirmed by the Bland-Altman

plots, which also exclude the dependency of the differences on the mean RBF values. The mean differences of ASL and DCE-MRI estimates between healthy and diseased kidneys are in very good agreement when averaging over all rats. When comparing the relative RBF values of healthy to AKI kidneys, the ratios are in good agreement between both methods and the healthy animal can be well distinguished from the other animals. Further, no significant differences in the absolute estimates of both methods was found when applying a paired t-test. The robustness of the ASL estimates was confirmed by repeated measurements that were conducted in two animals. The results indicate that the variability of the findings within one animal are small and unlikely to represent outliers. This provides evidence for the validity of the results despite the small sample size of only five animals with diseased kidneys. Repeated DCE-MRI measurements were not possible, as it would have taken too long for the animals to wait for a sufficient clearance of the contrast agent before starting a new measurement. However, the constant offset of the DCE-MRI estimates relative to the ASL estimates strengthens the validity of the DCE-MRI values. Nevertheless, the sample size was increased for the following studies.

In the studies of Winter et al. [2011]; Wu et al. [2011]; Cutajar et al. [2014] the estimates of quantified renal perfusion from ASL and DCE-MRI are directly compared. However, solely perfusion values of healthy kidneys were assessed and the studies do not allow to test the diagnostic significance of the respective method. Winter et al. [2011] report an average cortical RBF of $(328 \pm 59)\,\mathrm{ml/100\,g/min}$ (ASL) and $(357 \pm 96)\,\mathrm{ml/100\,g/min}$ (DCE-MRI). Perfusion was assessed in healthy rabbit kidneys on a 1.5 T scanner. The ASL findings are similar to the presented values for the healthy kidneys ($(416 \pm 124)\,\mathrm{ml/100\,g/min}$), however RBF estimates from DCE-MRI are clearly lower than in our study. In contrast to the presented study, the RBF of only one kidney per animal was assessed. The study of Wu et al. [2011] reports ASL and DCE-MRI estimates from nineteen healthy humans and investigates the correlation between the two modalities. Similar to the presented results, they found systematically higher DCE-MRI values that were not entirely comparable to the ASL estimates. Cutajar et al. [2014] imaged sixteen healthy volunteers and found a good agreement between ASL and DCE-MRI. A study that investigated renal perfusion in rats with unilateral arterial occlusion (RAS) was performed by Pedersen et al. [2010]. They measured hemodynamic parameters of the kidneys with dynamic susceptibility-weighted (DSC)-MRI using ultra small superparamagnetic iron oxide (USPIO) particles. RBF of 14 animals was measured and led to a mean cortical perfusion of $431\,\mathrm{ml/100\,g/min}$ and $410\,\mathrm{ml/100\,g/min}$ in the healthy and RAS kidneys, respectively. The findings in the healthy kidneys are in good agreement with the presented ASL estimates.

A second study on AKI rats with an increased number of animals was conducted to confirm the results of the first study and to improve the statistics. The primary goal was the detection of perfusion differences between healthy and AKI kidneys and the confirmation of the results of the initial study. Based on the findings of the initial study where both methods detected the expected differences between healthy and diseased kidneys, solely ASL was used to estimate renal perfusion. The decision was supported by the fact that the mean differences of ASL and DCE-MRI estimates between healthy

and diseased kidneys were in very good agreement when averaging over all rats. Further, no significant differences in the absolute estimates of both methods were found. The repeated ASL measurements indicated that the variability of the ASL findings within one animal are small and unlikely to represent outliers. The measurement of all fourteen rats with unilateral AKI were successful and showed the necessary image quality for a pixel-wise quantitation. The evaluation of the perfusion estimates yielded significantly different perfusion estimates for healthy and AKI kidneys, which confirmed the results of the initial study. The differences in RBF are well reflected in the Bland-Altman plot. The fact that the difference of zero is not included in the limits of agreement (± 1.96 standard deviations of the average difference) supports the findings of the paired t-test. Further, no dependency of the differences on the means is visible in the plot. All RBF ratios between AKI and healthy kidneys are all smaller than one and besides animal number five, a value of one is not even included in the standard deviation of the ratios. The mean RBF of the diseased kidneys is slightly higher than the estimate from the initial study. Regarding the standard deviations of the samples and the larger sample size of this study, the values are compatible. A very good agreement between the two studies is found for the mean perfusion of the AKI kidneys. The comparison of the results to related studies published in literature is identical to the discussion of the initial study. In a further, directly related study that was recently published, Hueper et al. [2014] used ASL to measure renal perfusion in mice with moderate and severe unilateral AKI. The authors compare renal perfusion before and at five time points after surgery. Seven days after surgery, they found significantly reduced RBF values for both cases. This is in agreement with our study.

In a third study, renal perfusion was measured in rats with a renal graft. Animals were either imaged seven days or six months after surgery, when an acute and a chronic transplant rejection was expected, respectively. As the rats were nephrectomized prior to receiving the donor organ, no control group was available. Due to the lack of an intra-animal control the sample size was increased compared to the AKI studies. Overall, 23 rats with acute and 20 animals with chronic rejection were imaged without incidents. The gained data were of good quality and perfusion maps could be calculated for all subjects. The application of a two-sample t-test revealed that absolute perfusion is significantly different in the two models. Thereby, the mean cortical blood flow in kidneys seven days after surgery was found to be lower than in the models of chronic rejection. This difference is also visible in the presented boxplot. The comparison of the results to the findings of the previously presented studies, shows that the mean RBF in both rejection models is lower than in the healthy kidneys of the AKI models. This leads to the conclusion that the renal grafts are generally impaired, also six month after surgery. First measurements of renal perfusion in transplanted kidneys with ASL were presented by Lanzman et al. [2010]. The authors report significant differences in cortical perfusion between stable/good allograft function and patients with an acute deterioration of renal function. This is in agreement with the presented results that show a lower renal perfusion in grafts with acute rejection. Artz et al. [2011b] used ASL to measure RBF in healthy and transplanted kidneys and found that cortical perfusion is higher in native kidneys compared to transplanted kidneys with a good function, which supports the finding that cortical perfusion in renal transplants is generally

lower than in native kidneys.

Regarding the presented perfusion estimates, the two AKI studies suggest that both DCE-MRI and ASL detect the hypoperfusion of the injured kidney and show significantly different values for normal kidneys compared to diseased kidneys. In a third study, significantly different values were found between acutely and chronically rejected renal grafts. In the initial study it was found that, except for one animal, the perfusion estimates in healthy and diseased kidneys are systematically higher for DCE-MRI. This is also reflected in the mean perfusion estimates when averaged over all animals of the initial study. At least, the mean ASL value of the healthy kidneys in the second study is in agreement with the mean DCE-MRI value for healthy kidneys in the first study. In the AKI studies, it is evident that in some animals the cortical perfusion of the diseased kidney is higher than the RBF in the healthy kidney of other rats, even when values of only one method are compared. The same observation can be made for the third study, when comparing the absolute values of single kidneys. Intramethodical variations are mainly attributed to different physiological conditions of the animals. Although the induction of AKI and the transplantation procedure was the same for each animal, the rats and particularly the kidneys can respond differently to a certain degree which leads to a different extent of the injury. However, this can only explain variations in the differences in RBF between healthy and diseased kidneys and chronically and acutely rejected organs, respectively. A potential factor leading to intramethodical variations is the different impact of the anesthesia during MRI on the animals and their kidney function. Especially, thiobutabarbital sodium can eventually alter the kidney function [Rieg et al., 2004]. Also, the ad libitum approach regarding the fluid intake prior to the MRI experiment might result in different physiological states of the kidneys. In future studies, going without fluids for some hours prior to the experiment might be beneficial for consistency but is difficult in terms of ethics. Anyway, the effect is thought to be minor compared to the ones mentioned above. Generally perfusion in small animals is sensitive to the body temperature. Although consecutive ASL measurements showed no changes in RBF our study is limited by the lack of temperature monitoring as absolute perfusion values might be influenced right after anesthesia. However, the main focus of this study, the intra-animal comparison, is not affected. An aspect that can lead to intra- as well as intermethodical variations is motion due to the respiratory cycle. This is a general problem when measuring in the abdomen. Although, motion was very weak in our case, it can generally lead to a blurring of the images which can invalidate the true contrast that is essential for the quantitation as it directly reflects the perfusion (ASL) and the tissue contrast uptake (DCE-MRI), respectively. Both imaging sequences acquire the central k-space lines first which assures that the image contrast is captured very rapidly. This lowers the motion sensitivity of both imaging sequences significantly but cannot fully eliminate it. For DCE-MRI a further reduction might be achieved by the usage of alternative k-space samplings like radial or BLADE [Lietzmann et al., 2012] or through post-processing using image registration techniques [Zöllner et al., 2009; Hodneland et al., 2014]. Unfortunately, FAIR ASL might not only be sensitive to motion during imaging but also to motion during the inflow time. In such case, the perfusion signal can be invalidated when the imaging slice is shifted outside the volume of the slice-selective inversion which leads to an overestimation of

absolute perfusion. Regarding the observed motion and the fact that the inversion slice was twice as thick as the imaging slice, we consider these errors to be negligible. Motion can also lead to a slice-selective inversion that labels the aorta at a point cranial to the branch of the renal arteries. Generally, this would result in an underestimation of RBF. Regarding the small diameter of the aorta and the high blood flow in the kidneys, the effect is considered to be negligible. Remedy from motion corrupted ASL measurements can be found in respiratory triggering or navigators [Song et al., 2010].

Compared to ASL, DCE-MRI has the advantage that functional parameters beyond perfusion can be extracted. However, quantitation of DCE-MRI heavily relies on a good selection of the AIF [Mendichovszky et al., 2009]. Slight variations can influence the outcome of the pharmacokinetic modeling and may contribute to inter-animal variation. Generally, it would be desirable to measure a local AIF. While this is already challenging in humans, it is nearly impossible in small animals. Therefore, the AIF was measured in the aorta to exclude partial volume effects due to an insufficient vessel size. The employed, well-standardized warm ischemia model damages tubuli and the microvascular structure of the kidney [Le Dorze et al., 2009]. Nevertheless, errors in RBF quantification due to the dispersion of the AIF [Calamante, 2005] on the path to the renal cortex cannot be fully excluded. However, these errors are expected to be small and, if present, should have no considerable effect on the identification of the hemodynamic abnormalities in the diseased kidney, i.e. the decreased perfusion compared to the healthy kidney. Especially, since the warm ischemia model is known to decrease renal perfusion, the lower RBF will exceed potential underestimations in absolute perfusion caused by dispersion. This is also supported by the fact that the mean RBF differences between healthy and diseased kidney is identical for ASL and DCE-MRI. Furthermore, the exact vascular transit function is unknown and a local AIF is not accessible. Hence, an attempt to correct possible dispersion errors would very likely lead to an erroneous correction. Generally, DCE-MRI benefits from a high temporal and spatial resolution as the sampling of the bolus curve is decisive and the possibility to easily distinguish different anatomical regions should be given. In our case, the temporal resolution is higher by a factor of four than the constraint demanded by [Michaely et al., 2008] for humans. The data showed that this resolution sufficiently accounted for the faster blood circulation in rats.

Absolute values of renal perfusion measured with ASL are calculated based on the formula given in [Kim, 1995] which includes some simplifications. The model assumes that the labeled blood water relaxes with the T_1 of tissue. However, before the labeled blood moves into the extravascular space, it relaxes with the T_1 of arterial blood. The T_1 of of the renal cortex (1.14 s [de Bazelaire et al., 2004]) is smaller than that of arterial blood at 3 T ($\sim 1.6\,s$, [Lu et al., 2004]) which can lead to an overestimation of perfusion, as the signal decay is slower than predicted by the model. A further improvement might be to measure a T_1-map of the kidneys. This way the global value used for quantitation could be substituted by a value that reflects the longitudinal relaxation time in the according pixel itself. Especially, for the diseased kidney, T_1-times may differ from the values found in literature. A fact that can lead to an underestimation of perfusion is the transit delay that is set to zero in the used model. However, in pathologic

tissue it is known to be significantly prolonged [Chalela et al., 2000; Bokkers et al., 2009]. Quantification errors due to transit delays can be avoided by the application of additional saturation pulses like in Q2TIPS [Luh et al., 1999]. Regarding the issue of the small perfusion signal, the measurement could be improved by using background suppression to zero the static tissue signal and thereby increase the relative perfusion signal. Another critical issue of pulsed ASL sequences is the slice-selective inversion pulse and the quality of its inversion, regarding inversion accuracy and the shape of the inversion slab. Although the used inversion pulse showed a homogeneous, complete inversion and a steep transition zone when applied in a water phantom, its inversion capabilities might be different in the abdomen due to air-tissue transitions that cause inhomogeneities in the magnetic field. An incomplete slice-selective inversion can lead to increased perfusion estimates.

Adiabatic Inversion Pulses

The above discussion of quantitative perfusion measurements with pulsed ASL in small animals has pointed out the importance of the slice-selective inversion pulse for robust measurements. On the one hand, to maximize the perfusion signal, the inversion efficiency is crucial. On the other hand, to reduce the transit delay and to achieve a sharp edge of the labeled blood bolus, steep transition zones between inverted and fully relaxed magnetization, are of great importance [Yongbi et al., 1999]. Therefore, as part of the development of a 3D FAIR ASL sequence, special emphasis was placed on the design and the verification of sophisticated adiabatic inversion pulses.

Generally, for adiabatic pulses a compromise between the percentage of truncation, the pulse duration and the hyperbolic secant parameters μ and β has to be found. Higher values of μ yield squarer inversion profiles [Silver et al., 1984], which means that for a given bandwidth, β should be decreased as far as possible. Also, the adiabatic threshold increases linearly with β but only with the square root of μ. Unfortunately, for a given bandwidth, smaller values of β increase the width of the pulse and lead to a higher degree of truncation if the pulse length is kept constant. Truncation, in turn, corrupts the slice profile. Therefore, for a given pulse duration, the value of β was decreased as long the B_1 amplitude at the beginning and end of the pulse was smaller than the defined truncation limit [Payne and Leach, 1997]. Then, a further increase of μ would only be possible by increasing the bandwidth and thereby increasing the gradient amplitude. However, for adiabatic pulses, the bandwidth is rather limited by the maximal available gradient amplitude or the SAR of the pulse than by the coil voltage that is necessary to meet the adiabatic condition. A relation that was also found by Ordidge et al. [1996]. FOCI pulses use an increased amplitude of the slice-selection gradient at the beginning and end of the pulse, which does not require an increased peak amplitude of the B_1 field. This way, the width of the transition zones is decreased compared to the standard HS pulse without increasing the requirements on the maximal coil voltage.

The superior slice profile quality of the FOCI pulse compared to the HS pulse was confirmed experimentally and numerically. The fact that no phase-encoding was used to

measure the slice profiles can potentially lead to artifacts as the borders of the phantom also contribute to the signal. However, the good agreement between measurement and simulations shows that the effects are negligible. The usage of phase-encoding might anyway be used to totally exclude possible distortions.

To understand the formation of the slice profile and its evolution during the transmission of the inversion pulse, slice profiles were measured and simulated for several fractions of the total pulse length. The general course of the simulation is in good agreement with the measurement. The final slice profiles are nearly identical. By comparing the results of the individual time steps, some deviations can be observed. Generally, the simulation seems to be "faster" than the measurement. Further, between 30 % and 40 % of the total pulse duration, the simulation behaves unexpected. Magnetization that is already fully inverted in one step, is nearly completely relaxed in the next step. A behaviour that is unrealistic as the T_1 relaxation cannot be accelerated. This error is probably an issue of the hard pulse approximation and the discretization, however, it has no influence on the final slice profile. Ordidge et al. [1996] show simulated profiles at three time points during an HS pulse. Their results are in good agreement with the presented simulations. Both, the experimental and the numerical time course of the slice profile show that the transition zones between inverted and uninverted magnetization are created at the beginning and end of the RF pulse. This explains the superior slice profile of the FOCI pulse and confirms its clever design, as the gradient is increased at exactly these positions and yields a better separation of magnetization with different frequencies. The inversion efficiency of all pulses was assessed by measuring the mean longitudinal magnetization within the central 80 % of the nominal slice thickness. Its standard deviation is thereby a good indicator of the homogeneity of the inversion.

The effect of an increased bandwidth was tested for HS and FOCI pulse. The bandwidth-independent pulse parameters were the same as for the initial comparison of HS and FOCI slice profiles to allow for a fair comparison. It can be observed that especially the profile of the HS pulse shows steeper transition zones, which is expected due to the higher bandwidth and the increased gradient amplitude. A second observation is the incomplete inversion, that is present for both pulses. While the profile of the HS pulse still shows a homogeneous distribution of the longitudinal magnetization, the FOCI pulse profile is nearly fully inverted at the edges and shows a decreasing inversion efficiency towards the center of the slice profile. Both effects, are caused by an insufficient coil voltage, i.e. an insufficient B_1-amplitude, which leads to a violation of the adiabatic condition. The typical shape of the FOCI profile is explained by the higher gradient at the beginning and end of the pulse which leads to higher degree of inversion at the edges of the profile. The maximal possible bandwidth for a given adiabatic threshold depends on the maximal available coil voltage of the transmitter coil. Therefore, the used bandwidth values are not universal. However, they serve the purpose of demonstrating the effect of a violated adiabatic condition by means of a bandwidth that was chosen too high.

The investigation of off-resonance effects showed a strongly decreased spatial displace-

ment of the FOCI pulse compared to the HS pulse. This characteristic is expected, as the spatial displacement is inversely proportional to the amplitude of the slice selection gradient. Hence, the increased gradient amplitude of the FOCI pulse is not only beneficial for the quality of the slice profile but also for its robustness against off-resonance. Simulation and measurement are in good agreement regarding the spatial displacement, however the measurements show a slight decrease in inversion efficiency and homogeneity. The presented results confirm the findings published by Ordidge et al. [1996] and Payne and Leach [1997].

Simulations show that the general effect of relaxation processes during RF transmission are identical for HS and FOCI pulses. Generally, T_1 relaxation decreases the completeness of the inversion. The effect is stronger for the left transition zone as the magnetization at that position is inverted earlier than the right transition zone (cf. Figure 4.17) and hence, has more time to relax. However, this order is only defined by the sign of the frequency sweep. Transversal relaxation leads to a change of the longitudinal magnetization outside of the inversion slab, broadening the profile at positions where the longitudinal magnetization is close to one. The effect is symmetric since dephasing by T_2 relaxation depends on the time the magnetization spends in the transversal plane. This time, in turn, depends on the magnitude of the effective field as higher amplitude leads to slower flipping of the magnetization. Further, with T_2 relaxation an incomplete inversion is present but it is not as prominent as for purely longitudinal relaxation. If both relaxations are present, the previously observed effects are combined and lead to a further decrease of the inversion efficiency. However, as the effects are non-linear, the combination is not just the sum of both. Measurements and simulations, similar to the presented results, have been published by Frank et al. [1997], however only HS pulses and no FOCI pulses were studied. For realistic values, the influence of relaxation is barely visible. Anyway, relaxation should be taken into account, especially for applications where the slice profile and the inversion efficiency are decisive or the relaxation times are of the order of the pulse duration. Besides for the last simulation, the combinations of relaxation times are unrealistic, however serve the purpose of demonstrating the isolated effect of only one phenomenon. Due to that and the fact that the exact estimation of relaxation times is difficult, no measurements were conducted.

Dual-band RF pulses can be realized by modulating the B_1 envelope of an RF pulse with a cosine function. The frequency of the cosine together with the amplitude of the slice-selection gradient determines the separation of the excited slices. The idea is based on the k-space formalism where excitation profiles and RF envelopes are connected through a Fourier transformation. Different approaches for adiabatic dual-band inversion can be found in the literature [Goelman, 1997; Ouwerkerk, 2014]. In this work, the Fourier approach, which is actually only valid in the small flip angle regime, was adopted for adiabatic inversion pulses. In a first measurement, the feasibility could be shown, however the profiles showed typical signs of a violated adiabatic condition. It would have been possible to adapt the pulse parameters in a way that the condition was fulfilled, however, at expense of the profile quality. The problem was solved by using the VERSE transformation to reduce the B_1 peak amplitude of the

pulse. An analytical function based on the Fermi function was used as a scaling function. Compared to the composite scaling function of a two-speed VERSE approach, it has the advantage of being continuous which facilitates the implementation and the necessary calculations. Further, errors due to discretization are minimized. By using the VERSE transformation, the peak B_1 amplitude could be minimized to 60 % of the original value. The reduction was sufficient to account for the increased adiabatic threshold and the measurement showed a complete inversion of two symmetrical slices. The high quality of the single-band inversion profile was conserved. A further reduction of the B_1 amplitude would have been possible, however the shape of the scaling function leads to a strong increase of the gradient amplitude at the beginning and end of the pulse and has to stay within the hardware limits. The results of the dual-band inversion using a FOCI pulse was confirmed by simulations, that showed an excellent agreement with the measurements. Besides its application for dual-band inversion, the usage of VERSE-transformed adiabatic inversion pulses can generally be beneficial for ASL [He and Blamire, 2010]. Dual-band adiabatic inversion pulses might be helpful for applications where multiple frequency bands need to be inverted. Possible applications are in localized spectroscopy [Ordidge et al., 1996], T_2 suppression in ultra-short echo time imaging [Larson et al., 2007] or ASL. For the latter, the dual-band property could be used for pulsed ASL measurements of paired organs like the kidneys or for vascular territory mapping [Davies and Jezzard, 2003].

3D ASL Measurement

The design of a sophisticated adiabatic inversion pulse, discussed in the previous section, was carried out as part of the development of a 3D FAIR ASL sequence. Compared to widely used 2D multi-slice acquisitions and most commercial implementations of ASL, the sequence allows the measurement of absolute perfusion in a whole volume. The sequence combines the FAIR labeling scheme with a 3D TrueFISP readout. So far, non-EPI 3D ASL sequences either used a 3D GRASE [Günther et al., 2005] readout sequence or a 3D FSE [Dai et al., 2008]. These approaches minimize susceptibility artifacts compared to EPI sequences, however, a compromise between temporal resolution, blurring in slice direction or lower perfusion signal per unit time was reported. The 3D bSSFP has the potential to overcome some of these limitations [Park et al., 2013]. The sequence presented in this work combines a 3D bSSFP sequence with a PASL labeling scheme. In addition, it includes several features such as pre- and post-labeling saturation, background suppression and Q2TIPS saturation pulses. In the following, the results of the design and optimization of each of the components will be discussed. Finally, the outcome of a 3D perfusion measurement of the brain of a healthy volunteer will be reviewed.

The general layout and pulse scheme of the sequence is shown in Figure 4.24. Overall, the sequence can be divided into two parts, the preparation of the magnetization and the data acquisition with the 3D TrueFISP readout. The magnetic preparation starts with the pre-saturation of the imaging volume to guarantee identical initial conditions for each experiment. Further, a first suppression of the tissue signal is achieved. The WET saturation scheme, a combination of four RF pulses interrupted by spoiler gradi-

ents, was used to accomplish a high degree of saturation. Ogg et al. [1994] showed that the four pulse WET scheme achieves a better water suppression than CHESS [Frahm et al., 1989] and is essentially independent of T_1 and B_1. In this work, the combination of flip angles has been optimized numerically to achieve an optimal suppression. The residual magnetization after WET saturation with the optimized flip angles was calculated for a range of T_1 values and deviations from the nominal flip angles. Apart from the combination of short T_1 times and decreased flip angles, the residual magnetization is below 3% of the equilibrium magnetization. The calculated set of flip angles differs from the one found by Golay et al. [2005], however, this can be explained by the large number of local minima found by the numerical minimization, which all lead to a good saturation. The calculation bases on the assumption that the transversal magnetization is completely spoiled after each RF pulse, which should be valid considering the length of 7 ms of the spoiler gradients. Further, to avoid coherences, the amplitude, polarity, and axis of the gradients are different after every RF pulse. Anyway, to fully exclude any residual transversal magnetization, a calculation based on gradient amplitude, axis and voxel size as described in Bernstein et al. [2004], could be included. Further, a variation of the phase of the RF pulses similar to RF spoiling [Zur et al., 1991] could be considered. The saturation of the imaging volume required the usage of spatially-selective RF pulses. The quality of the slice profile of *sinc*-shaped pulses is insufficient for flip angles larger than 90°. While the transition zones might be acceptably steep, the homogeneity of the excitation is insufficient. Furthermore, a compromise between the bandwidth, i.e. the profile quality, and the SAR of the pulse has to be found. Because of the mentioned reasons, the RF pulses employed in the WET scheme were calculated using the SLR algorithm. Simulations showed a homogeneous excitation with steep transition zones even for the 117° excitation pulse. RF clipping was avoided by using a two-speed VERSE approach, which also reduced the SAR of the pulses. The pre-labeling saturation is followed by the FOCI pulse, which is either acting globally (control image) or slice-selective (tag image). The design and properties of the pulse have been extensively discussed in the previous section and the optimized pulse parameters have been adopted for its usage in the ASL sequence. To estimate the minimal slice-thickness of the slice-selective inversion with respect to the size of the readout volume, an experiment similar to the one described in Section 4.1.1 was conducted. To prove the superior properties of the FOCI pulse compared to the HS pulse, the experiment was conducted with both pulses. While the inversion slab of the HS pulse needs to be 27.5 mm larger than the imaging slab to avoid subtraction errors, the FOCI pulse only needs to be chosen 10 mm larger. This is a great advantage regarding transit delays and perfusion quantitation [Yongbi et al., 1999].

The perfusion signal is very low compared to the signal of static tissue. This means that only small fluctuations in the tissue signal can corrupt the ASL signal. Such fluctuations are mainly caused by physiological noise [Wu et al., 2009]. The implemented background suppression scheme aims to null the signal of static tissue at the time of the readout. This way, both signals are of the same order, such that tissue signal fluctuations do not necessarily lead to an erroneous perfusion signal. Generally, by saturating the imaging region directly after labeling and applying carefully timed non-selective inversion pulses, an arbitrary number of T_1 species can be nulled at the

beginning of data acquisition. In the presented sequence, the saturation was achieved by using the WET scheme optimized for pre-labeling saturation. For the global inversion the same FOCI pulses as for the labeling were used, guaranteeing robustness against B_1 variations. Ideal inversion pulses do not change the absolute value of the ASL signal. However, as discussed in the previous section, T_1 and T_2 relaxation lead to imperfection of the inversion pulses that will attenuate the ASL signal. Garcia et al. [2005] showed that even with optimized inversion pulses, the usage of four global inversion pulses leads to a loss of 25% of the ASL signal. This value decreases with the number of inversion pulses, however, with two pulses, the signal loss still amounts to 17% [Ye et al., 2000] and with only one pulse to 9% [Duyn et al., 2001]. Nevertheless, the suppression of static tissue signal leads to an improved stability and sensitivity, which was demonstrated by the comparison of perfusion-weighted images, acquired with and without background suppression. Further, Vidorreta et al. [2013] found that the combination of 3D single-shot readouts and BS considerably improves the performance of ASL sequences. The timing of the inversion pulses is calculated based on the T_1 relaxation times of the tissue. For two inversion pulses and some special ratios of relaxation times, an analytical solution exists [Günther et al., 2005]. Generally, the timing of the inversion pulses can only be derived from numerical minimization of the longitudinal magnetization. An optimization that does not select particular T_1 species but minimizes the signal across a range of typical T_1 times was proposed by Maleki et al. [2012]. Independent of the minimization method, care has to be taken with background suppression. In cases where the zero-crossing occurs close to the beginning of the readout, the usage of magnitude images to calculate the perfusion-weighted image can lead to large errors if the longitudinal magnetization in label and control image is of opposite sign. These errors can be avoided by subtracting the complex data or leaving a positive magnetization of the static tissue. The latter, however, is difficult to realize as the exact T_1 relaxation times are unknown.

The quantitation of perfusion from tag-control pairs taken at one specific inflow time can lead to incorrect estimates if the transit delay in the specific region is unknown. These errors can be avoided by truncating the bolus of labeled blood. Therefore, additional saturation pulses have been implemented in the presented sequence, following the Q2TIPS approach. In order to achieve a homogeneous excitation and a sharp profile, the pulses were designed using the SLR algorithm. In contrast, to the WET saturation, the Q2TIPS pulses were implemented as dual-band pulses. To account for the doubled B_1 amplitude requirements, the pulses were VERSE-transformed and the bandwidth was decreased compared to the RF pulses used for WET. For the FAIR preparation scheme, the implementation as dual-band saturation pulse has the advantage that the inflow of labeled arterial and labeled venous blood is interrupted. Further, at the time of the readout, signal contributions from outside the imaging volume are suppressed. The slice profile of the VERSE-transformed dual-band pulse was verified by simulations. Steep edges of the excitation profile are important, as the trailing edge of the labeled blood is sharply truncated and the thin-slice saturation band can be positioned closer to the imaging volume.

While investigations of the magnetization transfer (MT) effects associated with the

labeling pulse have led to the development of ASL tagging schemes that compensate or avoid MT effects (such as FAIR), there are only two studies that investigated the MT effect by the Q2TIPS pulse train. Both studies [De Vita et al., 2012; Petr et al., 2013] report a significant MT effect, which reduces the T_1 of tissue as well as M_0. As a consequence, background suppression efficiency is reduced and the received absolute perfusion values are underestimated. To minimize MT effects by Q2TIPS saturation pulses the authors suggest to reduce the density of the pulse train and the usage of an extended model for perfusion quantitation, respectively. The signal of the prepared magnetization was acquired using a 3D TrueFISP readout. The steady-state signal of SSFP sequences does not depend on any magnetic preparation. Therefore, the challenge is to acquire the data during the transient state. Further, as signal differences due to unequal magnetic preparations get smaller with every TR-interval, the contrast relevant data should be recorded first. This is particularly important, as the signal will be close to the steady-state signal at the end of the readout due to the large number of phase encoding steps of the 3D readout. The prioritized recording of the central k-space lines was accomplished by using a spiral reordering scheme. In case of an anisotropic FOV in both phase encoding directions, further benefits might be achieved by sorting the k-space lines in the phase encoding plane according to their distance to k-space center. To avoid signal oscillations during the transient state, the flip angles of the first ten excitation pulses followed a Kaiser-Bessel function. In a simulation, the effect of the Kaiser-Bessel ramp on the time course of the signal was confirmed and showed a continuous and smooth trend towards the steady-state signal. Due to the usage of a short TR of only 3 ms and additional shimming prior to the measurements, no problems with banding artifacts were encountered. Care has to be taken, when GRAPPA is used to accelerate the image acquisition as the signal is inversely proportional to the square root of the acceleration factor. Anyway, due to spiral reordering, the main advantage of GRAPPA is not the improved contrast but the reduced overall measurement time.

The initial application of the developed 3D ASL sequence in the brain of a healthy volunteer was successful and yielded very good results. The mean perfusion values and standard deviations were found to be $f_{\mathrm{GM}} = (51 \pm 17)\,\mathrm{ml}/100\,\mathrm{g}/\mathrm{min}$ and $f_{\mathrm{WM}} = (24 \pm 8)\,\mathrm{ml}/100\,\mathrm{g}/\mathrm{min}$ for gray and white matter, respectively. They are in very good agreement with values measured with the "gold-standard" method, i.e. PET scanning with ^{15}O-labeled water, where Leenders et al. [1990] report $(54.5 \pm 12.3)\,\mathrm{ml}/100\,\mathrm{g}/\mathrm{min}$ for gray matter and $(22.2 \pm 4.9)\,\mathrm{ml}/100\,\mathrm{g}/\mathrm{min}$ for white matter. The large error bars of the values derived from ASL can be explained by the low SNR of the perfusion signal and might be improved by further optimization of the data readout or by increasing the number of tag-control pairs. Further, pCASL labeling could be used which is known for its higher SNR but also for its difficult practical implementation that faces a number of challenges [Wong et al., 1998b]. The error of gray matter perfusion might also originate from partial volume effects, due to its difficult delineation. However, the value is in line with absolute gray matter perfusion values found by other ASL studies. For example, Günther et al. [2005] report $(62 \pm 15)\,\mathrm{ml}/100\,\mathrm{g}/\mathrm{min}$, averaged over five subjects that where measured with a similar 3D single-shot readout and a FAIR labeling scheme. Gai et al. [2011] used a STAR labeling scheme and a 3D EPI readout to assess brain perfusion in five healthy volunteers. They found values of $(55.8 \pm 8.4)\,\mathrm{ml}/100\,\mathrm{g}/\mathrm{min}$ and

(10.1 ± 2.4) ml/100 g/min for gray and white matter, respectively. However, they state that the latter value should not be taken as accurate. So far, the largest ASL study with 284 volunteers was conducted by Petersen et al. [2010] who used a STAR labeling scheme and 2D multi-slice EPI readout combined with multi-*TI* Look-Locker strategy [Günther et al., 2001] and a model-free deconvolution approach. The population mean of gray matter perfusion was found to be (47.4 ± 7.5) ml/100 g/min and is in good agreement with the value reported in this work.

During the measurement, the head of the volunteer was pinched with foam material, to avoid movements that lead to errors in the difference images. The thickness of the slice-selective inversion pulse was chosen to be 20 mm thicker than the readout volume. Compared to the minimal inversion slice thickness estimated by the preliminary measurement, additional 10 mm were added. This had a negligible effect on the transit delay, however, assured that the edges of the slice-selective inversion have no influence on the readout volume. Based on simulations of the excitation profiles, the thickness of the WET RF pulses for pre- and post-labeling saturation was chosen identical to that of the slice-selective inversion. The timing of the global inversion pulses was such that the signal nulling occurred 100 ms before the readout to avoid subtraction errors. Due to potential signal losses discussed above, only two T_1 species were nulled, i.e. gray matter and white matter. The inflow time TI of 1800 ms and the labeled blood bolus length of 800 ms were chosen according to recommendations in a recent ASL position paper [Alsop et al., 2013]. 30 tag-control pairs were recorded to increase the perfusion signal through averaging. Together with the recording of the M_0 data, the overall measurement time was about 18 minutes. This scan time is longer than the scan time of other 3D ASL studies, however, has yet not been optimized. After averaging the images according to their magnetic preparation, the ΔM volume was calculated by a voxel-wise subtraction of control from tag data. M_0 was computed using the steady-state signal equation and absolute perfusion values were calculated for each voxel. Values for gray and white matter where assessed by placing ROIs in the respective regions. While white matter could be easily identified, the TrueFISP signal dependency on the ratio T_2/T_1 complicated the delineation of gray matter. For future measurements, T_1-weighted images with a higher resolution might be more desirable.

Most disorders of perfusion in the brain result in focal changes that are easily detectable in ΔM images. Hence, the visualization of ASL difference images is most useful in clinical routine. However, some diseases (hypercapnia , hypoxic ischemic injury) cause global changes in brain perfusion [Nöth et al., 2006; Brierley, 1976]. Therefore, it is helpful to generate maps in quantitative units. For that, a simplified model was used which is an adapted version of the model that was discussed in Section 5. Due to the truncation of the bolus, the assumption that the entire labeled blood is delivered to the tissue of interest, leads to less quantitation errors. Still, while transit delays in healthy gray matter are between 500 and 1500 ms [MacIntosh et al., 2010], transit delays can be longer than 2000 ms in white matter and areas affected by cerebro-vascular diseases. In such cases, perfusion quantitation from data taken at a single TI is critical and a so-called multi-TI measurement is often more accurate. Multi-TI measurements sample the time course of the perfusion signal by taking data at a different inflow times. For

perfusion quantitation, the general kinetic model can then be fitted to the data, which also allows to estimate transit delays. The parameter estimation from multi-TI data is an active area of research and requires an exact understanding of the underlying model [Parkes, 2005] and the impact of imaging parameters. It is also associated with a prolonged measurement time, if no trade-offs regarding resolution and the number of averages, are made. The chosen simplified model is known for its robustness and simplicity. Further, the assumption that there is no outflow of labeled blood water is justified regarding the much larger size of the tissue water pool compared to the blood water pool and the rapid water exchange between blood and tissue [Zhou et al., 2001]. On close examination, the labeled blood first relaxes with the T_1 of blood water and after exchanging into the tissue, with the T_1 of the tissue. The used model simplifies this bi-exponential decay by assuming equal relaxation times governed by the T_1 of blood. However, errors arising from this assumption are relatively small. The quantitation model requires two parameters that are normally not assessed during an ASL experiment, the T_1 of arterial blood and the blood-tissue partition coefficient λ. Both are normally taken from literature and represent potential sources of error. For example, the reported values for T_1 of arterial blood ranges from 1526 ms [Lu et al., 2004] to 1932 ms [Stanisz et al., 2005]. For λ, a global value is used for the whole brain, while it should actually be different for each voxel. Different methods have been proposed to measure [Roberts et al., 1996] or to determine [Ahlgren, 2011] the coefficient, however, a brain average value is in widespread use and the associated quantitation errors are expected to be less than 10% [Alsop et al., 2013]. The value of λ is used to scale the signal intensity of tissue to that of blood by using the tissue equilibrium magnetization data M_0. As the absolute perfusion values are inversely proportional to M_0, it should have a high SNR and should be well co-registered to the ΔM images. When using background suppression, this might be challenging, due to the large differences in signal intensities. Therefore, motion during the measurement should be generally prevented, e.g. by pinching the head with foam material. While absolute quantitation with multi-TI is possible without M_0 data, such data is required to quantitate perfusion from single-TI measurements. It is recommended that proton-density-weighted data is used for M_0, that is recorded with the same readout as used for the ASL experiment. For that, a short echo time but a $TR > 5000$ ms should be used, which leads to unacceptably long acquisition times in combination with the large number of phase-encoding steps of a 3D readout. Therefore, a new approach was followed in this work, where M_0 was calculated from steady-state data, using the steady-state signal equation of the TrueFISP sequence. Although, the large number of excitation pulses, necessary to reach the steady-state, may lead to MT effects in the M_0 data [Bieri and Scheffler, 2006], this seemed like a reasonable approach compared to the acquisition of proton-density-weighted data. Alternatively, data recorded without additional TR-cycles could be used for M_0 [Martirosian et al., 2004] but would require a theoretical study that inspects the perfusion signal during the transient state depending on the k-space sampling strategy. Such an analysis could also be used to optimize the flip angle for a maximal perfusion signal.

6
Summary & Outlook

Microvascular perfusion is an important parameter of high clinical value as it yields important informations on the organ viability and function. In MRI, basically two methods exist to calculate maps of absolute perfusion values. While DCE-MRI and DSC-MRI involve the injection of an exogenous contrast agent whose usage may be contraindicated, ASL represents a completely non-invasive method that uses arterial blood as endogenous tracer. Although ASL estimates have been compared to "gold-standard" methods, its clinical acceptance and credibility is still very low. The main reasons therefore are the variety of possible implementations, the presupposed knowledge as well as a lack of studies testing its diagnostic significance.

Therefore, one objective of this work was to test and validate the clinical value of quantitative perfusion measurements with ASL. On the one hand, this was accomplished by a comparison of its findings to those of DCE-MRI. On the other hand, animal models of renal diseases that are known to alter perfusion, were used to test the discriminative power. To facilitate the transfer into clinical research or even routine, the ASL measurement was successfully established on a clinical whole-body MR scanner.

An initial study in rats with unilateral AKI was presented, which showed that both ASL and DCE-MRI yield significantly different values for healthy and diseased kidneys. This demonstrates that both methods are equally capable to detect the hypoperfusion of an AKI kidney compared to the perfusion of a healthy kidney. Regarding the diagnostic significance, the study indicates that ASL is a capable alternative to DCE-MRI, leaving it open to physicians to choose between two comparable methods. Especially for patients with impaired kidney function where the injection of gadolinium-based contrast agents may be contraindicated, ASL might be favored. Furthermore, ASL has the advantage that it can be repeated as often as necessary. A second study with an increased number of AKI rats was conducted to confirm the results of the initial study and to increase the statistical power. Based on the findings of the initial study, solely ASL was used to asses renal perfusion. Again, significantly different estimates were found for healthy and diseased kidneys which confirmed the capability of ASL to discriminate normal from abnormal microvascular perfusion. Finally, an animal model of

renal transplantation was used to test perfusion differences in transplanted kidneys with acute and chronic rejection. The measurements yielded significantly lower perfusion values in the acutely rejected transplants compared to the grafts with chronic rejection. No native control organs were available, however, a comparison to the healthy kidneys of the AKI animals suggests that the mean blood flow in both rejection models is lower than in the healthy kidneys of the AKI models. A future study, that includes a control group with native kidneys has the potential to verify this tendency.

Nevertheless, regarding absolute perfusion values, the initial study showed that nontrivial differences and variations remain when comparing ASL to DCE-MRI. This indicates that further investigation and the comparison to a gold standard, e.g. PET scanning with ^{15}O-labeled water, is needed. ASL has proven its diagnostic significance when a native control organ exists or two groups with known pathophysiologies are compared. However, the detection of abnormal global changes of perfusion requires dependable absolute values that can be compared to literature values. Such a comparison is always difficult as especially renal perfusion depends on the individual subject and its actual physiological state. For example, renal perfusion will be higher after water load and naturally underlies variations during one day. This problem remains for all quantitative measurement techniques and is not only related to ASL. Fortunately, the possibility to compare perfusion estimates to that of a healthy contralateral organ or healthy tissue within one organ, is often given. Even if absolute values differ from the true value, the ability to detect relative blood flow changes is the crucial requirement for clinical diagnosis. For ASL, this ability was demonstrated in this work. Future studies may now test, to what extent even small blood flow changes can be detected.

The major goal of this work was the development of a 3D ASL sequence that enables the spatially resolved measurement of quantitative perfusion values in a whole volume. In contrast, the majority of ASL sequences described in literature use 2D single-slice or 2D multi-slice readouts. Compared to multi-slice acquisitions, 3D measurements have the advantage of a relatively high SNR, no limitations on the number of slices, a good suitability for background suppression and no slice-dependency of the perfusion signal. The presented sequence includes several features, each of which has been separately optimized. Special emphasis was put on the design and implementation of the slice-selective inversion pulse, whose properties have been simulated as well as experimentally verified. Furthermore, the quality of the inversion profile was studied with respect to different aspects like relaxation and off-resonance. To guarantee identical initial conditions in the imaging region, the sequence includes a pre-saturation module that follows the WET scheme. The flip angles of the four WET RF pulses have been numerically optimized to achieve a high degree of signal suppression over a broad range of T_1 and B_1 values. The sequence further includes a background suppression module that aims to null the signal of static tissue to avoid erroneous perfusion signals due to physiological noise from movement or cardiac induced modulations. Q2TIPS saturation pulses are applied to increase the accuracy of absolute perfusion estimates. To interrupt the inflow of blood from both sides of the imaging volume, the Q2TIPS RF pulses were implemented as dual-band pulses. To account for the doubled requirement on the maximal B_1 amplitude, all dual-band pulses underwent VERSE-transformation.

High quality slice profiles of both WET and Q2TIPS RF pulses were ensured by using the SLR algorithm. Their excitation profiles were verified in simulations. Based on the high image quality and perfusion signal delivered by the 2D TrueFISP that was employed for renal perfusion imaging in small animals, a 3D TrueFISP readout was chosen for data acquisition. While literature reports on single-shot 3D ASL sequences show a prevalence for GRASE and spiral FSE, the 3D TrueFISP sequence has the potential to overcome some of their shortcomings. In addition, the TrueFISP readout is suitable for abdominal imaging. A spiral reordering scheme was used to first record the contrast relevant data after magnetic preparation. To avoid the typical signal oscillations during the transient phase of the sequence, a Kaiser-Bessel ramp was used.

In an initial measurement, the sequence was used for a whole-brain perfusion measurement in a healthy volunteer. Absolute perfusion values were calculated for each voxel. Gray and white matter perfusion were extracted by drawing ROIs that depict the respective tissue. The received values are in very good agreement with findings from the "gold-standard" method of PET scanning with ^{15}O-labeled water, as well as with reports from other ASL studies. In addition to the good quality of the perfusion maps and the high spatial resolution, this demonstrates the successful development of a 3D ASL sequence for quantitative perfusion MRI. Nevertheless, this was only an initial study and further measurements are needed to test its robustness and reproducibility. Future work should also include the comparison to alternative readout modules like GRASE or different labeling schemes like pCASL. Ideally, absolute perfusion estimates are verified by methods that use exogenous contrast agents. Moreover, while still in a clinically acceptable range, the acquisition time is much longer than in comparable sequences. An instance, that may be improved by reducing the time between adjacent measurements. Still, the results of the initial measurement are very promising and the developed sequence does not only have a large potential for research applications but also for clinical usage. As the 3D TrueFISP is suitable for abdominal imaging, the sequence may be adapted to assess renal perfusion. In this context, the usage of the developed dual-band adiabatic inversion pulse can improve renal ASL as it allows the slice-selective inversion of paired organs without labeling the aorta. Future implementations may also include automated segmentations of gray and white matter or renal cortex and medulla. This way, partial volume effects in connection with the extraction of absolute perfusion values of different tissue types can be avoided.

In conclusion, both subjectives of this work were achieved. A 3D ASL sequence to assess quantitative perfusion values in a whole volume was developed and tested. Further, it was shown that ASL is a capable diagnostic tool that can detect the abnormal blood flow in diseased kidneys relative to healthy kidneys. The diagnostic value in combination with the possibility of a 3D assessment of absolute perfusion values, makes ASL a promising technique for a future standard tool in clinical routine. This is strengthened by its capacity as a completely non-invasive technique that allows its application in patients where the usage of exogenous contrast agents is contraindicated or in elderly and pediatric populations. In addition, ASL benefits twofold from higher magnetic field strengths that may be offered by future MR tomographs. Once by the increased overall signal and once by the longer longitudinal relaxation times.

A
Appendix

A.1 Initial Study

Table A.1: *Ratios of renal perfusion between left (diseased) and right (healthy) kidneys in the initial study. Values were calculated based the findings given in Table 4.1 and are plotted in Figure 4.9.*

rat	ASL	DCE-MRI
	RBF ratio left/right	RBF ratio left/right
1*	0.97 ± 0.26	1.03 ± 0.41
2	0.72 ± 0.15	0.74 ± 0.37
3	0.56 ± 0.21	0.65 ± 0.27
4	0.57 ± 0.15	0.90 ± 0.43
5	0.81 ± 0.19	0.74 ± 0.29
6	0.73 ± 0.15	0.64 ± 0.28
mean	0.68 ± 0.11	0.73 ± 0.10

*Animal with two healthy kidneys, value excluded when calculating the mean ratio of AKI rats.

Table A.2: *ASL perfusion estimated of four consecutive measurements in two animals. All values are in ml/100 g/min.*

measurement	rat 2		rat 4	
	left(AKI)	right(healthy)	left(AKI)	right(healthy)
1	456 ± 71	634 ± 94	289 ± 63	504 ± 69
2	425 ± 92	615 ± 100	286 ± 64	502 ± 95
3	430 ± 96	651 ± 98	274 ± 68	507 ± 83
4	433 ± 78	650 ± 103	272 ± 70	509 ± 100
mean	436 ± 42	638 ± 49	280 ± 33	506 ± 44

A.2 Animal Model of Acute Kidney Injury

Table A.3: *Renal cortical perfusion in rats with unilateral acute kidney injury as measured with ASL. All values are given in ml/100 g/min.*

rat	ASL	
	left (AKI)	right (healthy)
1	417 ± 62	569 ± 50
2	109 ± 48	449 ± 56
3	277 ± 59	574 ± 60
4	322 ± 95	530 ± 66
5	193 ± 58	260 ± 54
6	361 ± 61	513 ± 64
7	244 ± 58	490 ± 77
8	352 ± 55	486 ± 69
9	302 ± 54	460 ± 74
10	295 ± 57	430 ± 68
11	366 ± 66	587 ± 82
12	313 ± 60	641 ± 115
13	175 ± 91	470 ± 71
14	294 ± 86	543 ± 90
mean	287 ± 83	500 ± 91

Table A.4: *Ratios of renal perfusion (cf. Table A.3) between left (diseased) and right (healthy) kidneys. The ratios are plotted in Figure 4.12.*

rat	ASL	rat	ASL
	RBF ratio left/right		RBF ratio left/right
1	0.73 ± 0.13	8	0.72 ± 0.15
2	0.24 ± 0.11	9	0.66 ± 0.16
3	0.48 ± 0.11	10	0.69 ± 0.17
4	0.61 ± 0.19	11	0.62 ± 0.14
5	0.74 ± 0.27	12	0.49 ± 0.13
6	0.70 ± 0.15	13	0.37 ± 0.20
7	0.50 ± 0.14	14	0.54 ± 0.18
mean			0.58 ± 0.15

A.3 Animal Model of Renal Transplantation

Table A.5: *Renal cortical perfusion in rats with a donor kidney. Listed are the values for both the acute (left) and the chronic rejection model (right). All values are given in ml/100 g/min.*

acute model		chronic model	
rat	ASL	rat	ASL
1	193 ± 54	24	170 ± 81
2	251 ± 42	25	237 ± 67
3	176 ± 48	26	214 ± 64
4	191 ± 60	27	352 ± 91
5	325 ± 54	28	424 ± 72
6	288 ± 95	29	356 ± 71
7	381 ± 63	30	427 ± 75
8	183 ± 85	31	380 ± 54
9	198 ± 40	32	171 ± 62
10	190 ± 55	33	485 ± 66
11	330 ± 48	34	404 ± 74
12	205 ± 63	35	205 ± 56
13	309 ± 67	36	374 ± 61
14	263 ± 58	37	271 ± 60
15	116 ± 36	38	267 ± 62
16	276 ± 51	39	399 ± 67
17	300 ± 66	40	307 ± 55
18	236 ± 66	41	566 ± 61
19	302 ± 52	42	413 ± 80
20	210 ± 45	43	498 ± 120
21	124 ± 52		
22	263 ± 57		
23	217 ± 69		
mean	240 ± 67		346 ± 112

List of Figures

List of Tables

Bibliography

Abragam, A. (1961). *The Principles of Nuclear Magnetism*. Oxford University Press, New York.

Ahlgren, A. (2011). *Perfusion MRI: Non-Linear Stochastic Regularization for Deconvolution of Model-Free Arterial Spin Labelling Data*. Master's thesis.

Alsop, D. and Detre, J. A. (1998). Multisection cerebral blood flow MR imaging with continuous arterial spin labeling. *RADIOLOGY-OAK BROOK IL-*, 208:410–416.

Alsop, D. C., Detre, J. A., Golay, X., Günther, M., Hendrikse, J., Hernandez-Garcia, L., Lu, H., MacIntosh, B. J., Parkes, L. M., Smits, M., van Osch, M. J. P., Wang, D. J. J., Wong, E. C., and Zaharchuk, G. (2013). Recommended implementation of arterial spin-labeled perfusion MRI for clinical applications: A consensus of the ISMRM perfusion study group and the European consortium for ASL in dementia. *Magnetic Resonance in Medicine*, page in press.

Amann, K., Büttner, M., Benz, K., and Schöcklmann, H. (2011). Nierentransplantatpathologie. *Der Pathologe*, 32(2):124–134.

Ames 3rd, A., Wright, R., Kowada, M., Thurston, J., and Majno, G. (1968). Cerebral ischemia. II. The no-reflow phenomenon. *The American Journal of Pathology*, 52(2):437.

Artz, N. S., Sadowski, E. A., Wentland, A. L., Djamali, A., Grist, T. M., Seo, S., and Fain, S. B. (2011a). Reproducibility of renal perfusion mr imaging in native and transplanted kidneys using non-contrast arterial spin labeling. *Journal of Magnetic Resonance Imaging*, 33(6):1414–1421.

Artz, N. S., Sadowski, E. A., Wentland, A. L., Grist, T. M., Seo, S., Djamali, A., and Fain, S. B. (2011b). Arterial spin labeling mri for assessment of perfusion in native and transplanted kidneys. *Magnetic Resonance Imaging*, 29(1):74–82.

Bernstein, M. A., King, K. F., and Zhou, X. J. (2004). *Handbook of MRI pulse sequences*. Elsevier Academic Press.

Bevington, P. R. and Robinson, D. K. (1969). *Data reduction and error analysis for the physical sciences*. McGraw-Hill, New York.

Bieri, O. and Scheffler, K. (2006). On the origin of apparent low tissue signals in balanced SSFP. *Magnetic Resonance in Medicine*, 56(5):1067–1074.

Bland, J. M. and Altman, D. G. (1986). Statistical methods for assessing agreement between two methods of clinical measurement. *The Lancet*, 327(8476):307–310.

Bloch, F. (1946). Nuclear induction. *Physical Review*, 70:460–474.

Bloembergen, N., Purcell, E., and Pound, R. (1947). Nuclear magnetic relaxation. *Nature*, 160(4066):475.

Bokkers, R., van der Worp, H., Mali, W., and Hendrikse, J. (2009). Noninvasive MR imaging of cerebral perfusion in patients with a carotid artery stenosis. *Neurology*, 73(11):869–875.

Bokkers, R. P., Bremmer, J. P., Van Berckel, B. N., Lammertsma, A. A., Hendrikse, J., Pluim, J. P., Kappelle, L. J., Boellaard, R., and Klijn, C. J. (2010). Arterial spin labeling perfusion MRI at multiple delay times: a correlative study with H215O positron emission tomography in patients with symptomatic carotid artery occlusion. *Journal of Cerebral Blood Flow & Metabolism*, 30(1):222–229.

Bonventre, J. V. and Yang, L. (2011). Cellular pathophysiology of ischemic acute kidney injury. *The Journal of Clinical Investigation*, 121(11):4210.

Boss, A., Martirosian, P., Klose, U., Nägele, T., Claussen, C. D., and Schick, F. (2007). FAIR-TrueFISP imaging of cerebral perfusion in areas of high magnetic susceptibility differences at 1.5 and 3 Tesla. *Journal of Magnetic Resonance Imaging*, 25(5):924–931.

Bracewell, R. N. (1980). *The Fourier transform and its applications*. McGraw-Hill, New York.

Brierley, J. (1976). Cerebral hypoxia. *Greenfield's Neuropathology*, 3:43–85.

Brix, G., Kiessling, F., Lucht, R., Darai, S., Wasser, K., Delorme, S., and Griebel, J. (2004). Microcirculation and microvasculature in breast tumors: pharmacokinetic analysis of dynamic MR image series. *Magnetic Resonance in Medicine*, 52(2):420–429.

Brix, G., Semmler, W., Port, R., Schad, L. R., Layer, G., and Lorenz, W. J. (1991). Pharmacokinetic parameters in CNS Gd-DTPA enhanced MR imaging. *Journal of Computer Assisted Tomography*, 15(4):621–628.

Broome, D. R. (2008). Nephrogenic systemic fibrosis associated with gadolinium based contrast agents: a summary of the medical literature reporting. *European Journal of Radiology*, 66(2):230–234.

Buxton, R. B. (2009). *Introduction to functional magnetic resonance imaging: principles and techniques*. Cambridge University Press.

Buxton, R. B., Frank, L. R., Wong, E. C., Siewert, B., Warach, S., and Edelman, R. R. (1998). A general kinetic model for quantitative perfusion imaging with arterial spin labeling. *Magnetic Resonance in Medicine*, 40(3):383–396.

Calamante, F. (2005). Bolus dispersion issues related to the quantification of perfusion MRI data. *Journal of Magnetic Resonance Imaging*, 22(6):718–722.

Calamante, F., Williams, S. R., van Bruggen, N., Kwong, K. K., and Turner, R. (1996). A model for quantification of perfusion in pulsed labelling techniques. *NMR in Biomedicine*, 9(2):79–83.

Chalela, J. A., Alsop, D. C., Gonzalez-Atavales, J. B., Maldjian, J. A., Kasner, S. E., and Detre, J. A. (2000). Magnetic resonance perfusion imaging in acute ischemic stroke using continuous arterial spin labeling. *Stroke*, 31(3):680–687.

Colvin, R. B. and Smith, R. N. (2005). Antibody-mediated organ-allograft rejection. *Nature Reviews Immunology*, 5(10):807–817.

Conolly, S., Glover, G., Nishimura, D., and Macovski, A. (1991). A reduced power selective adiabatic spin-echo pulse sequence. *Magnetic Resonance in Medicine*, 18(1):28–38.

Conolly, S., Nishimura, D., Macovski, A., and Glover, G. (1988). Variable-rate selective excitation. *Journal of Magnetic Resonance (1969)*, 78(3):440–458.

Cornell, L. D., Smith, R. N., and Colvin, R. B. (2008). Kidney transplantation: mechanisms of rejection and acceptance. *Annual Review of Pathology: Meachanisms of Disease*, 3:189–220.

Cutajar, M., Thomas, D. L., Hales, P. W., Banks, T., Clark, C. A., and Gordon, I. (2014). Comparison of ASL and DCE-MRI for the non-invasive measurement of renal blood flow: quantification and reproducibility. *European Radiology*, pages 1–9.

Dai, W., Garcia, D., de Bazelaire, C., and Alsop, D. C. (2008). Continuous flow-driven inversion for arterial spin labeling using pulsed radio frequency and gradient fields. *Magnetic Resonance in Medicine*, 60(6):1488–1497.

Davies, N. P. and Jezzard, P. (2003). Selective arterial spin labeling (SASL): Perfusion territory mapping of selected feeding arteries tagged using two-dimensional radiofrequency pulses. *Magnetic Resonance in Medicine*, 49(6):1133–1142.

de Bazelaire, C. M., Duhamel, G. D., Rofsky, N. M., and Alsop, D. C. (2004). MR imaging relaxation times of abdominal and pelvic tissues measured in vivo at 3.0 T: preliminary results 1. *Radiology*, 230(3):652–659.

De Vita, E., Günther, M., Golay, X., and Thomas, D. L. (2012). Magnetisation transfer effects of Q2TIPS pulses in ASL. *Magnetic Resonance Materials in Physics, Biology and Medicine*, 25(2):113–126.

Deimling, M. and Heid, O. (1994). Magnetization prepared true FISP imaging. In *Proceedings of the 2nd Annual Meeting of ISMRM, San Francisco*, page 495.

Detre, J. A., Leigh, J. S., Williams, D. S., and Koretsky, A. P. (1992). Perfusion imaging. *Magnetic Resonance in Medicine*, 23(1):37–45.

Detre, J. A., Wang, J., Wang, Z., and Rao, H. (2009). Arterial spin-labeled perfusion MRI in basic and clinical neuroscience. *Current Opinion in Neurology*, 22(4):348–355.

Dixon, W. T., Du, L. N., Faul, D. D., Gado, M., and Rossnick, S. (1986). Projection angiograms of blood labeled by adiabatic fast passage. *Magnetic Resonance in Medicine*, 3(3):454–462.

Dixon, W. T., Sardashti, M., Castillo, M., and Stomp, G. P. (1991). Multiple inversion recovery reduces static tissue signal in angiograms. *Magnetic Resonance in Medicine*, 18(2):257–268.

Dorland, W. A. N. (2011). *Illustrated Medical Dictionary*. WB Saunders Company.

Duhamel, G. and Alsop, D. (2004). Single-shot susceptibility insensitive whole brain 3D fMRI with ASL. In *12th ISMRM Scientific Meeting, Kyoto, Japan*.

Dujardin, M., Sourbron, S., Luypaert, R., Verbeelen, D., and Stadnik, T. (2005). Quantification of renal perfusion and function on a voxel-by-voxel basis: A feasibility study. *Magnetic Resonance in Medicine*, 54(4):841–849.

Duyn, J. H., Tan, C. X., Gelderen, P. v., and Yongbi, M. N. (2001). High-sensitivity single-shot perfusion-weighted fMRI. *Magnetic Resonance in Medicine*, 46(1):88–94.

Edelman, R. R., Darby, D. G., and Warach, S. (1994). Qualitative Mapping of Cerebral Blood Flow and Functional Localization with Echo-planar MR Imaging and Signal Targeting with Alternating Radio Frequency. *Radiology*, 192:513–520.

Ehrenfest, P. (1927). Bemerkung über die angenäherte Gültigkeit der klassischen Mechanik innerhalb der Quantenmechanik. *Zeitschrift für Physik A*, 45(7-8):455–457.

Forsén, S. and Hoffman, R. A. (1963). Study of moderately rapid chemical exchange reactions by means of nuclear magnetic double resonance. *The Journal of Chemical Physics*, 39:2892.

Fourier, J. (1822). Théorie analytique dela chaleur. *Didot, Paris*.

Frahm, J. a., Bruhn, H., Gyngell, M., Merboldt, K., Hänicke, W., and Sauter, R. (1989). Localized high-resolution proton NMR spectroscopy using stimulated echoes: Initial applications to human brain in vivo. *Magnetic Resonance in Medicine*, 9(1):79–93.

Frank, L. R., Wong, E. C., and Buxton, R. B. (1997). Slice profile effects in adiabatic inversion: application to multislice perfusion imaging. *Magnetic Resonance in Medicine*, 38(4):558–564.

Gai, N. D., Talagala, S. L., and Butman, J. A. (2011). Whole-brain cerebral blood flow mapping using 3D echo planar imaging and pulsed arterial tagging. *Journal of Magnetic Resonance Imaging*, 33(2):287–295.

Gai, N. D. and Zur, Y. (2007). Design and optimization for variable rate selective excitation using an analytic RF scaling function. *Journal of Magnetic Resonance*, 189(1):78–89.

Ganter, C. (2006). Steady state of gradient echo sequences with radiofrequency phase cycling: analytical solution, contrast enhancement with partial spoiling. *Magnetic Resonance in Medicine*, 55(1):98–107.

Garcia, D. M., Duhamel, G., and Alsop, D. C. (2005). Efficiency of inversion pulses for background suppressed arterial spin labeling. *Magnetic Resonance in Medicine*, 54(2):366–372.

Gerlach, W. and Stern, O. (1922a). Der experimentelle Nachweis der Richtungsquantelung im Magnetfeld. *Zeitschrift für Physik A*, 9(1):349–352.

Gerlach, W. and Stern, O. (1922b). Der experimentelle Nachweis des magnetischen Moments des Silberatoms. *Zeitschrift für Physik A*, 8(1):110–111.

Gevers, S., van Osch, M. J., Bokkers, R. P., Kies, D. A., Teeuwisse, W. M., Majoie, C. B., Hendrikse, J., and Nederveen, A. J. (2011). Intra-and multicenter reproducibility of pulsed, continuous and pseudo-continuous arterial spin labeling methods for measuring cerebral perfusion. *Journal of Cerebral Blood Flow & Metabolism*, 31(8):1706–1715.

Goelman, G. (1997). Two methods for peak RF power minimization of multiple inversion-band pulses. *Magnetic Resonance in Medicine*, 37(5):658–665.

Golay, X., Petersen, E. T., and Hui, F. (2005). Pulsed star labeling of arterial regions (PULSAR): a robust regional perfusion technique for high field imaging. *Magnetic Resonance in Medicine*, 53(1):15–21.

Golay, X., Stuber, M., Pruessmann, K. P., Meier, D., and Boesiger, P. (1999). Transfer insensitive labeling technique (TILT): application to multislice functional perfusion imaging. *Journal of Magnetic Resonance Imaging*, 9(3):454–461.

Gregori, J. (2009). *Dynamic arterial spin labeling measurements of physiological parameters permeability and oxygenation*. PhD thesis.

Griswold, M. A., Jakob, P. M., Heidemann, R. M., Nittka, M., Jellus, V., Wang, J., Kiefer, B., and Haase, A. (2002). Generalized autocalibrating partially parallel acquisitions (GRAPPA). *Magnetic Resonance in Medicine*, 47(6):1202–1210.

Günther, M., Bock, M., and Schad, L. R. (2001). Arterial spin labeling in combination with a look-locker sampling strategy: Inflow turbo-sampling EPI-FAIR (ITS-FAIR). *Magnetic Resonance in Medicine*, 46(5):974–984.

Günther, M., Oshio, K., and Feinberg, D. A. (2005). Single-shot 3D imaging techniques improve arterial spin labeling perfusion measurements. *Magnetic Resonance in Medicine*, 54(2):491–498.

Haacke, E. M., Brown, R. W., Thompson, M. R., and Venkatesan, R. (1999). *Magnetic Resonance Imaging*. Wiley-Liss New York.

Haase, A., Frahm, J., Matthaei, D., Hanicke, W., and Merboldt, K.-D. (1986). FLASH imaging. Rapid NMR imaging using low flip-angle pulses. *Journal of Magnetic Resonance (1969)*, 67(2):258–266.

Hahn, E. L. (1950). Spin echoes. *Physical Review*, 80(4):580.

Hargreaves, B. A., Vasanawala, S. S., Pauly, J. M., and Nishimura, D. G. (2001). Characterization and reduction of the transient response in steady-state MR imaging. *Magnetic Resonance in Medicine*, 46(1):149–158.

He, J. and Blamire, A. M. (2010). Application of variable-rate selective excitation pulses for spin labeling in perfusion MRI. *Magnetic Resonance in Medicine*, 63(3):842–847.

Henkelman, R., Stanisz, G., and Graham, S. (2001). Magnetization transfer in MRI: a review. *NMR in Biomedicine*, 14(2):57–64.

Henkelman, R. M., Huang, X., Xiang, Q.-S., Stanisz, G., Swanson, S. D., and Bronskill, M. J. (1993). Quantitative interpretation of magnetization transfer. *Magnetic Resonance in Medicine*, 29(6):759–766.

Hennig, J., Nauerth, A., and Friedburg, H. (1986). RARE imaging: a fast imaging method for clinical MR. *Magnetic Resonance in Medicine*, 3(6):823–833.

Herscovitch, P. and Raichle, M. E. (1985). What is the correct value for the brain-blood partition coefficient for water? *Journal of Cerebral Blood Flow & Metabolism*, 5(1):65–69.

Hinshaw, W. S. (1976). Image formation by nuclear magnetic resonance: The sensitive-point method. *Journal of Applied Physics*, 47(8):3709–3721.

Hodneland, E., Lundervold, A., Rørvik, J., and Munthe-Kaas, A. Z. (2014). Normalized gradient fields for nonlinear motion correction of DCE-MRI time series. *Computerized Medical Imaging and Graphics*, 38(3):202 – 210.

Hueper, K., Gutberlet, M., Rong, S., Hartung, D., Mengel, M., Lu, X., Haller, H., Wacker, F., Meier, M., and Gueler, F. (2014). Acute kidney injury: arterial spin labeling to monitor renal perfusion impairment in mice-comparison with histopathologic results and renal function. *Radiology*, 270(1):117–124.

Ito, H., Tomooka, T., Sakai, N., Yu, H., Higashino, Y., Fujii, K., Masuyama, T., Kitabatake, A., and Minamino, T. (1992). Lack of myocardial perfusion immediately after successful thrombolysis. a predictor of poor recovery of left ventricular function in anterior myocardial infarction. *Circulation*, 85(5):1699–1705.

Jakob, P. M., Grisowld, M. A., Edelman, R. R., and Sodickson, D. K. (1998). AUTO-SMASH: a self-calibrating technique for SMASH imaging. *Magnetic Resonance Materials in Physics, Biology and Medicine*, 7(1):42–54.

Jaynes, E. (1955). Matrix treatment of nuclear induction. *Physical Review*, 98(4):1099.

Jerosch-Herold, M., Seethamraju, R. T., Swingen, C. M., Wilke, N. M., and Stillman, A. E. (2004). Analysis of myocardial perfusion MRI. *Journal of Magnetic Resonance Imaging*, 19(6):758–770.

Karger, N., Biederer, J., Lüsse, S., Grimm, J., Steffens, J.-C., Heller, M., and Glüer, C.-C. (2000). Quantitation of renal perfusion using arterial spin labeling with FAIR-UFLARE. *Magnetic Resonance Imaging*, 18(6):641–647.

Kety, S. S. and Schmidt, C. F. (1945). The determination of cerebral blood flow in man by the use of nitrous oxide in low concentrations. *American Journal of Physiology*, 143:53–66.

Kim, S.-G. (1995). Quantification of relative cerebral blood flow change by flow-sensitive alternating inversion recovery (FAIR) technique: Application to functional mapping. *Magnetic Resonance in Medicine*, 34(3):293–301.

Kim, S.-G. and Tsekos, N. V. (1997). Perfusion imaging by a flow-sensitive alternating inversion recovery (FAIR) technique: Application to functional brain imaging. *Magnetic Resonance in Medicine*, 37(3):425–435.

Kinsey, G. R., Li, L., and Okusa, M. D. (2008). Inflammation in acute kidney injury. *Nephron Experimental Nephrology*, 109(4):e102–e107.

Kinsey, G. R. and Okusa, M. D. (2011). Pathogenesis of acute kidney injury: foundation for clinical practice. *American Journal of Kidney Diseases*, 58(2):291–301.

Klotz, S. (2013). *Experimentelle Untersuchung des nephroprotektiven Potenzials von N-Okatnoyl-Dopamin in vivo bei akutem ischämischen Nierenversagen und nach Nierentransplantation*. PhD thesis.

Krämer, P. (2014). *Entwicklung von Methoden zur 3D Messung der T_1- und T_2-Relaxationszeiten mit Steady-State Bildgebung bei 3 T*. PhD thesis.

Kwong, K. K., Belliveau, J. W., Chesler, D. A., Goldberg, I. E., Weisskoff, R. M., Poncelet, B. P., Kennedy, D. N., Hoppel, B. E., Cohen, M. S., and Turner, R. (1992). Dynamic magnetic resonance imaging of human brain activity during primary sensory stimulation. *Proceedings of the National Academy of Sciences*, 89(12):5675–5679.

Kwong, K. K., Chesler, D. A., Weisskoff, R. M., Donahue, K. M., Davis, T. L., Ostergaard, L., Campbell, T. A., and Rosen, B. R. (1995). Mr perfusion studies with T_1-weighted echo planar imaging. *Magnetic Resonance in Medicine*, 34(6):878–887.

Lanzman, R. S., Wittsack, H.-J., Martirosian, P., Zgoura, P., Bilk, P., Kröpil, P., Schick, F., Voiculescu, A., and Blondin, D. (2010). Quantification of renal allograft perfusion using arterial spin labeling MRI: initial results. *European Radiology*, 20(6):1485–1491.

Larson, P. E., Conolly, S. M., Pauly, J. M., and Nishimura, D. G. (2007). Using adiabatic inversion pulses for long-T_2 suppression in ultrashort echo time (UTE) imaging. *Magnetic Resonance in Medicine*, 58(5):952–961.

Lassen, N. A. and Perl, W. (1979). Tracer kinetic methods in medical physiology.

Lauterbur, P. C. et al. (1973). Image formation by induced local interactions: examples employing nuclear magnetic resonance. *Nature*, 242(5394):190–191.

Le Dorze, M., Legrand, M., Payen, D., and Ince, C. (2009). The role of the microcirculation in acute kidney injury. *Current Opinion in Critical Care*, 15(6):503–508.

Le Roux, P. (1988). Exact synthesis of radio frequency waveforms. In *Proc. 7th SMRM*, volume 1049.

Le Roux, P. (2003). Simplified model and stabilization of SSFP sequences. *Journal of Magnetic Resonance*, 163(1):23–37.

Leenders, K., Perani, D., Lammertsma, A., Heather, J., Buckingham, P., Jones, T., Healy, M., Gibbs, J., Wise, R., Hatazawa, J., et al. (1990). Cerebral blood flow, blood volume and oxygen utilization normal values and effect of age. *Brain*, 113(1):27–47.

Levenberg, K. (1944). A method for the solution of certain problems in least squares. *Quarterly of Applied Mathematics*, 2:164–168.

Levitt, M. H. (2008). *Spin dynamics: basics of nuclear magnetic resonance*. John Wiley & Sons.

Lietzmann, F., Zöllner, F. G., Attenberger, U. I., Haneder, S., Michaely, H. J., and Schad, L. R. (2012). DCE-MRI of the human kidney using BLADE: A feasibility study in healthy volunteers. *Journal of Magnetic Resonance Imaging*, 35(4):868–874.

Lu, H., Clingman, C., Golay, X., and van Zijl, P. (2004). Determining the longitudinal relaxation time T_1 of blood at 3.0 Tesla. *Magnetic Resonance in Medicine*, 52(3):679–682.

Luh, W. M., Wong, E. C., Bandettini, P. A., and Hyde, J. S. (1999). QUIPSS II with thin-slice TI1 periodic saturation: a method for improving accuracy of quantitative perfusion imaging using pulsed arterial spin labeling. *Magnetic Resonance in Medicine*, 41(6):1246–1254.

MacIntosh, B. J., Filippini, N., Chappell, M. A., Woolrich, M. W., Mackay, C. E., and Jezzard, P. (2010). Assessment of arterial arrival times derived from multiple inversion time pulsed arterial spin labeling MRI. *Magnetic Resonance in Medicine*, 63(3):641–647.

Maleki, N., Dai, W., and Alsop, D. C. (2012). Optimization of background suppression for arterial spin labeling perfusion imaging. *Magnetic Resonance Materials in Physics, Biology and Medicine*, 25(2):127–133.

Mani, S., Pauly, J., Conolly, S., Meyer, C., and Nishimura, D. (1997). Background suppression with multiple inversion recovery nulling: applications to projective angiography. *Magnetic Resonance in Medicine*, 37(6):898–905.

Mansfield, P. (1977). Multi-planar image formation using NMR spin echoes. *Journal of Physics C: Solid State Physics*, 10(3):L55.

Marquardt, D. W. (1963). An algorithm for least-squares estimation of nonlinear parameters. *Journal of the Society for Industrial & Applied Mathematics*, 11(2):431–441.

Martirosian, P., Klose, U., Mader, I., and Schick, F. (2004). FAIR true-FISP perfusion imaging of the kidneys. *Magnetic Resonance in Medicine*, 51(2):353–361.

Meier, P. and Zierler, K. L. (1954). On the theory of the indicator-dilution method for measurement of blood flow and volume. *Journal of Applied Physiology*, 6(12):731–744.

Mendichovszky, I., Cutajar, M., and Gordon, I. (2009). Reproducibility of the aortic input function (AIF) derived from dynamic contrast-enhanced magnetic resonance imaging (DCE-MRI) of the kidneys in a volunteer study. *European Journal of Radiology*, 71(3):576–581.

Michaely, H., Herrmann, K., Nael, K., Oesingmann, N., Reiser, M., and Schoenberg, S. (2007). Functional renal imaging: nonvascular renal disease. *Abdominal Imaging*, 32(1):1–16.

Michaely, H. J., Sourbron, S. P., Buettner, C., Lodemann, K.-P., Reiser, M. F., and Schoenberg, S. O. (2008). Temporal constraints in renal perfusion imaging with a 2-compartment model. *Investigative Radiology*, 43(2):120–128.

Mildner, T., Trampel, R., Möller, H. E., Schäfer, A., Wiggins, C. J., and Norris, D. G. (2003). Functional perfusion imaging using continuous arterial spin labeling with separate labeling and imaging coils at 3 T. *Magnetic Resonance in Medicine*, 49(5):791–795.

Nankivell, B. J. and Alexander, S. I. (2010). Rejection of the kidney allograft. *New England Journal of Medicine*, 363(15):1451–1462.

Nankivell, B. J. and Kuypers, D. R. (2011). Diagnosis and prevention of chronic kidney allograft loss. *The Lancet*, 378(9800):1428–1437.

Nöth, U., Meadows, G. E., Kotajima, F., Deichmann, R., Corfield, D. R., and Turner, R. (2006). Cerebral vascular response to hypercapnia: determination with perfusion MRI at 1.5 and 3.0 Tesla using a pulsed arterial spin labeling technique. *Journal of Magnetic Resonance Imaging*, 24(6):1229–1235.

Nyquist, H. (1928). Thermal agitation of electric charge in conductors. *Physical Review*, 32(1):110–113.

Ogg, R. J., Kingsley, R., and Taylor, J. S. (1994). Wet, a T_1- and B_1-insensitive water-suppression method for in vivo localized ^{1}H NMR spectroscopy. *Journal of Magnetic Resonance, Series B*, 104(1):1–10.

Oppelt, A., Graumann, R., Barfuss, H., Fischer, H., Hartl, W., and Schajor, W. (1986). FISP: eine neue schnelle Pulssequenz fr die Kernspintomographie. *Electomedica*, 54:15–18.

Ordidge, R. J., Wylezinska, M., Hugg, J. W., Butterworth, E., and Franconi, F. (1996). Frequency offset corrected inversion (FOCI) pulses for use in localized spectroscopy. *Magnetic Resonance in Medicine*, 36(4):562–566.

Østergaard, L., Sorensen, A. G., Kwong, K. K., Weisskoff, R. M., Gyldensted, C., and Rosen, B. R. (1996a). High resolution measurement of cerebral blood flow using intravascular tracer bolus passages. Part II: Experimental comparison and preliminary results. *Magnetic Resonance in Medicine*, 36(5):726–736.

Østergaard, L., Weisskoff, R. M., Chesler, D. A., Gyldensted, C., and Rosen, B. R. (1996b). High resolution measurement of cerebral blood flow using intravascular tracer bolus passages. Part I: Mathematical approach and statistical analysis. *Magnetic Resonance in Medicine*, 36(5):715–725.

Ouwerkerk, R. (2014). Adiabatic multi-band RF pulses for selective signal suppression in a magnetic resonance imaging. US Patent 8,633,695.

Park, S.-H., Wang, D. J. J., and Duong, T. Q. (2013). Balanced steady state free precession for arterial spin labeling MRI: Initial experience for blood flow mapping in human brain, retina, and kidney. *Magnetic Resonance Imaging*, 31(7):1044–1050.

Parkes, L. M. (2005). Quantification of cerebral perfusion using arterial spin labeling: Two-compartment models. *Journal of Magnetic Resonance Imaging*, 22(6):732–736.

Pauli, W. (1924). Zur Frage der theoretischen Deutung der Satelliten einiger Spektrallinien und ihrer Beeinflussung durch magnetische Felder. *Naturwissenschaften*, 12(37):741–743.

Pauly, J., Le Roux, P., Nishimura, D., and Macovski, A. (1991). Parameter relations for the Shinnar-Le Roux selective excitation pulse design algorithm [NMR imaging]. *IEEE Transactions on Medical Imaging*, 10(1):53–65.

Payne, G. S. and Leach, M. O. (1997). Implementation and evaluation of frequency offset corrected inversion (FOCI) pulses on a clinical mr system. *Magnetic Resonance in Medicine*, 38(5):828–833.

Pedersen, M., Laustsen, C., Perot, V., Basseau, F., Moonen, C., and Grenier, N. (2010). Renal hemodynamics and oxygenation in transient renal artery occluded rats evaluated with iron-oxide particles and oxygenation-sensitive imaging. *Zeitschrift für Medizinische Physik*, 20(2):134–142.

Petersen, E., Zimine, I., Ho, Y. L., and Golay, X. (2006a). Non-invasive measurement of perfusion: a critical review of arterial spin labelling techniques. *British Journal of Radiology*, 79(944):688–701.

Petersen, E. T., Lim, T., and Golay, X. (2006b). Model-free arterial spin labeling quantification approach for perfusion MRI. *Magnetic Resonance in Medicine*, 55(2):219–232.

Petersen, E. T., Mouridsen, K., and Golay, X. (2010). The QUASAR reproducibility study, Part II: Results from a multi-center Arterial Spin Labeling test–retest study. *Neuroimage*, 49(1):104–113.

Petr, J., Schramm, G., Hofheinz, F., Langner, J., and Hoff, J. (2013). Modeling magnetization transfer effects of Q2TIPS bolus saturation in multi-TI pulsed arterial spin labeling. *Magnetic Resonance in Medicine*.

Pettigrew, R., Avruch, L., Dannels, W., Coumans, J., and Bernardino, M. (1986). Fast-field-echo MR imaging with Gd-DTPA: physiologic evaluation of the kidney and liver. *Radiology*, 160(2):561–563.

Prasad, P. V. and Priatna, A. (1999). Functional imaging of the kidneys with fast MRI techniques. *European Journal of Radiology*, 29(2):133–148.

Pruessmann, K. P., Weiger, M., Scheidegger, M. B., Boesiger, P., et al. (1999). SENSE: sensitivity encoding for fast MRI. *Magnetic resonance in medicine*, 42(5):952–962.

Purcell, E. M., Torrey, H. C., and Pound, R. V. (1946). Resonance absorption by nuclear magnetic moments in a solid. *Phys. Rev.*, 69:37–38.

Rabi, I., Millman, S., Kusch, P., and Zacharias, J. (1939). The molecular beam resonance method for measuring nuclear magnetic moments. the magnetic moments of ${}^{3}_{6}$Li, ${}^{3}_{7}$Li and ${}^{9}_{1}$9F. *Physical Review*, 55(6):526.

Rieg, T., Richter, K., Osswald, H., and Vallon, V. (2004). Renal function in mice: alpha-chloralose versus thiobutabarbital anesthesia. In *Naunyn-Schmiedebergs Archives of Pharmacology*, volume 369, pages R102–R102. Springer Verlag, New York.

Roberts, D. A., Detre, J. A., Bolinger, L., Insko, E. K., Lenkinski, R. E., Pentecost, M. J., and Leigh Jr, J. S. (1995). Renal perfusion in humans: MR imaging with spin tagging of arterial water. *Radiology*, 196(1):281–286.

Roberts, D. A., Rizi, R., Lenkinski, R. E., and Leigh, J. S. (1996). Magnetic resonance imaging of the brain: Blood partition coefficient for water: Application to spin-tagging measurement of perfusion. *Journal of Magnetic Resonance Imaging*, 6(2):363–366.

Roemer, P., Edelstein, W., Hayes, C., Souza, S., and Mueller, O. (1990). The NMR phased array. *Magnetic Resonance in Medicine*, 16(2):192–225.

Rosen, B. R., Belliveau, J. W., Vevea, J. M., and Brady, T. J. (1990). Perfusion imaging with NMR contrast agents. *Magnetic Resonance in Medicine*, 14(2):249–265.

Runge, V., Clanton, J., Herzer, W., Gibbs, S., Price, A., Partain, C., and James, A. (1984). Intravascular contrast agents suitable for magnetic resonance imaging. *Radiology*, 153(1):171–176.

Salmeron, B. and Stein, E. (2001). Pharmacological applications of magnetic resonance imaging. *Psychopharmacology Bulletin*, 36(1):102–129.

Schewzow, K. (2010). Nierenperfusionsbildgebung mittels Arterial Spin Labeling bei 3 Tesla. Master's thesis.

Schwabl, F. (1998). *Quantenmechanik (QM I)*. Springer.

Shinnar, M., Bolinger, L., and Leigh, J. S. (1989a). The use of finite impulse response filters in pulse design. *Magnetic Resonance in Medicine*, 12(1):81–87.

Shinnar, M., Eleff, S., Subramanian, H., and Leigh, J. S. (1989b). The synthesis of pulse sequences yielding arbitrary magnetization vectors. *Magnetic Resonance in Medicine*, 12(1):74–80.

Shinnar, M. and Leigh, J. S. (1989). The application of spinors to pulse synthesis and analysis. *Magnetic Resonance in Medicine*, 12(1):93–98.

Silva, A. C., Zhang, W., Williams, D. S., and Koretsky, A. P. (1995). Multi-Slice MRI of Rat Brain Perfusion During Amphetamine Stimulation Using Arterial Spin Labeling. *Magnetic Resonance in Medicine*, 33(2):209–214.

Silver, M., Joseph, R., Chen, C.-N., Sank, V., and Hoult, D. (1984). Selective population inversion in NMR. *Nature*, 310:681–683.

Silver, M., Joseph, R., and Hoult, D. (1985). Selective spin inversion in nuclear magnetic resonance and coherent optics through an exact solution of the Bloch-Riccati equation. *Physical Review A*, 31(4):2753.

Slichter, C. P. (1990). *Principles of magnetic resonance*, volume 1. Springer.

Sodickson, D. K. and Manning, W. J. (1997). Simultaneous acquisition of spatial harmonics (SMASH): fast imaging with radiofrequency coil arrays. *Magnetic Resonance in Medicine*, 38(4):591–603.

Song, R., Loeffler, R. B., and Hillenbrand, C. M. (2010). Improved renal perfusion measurement with a dual navigator-gated Q2TIPS FAIR technique. *Magnetic Resonance in Medicine*, 64(5):1352–1359.

Song, T., Laine, A. F., Chen, Q., Rusinek, H., Bokacheva, L., Lim, R. P., Laub, G., Kroeker, R., and Lee, V. S. (2009). Optimal k-space sampling for dynamic contrast-enhanced MRI with an application to MR renography. *Magnetic Resonance in Medicine*, 61(5):1242–1248.

Sourbron, S. (2005). *Perfusion quantification with bolus-tracking MRI*. PhD thesis.

Sourbron, S., Dujardin, M., Makkat, S., and Luypaert, R. (2007a). Pixel-by-pixel deconvolution of bolus-tracking data: optimization and implementation. *Physics in Medicine and Biology*, 52(2):429.

Sourbron, S., Luypaert, R., Morhard, D., Seelos, K., Reiser, M., and Peller, M. (2007b). Deconvolution of bolus-tracking data: a comparison of discretization methods. *Physics in Medicine and Biology*, 52(22):6761.

Sourbron, S., Luypaert, R., Van Schuerbeek, P., Dujardin, M., and Stadnik, T. (2004). Choice of the regularization parameter for perfusion quantification with MRI. *Physics in Medicine and Biology*, 49(14):3307.

Sourbron, S., Stubbe, I., Luypaert, R., and Osteaux, M. (2003). Discretising the convolution product in DSC-MRI based quantification of CBF. *Magnetic Resonance Materials in Physics, Biology and Medicine*, 16:134.

Sourbron, S. P. and Buckley, D. L. (2013). Classic models for dynamic contrast-enhanced MRI. *NMR in Biomedicine*.

Sourbron, S. P., Michaely, H. J., Reiser, M. F., and Schoenberg, S. O. (2008). MRI-measurement of perfusion and glomerular filtration in the human kidney with a separable compartment model. *Investigative Radiology*, 43(1):40–48.

Stanisz, G. J., Odrobina, E. E., Pun, J., Escaravage, M., Graham, S. J., Bronskill, M. J., and Henkelman, R. M. (2005). t_1, t_2 relaxation and magnetization transfer in tissue at 3t. *Magnetic Resonance in Medicine*, 54(3):507–512.

Student, B. (1908). The probable error of a mean. *Biometrika*, 6(1):1–25.

Sutton, T. A., Fisher, C. J., and Molitoris, B. A. (2002). Microvascular endothelial injury and dysfunction during ischemic acute renal failure. *Kidney International*, 62(5):1539–1549.

Talagala, S. L., Ye, F. Q., Ledden, P. J., and Chesnick, S. (2004). Whole-brain 3D perfusion MRI at 3.0 T using CASL with a separate labeling coil. *Magnetic Resonance in Medicine*, 52(1):131–140.

Tannús, A., Garwood, M., et al. (1997). Adiabatic pulses. *NMR in Biomedicine*, 10(8):423–434.

Terasaki, P. I. and Cai, J. (2005). Humoral theory of transplantation: further evidence. *Current Opinion in Immunology*, 17(5):541–545.

Tofts, P. S. and Kermode, A. G. (1991). Measurement of the blood-brain barrier permeability and leakage space using dynamic MR imaging. 1. Fundamental concepts. *Magnetic Resonance in Medicine*, 17(2):357–367.

Vidorreta, M., Wang, Z., Rodríguez, I., Pastor, M. A., Detre, J. A., and Fernández-Seara, M. A. (2013). Comparison of 2D and 3D single-shot ASL perfusion fMRI sequences. *Neuroimage*, 66:662–671.

Vogt, F., Eggebrecht, H., Laub, G., Kroeker, R., Schmidt, M., Barkhausen, J., and Ladd, S. (2007). High spatial and temporal resolution MRA (TWIST) in acute aortic dissection. *Proc ISMRM, Berlin*, page 92.

Waaga, A. M., Gasser, M., Laskowski, I., and Tilney, N. L. (2000). Mechanisms of chronic rejection. *Current Opinion in Immunology*, 12(5):517–521.

Weber, M.-A., Henze, M., Tüttenberg, J., Stieltjes, B., Meissner, M., Zimmer, F., Burkholder, I., Kroll, A., Combs, S. E., Vogt-Schaden, M., et al. (2010). Biopsy targeting gliomas: do functional imaging techniques identify similar target areas? *Investigative Radiology*, 45(12):755–768.

Williams, D. S., Detre, J. A., Leigh, J. S., and Koretsky, A. P. (1992). Magnetic resonance imaging of perfusion using spin inversion of arterial water. *Proceedings of the National Academy of Sciences*, 89(1):212–216.

Wilman, A. H. and Riederer, S. J. (1996). Improved centric phase encoding orders for three-dimensional magnetization-prepared mr angiography. *Magnetic Resonance in Medicine*, 36(3):384–392.

Winter, J. D., St Lawrence, K. S., and Cheng, H.-L. M. (2011). Quantification of renal perfusion: Comparison of arterial spin labeling and dynamic contrast-enhanced MRI. *Journal of Magnetic Resonance Imaging*, 34(3):608–615.

Wolff, S. D. and Balaban, R. S. (1989). Magnetization transfer contrast (MTC) and tissue water proton relaxation in vivo. *Magnetic Resonance in Medicine*, 10(1):135–144.

Wong, E. C., Buxton, R. B., and Frank, L. R. (1997). Implementation of quantitative perfusion imaging techniques for functional brain mapping using pulsed arterial spin labeling. *NMR in Biomedicie*, 10(4-5):237–249.

Wong, E. C., Buxton, R. B., and Frank, L. R. (1998a). Quantitative imaging of perfusion using a single subtraction (QUIPSS and QUIPSS II). *Magnetic Resonance in Medicine*, 39(5):702–708.

Wong, E. C., Buxton, R. B., and Frank, L. R. (1998b). A theoretical and experimental comparison of continuous and pulsed arterial spin labeling techniques for quantitative perfusion imaging. *Magnetic Resonance in Medicine*, 40(3):348–355.

World Kidney Day (2014). Chronic kidney disease & aging [press release]. *Retrieved from http://www.worldkidneyday.org/materials/press-materials/.*

Wu, W.-C., Edlow, B. L., Elliot, M. A., Wang, J., and Detre, J. A. (2009). Physiological modulations in arterial spin labeling perfusion magnetic resonance imaging. *IEEE Transactions on Medical Imaging*, 28(5):703–709.

Wu, W.-C., Fernández-Seara, M., Detre, J. A., Wehrli, F. W., and Wang, J. (2007). A theoretical and experimental investigation of the tagging efficiency of pseudocontinuous arterial spin labeling. *Magnetic Resonance in Medicine*, 58(5):1020–1027.

Wu, W.-C., Su, M.-Y., Chang, C.-C., Tseng, W.-Y. I., and Liu, K.-L. (2011). Renal perfusion 3 T MR imaging: a comparative study of arterial spin labeling and dynamic contrast-enhanced techniques. *Radiology*, 261(3):845–853.

Ye, F. Q., Frank, J. A., Weinberger, D. R., and McLaughlin, A. C. (2000). Noise reduction in 3D perfusion imaging by attenuating the static signal in arterial spin tagging (ASSIST). *Magnetic Resonance in Medicine*, 44(1):92–100.

Yongbi, M. N., Yang, Y., Frank, J. A., and Duyn, J. H. (1999). Multislice perfusion imaging in human brain using the C-FOCI inversion pulse: comparison with hyperbolic secant. *Magnetic Resonance in Medicine*, 42(6):1098–1105.

Zhang, W., Silva, A. C., Williams, D. S., and Koretsky, A. P. (1995). NMR measurement of perfusion using arterial spin labeling without saturation of macromolecular spins. *Magnetic Resonance in Medicine*, 33(3):370–376.

Zhou, J., Wilson, D. A., Ulatowski, J. A., Traystman, R. J., and van Zijl, P. C. (2001). Two-compartment exchange model for perfusion quantification using arterial spin tagging. *Journal of Cerebral Blood Flow & Metabolism*, 21(4):440–455.

Zierler, K. L. (1962). Theoretical basis of indicator-dilution methods for measuring flow and volume. *Circulation Research*, 10(3):393–407.

Zimmer, F., Zöllner, F. G., Hoeger, S., Klotz, S., Tsagogiorgas, C., Krämer, B. K., and Schad, L. R. (2013). Quantitative Renal Perfusion Measurements in a Rat Model of Acute Kidney Injury at 3T: Testing Inter-and Intramethodical Significance of ASL and DCE-MRI. *PloS one*, 8(1):e53849.

Zöllner, F. G., Sance, R., Rogelj, P., Ledesma-Carbayo, M. J., Rørvik, J., Santos, A., and Lundervold, A. (2009). Assessment of 3D DCE-MRI of the kidneys using non-rigid image registration and segmentation of voxel time courses. *Computerized Medical Imaging and Graphics*, 33(3):171–181.

Zöllner, F. G., Weisser, G., Reich, M., Kaiser, S., Schoenberg, S. O., Sourbron, S. P., and Schad, L. R. (2013). UMMPerfusion: an open source software tool towards quantitative MRI perfusion analysis in clinical routine. *Journal of Digital Imaging*, 26(2):344–352.

Zur, Y., Stokar, S., and Bendel, P. (1988). An analysis of fast imaging sequences with steady-state transverse magnetization refocusing. *Magnetic Resonance in Medicine*, 6(2):175–193.

Zur, Y., Wood, M., and Neuringer, L. (1991). Spoiling of transverse magnetization in steady-state sequences. *Magnetic Resonance in Medicine*, 21(2):251–263.

Danke!

Viele Leute haben auf unterschiedlichste Art und Weise zum Gelingen dieser Arbeit beigetragen. Mein besonderer Dank gilt in diesem Zusammenhang...

...Prof. Dr. Lothar Schad, der mir die Möglichkeit gab an seinem Lehrstuhl zu promovieren und mich bei meiner Arbeit in jeglicher Hinsicht immer vollstens unterstützt hat.

...Prof. Dr. Wolfgang Schlegel, der sich kurzfristig bereit erklärt hat diese Arbeit zu begutachten und Teil meines Prüfungskomitees zu sein.

...Dr. Frank Zöllner für die Unterstützung, sein Engagement, seine Hilfsbereitschaft und vieles mehr.

...Dr. Sarah Klotz, PD Dr. Simone Höger und Prof. Dr. Benito Yard für die tolle Zusammenarbeit. Insbesondere Sarah danke ich für unterhaltsame Stunden am Scanner und dafür, dass wir dabei nie verhungert sind.

...Dr. Florian Lietzmann, für 3 ± 2 großartige Jahre Perfusions-Büro.

...Dr. Philipp Krämer und Dr. Simon Konstandin für ihre kompetente fachliche Hilfe, wenn ich mal keine "IDEA" mehr hatte. Philipp danke ich außerdem fürs Bereitstellen der "TruFi".

...allen aktuellen und ehemaligen Mitgliedern des CKM-Teams, in dem ich mich immer sehr wohl gefühlt habe und dem ich viele sportliche, unterhaltsame und gesellige Stunden verdanke. Stellvertretend genannt seien: Dr. Sebastian Baier, Dr. Patrick Heiler, Dr. Moritz Mie, Dr. Christina Hopfgarten, Åsmund Kjørstad, Jonathan Lommen und Nadja Meßner.

...Frank, Simon, Konni, Philipp und Flo fürs Korrekturlesen dieser Arbeit.

...meinen Freunden in Heidelberg und Umgebung, die mich teilweise schon seit Beginn des Studiums begleiten und diese Zeit zu etwas ganz Besonderem gemacht haben. Dies sind insbesondere: Marco, Marc, Tobi, Konni, Alex, Fritsch, Yvo, Nathan und natürlich die "Berts". Mein Dank gilt außerdem Michael, nicht nur für die unzähligen Trainings- und Wettkampfkilometer.

...meinen Eltern Jürgen und Regata, die durch jedwede Unterstützung und ihr Vertrauen diese Arbeit überhaupt erst ermöglicht haben, sowie meinen Schwestern Ani und Leni und meinem Opa Rudi. Danke, dass ihr immer für mich da seid!

...meiner Freundin Linda: "Danke, dass es Dich gibt!"